Determining sediment flux of the Rhine over the next 10,000 years using Badlands

A feasibility study on using Badlands for future climatic and anthropogenic land use changes with a case study on determining the sediment flux of the Lower Rhine

Jesse M. Steinvoort

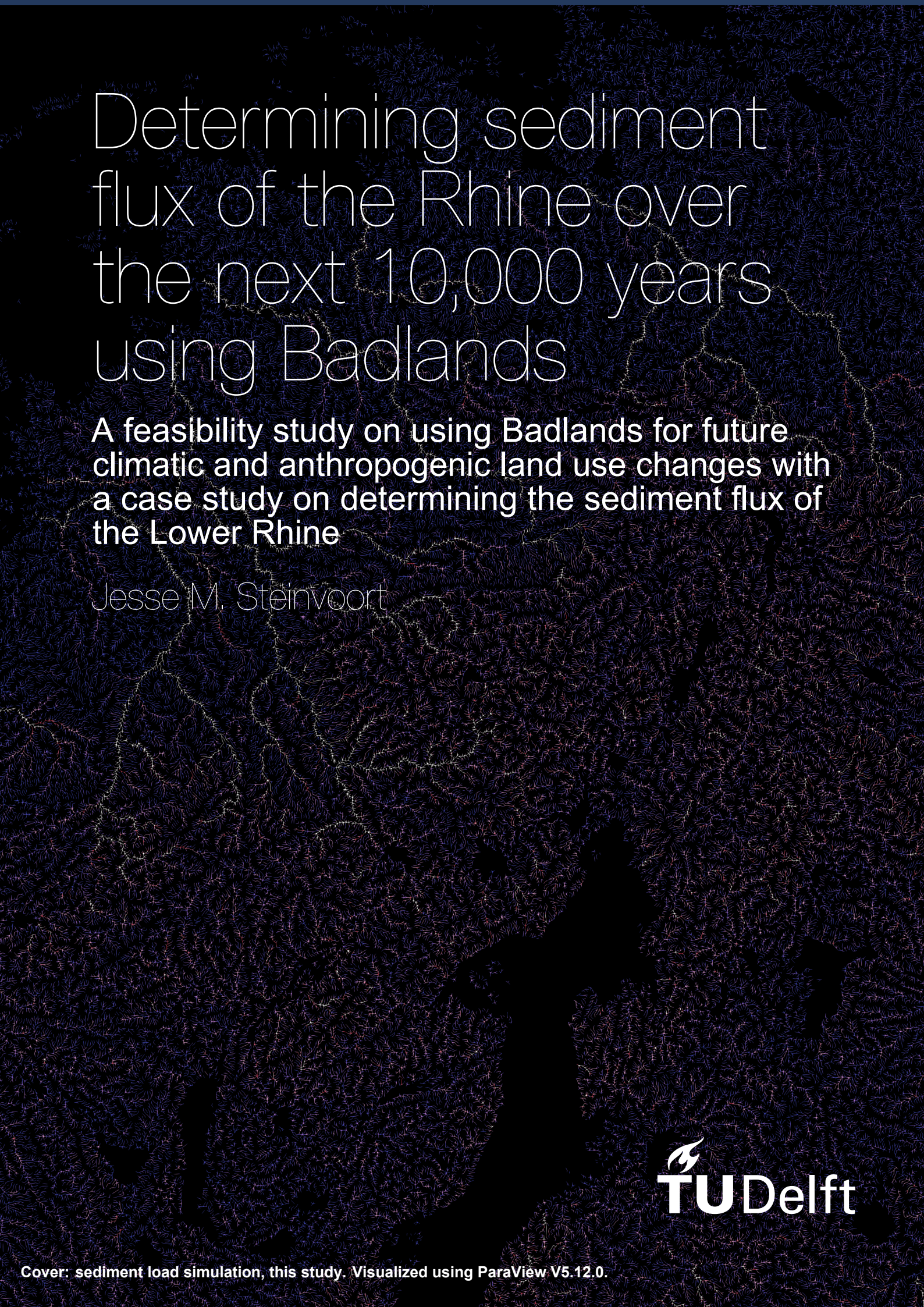

TU Delft

Cover: sediment load simulation, this study. Visualized using ParaView V5.12.0.

Determining sediment flux of the Rhine over the next 10,000 years using Badlands

A feasibility study on using Badlands for future climatic and anthropogenic land use changes with a case study on determining the sediment flux of the Lower Rhine

Thesis report

by

Jesse M. Steinvoort

to obtain the degree of Master of Science
at the Delft University of Technology
to be defended publicly on June 26, 2024 at 13:00

Thesis committee:

Chair:	Dr. R.J.G. Charton
Supervisors:	Dr. S.C. Toby
	Dr. K.B.J. Dunne
Place:	Faculty of Civil Engineering and Geosciences, Delft
Project Duration:	February, 2024 - June, 2024
Student number:	4679814

Faculty of Civil Engineering and Geosciences · Delft University of Technology

Abstract

Sediments play a crucial role in civil engineering branches like delta and river flood risk management and in maintaining natural ecosystems. Changes in the availability of sediment can have a major impact on all of these. It is therefore crucial to understand how sediment load in a source-to-sink system behaves in changing environments. Studies quantifying these behaviors often do not span further than a few decades to a hundred years. Carbon emissions will likely have an effect on our climate on the much larger scale of millennia. Humans have begun to plan and adapt their behavior to mitigate climate change by way of greenification of urban areas and replacing traditional agricultural practices by more sustainable alternatives. This study looks at the influence of climate change and different anthropogenic land use changes on the sediment load of the river Rhine by integrating tectonics, sea-level and precipitation change, and land use change for the coming 10,000 years using Badlands. This is done by utilizing a scenario-based approach. The essential role of topsoil dynamics, and a lack thereof in traditional landscape evolution models, such as Badlands, was identified. Using a general scale of topsoil and bedrock erodibilities calibrated to produce realistic sediment load in the Rhine, we found that any implementation of more sustainable land use like agroforestry is predicted to decrease the sediment load of the Rhine in most climate change scenarios, agreeing with similar studies that focused on short-term modeling. Implementing non-uniform precipitation change resulted in significantly different outcomes than using a uniform approximation, so it is advised to implement region-based precipitation change. Furthermore, Badlands has shown impressive versatility and adaptability, and shows potential to be used for the growing demand of studies that focus on predicting future influences of different processes in light of climate change using a holistic process-based approach.

Acknowledgments

This thesis has been prepared using European Union's Copernicus Land Monitoring Service information: available at Copernicus Land Monitoring Service (CLMS), 2020, and I acknowledge the E-OBS dataset from the EU-FP6 project UERRA (https://www.uerra.eu) and the Copernicus Climate Change Service, and the data providers in the ECA&D project (https://www.ecad.eu).

I am grateful for the opportunity to do my master thesis at the Applied Geology section at the TU Delft. I especially would like to express my gratitude to my supervisors Dr. Rémi Charton, Dr. Stephan Toby, and Dr. Kieran Dunne for providing excellent guidance and advice throughout my thesis, as well as giving me the freedom and opportunity to take my thesis in the direction that I wanted. Their support made it possible for this thesis to reach its full potential within the relatively limited time that was available for it.

I would like to extend my gratitude to Tristan Salles, developer of Badlands, for his valuable advice and swift replies to e-mails regarding Badlands. I would also like to thank Rémi and Katrin for letting me use their office to work, and for the fun and insightful conversations I had there.

I am very grateful to my partner Yvonne, who has helped me improve the quality of my thesis considerably through her valuable advice, as well as supporting me emotionally throughout this journey. Lastly I would like to acknowledge the support from my family and friends throughout this thesis.

Jesse Marinus Steinvoort,
Zwijndrecht, June 2024

Contents

Nomenclature

List of Abbreviations

AOI	Area of Interest
CFL	Courant–Friedrichs–Lewy
CHR	International Commission for the Hydrology of the Rhine basin
CLC	CORINE Land Cover
CLMS	Copernicus Land Monitoring Service
CORINE	Coordination of Information on the Environment
CRS	Coordinate Reference System
DTB	Depth-to-Bedrock
EMODnet	European Marine Observation and Data Network
EPSG	European Petroleum Survey Group
ESDB	European Soil Database
ESS	Earth System Science
FAO	Food and Agriculture Organization of the United States
GHG	Green House Gasses
GIA	Glacial Isostatic Adjustment
GMSL	Global Mean Sea Level
HDF	Hierarchical Data Format
ICPR	International Commission for the Protection of the Rhine
IPBES	Intergovernmental Science-Policy Platform on Biodiversity and Ecosystem Services
IPCC	Intergovernmental Panel on Climate Change
KS	Kolmogorov–Smirnov
LEM	Landscape Evolution Model
LGM	Last Glacial Maximum
LUCAS	Land Use/Cover Area frame Survey
MSL	Mean Sea Level
NTFPs	Non-timber Forest Products
POC	Proof of Concept
RCP	Representative Concentration Pathway
RQ	Research Question
RUSLE	Revised Universal Soil Loss Equation
SDGs	Sustainable Development Goals
SFD	Single–Flow–Direction
SLEM	Soil-Landscape Evolution Model
SPF	Soil Production Function
SPR	Soil Production Rate
SSP	Shared Socio-Economic Pathway
TIN	Triangulated Irregular Network
TRI	Topographic Ruggedness Index
TWI	Topographic Wetness Index
ULE	Urban Land Expansion
URG	Upper Rhine Graben
USGS	United States Geological Survey
WGS	World Geodetic System

Constants

g	Gravitational acceleration [m/s^2]
l, m, n	Dimensionless positive constants (Eq. 2.1)
m_t, n_t	Dimensionless positive constants (Eq. 2.2)

List of Symbols

$\lvert\nabla z_h\rvert$	Slope gradient on hillslopes
ΔP	Change in precipitation [%]

Δt_{max}	Time step limit
$\Delta_{\%,ab}$	Percentile difference between value a and b.
$\dot{\epsilon}$	Erosion rate [m/y *or* mm/y]
$\hat{\dot{\epsilon}}$	Mean erosion rate [mm/y]
κ	Wave number, $2\pi/L$ [1/m]
κ_d	Dimensional coefficient describing erodibility [tonne ha h MJ^{-1} ha^{-1} mm^{-1}]
κ_l	Scaling parameter
κ_t	Dimensional coefficient describing channel sediment transportability
κ_{hn}	Diffusion coefficient [m^2/s]
∇	Gradient operator, $\frac{\partial}{\partial x}\hat{\vec{i}} + \frac{\partial}{\partial y}\hat{\vec{j}} + \frac{\partial}{\partial z}\hat{\vec{k}}$
$\nabla^2 z_v$	Valley-bottom curvature
Ω	Surface area of Voronoi polygon
ω	Angular frequency, $2\pi/T$ [Hz]
ϕ	Porosity [-]
ρ_s	Sediment density [kg/m^3]
ρ_w	Water density [kg/m^3]
τ_c	Critical shear stress [Pa]
τ_w	Wave-induced bed shear stress [Pa]
θ	Angle of wave incidence [°]
$\vec{k}$	Unit vector parallel to breaking depth contour
$\vec{v}_l$	Longshore current velocity [m/s]
A	Drainage area [m^2]
a	Wave amplitude [m]
A_b	Wave-orbital semi-excursion [m]
c	Celerity (wave propagation velocity) [m/s]
C_e	Entrainment coefficient
C_h	Cover term
d	Water depth [m]
d_{50}	Median sediment grain size [m *or* μm]
f_i	Area fraction of component i
f_w	Wave friction factor
H	Wave height [m]
h_e	Erosion thickness [m]
h_i	Average surface height of node *i*
H_s	Significant wave height [m]
h_{av}	Average soil/sedimentary deposit thickness on uplands [m]
h_{uv}	Average thickness of upland valley bottom sedimentary deposits [m]
K	K-factor or erodibility factor, see κ_d
k_b	Bed roughness, $\frac{2\pi d_{50}}{12}$
K_{St}	Erodibility factor corrected for stoniness
L	Wavelength [m]
Li	Land use scenario *i*
l_{ij}	TIN arc length [°]
M	Textural factor of soil
m_c	Clay fraction content [%]
m_{silt}	Silt fraction content [%]
m_{vfs}	Very fine sand fraction content [%]
n_i	Number of neighbors connected to node *i*
OM	Organic matter content of soil
P	Net Precipitation
p	Permeability class of soil
Pi	Precipitation scenario *i*
Q_s	Fluvial incision rate [m/y]
q_s	Total volumetric sediment flux per unit width [m^3/s]
Q_t	Volumetric sediment transport capacity
$q_{s,ref}$	Reference volumetric sediment flux per unit width [m^3/s]
S	Local slope [m/km *or* ‰]
s	Structure class of soil
Si	Sea level scenario *i*

S_c	Critical slope [m/km *or* ‰]
St	Stoniness correction factor
T	Wave period [s]
Ti	Vertical displacement (Tectonic) scenario *i*
U	Source term representing baselevel change
$u_{w,b}$	Maximum bottom wave-orbital velocity [m/s]
w_{ij}	Width of edge between nodes *i,j*
z	Vertical coordinate [m]

List of Figures

List of Tables

1

Introduction

The sediment flux in a source-to-sink system is determined by the effects of climate, sea-level, tectonics, and sediment availability and mobility (Salles and Hardiman, 2016). Apart from the tectonic influence, the others are heavily influenced by global climate change (Intergovernmental Panel on Climate Change: IPCC (2022)). Sediment flux is an essential part in fluvial, deltaic, and marine sedimentary systems, and changes in this sediment flux can have significant impacts on society (J. R. Cox, Dunn, et al., 2021; Yi et al., 2021). As a large part of the Netherlands is situated on fluvial and deltaic systems (e.g. Lower Rhine-Meuse delta) and relies heavily on available sediments to create coastal defenses, it is essential to identify the influence of climatic changes, sea level changes, and sediment availability and movement in light of different climate scenarios. In order to efficiently and accurately model future sediment flux, we need to incorporate all of these influences into a predictive landscape evolution model. Numerous numerical models have been proposed to simulate the evolution of Earth's surface over geological timescales, based on different driving mechanisms like tectonics or climatic variability (Howard et al., 1994; Salles and Hardiman, 2016; Tucker and Hancock, 2010; Whipple and Tucker, 2002). Badlands is an integrative framework that provides a flexible description between land, marine, and reef systems (Salles and Hardiman, 2016). Its focus lies primarily "in the description of Earth surface evolution and sedimentary basins formation over regional to continental scale and geological time (thousands to millions of years)", with a possible temporal resolution of 100 years (Salles and Hardiman, 2016). As part of a research group that focus on predicting future landscapes, the feasibility of Badlands for future landscape prediction is evaluated. Sediment load and discharge are outputs that can be validated by present-day data and thus will be used as a proxy for Badlands' ability to predict the future environment. Using this Landscape Evolution Model (LEM), simulations can be run with predicted sea level curves based on climate scenarios. Precipitation rates can be changed, as well as parameters like the erodibility and vertical displacement of a system based on natural or anthropological factors (e.g. policy on ground/water usage). Then, the output consisting of accumulated uplift, together with erosion and temporal scales are used to find the sediment flux in the targeted area. This thesis will focus on a case study that consists of a process based simulation of the Rhine for 10,000 years in the future (from 2024) in time steps of 200 years. To this end, the area of Western and Central Europe that includes the full source-to-sink system of the Rhine will be used.

1.1. Societal Relevance

In the last three centuries, human actions have become a main driver of global climate change. This has led to the term 'Anthropocene' being coined as early as the 1980's and popularized by, amongst others, Crutzen (2002), describing a new age of major human involvement on global environment. As a response to this, Rockström et al. (2009) have developed the 'planetary boundaries framework' which draws on the rapidly emerging transdisciplinary endeavor called Earth System Science (ESS) (Steffen et al., 2020). The goal of this endeavor is to achieve a deep integration of human dynamics with biophysical and (bio-)geochemical processes, in order to build a "truly unified understanding of the Earth System" (Steffen et al., 2020). The planetary boundaries framework identifies nine primary processes that play critical roles in the stability and resilience of Earth system as a whole. It also aims to delineate and quantify levels of human-caused perturbations that could allow Earth to remain in the relatively stable interglacial state known as the Holocene (K. Richardson et al., 2023; Rockström et al., 2009). In 2023, Richardson et al. (2023) have found that six of the nine boundaries are already transgressed. This is illustrated in Figure

1.1, showing the 2023 update to the planetary boundaries.

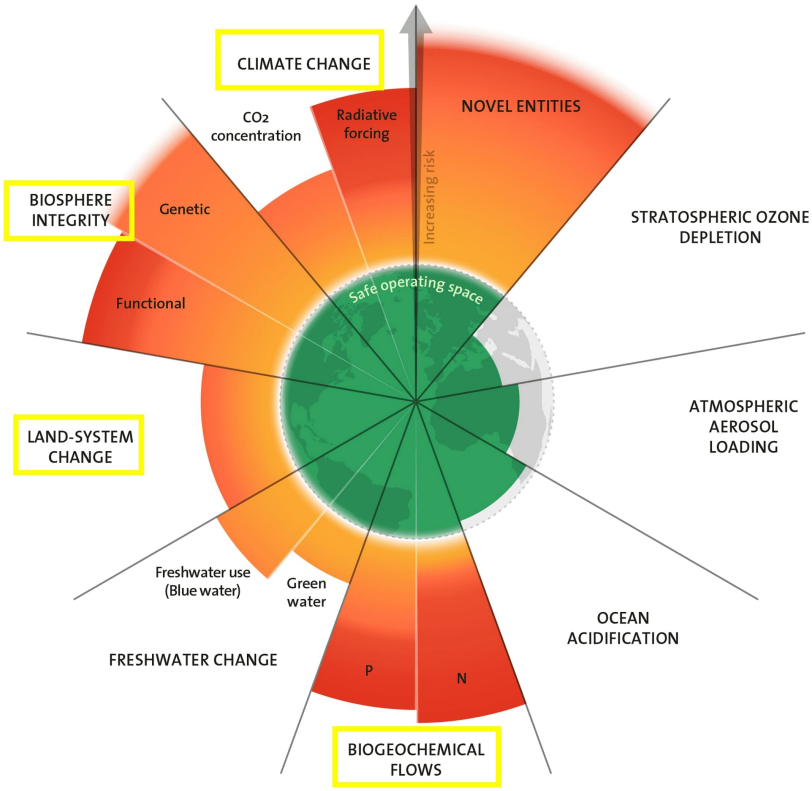

Figure 1.1: The nine planetary boundaries as of 2023, showing six have transgressed the level of safe operating space. The boundaries within a yellow rectangle indicate relevance to this thesis. Credit: Azote for Stockholm Resilience Centre, based on analysis in Richardson et al. (2023).

The case study in this thesis will focus on the impact of climate change and anthropogenic land use change on sediment flux in process-based simulations of the Rhine and Meuse rivers. The aim is to improve our understanding of these processes as they relate to the 'biogeochemical flow', 'land-system change', 'biosphere integrity' (through land use change), and 'climate change' planetary boundaries.

Often the research on climate change is limited to 'long-term' projections until the year 2100, or 2300 in some cases, as is clear from the reports of the Intergovernmental Panel on Climate Change and related studies (Arias et al., 2021; Collins et al., 2013; Horton et al., 2020; IPCC, 2022, 2014; Seneviratne et al., 2021). The IPCC reports stress the importance of a reduction of Green House Gasses (GHG), and in particular CO_2. However, even if the net-zero carbon emissions goal by 2050 is met, a considerable fraction of emitted carbon will remain in the atmosphere for tens to hundreds of thousands of years (Archer and Brovkin, 2008; Archer et al., 2009; Walker and Kasting, 1992). This means that in the absence of efficient, large-scale capture and storage of atmospheric carbon, the present atmospheric carbon and near future emissions can result in irreversible climate change on timescales of centuries to millennia, with surface temperatures remaining high and continued sea level rise at these scales (Clark et al., 2016; Meehl et al., 2005; Solomon et al., 2009; Wigley, 2005).

Due to the complexity of Earth systems, there is a lot of uncertainty in the consequences of both anthopogenic influence (e.g. land use, mining, water management) and climate change (e.g. temperature increase, changes in precipitation quantity as well as distribution and frequency of precipitation events, sea-level change) on sediment availability and mobility and the resulting sediment flux. This high degree of uncertainty calls for either a statistical or scenario-based approach to capture possible influences on the sediment flux (Ylla Arbos et al., 2021). In this study different climate change and anthropogenic land use scenarios will be simulated using Badlands, and then the results will be used to evaluate their relative contributions in sediment flux for the next 10,000 years. This temporal range is chosen due to three

reasons. One of the effects that is tested in this thesis has a minimum duration of 3600 years, and in order to see its effect stop the simulations have to be longer than that. Secondly, the range corresponds with the study of Clark et al. (2016) that is the basis for our sea level change and emission levels. And thirdly, it poses an approximate symmetry between the start of the Holocene (which began 11,700 years ago) and the major changes in climate throughout the last 10,000 years. This brings us to the introduction of our research questions.

1.2. Research Formulation

The main research question of this thesis can be formulated as follows:

Research Question 1

What is the impact of long-term climate change and anthropogenic land use on the sediment flux of the Rhine?

Sub questions are also investigated and answered during the process of this research project. These sub-research questions are:

Research Question 2

Can the current path and metrics of the Rhine be predicted by the process based landscape evolution model Badlands?

Research Question 3

Is Badlands suitable to be used for research regarding (future) anthropogenic land use change?

Research Question 4

Will either climate change scenarios or (anthropogenic) land use change have a dominant effect on the sediment flux in the Rhine source-to-sink system on a 10kyr temporal scale?

Research Question 5

Is there a significant difference in the predicted sediment flux in the simulated rivers between using either a uniform precipitation, or non-uniform precipitation change over the simulated period?

Research Question 6

How would the greenification of urban areas or reallocation of agricultural lands in Western and Central Europe influence the sediment flux in these climate scenarios? And in addition, how does this influence the sediment flux in the downstream area of the Rhine-Meuse delta located in the Netherlands?

Part I

Feasibility Study

Part I Description

In Part I of this thesis, a feasibility study for future prediction using the landscape evolution model Badlands is performed. In the first chapter we will briefly state what landscape evolution models are in general, and why we have chosen Badlands in particular for our research. This is followed by a detailed overview of the simulated processes and governing equations thereof used by Badlands, as well as the more technical aspects of their implementation.

A detailed description of the bedrock and topsoil erodibility for the area of interest that is the subject of our case study is given. The bedrock erodibility is based on the geology of the region, which is also discussed here. Together with the calibration of the inputs, this leads to a generalized scale of bedrock and topsoil erodibility factors in the correct units for Badlands input. The depth of the topsoil layer and how to implement this is also explored.

We will perform different simulations in order to investigate the behavior and validity of model outputs. First, the ability of Badlands to recreate the major rivers in our area of interest (Western and Central Europe) is explored, as well as which resolution is the best for this purpose. We will evaluate the sediment load and discharge outputs of these initial runs and compare them to observed data of the river Rhine to validate the results. Based on these observations, we calibrate the inputs of precipitation and topsoil erodibility until the produced sediment load and discharge outputs conform to the observed values.

Key results show the identification of a lake in the modern day area of the Upper Rhine Graben. This prevents reliable evaluation of erosional and depositional processes in this area, inhibiting the use of sediment flux originating upstream from the Upper Rhine in our comparison with observed values. Consequently, the research area is decreased to the upper half of Central and Western Europe, with a focus on the Lower Rhine reach. We also decide on the temporal range of the uplift in the area of interest due to glacial isostatic rebound. Calibration of the inputs results in sediment load and discharge representative of observed data from the Lower Rhine. Due to a discrepancy between the bedrock incision model and the adjusted topsoil erodibility we see that Badlands is not able to reproduce this sediment load for the full 10,000 years of simulation.

The inputs are calibrated such that the temporal range of the validated range of sediment load is maximized to be approximately 5,000 years. The feasibility study confirms the potential of Badlands to simulate the major rivers in our area of interest and predict sediment flux for a limited time in the future for the Lower Rhine specifically. The final simulation is used as the reference simulation for our case study that is the subject of Part II of this thesis.

2

Landscape Evolution Modeling

2.1. Landscape Evolution Models

A Landscape Evolution Model (LEM) is essentially a set of mathematical equations that are used to describe the evolution of landforms. These models have been around since the early 1960s, and have continued to grow in both number and sophistication (Tucker, 2009). Most commonly, models about landscape evolution are used descriptively, in which case they are used to learn about landscapes in the general sense (Temme et al., 2022). Following the Temme et al. (2022) study on landscape evolution modeling, it was found that studies using landscape evolution models predictively, meaning to simulate the evolution of a landscape correctly, are least common. Most of the postdictive, and all of the predictive LEMs calculate forward in time. This is usually done by starting at a relatively well known paleo-landscape and simulate towards another landscape, often the present (Temme et al., 2022). The expanding pool of available datasets on different timescales allows for better calibration of LEMs, resulting in more predictive, smaller temporal scale (human timescales as opposed to geological timescales) studies. These studies are thought to become more important for policy makers in the future (Korup, 2002). In this study, the landscape evolution model Badlands will be used to this end (Badlands Group, 2019). Salles, Ding, and Brocard (2018); Salles, Ding, Webster, et al. (2018); Salles and Hardiman (2016), and Salles et al. (2023) describe the capabilities of this software. Using scientifically agreed upon equations and methods to describe natural processes, the influence of tectonics, climate, sea level, erosion, and deposition will be used to predict the future landscape, and more importantly evaluate the impact of future climatic and anthropogenic land use change on sediment flux. The way different climate realizations are modeled, is through the input of parameters that agree with these scenarios. An example of this is the predicted sea level change and precipitation change due to global warming. Badlands was chosen over other landscape evolution models due to its unique combination of available input parameters, necessary outputs (e.g., sediment load), the necessary temporal and spatial resolution, as well as familiarity with the language in which the framework is written (Python). A concise overview of landscape evolution models that are either similar to Badlands or specialize in one of the elements implemented in Badlands, but did not fulfill all our needs are given in Appendix A.

The *Basin and Landscape Dynamics* (Badlands) model has been specifically designed to bridge the existing gap in LEMs by combining the climate, sea-level, tectonics, and sediment availability and movement (Salles and Hardiman, 2016). In addition to this, Badlands offers a complementary approach to modeling and evaluating effects of climate change in systems that are typically beyond the few hundred years at maximum that are covered by resource intensive climate models. An example of such a system are reef colonies. They typically have lifespans of more than 500 years, but are intricately linked to past and future climate change (Salles, Ding, Webster, et al., 2018). The Salles, Ding, Webster, et al. (2018) study has used Badlands to recreate the evolution of the Great Barrier Reef over the last 14,000 years until the present, and found their results agreeing with literature, geological records, as well as present day observations of the reef, providing ”useful insights and quantitative metrics that could be used to better constrain the effects of deglacial to Holocene climatic variability on sediment dynamics” in the region of the Great Barrier Reef (Salles, Ding, Webster, et al., 2018). Although, amongst others, the addition of tidal currents, wind induced wave generation, and the direct implementation of changing temperatures are mentioned as ways to improve the software, these are not available (yet). Thus we will need to incorporate future temperature change through other available inputs.

Although Badlands is shown to produce credible results on the timescales we are interested in, it has, at the time of writing and to the authors knowledge, not been validated for modeling into the future. This thesis could play an albeit minor role in this process of validation of Badlands for future prediction.

2.2. Simulated Processes and Governing Equations

The sediment flux in a source-to-sink system is determined by the effects of climate, sea-level, tectonics, and sediment availability and movement (Salles and Hardiman, 2016). In order to efficiently and accurately model future sediment flux, we will need to incorporate all of these influences. Badlands provides an "integrative framework that provides a simple and adaptable numerical tool to explore Earth surface dynamics and quantify the feedback mechanisms between climate, tectonics, erosion and sedimentation" (Badlands Group, 2019). These feedback mechanisms and the main components of the Badlands workflow are shown in Figure 2.1.

The processes shown in this figure can be computed through one of several available models, depending on which model is preferred for your specific requirements or valid assumptions (Badlands Group, 2019). Next, we will explore which of these models will be used to describe fluvial, and hillslope processes, sediment transport parallel to the coast caused by waves (wave-induced longshore drift), the production of carbonates (i.e., reefs), and additional extrinsic forcings which can be applied: sea-level changes, tectonics (subsidence, uplift, as well as horizontal displacements), rainfall patterns, and boundary wave conditions.

2.2.1. Fluvial Processes

In a source-to-sink system, fluvial systems play a crucial role in the transfer of sediments from where sediments are created through weathering and erosion (the source) to where the sediments are deposited (the sink). In flowing from higher topographies towards lower topographies, the transportation of water and sediments causes significant changes in the landscape. This means being able to quantify the influence of both the water and sediment transport and deposition on the topography is crucial to model accurate landscape evolution (Whipple and Tucker, 2002). Figure 2.2 shows a fluvial system with some of its characteristic landscapes.

The erosion rate caused by a water current can be limited by either the detachment of particles (e.g., due to a strong cohesive substrate), or due to the transport capacity of the flow (Tucker and Hancock, 2010). This led to the development of two different approaches towards the modeling of fluvial incision: the detachment-limited, and transport-limited models (Howard et al., 1994; Whipple and Tucker, 2002). The detachment-limited model is the default model in Badlands, but both are available (Salles, Ding, and Brocard, 2018). Detachment of particles happens when the shear stress applied to the soil surface exceeds the cohesive strength of the soil (critical shear stress, Merritt et al. (2003)). This can be due to multiple processes, including raindrop impact (Loch, Silburn, et al., 1997) and overland flow (Merritt et al., 2003). The erosion rate $\dot{\epsilon}$ described by the detachment-limited model is given by Equation 2.1.

$$\dot{\epsilon} = \kappa_d P^l (PA)^m S^n, \tag{2.1}$$

where κ_d is a dimensional coefficient that describes the erodibility of the channel bed as function of bed roughness, rock strength, and climate (the erodibility factor). A is the drainage area, S is the local slope, and P is the net precipitation. l, m, and n are dimensionless positive constants. The default formulation assumes $l = 0$, $m = 0.5$, and $n = 1$ (Badlands Group, 2019). The steady state gradient for a detachment-limited channel is determined by a combination of the rate of rock uplift or base level fall and the ability of the river to erode the bed (Whipple and Tucker, 2002). What follows from this model however, is that the long-term sediment carrying capacity will greatly exceed the sediment supply (Whipple and Tucker, 2002). In addition to this, according to Van der Beek (2013) the utility of this model on large spatial scales is limited as it will predict river channels to be incised everywhere, with exception in cases where $A = 0$ or $S = 0$. The advantage of this model is the small restriction on computational time steps when running the model (Badlands Group, 2019).

In order to take the transport capacity of the river into account, we introduce transport-limited models. The volumetric sediment transport capacity Q_t is given by Equation 2.2, and is defined using a power law function of unit stream power (Salles, Ding, and Brocard, 2018).

$$Q_t = \kappa_t (PA)^{m_t} S^{n_t}. \tag{2.2}$$

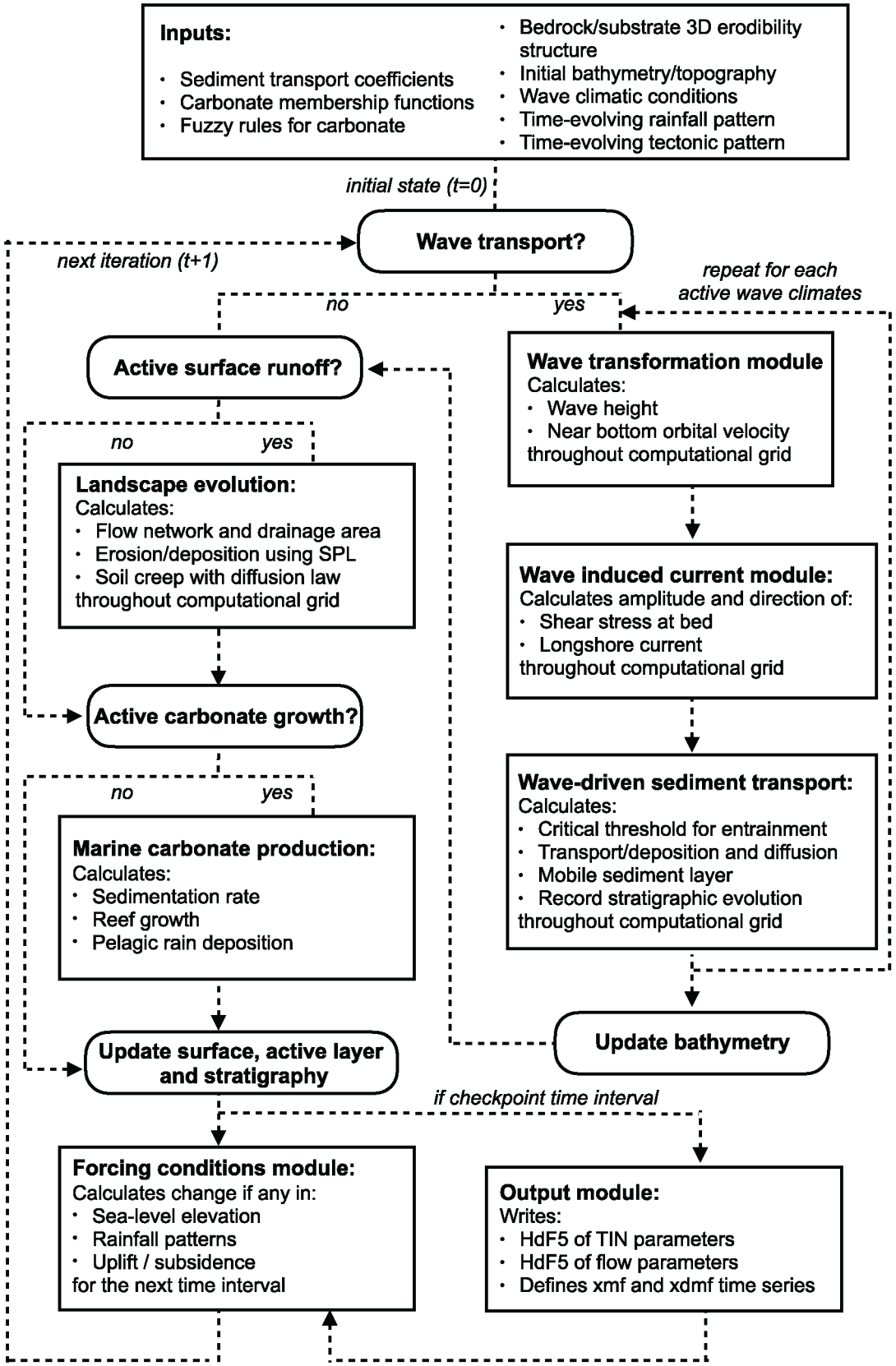

Figure 2.1: The feedback mechanisms and main workflow components of Badlands. From Salles, Ding, and Brocard (2018).

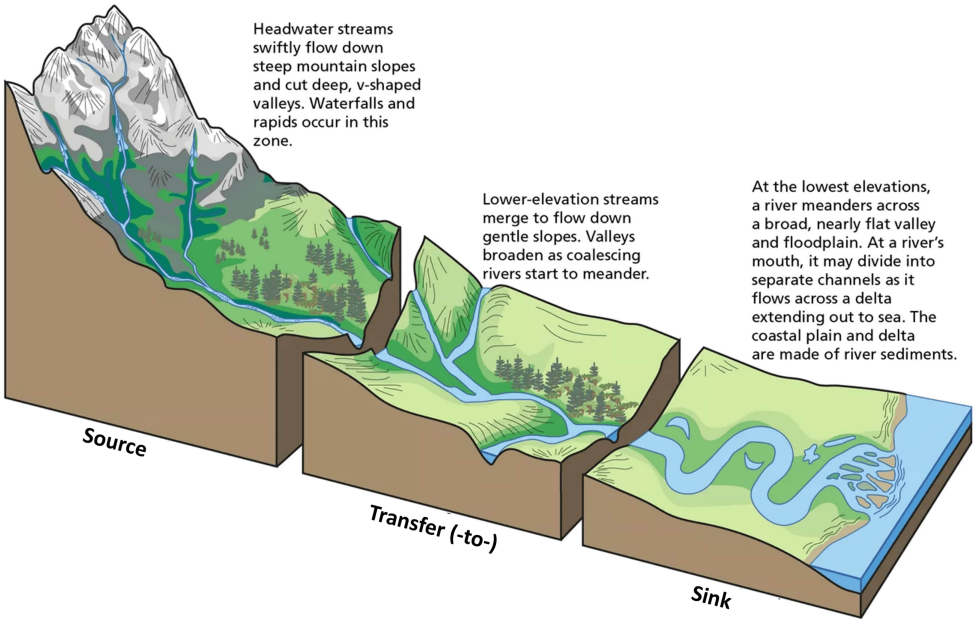

Figure 2.2: A fluvial system. Adapted from US National Park Service (2022).

Here κ_t is a dimensional coefficient that describes the transportability of channel sediment, m_t and n_t are dimensionless positive constants set to 1.5 and 0.5, respectively (Badlands Group, 2019). The other parameters are the same as in Equation 2.1. This equation assumes that the threshold of motion (i.e., the critical shear stress) is negligible (Crosby et al., 2007). Now we introduce an additional term in the stream power model:

$$\dot{\epsilon} = \kappa_d f(Q_s)(PA)^m S^n, \tag{2.3}$$

where $f(Q_s)$ represents a variety of plausible models that describe the dependence of river incision rate (Q_s) on sediment flux (Salles, Ding, and Brocard, 2018). For the detachment-limited model, this term is unity. In addition to this, Badlands offers five possible formulations of $f(Q_s)$. One of these is the *Almost Parabolic*, a 'tool and cover' formulation. Qualitative and experimental observations have both shown the dual role of sediment flux in the erosion process (Badlands Group, 2019). First, with a sediment flux that is low relative to carrying capacity, the erosion potential increases with the sediment flux (through bedrock abrasion and plucking, i.e., the tool effect). Secondly, the increase in sediments on the channel bed will protect the bed from saltating particles, which inhibits erosion (i.e., the cover effect) (Salles, Ding, and Brocard, 2018; Turowski et al., 2007). Gravel-river beds typically have a layer of coarse grains on the surface which protects the finer grains underneath from eroding. Sklar and Dietrich (2006) stressed that incision models without a cover term will likely overpredict incision rates for high sediment supply rates. A modified 'almost parabolic' model proposed by Turowski et al. (2007) takes this cover term into account. The $f(Q_s)$ term for this *Dynamic Cover* model is given by Equation 2.4.

$$f(Q_s) = \exp\left[-\left(\frac{Q_s/Q_t - 0.35}{C_h}\right)^2\right], \tag{2.4}$$

where:

$$\begin{cases} C_h = 0.22 & \text{for} \quad Q_s/Q_t \leq 0.35 \\ C_h = 0.6 & \text{for} \quad Q_s/Q_t > 0.35. \end{cases} \tag{2.5}$$

The main fluvial system in the area of interest (AOI) for our case study, namely Western and Central Europe, which is described in detail in section 5, is a gravel bed river (European Sediment Network, n.d.-b). Therefore, the *Dynamic Cover* model is chosen for our simulations.

While this model takes into account the bedload cover, we have not discussed the relation between the fluvial incision rate in proportion to the bedload material (i.e., gravels) that is present in the stream, *and*

the slope of the bed. In Badlands, the amount of bedload material is assumed to be slope-dependent for any point in the landscape (Badlands Group, 2019). The rock uplift rate as well as the rock strength have an indirect effect on this slope. This may be due to their influence on the size distribution of the channel supplied sediments, but this process is still poorly understood (Sklar and Dietrich, 2006). Turowski et al. (2007) state that the stochastic sediment supply from hillslopes, which is modulated by the temporal variation in water discharge, causes a high variability in extent and thickness of alluvial cover in mountain channels. This increases the difficulty for finding a discernible geometric signature of tool-dominated regimes (Turowski et al., 2007). In other words, it is very difficult to find a good relation between the incision rate due to bedload present in the stream (e.g., through saltation: the tool effect) and geometric characteristics of a channel (e.g., width or slope of the channel). For this reason, we will assume the default Badlands setting of 'no dependence'.

The dependence of climate-dependent chemical weathering on river bedrock incision is determined by the exponent l in Eq. 2.3. Although an increase of atmospheric CO_2 will likely cause an increase in chemical weathering in the future, this process is believed to respond on 10-100 Myr timescales (Lipp et al., 2021). As we are only looking at a timescale of 10 kyr, this effect is assumed to be negligible and kept at the default setting in Badlands ($l = 0$).

2.2.2. Hillslope Processes

Hillslopes constitute the margins of eroding uplands and valley flanks (Baker, n.d.). The erosion of these hillslopes regulates topographic relief, as well as sediment yield, and geomorphic response to climate change and tectonic forcing (Roering, Kirchner, Sklar, and Dietrich, 2001). Along the hillslope, the main driver for sediment transport is assumed to be gravity, and that the "flux of sediment is proportional to the gradient of topography" (Salles, Ding, and Brocard, 2018). Commonly, this process is simulated using a linear diffusion law, or 'soil creep' (Salles and Duclaux, 2015; Tucker and Hancock, 2010). According to Foufoula-Georgiou et al. (2010); Tucker and Bradley (2010), and Larsen and Montgomery (2012) the linear diffusion approximation is only rarely appropriate, although it is possible to combine the linear approximation with threshold hillslope transport to create a more accurate result (DiBiase et al., 2010). This combination is however not available in Badlands, and thus we will use the alternative non-linear formulation of diffusive hillslope transport as proposed by Andrews and Bucknam (1987), Roering, Kirchner, and Dietrich (2001), and Roering, Kirchner, Sklar, and Dietrich (2001). This formulation is given by Equation 2.6.

$$\frac{\partial z}{\partial t} = \nabla \cdot \frac{\kappa_{hn} \nabla z}{1 - (|\nabla z| / S_c)^2}, \tag{2.6}$$

where ∇z is the vertical gradient, κ_{hn} is the diffusion coefficient, and S_c is the critical slope. When the slope values approach the critical slope, the flux rates increase to infinity (Salles, Ding, and Brocard, 2018). This causes convex to planar profiles as the hillslope processes will dominate when the slope values approach the critical slope (taken to be S_c = 0.8 (DiBiase et al., 2010; Larsen and Montgomery, 2012)) or exceed it (Salles, Ding, and Brocard, 2018). An additional critical slope can be introduced to the simulation. When this critical slope is exceeded, slope failure is triggered. According to Shiferaw (2021) the base failure slope of sandy soil has been found to be 36.87°, while clayey soils showed base failure at slopes smaller than 18%, derived using a strength reduction method of analysis. For our simulations, we will use the average value of 27.4%, as only one value of input is possible.

2.2.3. Wave-induced Longshore Drift

Longshore drift, also known as littoral drift, is the transportation of sediments along a coast that is parallel to the shoreline. This process is shown in Figure 2.3. One way of simulating wave-induced longshore drift is by using linear wave theory to describe the wave motion (Mil-Homens, 2016; Stokes, 1847). The propagation velocity of an individual wave, also known as *celerity* (c), is given by Equation 2.7.

$$c = \sqrt{\frac{g}{\kappa} \tanh{(\kappa d)}}, \tag{2.7}$$

where g is the gravitational acceleration, $\kappa = 2\pi/L$ is the wave number with L the wavelength, and d is the water depth (Salles, Ding, and Brocard, 2018). Using Huygens principle, the wave front propagation, including refraction, is calculated using Equation 2.7 and the wave length (Tetzlaff, 2005). The Badlands

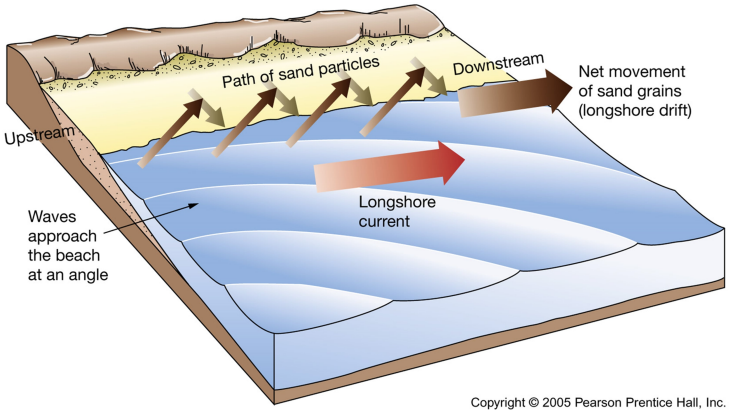

Figure 2.3: Longshore current and longshore drift. From Salles (2022).

algorithm then deduces the wave travel time and defines the wave directions from lines that are perpendicular to the wave front. The wave height H is then calculated along the wave front propagation (Salles, Ding, and Brocard, 2018). Both wave energy dissipation in shallow environments and wave-breaking conditions are taken into account. According to linear wave theory, the horizontal orbital velocity (or maximum bottom wave-orbital velocity, $u_{w,b}$) is given by Equation 2.8 (Bosboom and Stive, 2021):

$$u_{w,b}(z) = \omega a \frac{\cosh\left(\kappa(d+z)\right)}{\sinh\left(\kappa d\right)}, \tag{2.8}$$

with $\omega = 2\pi/T$ the angular frequency, T the wave period, and a is the wave amplitude. In shallow water approximation ($d/L > 1/20$), the expression for our maximum bottom wave-orbital velocity can be simplified as follows (Bosboom and Stive, 2021):

$$u_{w,b} = \frac{H}{2}\sqrt{\frac{g}{d}}, \tag{2.9}$$

where H is the wave height. The maximum (wave-induced) bed shear stress for linear waves (τ_w) without superimposed current is given by Equation 2.10.

$$\tau_w = \frac{1}{2}\rho_w f_w u_{w,b}^2. \tag{2.10}$$

Here ρ_w is the water density, and f_w is the wave friction factor first introduced by Jonsson, 1966. Badlands uses the simpler relationship for f_w as given by Soulsby et al., 1993, given by Equation 2.11.

$$f_w = 1.39\left(\frac{A_b}{k_b}\right)^{-0.52}, \tag{2.11}$$

where $k_b = \frac{2\pi d_{50}}{12}$ is the bed roughness, with d_{50} the median sediment grain size at the bed. A_b is the wave-orbital semi-excursion at the bed, given by $A_b = \frac{u_{w,b}T}{2\pi}$ (Salles, Ding, and Brocard, 2018). Some of the wave-related principles and definitions discussed are shown in Figure 2.4. The wave characteristics and induced bottom shear stress are computed for each wave condition by the wave transformation model incorporated into Badlands (Salles, Ding, and Brocard, 2018).

The part of the North Sea that is included in our area of interest is near the shore. This means that the longshore current (as shown in Figure 2.3) runs parallel to the shoreline and will contribute significantly to sediment transport (Longuet-Higgins, 1970; Soulsby, 1997). The longshore current velocity ($\vec{v_l}$) is given by Equation 2.12.

$$\vec{v_l} = \kappa_l u_{w,b} \cos\left(\theta\right) \sin\left(\theta\right)\vec{k}, \tag{2.12}$$

where κ_l is a scaling parameter, θ the angle of incidence of the incoming waves, and $\vec{k}$ is the unit vector parallel to the breaking depth contour (Salles, Ding, and Brocard, 2018) (this is the depth contour at which the wave height becomes greater than a certain fraction of the water depth, causing the wave to 'break' (Bosboom and Stive, 2021)).

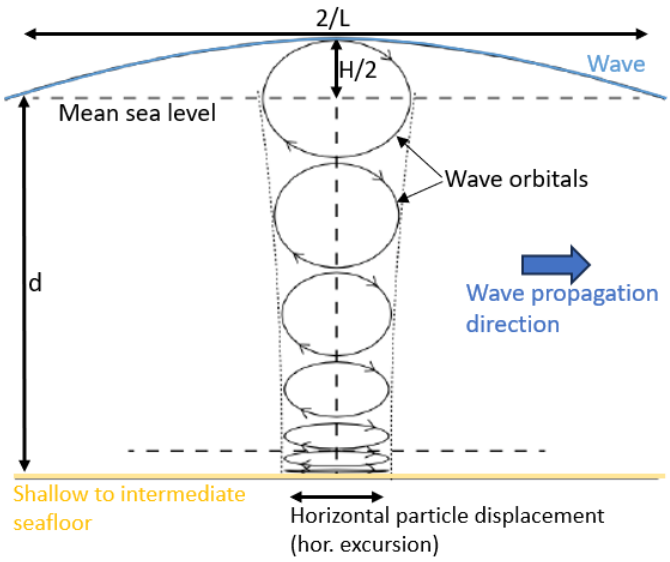

Figure 2.4: Marine wave principles. Adapted from Bosboom and Stive (2021).

Erosion at the sea floor can be described as when stationary sediment on the sea floor gets incorporated into a fluid flow. This erosional process is called *entrainment* (Thomas, 2008). In order to quantify this process we define a critical shear stress τ_c as follows:

$$\tau_c = \theta_c g d_{50} (\rho_s - \rho_w), \tag{2.13}$$

with θ_c the critical incidence angle, and ρ_s and ρ_w are the sediment and water density, respectively. When the wave-induced shear stress (Equation 2.10) is larger than the critical shear stress, bed sediment is entrained. The erosion thickness (h_e) is limited to the upper sedimentary layer, and is given by Equation 2.14 (Salles, Ding, and Brocard, 2018).

$$h_e = C_e \ln \left(\frac{\tau_w}{\tau_c} \right). \tag{2.14}$$

Here, C_e is an entrainment coefficient which controls the relationship between the shear stress and the erosion rate (Warrlich et al., 2002). As soon as the sediments are entrained, they are transported parallel to the longshore current and are deposited in the regions where the wave-induced shear stress is smaller than the critical shear stress ($\tau_w < \tau_c$) (Barrett and Webster, 2017).

2.2.4. Carbonate Production

Carbonate production, or the spatial and temporal evolution of coral reef systems, are an option that can be enabled in Badlands. Depleted remnant oyster populations can be found in the Dutch North Sea, but are functionally extinct in the Belgium and German North Sea (OSPAR Commission, 2020). While there are projects in place for the artificial (re-)creation of (native) oyster beds and reefs in different regions across the European North Sea, these projects are in the starting phase (“Blauwwind’s offshore wind farm successful breeding ground for flat oysters”, 2024; “Oysters and artificial reefs in the water for new nature in wind farm on the North Sea”, 2018). In addition to this, diseases/parasites, microplastics (Green, 2016), adverse climate change effects, and the lack of suitable substrate hampers are causing major problems regarding the growth of the oyster populations (OSPAR Commission, 2020). For these reasons, carbonate production will not be taken into account in our simulations.

2.2.5. Extrinsic Forcing

There are four external forcing conditions available in Badlands (Badlands Group, 2019). These are tectonics, rainfall regimes, sea-level fluctuations, and boundary wave conditions. We will discuss what they are here briefly, and in later sections they will be described in detail.

Tectonics
The tectonic forcing is implemented through uplift, subsidence, and horizontal displacements, driven by a series of temporal maps that have spatial cumulative displacements (Salles, Ding, and Brocard, 2018). There is a strong coupling between tectonics and surface processes (Thieulot et al., 2014) as described in the previous sections. The enhancement of 3D deformation localization in order to better couple tectonics with the surface processes is implemented using the node refinement technique proposed by Thieulot et al. (2014) (Badlands Group, 2019). Tectonic displacements can change the density of the nodes over time, which can result in unbalanced resolutions in the grid. The displaced surface will be modified, either adding or removing nodes in order to ensure homogeneous node distribution (Salles, Ding, and Brocard, 2018; Salles and Hardiman, 2016). The subsidence and uplift found in our areas of interest will be discussed more in section 5.

Sea-level Fluctuations and Wave Conditions
Sea-level is one of the ways climate change scenarios can be implemented (Salles, Ding, and Brocard, 2018). For this study, four sea-level curves for the next 10kyr will be used that correspond to different emission scenarios as described in section 6. These curves can be directly used as an input for a simulation in Badlands. The sea influences erosion in two main ways in Badlands. As a base-level change it affects upstream processes and directly impacts the area of interest as it is flooded. The waves also erode and transport sediments, which brings us the the wave conditions.

In order to simulate the wave-induced longshore drift as discussed previously, the wave transformation model can be performed for time intervals between 5 and 50 years (Badlands Group, 2019). At any given time interval, the significant wave height and percentage of activity for the deep-water wave conditions is defined (Salles, Ding, and Brocard, 2018). In other words, Badlands has the ability to define wave climate events: this means that at a user-defined percentage of the time within the total runtime, a certain wave climate is active. What this allows the user to do is to define different dominant wave orientations and other parameters in a coastline where the wave parameters are expected to change over time. Lastly, the bathymetry is used to compute the associated wave parameters. The bathymetry as well as other wave parameters for the North Sea are given in section 5.1.2.

Rainfall Regimes
Precipitation can be implemented in three different ways in Badlands. Either through a uniform distributed precipitation map, a set of maps that represent spatially changing rainfall regimes, or the linear orographic precipitation model from Smith and Barstad (2004). The latter uniquely takes into account the coupling between precipitation patterns and topography (Salles, Ding, and Brocard, 2018). In section 6 the precipitation and expected changes therein that are found in our area of interest show that the expected precipitation changes have an inverse relation to the topography. This, in addition to an unstable atmosphere (e.g., CO_2 emissions and its consequences), means that the orographic precipitation model from Smith and Barstad (2004) may not predict accurate precipitation in our area for thousands of years in the future.

In order to still accurately portray topographical influence on precipitation, we will implement a set of maps that represent spatially changing rainfall regimes, with a realistic precipitation map as our base input on which predicted changes are applied. This map is constructed from real precipitation data, which, naturally, was influenced by the local topography and climate conditions. The precipitation map, as well as predicted precipitation changes that will be used in our simulations is discussed in section 6.

2.3. Implementation

2.3.1. Discretizations

The geomorphic equations discussed in the previous section are solved in Badlands through the use of an irregular spatial discretization scheme (Braun and Sambridge, 1997; Salles and Hardiman, 2016). The area of interest will be converted to a topographical grid to be used as input for Badlands. This map will be imported as a CRS: WGS84/Pseudo-Mercator coordinate dataset from the EPSG registry (MapTiler Team et al., 2022). This will then be converted to a triangulated irregular network (TIN) by generating a set of irregular points (or *nodes*) based on the input coordinate dataset. A Delaunay triangulation will define the connectivity between each adjacent node, while the surface area associated with each node and the width of the interface between pairs of adjacent nodes is defined by the associated Voronoi diagram (Delaunay et al., 1934; Tucker et al., 2001; Voronoi, 1908). This is illustrated in Figure 2.5, where an irregular

computational mesh including nodes (dots), triangulated grid (black lines), and Voronoi diagram (gray lines) is presented in addition to two examples of physical processes being implemented using the grid. The

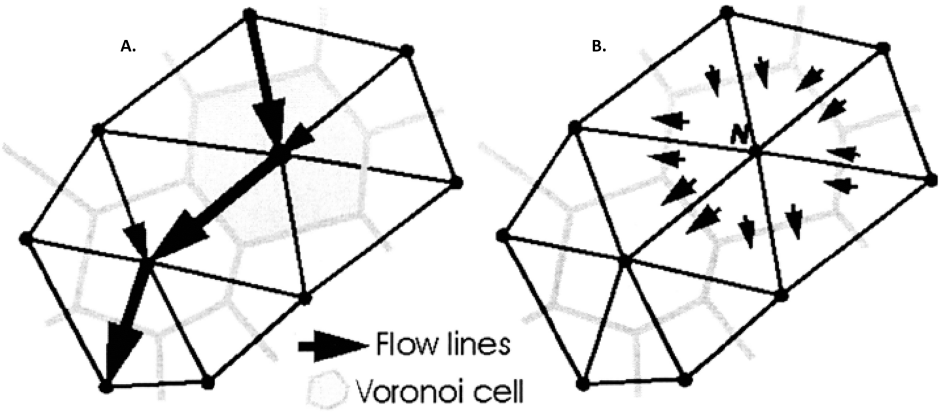

Figure 2.5: An irregular computational mesh, where each Voronoi polygon represents a finite volume cell. A: A streamflow is routed downslope along triangle edges from node to node, following the route of greatest negative gradient. B: A 2D diffusive sediment exchange between node *N* and neighboring nodes. Multiplying unit flux by the width of the Voronoi polygon edge shared between two nodes gives the total mass exchange rate. From Tucker et al. (2001).

Triangle library from Shewchuk, 2002 is used to generate a computational mesh. The generated scattered points from *Triangle* will ensure that the created TIN resolution matches the user-defined resolution (Salles and Hardiman, 2016).

Using the dual Delaunay-Voronoi framework as discussed above, the continuity (or transport) equation can be solved using a finite volume approach (Salles and Hardiman, 2016). The sediment flux through a node *i* to a node *j* is considered positive when the net sediment flux is from *i* to *j*, and vice versa. In the finite volume approach, the flux entering (or exiting) a certain cell is equal to the flux that is exiting (or entering) the adjacent cell. In other words, it is a conservative approach. The integration of the conservation equation for a node *i* is given by Equation 2.15 (Salles and Hardiman, 2016).

$$\frac{\mathrm{d}h}{\mathrm{d}t} = U - \frac{1}{\Omega_i}\left(\sum_{j=1}^{n_j} w_{ij} q_{s,ij}\right), \tag{2.15}$$

where h is the average surface height of node *i*, U is a source term representing a base level change (e.g., tectonic uplift), Ω_i is the surface area of the Voronoi polygon, n_i is the number of neighbors connected to node *i*, w_{ij} is the width of a triangle edge between the two nodes *i* and *j*, and $q_{s,ij}$ is the total volumetric sediment flux between the two adjacent cells separated by this edge (as in Figure 2.5). Similar to Figure 2.5, $w_{ij}q_{s,ij}$ is the total mass exchange rate between two cells per unit width (Salles and Hardiman, 2016; Tucker et al., 2001).

When using a regular grid for simulating a streamflow, a directional bias may arise (Dunn, 2010). By using a triangulated grid this bias is prevented from occurring, and as briefly mentioned in section 2.2.5, complex movement of the grid, by for example tectonic movement, can cause 3D advection of nodes (Salles and Hardiman, 2016). When a TIN is altered through advection, the *Triangle* library ensures that the grid is a Delaunay triangulated grid in which occurrence of a low node density area is prevented, and the user-required resolution of surface processes is enforced. On the other side, when the density of nodes becomes too high, it can cause a significant decline of the surface process model speed. This is circumvented by implementing a node deletion/merging algorithm as briefly mentioned in section 2.2.5. The deletion and merging criteria are ”based on the distance between neighboring nodes and the minimal interior angle of each Delaunay triangulation” (Salles and Hardiman, 2016).

In order to avoid numerical instabilities, the size of the time steps is determined by using a Courant–Friedrichs–Lewy (CFL) like condition (Courant et al., 1967; Refice et al., 2012). Through

each of the two processes an upper time step limit is provided (Salles and Hardiman, 2016). Then, the minimum value between the two CFL limits is used as time step for the next iteration. The time step limit Δt_{max} is then given by Equation 2.16, following Refice et al., 2012.

$$\Delta t_{max} < \min_{i,j} \left[\left(\frac{l_{ij}^2}{2\kappa_{hn}} \right), \left(\frac{l_{ij}}{\epsilon q_{w,i}^m (\nabla z_{i,j})^{n-1}} \right) \right], \tag{2.16}$$

where l_{ij} is the TIN arc length, m and n are the same positive constants from Equation 2.3. The rest of the parameters are the same as described earlier in the text.

2.3.2. Ordering and Partitioning

A key component in the algorithm used for solving channel incision and landscape evolution is finding the most efficient order of nodes for which the discharge and sediment transport is determined progressively (Salles and Hardiman, 2016). To this end, Badlands implements the ordering method with linear complexity (e.g., O(n)-efficient) from Braun and Willett (2013). This method is based on a single-flow-direction (SFD) approximation, which assumes the flow follows the path of steepest slope as shown in Figure 2.5 (O'Callaghan and Mark, 1984; Tucker et al., 2001; Wilson and Gallant, 2000). The algorithm follows the following steps:

1. A receiver list is defined, where a receiver is the neighbor of a given node with the lowest elevation.
2. The list of receivers is inverted to obtain the donor list.
3. A stack is created which starts from all nodes which are their own receivers (or base level nodes). Their corresponding donors will be added recursively, until a node without donors is reached.
4. The stack is inverted again, so that within each catchment all nodes upstream of a given node will be processed before moving on further downstream (Salles and Hardiman, 2016).

An improved upon parallelization scheme of Braun and Willett (2013) is used to improve the computational efficiency of the method. This is done by splitting each catchment into multiple sub-catchments (Salles and Hardiman, 2016). The individual sub-catchments will each drain into channel reaches, synchronized in an upstream to downstream order. This is the basis for "partitioning the simulated area into smaller units" (Salles and Hardiman, 2016), and is shown in Figure 2.6.

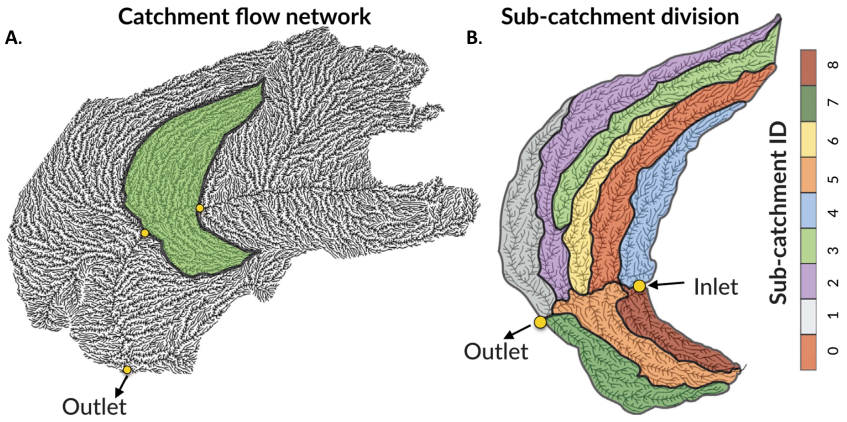

Figure 2.6: A: An entire stream-network-based catchment with a small portion highlighted in green. B: The result of subdividing the green area in A. into 9 sub-catchment units. From Salles and Hardiman (2016).

Hydrological models commonly apply the illustrated method to divide a large river catchment into smaller units (Arnold et al., 1998). The landscape evolution calculations are already organized in accordance with channel reaches. This means the parallelization scheme that is applied follows the natural river catchment organization, and information on sediment fluxes is passed between the sub-catchments at each time step in a sequential manner (Salles and Hardiman, 2016). The number of nodes in the TIN, as well as the size of the sub-catchment unit will determine the computational effort needed. As touched upon in the fourth point in the algorithm, the data exchange of lateral sediment fluxes between the nodes happens in order

of upstream to downstream nodes. This exchange is performed through message passing (Gropp et al., 1999) through ghost cells that are located at junctions between sub-catchments. The graph partitioning library *METIS* from Karypis and Kumar (1998) is used to balance computational load as well as minimize the message passing between processors (Salles and Hardiman, 2016). The implementation of this partitioning strategy in Badlands is shown in Figure 2.7. In Badlands, the METIS library uses a connectivity

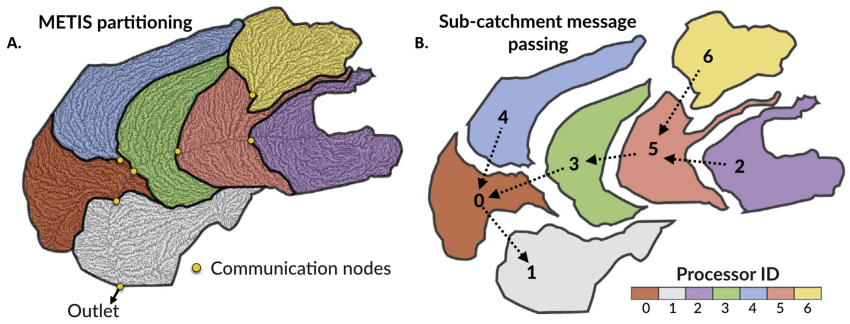

Figure 2.7: Implementation of the partitioning strategy in Badlands. A: Catchment communication node distribution between 7 processors. B: A hypothetical communication flux between the flow graph sub divisions. From Salles and Hardiman (2016).

table that is ”derived from Strahler stream order (Strahler, 1952) and surface water discharge” (Salles and Hardiman, 2016).

2.3.3. General Computational Structure & Visualization

In order to implement all the natural processes discussed above in a logical and efficient manner, the computation of some of these factors can be done in parallel, while other need to be done in series. The core computational steps, both serial and parallel, performed by Badlands are shown in Figure 2.8.

User input files and parameters can be given to Badlands through an XML parser. As seen in Figure 2.8, Badlands then produces parallel HDF5 (Hierarchical Data Format, HDF Group et al., 1997) outputs (Salles, 2016).

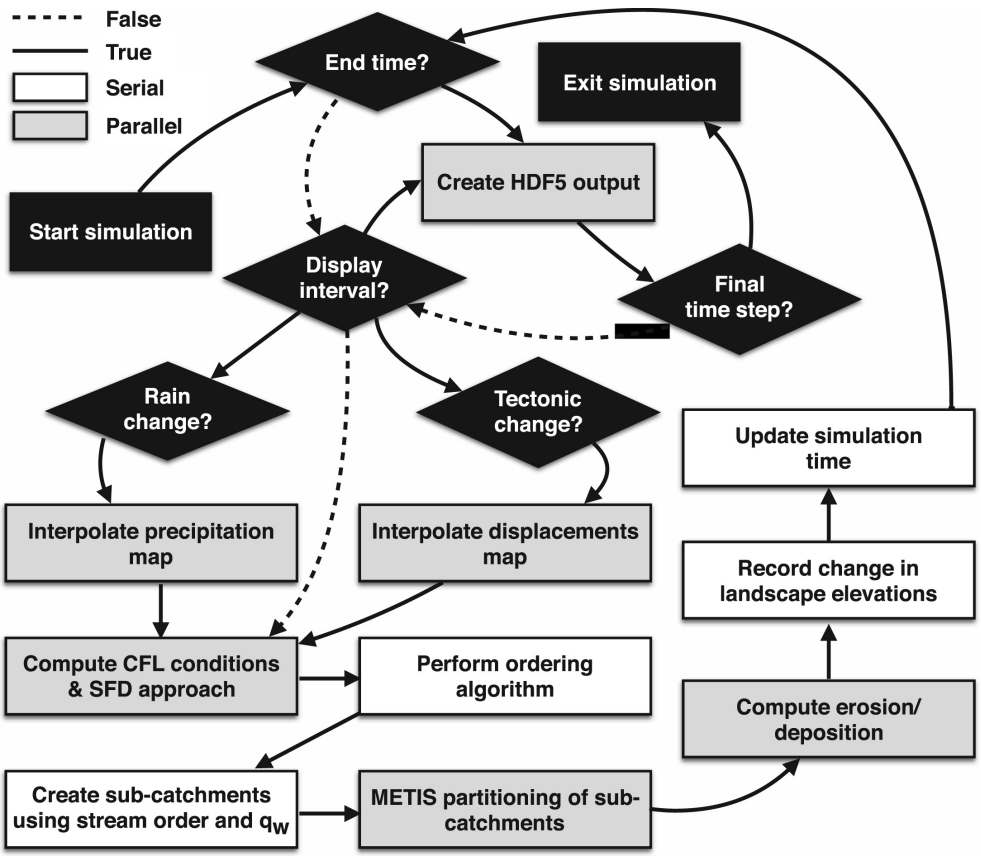

Figure 2.8: Core computational steps in Badlands showing serial and parallel computations. From Salles (2016).

3

Erodibility

Erodibility is one of the key inputs in Badlands and is essential for the implementation of different land use scenarios. Erodibility is generally expressed in terms of the erodibility factor (κ_d, or 'K-factor') and expresses the susceptibility of the soil/bedrock to erode. At regional or national levels, direct in situ measurements of the erodibility factor are not financially sustainable (Panagos et al., 2014). This is why Wischmeier and Smith (1978) and Renard et al. (Renard et al., 1997) proposed an algebraic approximation for the earlier developed soil erodibility nomograph by Wischmeier et al. (1971). This approximation depends on five soil parameters, namely the soil texture, organic matter, coarse fragments, the structure, and the permeability, and is given by Equation 3.1.

$$\text{K-factor} = [(2.1 \cdot 10^{-4} M^{1.14}(12 - OM) + 3.25(s - 2) + 2.5(p - 3))/100] \cdot 0.1317, \tag{3.1}$$

where M is the textural factor given by $M = (m_{silt} + m_{vfs}) \cdot (100 - m_c)$, where m_{silt} is the silt fraction (defined as particles of size $0.002 - 0.05$mm), m_{vfs} is the very fine sand fraction (defined as particles 0.05-0.1mm), and m_c is the clay fraction (particle size $<$0.002mm), all of which should be inserted in the equation in percentages. OM is the organic matter content of the soil, s is the soil structure class, and p is the permeability class. For information on the possible values of s and p and corresponding classes the reader is referred to Panagos et al. (2014). Lastly, the factor 0.1317 is the conversion factor for United States business units (ton acre hour)$\cdot$(hundreds of acre foot-ton inch)$^{-1}$ to international system units *t ha h ha^{-1} MJ^{-1} mm^{-1}*, simplified to *t h MJ^{-1} mm^{-1}* (Arunrat et al., 2022; Foster et al., 1981). The erodibility in Badlands is implemented through use of a map of erodibility factors κ_d. In our case a high-resolution dataset based on LUCAS (Land Use/Cover Area frame Survey) from Panagos et al. (2014) is used as the base map on which we will apply the necessary changes based on land use scenarios, given in Part II. The map is based around Equation 3.1 for the erodibility, but also includes the influence of 'stoniness': this is the effect of stones in the soil on erodibility calculated by $K_{st} = K \cdot St$, where K is the K-factor, St is the stoniness correction factor, and K_{St} is the erodibility factor corrected for stoniness (Panagos et al., 2014). Because the erodibility is location-dependent, we will already use the erodibility map that fits our case study. Due to EU regulation/cooperation, Switzerland is not (yet) included in this dataset, however an interpolated version which includes Switzerland is available and is used in this study. This interpolated map of our AOI is given in Figure 3.1. This map only includes the erodibility factor for the soil, and does not take into account artificial surfaces as well as bare rock, glaciers, and water bodies.

When we look at the case study in Part II of this thesis, it becomes clear that in the literature the effect of land use type is almost always given in erosion rate (or soil loss) rather than its erodibility factor. While a relation between the soil erosion and erodibility factor is given by Equations 2.1 and 2.3, these depend on region-specific parameters like the slope and net precipitation. In addition to this we can see from Equation 3.1 that the K-factor is dependent on local soil data specific to the area of study. To get a better understanding of all the different factors relevant for erosion we can look at the revised universal soil loss equation (RUSLE) given by Equation 3.2.

$$A = R \cdot K \cdot L \cdot S \cdot C \cdot P, \tag{3.2}$$

where A is the average annual soil loss, R the erosivity due to rainfall, K is the erodibility factor, L is the slope length, S the slope, C is a factor that describes cover management (e.g., cropping), and P is a

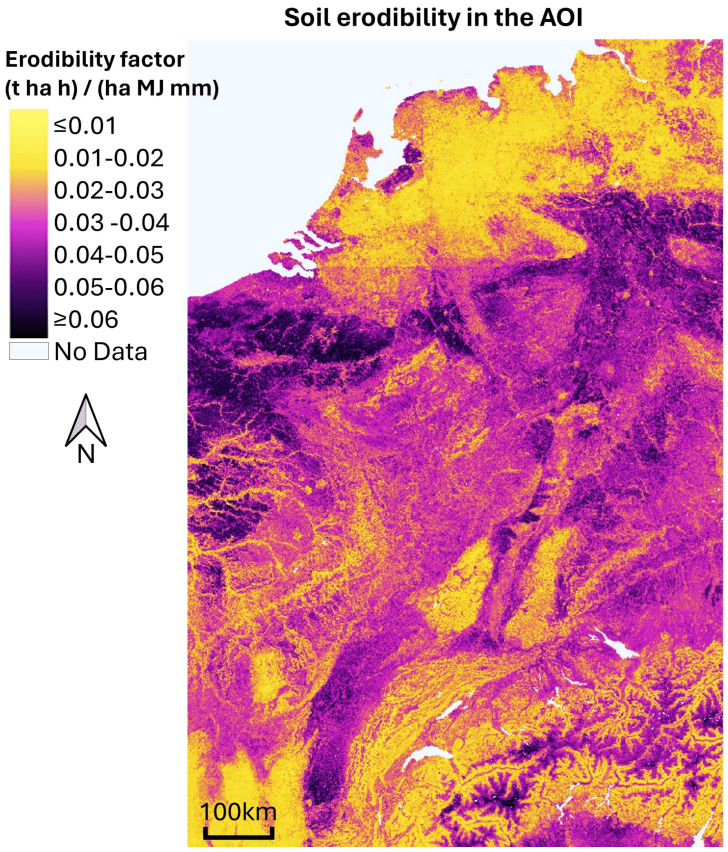

Figure 3.1: High resolution map of the soil erodibility (corrected for stoniness) in our case study area of Western and Central Europe, with interpolated values for Switzerland. Adapted from Panagos et al. (2014), prepared with QGIS (QGIS.org, 2024).

factor describing conservation practice (Foster et al., 1981; Renard et al., 1997). Although this equation already takes into account many factors regarding soil erosion, it still does not include factors that describe the sediment deposition along the slopes and the presence of dry vegetation that can be affected by rainfall seasonality (Macedo et al., 2021). This, together with the dependencies of the K-factor given by equation 3.1, we can see the calculation for the soil erosion at a certain location has many dependencies that are either highly regionally specific, or in general difficult to acquire. This means it is very difficult (if not impossible), and outside the scope of this thesis, to find a direct relation between the K-factor and erosion rate in an area as large as the subject of our case study: W. It is possible to find an indication for the change in erodibility factor due to agroforestry soil however. De Jalón et al. (de Jalón et al., 2017) have provided maps showing, amongst others, the tree cover in arable and pasture land, as well as a map with the K-factor for the same area (Brittany, France). When comparing the two, we see there is a clear correlation between the parameters: where tree cover is high, the K-factor tends to be low. In particular, the K-factor for the area that shows significant tree cover (more than 50%) in arable and pasture land (i.e., agroforestry) lies around 0.03 t h MJ^{-1} mm^{-1}, and locally decreasing to less than 0.02 t h MJ^{-1} mm^{-1} where the tree cover is higher than 80% (de Jalón et al., 2017). This is a significant decrease from the average erodibility value for Brittany, which was found to be 0.043 t h MJ^{-1} mm^{-1}. We cannot simply use these values for agroforestry in the area of our case study, however. Brittany is covered largely by the Armorican Massif, a principal mountain mass that is a part of the Hercynian Massifs that consist of metamorphic and magmatic rocks. Although Hercynian Massifs can be found in the area of interest (AOI) of our case study as the Rheno-Hercynian Zone including the Ardennes, the Vosges and Black Forest Mountains, as well as a presence in the Alps (Geyer et al., 2014), it is not a good representation of the general geology or soil type in our whole area of interest, which is much more heterogeneous. Because of this, and the complexity and local/regional character of K-factor calculations, we will use the percentile change between the average K-factor of Brittany and a value that represents agroforestry in that region. Because of the

variation in the amount and types of trees (which also affects the cover) throughout Central and Western Europe that we will represent in our case study, we will use the average value between the two values given for Brittanies erodibility factor based on its land cover/tree density. This means an erodibility factor of 0.025 t h MJ^{-1} mm^{-1} will be used for agroforestry land usage, resulting in a decrease of the erodibility factor by ca. 40% with respect to the more traditional types of agricultural land use.

As in Brittany, the geology of a region influences the material composition and structure of the soil, thereby changing its erodibility values. The erodibility values discussed now, however, only represent the top layer of (loose) soil. As we are simulating over 10,000 years, it is possible that at least in a part of the AOI, the topsoil will have been eroded away before the simulation time has passed. When we counter this by artificially increasing the soil layer thickness, it could lead to an unrealistically high sediment supply, increasing the sediment flux in the rivers, as well as erode areas that would otherwise not have due to erosion resistant bedrock. An example of this are the Vosges. This mountain range consists largely of igneous rocks as part of the Hercynian Massifs discussed above, which are resistant to weathering and erosion (Skinner et al., 2003). After the topsoil has eroded, the bedrock layer would resist the erosion more instead of continuing at the same rate and potentially completely eroding the mountain range away as if it were topsoil. To deal with this problem, we have to find a way to incorporate the bedrock as a separate, second layer underneath the soil, and for this we will need to find erodibility values for the bedrock. This will be discussed next.

3.0.1. Bedrock Erodibility Values

Typically fluvial incision of bedrock is a major component of landscape evolution models, especially when the simulations are ran for millions of years. Although basic models that describe the geotechnical controls on rock erodibility exist, the large scatter and trends in the results indicate that these controls are not yet fully understood (Turowski et al., 2023). Most studies trying to determine erodibility values for bedrock use a form of the stream power law (Equation 2.3) as a basis (Kent et al., 2020; Langston and Tucker, 2018; Mitchell and Yanites, 2021; Zondervan et al., 2020). These studies have not used the same variation of this law however, often using different values for the parameters n and m. This leads to a range of different units and influences the order of magnitude of the erodibility (Zondervan et al., 2020). Although the variation of erodibilities found for similar rocks in different climate regimes and environments indicate that the values for n and m are not as influential as the change in climate or the lithology, the units resulting from these coefficients make it impossible to meaningfully compare the values (Barnhart et al., 2020). To this end, Barnhart et al. (2020) have formulated a standardized erodibility factor K_c given by Equation 3.3.

$$K_c = K_p A_r^{(m_p - m_r)} S_r^{(n_p - n_r)}, \tag{3.3}$$

where m_r and n_r are the reference stream power law coefficients equal to 0.5 and 1, respectively. A_r is the reference drainage area, S_r is the reference slope. K_p is the published erodibility factor that needs to be converted, and m_p and n_p are the corresponding values for m and n. For our conversions, we will use the drainage area of the Rhine (285,000m^2), and follow the example of Barnhart et al. (2020) by using a standard slope of $S_r = 0.1$. The typical erodibility factor units for Badlands are given by [$T^{-1} \cdot L^{(1-2m)}$], where T is a specified time unit and L is a length unit. Filling in our reference value for $m_r = m = 0.5$ and years for the unit of time, we get the unit of yr^{-1}.

Zondervan et al. (2020) state that the erodibility values that were obtained through modeling exercises might significantly overestimate the true value while still able to produce realistic looking landscapes (these modeled erodibility values are usually not constrained by physical rock strength measurements, see Roy et al. (2015) and Yanites et al. (2017)), and stresses the importance of field calibration of the bedrock erodibility. With this in mind, we supply generalized erodibility values for different lithologies that were converted using Equation 3.3 in Table 3.1.

There are some lithologies that are present in our area of interest while not stated in the table. This is due to a lack of information on these materials in the literature, or the erodibilities that are available do not reasonably match the relative values in the table (i.e., differing many orders of magnitude and units resulting form a different law than stream power law). An example of such a material is dolomite. Although dolomite is harder than limestone (3.5-4 versus 3 on Mohs Hardness Scale, respectively), a distinct erodibility value for dolomitic limestones was not found in literature. For this reason we will approximate it with the K-factor of limestone, which is the closest alternative. For the same reason, marlstone will be approximated with the erodibility value for siltstone.

Table 3.1: Generalized bedrock erodibilities.

Lithologies	Generalized K-factor (yr^{-1})	Source
Granite & metamorphic	$1.87 \cdot 10^{-8}$	Stock and Montgomery, 1999
Volcanic & Volcaniclastic	$1.33 \cdot 10^{-5}$	
Mudstone	$1.99 \cdot 10^{-4}$	
Limestone	$(1.6 - 2 \pm 0.6) \cdot 10^{-6}$	Zondervan et al., 2020
Conglemerate	$(0.6 \pm 0.1) \cdot 10^{-5}$	
Sandstone	$2.26 \cdot 10^{-4} - 6.03 \cdot 10^{-5}$	Whipple et al., 2000
Siltstone	$9.6 \cdot 10^{-6}$	Pechlivanidou et al., 2018

As stated earlier, the erodibility factor present in the stream power law concerns the bedrock river incision, and not so much the topsoil (Murphy et al., 2016). This means the erodibility values presented for the topsoil that are several order of magnitudes higher than those of bedrock are likely to overestimate the sediment load in the rivers, as well as cause the topsoil layer to quickly erode away. In addition to this, their units are not compatible with the Badlands bedrock erodibility unit of yr^{-1}. First we will explore the layer thickness of the topsoil and general geology of Western and Central Europe in the next section, which results in a general bedrock erodibility map. Then, in section 3.2, we will discuss a way to reconcile the magnitude and unit differences between the topsoil and bedrock erodibilities.

3.1. Geology and Soil Depth

Because the erodibility factor plays an important role in the calibration of Badlands for our case study, the next section will talk in detail about the soil depth and geology of the region of interest. We will first introduce the geology of the AOI and its corresponding bedrock erodibility, followed by the soil depth.

3.1.1. Geology

Underneath the topsoil layer, a second layer of bedrock is added to ensure a more realistic long-term erosion in areas where the topsoil has been eroded away. This layer will be defined using the geology of our area of interest that is given in Figure 3.2. Different types of bedrock will influence how well, or with how much difficulty, the layer underneath the topsoil will erode. In order to implement this difference in erosion, the different eras and periods that are shown in the figure will be evaluated for their predominant rock types and thus coupled to their representative erodibility values.

Paleozoic

The Paleozoic is the era that lasted from ca. 541 to 252 million years ago. It composes of six periods, namely the Permian, Carboniferous, Devonian, Silurian, Ordovician, and Cambrian, in order of recency. Because the mountainous regions can be composed of lithologies originating from multiple periods we will discuss these areas under the section 'Unspecified or Varying Paleozoic'.

Silurian & Ordovician On our map not much of either the Silurian nor Ordovician can be found, and thus they are grouped together. These areas are mainly characterized by claystone and siltstone.

Unspecified or Varying Paleozoic The Central Massif, the Ardennes and Rhenish Massif (to a lesser degree), Vosges, Schwarzwald (Black forest region), and the Alps are all regions that contain high degrees of metamorphic rock due to the Hercynian orogeny, also known as the Variscan orogeny, and the Alpine orogeny (Neubauer, 2014; Skrzypek et al., 2014; Vaughan-Hammon et al., 2021). Apart from having the metamorphics in common, their respective lithologies vary and are usually spread over different periods. The Massif Central, the Vosges, and Schwarzwald (black forest mountain range) are mainly characterized by granitic rocks and smaller amounts of Early Carboniferous flysch deposits (siltstone, limestone, and sandstone in sequence). The Ardennes consist mainly of Devonian clay-, lime-, sandstones, and conglomerates, with Cambrian quartzite and metamorphic rocks like slate and schist in the southwest and the east bordering the Rhenish Massif. The Rhenish Massif is similar to the Ardennes, but differs due to the presence of Cenozoic extrusive rocks in its center and the south part which consists mainly of Permian sedimentary rocks (sandstone and conglomerate). The areas that are colored the same as the

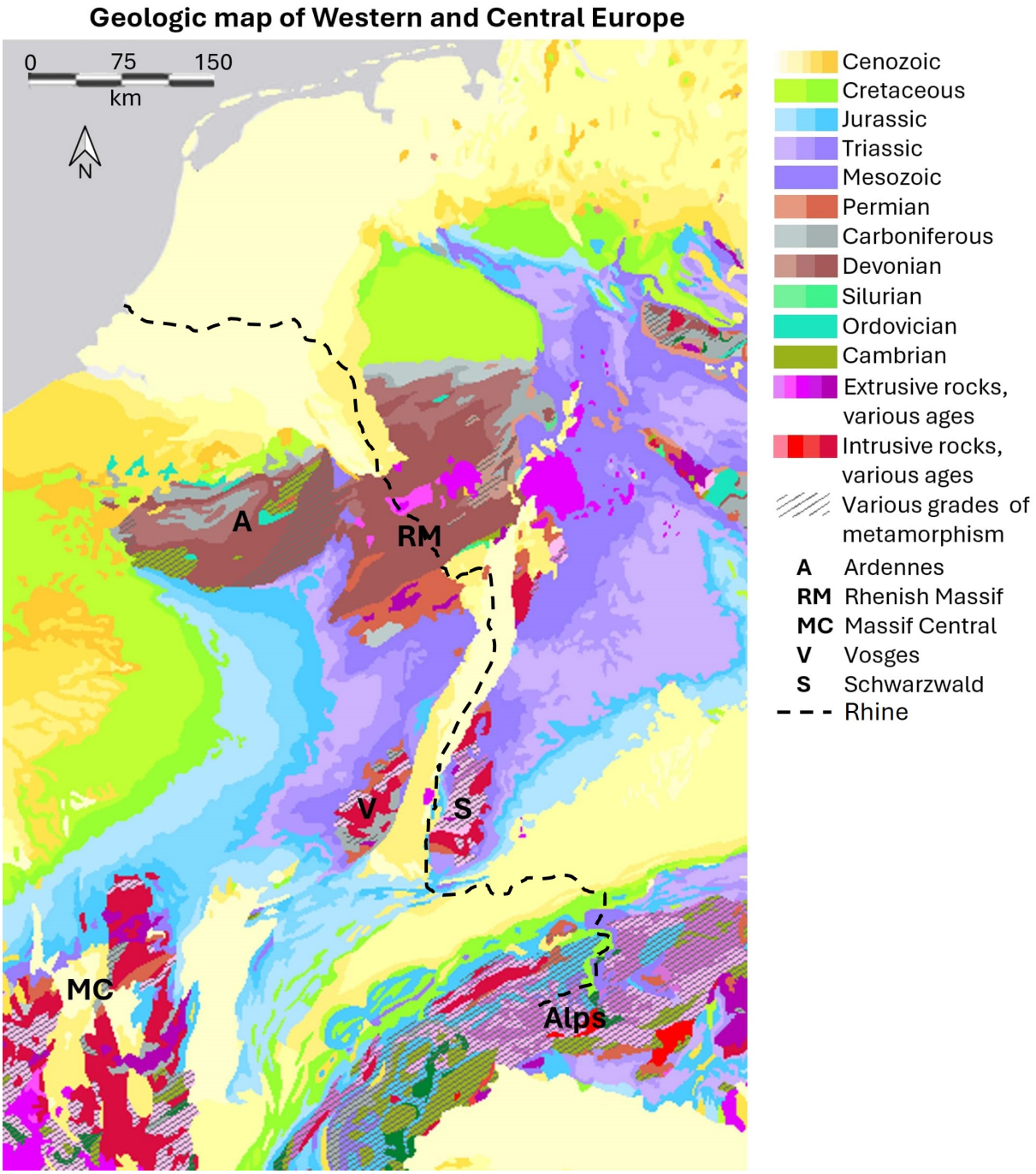

Figure 3.2: A geological map of Western-Central Europe showing some orogenic features and the approximate location of the Rhine. The gradient in the color bars in the legend indicate the epoch of the corresponding era or period where relevant: lighter colors indicate recency, e.g., the Cenozoic color bar indicates the Holocene until the Paleocene, from left to right. Map adapted from the International Geological Map of Europe and Adjacent Areas (BGR, 2005).

Cambrian in the western Alps and Massif Central are simplistically labeled as Paleozoic. All of the bedrock in the Alps are labeled as medium to high grade metamorphics. Examples are Mesozoic marble and mica schist, Jurassic marble and phyllite, Carboniferous-Permian meta-sandstones and meta-conglomerates, Ordovician amphibolites, and (not explicitly indicated on the map) Palaeozoic gneiss (BGR, 2005).

Mesozoic
The Mesozoic is the era that lasted from 252 to 66 million years ago. We will discuss this era using its three periods in order of recency: the Cretaceous, the Jurassic, and the Triassic period.

Cretaceous The Cretaceous period is mainly characterized by detrital and biogenic deposits. We primarily find marl-, and limestone, as well as chalk and sandstone (BGR, 2005).

Jurassic The Jurassic period is mainly characterized by biogenic deposits. The Late and Middle Jurassic rocks consist mostly out of limestone, marlstone, dolomite, and sandstone. The Early Jurassic is similar but also contains conglomerates and siltstone (BGR, 2005). Because the Late and Middle Jurassic deposits cover the majority of the Jurassic area in our area of interest (about four-fifth), we will calculate the erodibility value for the total Jurassic surface through their main components weighted by the area fraction.

Triassic The Triassic period is mainly characterized by detrital deposits. The Triassic area west of the Upper Rhine Graben has some evaporitic deposits as well. The Early Triassic consists of sandstone, siltstone, and mudstone. In both the Middle and Late Triassic, mudstones and dolomites are prevalent (BGR, 2005).

Cenozoic
The Cenozoic is the current era and started 66 million years ago. The surfaces of Belgium, the Netherlands, northern Germany, central France, the Upper Rhine Graben, as well as the North Alpine foreland basin are largely covered by the sedimentary deposits of the Cenozoic, consisting of silts, clays, sands, and gravels/conglomerate (BGR, 2005).

A notable exception to this are the Cenozoic volcanoes that are part of the Central European Volcanic Province (Abratis et al., 2015). These are indicated using the 'extrusive rocks' color scheme in Figure 3.2 and are located in the east and in the center of the Rhenish Massif. In the lower left corner of the Massif Central in the figure, some Cenozoic volcanic rocks are present as well. These areas consist of basalt and/or andesite (BGR, 2005).

Bedrock Erodibility Map
When we combine the rock types described in this section with the erodibility values from Table 3.1, it results in the bedrock erodibility map given by Figure 3.3. Due to the relatively short simulation times, no deeper lithologies will be explored for different erodibility maps. This means that the top bedrock layer will be assumed to be 'infinitely' deep within our simulations.

This map gives us a general idea of bedrock erodibility distribution throughout our area of interest. But as we have discussed before, the values used are difficult to compare to the topsoil erodibilities. This problem is discussed in the next section.

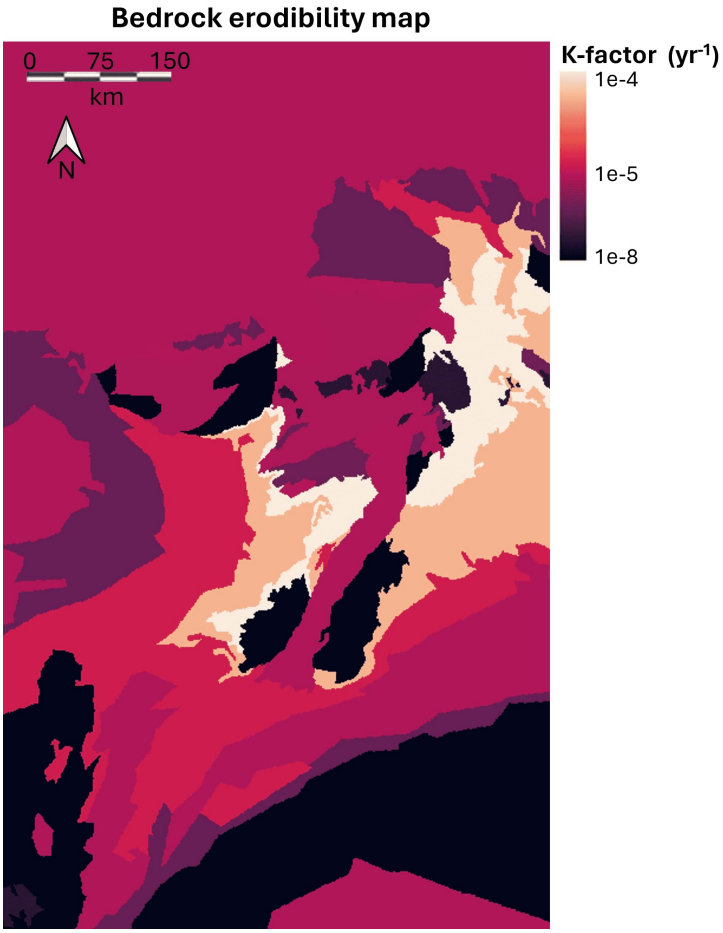

Figure 3.3: Bedrock erodibility map using values adjusted for units. Note that the color bar was scaled non-linearly to improve visibility. The different units for each value can be found in Table 3.1.

3.2. Evaluating Erodibility Compatibility

As is clear from previous sections, the way we can quantify the erodibility of topsoil/bedrock is through the use of the erodibility coefficient/K-factor. For bedrock, its value and associated units depend on the exact choice of stream power erosion law (Kirby and Whipple, 2001; Stock and Montgomery, 1999; Zondervan et al., 2020). The units for topsoil erodibility are determined by the units that are chosen for annual erosivity and soil loss in the universal soil loss equation (Foster et al., 1981; Renard et al., 1997). The annual erosivity is calculated by summing up the product of every storms maximum 30-minute intensity and its total energy, over all the storms in a year (Foster et al., 1981). The associated unit of this erosivity is $\frac{\text{MJ mm}}{\text{ha h yr}}$. The soil erodibility factor is the rate of soil loss per unit erosivity for a specified soil. Due to the unique units of this quantity, it is not possible to reconcile the values of topsoil with the bedrock erodibility through unit conversion. This means an alternative method is needed.

Following an extensive literature review, no topsoil erodibility factors in the units of yr^{-1}, nor conversion factors for the contemporary topsoil erodibility to units/values that are compatible with the incision/erosion laws as used in landscape evolution models were found. Because of this, a scaling factor is applied to the topsoil erodibilities through a process of educated trial and error described in section 4.2.2. The average erodibility for the different topsoil maps corresponding to the three land use scenarios as well as a selection of the bedrock erodibilities are put on one scale and shown in Figure 3.4, together with examples of these rocks.

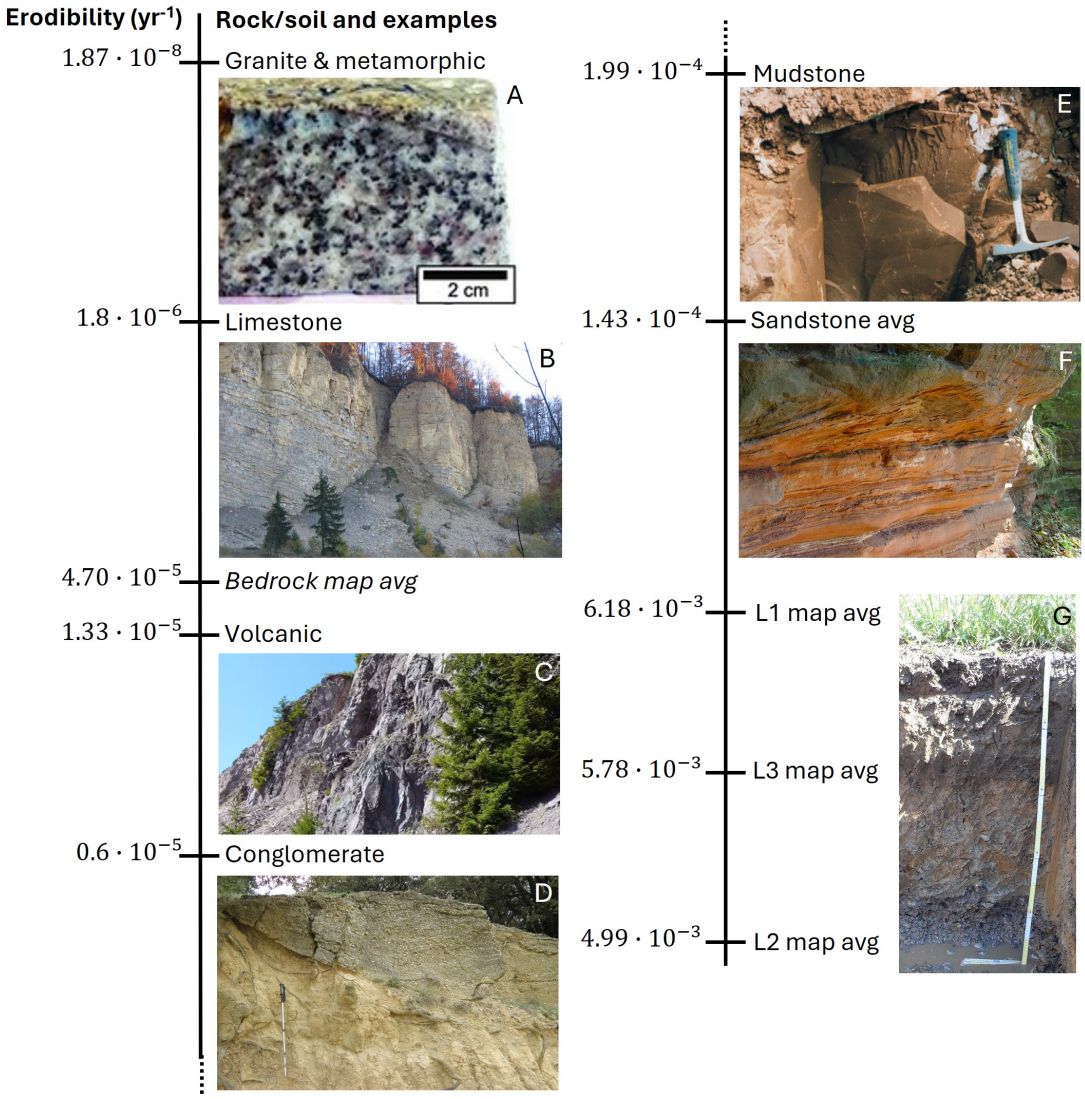

Figure 3.4: Scale of the erodibility values with visual examples of the rock types. avg = average. A: fine-grained granite from the Vosges, from Hasalová et al. (2015). B: Jurassic limestone beds near Hirschkopf (DE), from Appel (2005). C: Permian ryolite (volcanic rock) formation near Allzunah (DE), from Voigt (n.d.). D: Eocene conglomerate-filled channel cutting into floodplain at Agues-Vives (FR), with walking stick for scale. From Satterfield et al. (2019) and Suthren (2022). E: Early-Triassic mudstone of the Mercia mudstone group, in the East Midlands (UK), with a hammer for scale. From Hobbs et al. (2002). F: Triassic sandstone near Stadtroda (DE), from ArtMechanic (2002). G: soil profile near the Rhine at Freistett (DE-FR border), ruler gauge for scale. From Unterfrauner (2020).

3.2.1. Soil Depth

The soil depth at any location is influenced by many factors. Firstly we need to define what 'soil' means for our purposes. We will define the topsoil layer as the permeable layers above the bedrock. These layers are soil (in the more traditional sense), regolith (loose unconsolidated rock and dust), and sedimentary deposits (Pelletier et al., 2016). In order to estimate the thickness of these layers, Pelletier et al. (Pelletier et al., 2016) have defined four terms relating to landscape components. These are as follows:

1. Uplands: portions of the landscape that have experienced net erosion over geologic timescales (i.e., $\approx 10^5$ years or longer). In uplands, weathered bedrock can often be found within a few meters from the surface on hillslopes.
2. Lowlands: portions of the landscape that have experienced a net deposition of sediments over

geologic time scales. These areas tend to have a bedrock layer tens of meters below the surface.

3. Hillslope: defined as the areas that have unconfined flow of water across the land (overland flow) and a limited accumulation of sediments.
4. Valley bottom: the areas where the flow of water is confined within channel banks or valley sidewalls. Here, sedimentary deposits tend to be a few meters thick or thicker.

The spatial variation of soil thickness was modeled using the relationship between upland hillslope soil thickness, the mean upland curvature, and the mean annual rainfall at a global scale. The modeled soil thickness in Europe was then validated using high-resolution soil thickness data from the European Soil Database (ESDB) (Pelletier et al., 2016).

Regolith thickness in the uplands was estimated using the model proposed by Rempe and Dietrich (2014), using the estimated depth to the permanent water table which in turn was estimated using the 30-arcsecond equilibrium water table depth gridded data set of Fan et al. (2013). Due to the resolution of the Fan et al. (2013) data set, low-order valleys present in the uplands will generally not be taken into account. This was accounted for by dividing the water table depth of Fan et al. (2013) by a factor two, which would reflect the range of average water table depths within the 30-arcsecond grid cells, which generally vary from the maximum value given by Fan et al. (2013) to a value of zero near valley bottoms (Pelletier et al., 2016).

Sedimentary deposition was determined for both uplands and lowlands separately. In valley bottoms, the valley curvature and gradient of the hillslopes on the flanks of the valley were used to determine the deposited sediment layer thickness. It was assumed that the sideslopes of the valleys project down into a V-shape in the subsurface due to the predominance of fluvial processes over glacial processes globally. The average thickness of upland valley bottom sedimentary deposits h_{uv} is given by Equation 3.4.

$$h_{uv} \approx \frac{|\nabla z_h|^2}{4\nabla^2 z_v}, \tag{3.4}$$

where $|\nabla z_h|^2$ is the slope gradient for hillslopes, and $\nabla^2 z_v$ is the curvature of the valley bottom (Pelletier et al., 2016).

In lowlands, the sedimentary deposit thickness was determined using a generated 30-arcsecond grid of Topographic Ruggedness Index (TRI). The TRI is the average difference in elevation between a central pixel and its eight neighbors. This gives an impression of terrain relief at the grid cell scale. Depth-to-Bedrock (DTB) observations were then used to calibrate a predictive model for the DTB as a function of TRI (Pelletier et al., 2016).

Because uplands have both a hillslope soil thickness and valley bottom based estimate of sedimentary deposits, the pixels in these areas contain both values, weighted by their respective area fraction. As we are interested in only one value per grid cell for the total thickness of relatively porous and unconsolidated material, the average soil/sedimentary deposit thickness on uplands h_{av} is given by Equation 3.5.

$$h_{av} = \frac{h_{uh} f_h TWI_h + h_v (1 - f_h) TWI_h}{f_h TWI_h + (1 - f_h) TWI_h}, \tag{3.5}$$

where f represents the area fraction of valley bottoms versus hillslopes, h is the thickness, and the subscripts v and h represent the valley bottom and hillslope values, respectively. The subscript u corresponds to any value related to uplands. Lastly, we introduce the Topographic Wetness Index (TWI), which quantifies terrain driven variation in soil moisture (Kopecký et al., 2021). The TWI is used as a weighting factor besides the area fraction. This is necessary because the bottom valley fraction relative to the hillslope might be small, but the majority up to all of the water that is discharged from a drainage basin is routed through the valley bottoms (Pelletier et al., 2016).

The resulting dataset map that includes the average soil and sedimentary deposit thicknesses across upland hillslopes and valley bottoms is given by Figure 3.5.

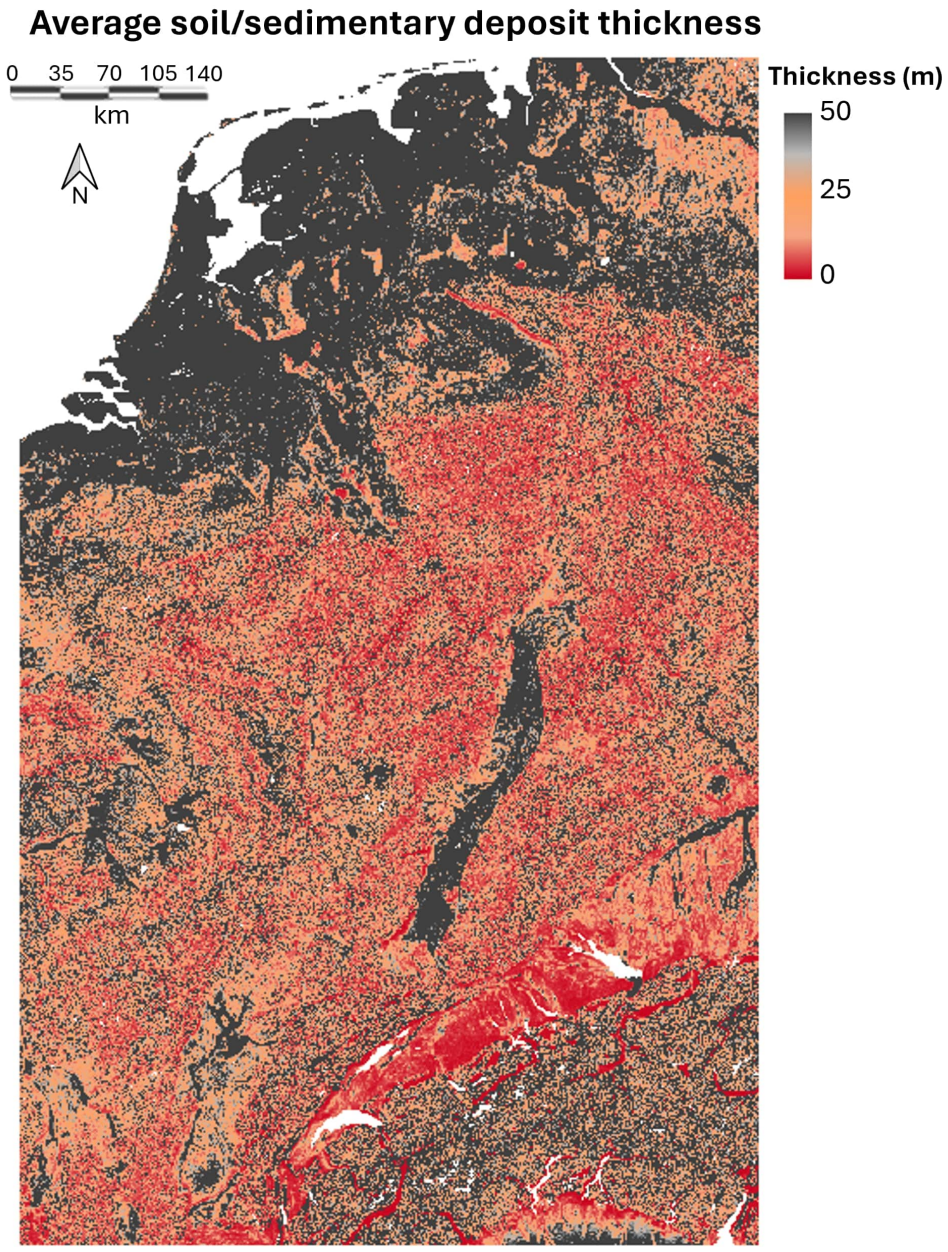

Figure 3.5: The average soil/sedimentary deposit thickness for Western and Central Europe, in meters. Data from Pelletier et al. (Pelletier et al., 2016).

4

Proof of Concept and Input Calibration

First, we will test the behavior of several parameters in order to understand and test the feasibility of Badlands to predict the future landscape, with a focus on the landscape of the area of our case study, Western and Central Europe. We will identify and quantify some potential problems, and will evaluate the effect of two possible tectonic cases on the Badlands output. Next, we will calibrate the erodibility and precipitation to produce outputs that are representative for modern day Europe. We define calibration as the selection and modification of input parameters such that the agreement of the output of a model with observed data is maximized (Oreskes et al., 1994; Trucano et al., 2006). In our case, this will be done based on sediment load and discharge values of the Rhine. The final calibrated output will serve as our base model that we will use for our case study in the next part of this thesis.

4.1. First (1,000 year) POC

The first thing we will discuss is a comparison between the three resolutions, and some general outcomes of these simulations. For this, we will use the simulations with a runtime of a thousand years. In Figure 4.1 the maximum discharge of the three simulations are given, which shows the main fluvial paths that were simulated compared to the true paths of the Rhine and Meuse. The resolutions that are used are 92$\times$147 (6,259m$\times$6,078m), 365$\times$886 (1,534m$\times$1,039m), and 1,824$\times$2,930 (307m$\times$313m). All the inputs and chosen parameters are based on our case study to maintain consistent results between the different parts of this thesis and these are all explained in Part II.

4.1.1. River Prediction

The first thing that is of note in Figure 4.1 is the different route of the 'Rhine' in the courser resolution as opposed to the finer resolution simulations. We see that instead of turning west towards the Netherlands, the 'Rhine' continues north merging with/following the path of the northerly river Weser and one of its headstreams (the Fulda) in Northern Germany. The finer resolution grids produced many of the main rivers and tributaries found in Central and Western Europe, as indicated in the middle figure, with the exception of the river Ems, shown in the left figure. When we compare the middle figure's 'Rhine' to the Rhine's actual course we see just one main difference: the simulated river continues northward a little further than the actual river, causing it to form the strong 'meander' between the spots marked with 'Mo' and 'Ma' in the figure. The simulated Rhine, in continuing northward, has actually reached the natural channel of its tributary the Main, which it follows 'back' downstream towards the true position of the Rhine. In the even finer grid on the most right of the figure we see an even better fit of the rivers.

An important difference between all three is the limit on the minimum width of the rivers, which is essentially determined by the size of a grid cell. As the width of a river is an important variable in the possible discharge and sediment flux, the smallest practical grid cell is preferred. The highest resolution grid cell in the figure is of the order of 300m. The width of the Rhine is quite variable, with a range from 50 to more than 750m wide (smaller widths are more frequent in the Alpine region, Klösch et al. (2021)). The average width of the Lower Rhine and Middle Rhine (from the Upper Rhine Graben until the Dutch-German border) is ca. 300m. This means the resolution of 1,824$\times$2,930 produces grid cells that are close to the average width of the Rhine, and are an accurate approximation of reality.

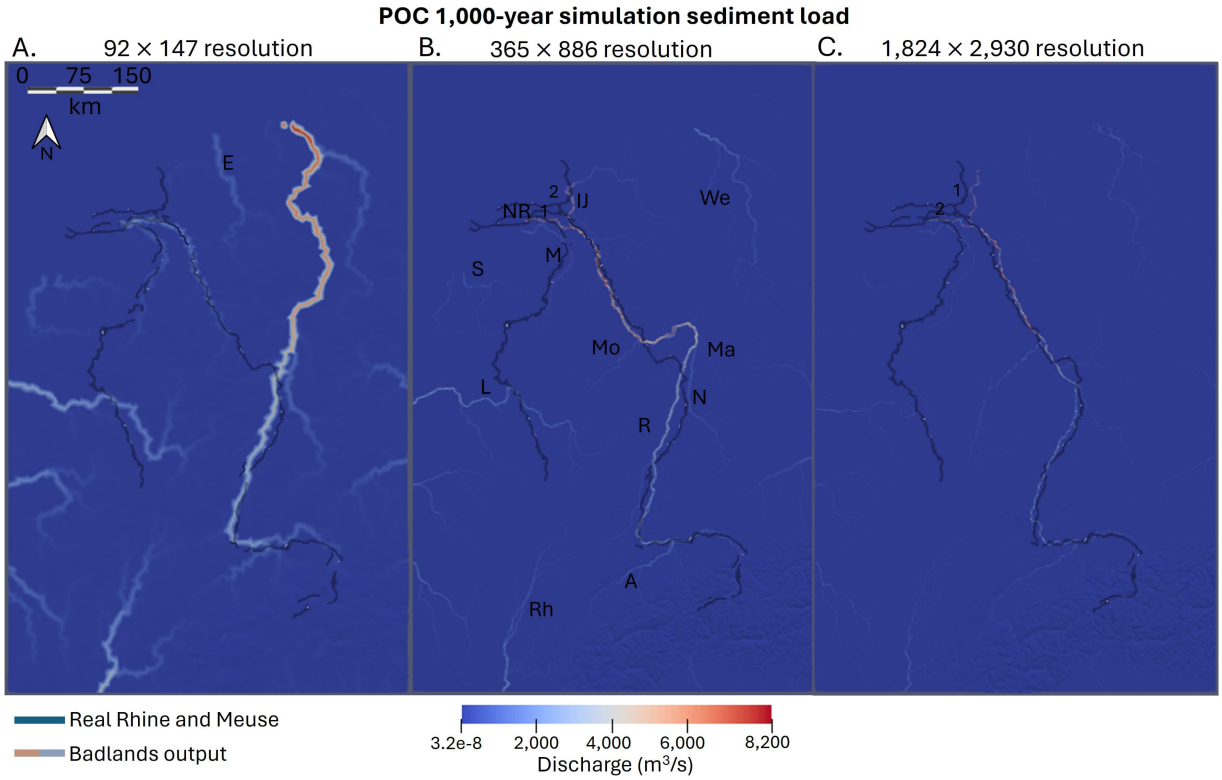

Figure 4.1: POC simulation discharge for three different resolutions given in grid cells. Images B and C are an overlay of two different time steps in order to show the divulsion of the Rhine from the Nederrijn (NR) to the IJssel (IJ) (or vice versa) indicated by the numbers 1 and 2. The rest of the letters indicate rivers that correspond largely to existing rivers in our AOI. A = Aare, E = Ems, L = Loire, M = Meuse, Ma = Main, Mo = Moselle, N = Neckar, R = Rhine, Rh = Rhône, S = Scheldt, Se = Seine, and We = Weser. Maps made using ParaView V5.12.0.

4.1.2. Discharge

The range of the discharge given is very high. As we have seen, the annual mean discharge of the Lower Rhine is around 2,300m^3/s, and values found more upstream of well under a 1,000m^3/s are normal. Although the discharge values are not outside the realm of possible discharges in the Lower Rhine, the simulation results look like a permanent flood scenario discharge throughout the river. There are several possible reasons why Badlands overestimates the mean discharge. Firstly, a peak discharge in the Alpine Rhine may reach 2,500m^3/s, confirming the flood-level discharge in the simulation result in this region. What looks to be unreflected in the results, however, is the major role of Lake Constance as a discharge buffer. While the input of the Alpine Rhine into the lake can reach values of 2,500m^3/s, the accompanying peak values at the outlet of Lake Constance are normally just over 1,000m^3/s (CHR, n.d.).

Secondly, the Upper Rhine Graben, a relatively low area surrounded by several mountain ranges, is classified as a lake in Badlands with the maximum lake depth set to 252m (the Depth of Lake Constance, which is the deepest lake in our AOI which is connected to the Rhine). This means this area will have an effect on both the discharge and the sediment flux as described later.

Thirdly, Badlands does not take into account any evapotranspiration: there is no temperature influence to evaporate any water from rivers or lakes, and no vegetation to absorb and hold water, and transpiring the water (back) into the atmosphere. Related to the lack of temperature is the effect of snow in the Alps. Although the increase in liquid precipitation (with respect to snowfall in the Alps) and different snow and ice melting dynamics can offset the effect that evaporation has on the discharge to some degree, a study found that the discharge of the Rhine is generally expected to decrease due to evaporation (Buitink et al., 2021).

Fourthly, and related to the lack of vegetation, Badlands does not allow for infiltration of the soil. For

this to be taken into account, parameters concerning the water table depth, hydraulic properties of the subsurface, and the moisture content of the soil and loose sediments (Ferré and Warrick, 2005) will have to be added to Badlands. Without the inclusion of the soil infiltration process, any precipitation that occurs will be treated as runoff (i.e., not infiltrating the soil), and thus finds its way to fluvial channels much faster and in greater quantities than if a part of this precipitation had reached the channel through the soil/subsurface flow. The last reason is the absence of anthropogenic water management. This can be divided in two main contributions: the removal of water from the rivers for drinking/industrial/agricultural purposes, and the management of the discharge through dams and sluices in both the main river and its tributaries (Frings, Gehres, et al., 2014; Klösch et al., 2021; Uehlinger et al., 2009). Uehlinger et al. (2009) state that 120 waterworks in total remove ca. 2.73 billion m^3 annually from the Rhine. Of course water that is used for irrigation is partially returned to the river through groundwater flow, as well as industrial wastewater. The increase of infiltration rate due to vegetation and proper agricultural land management (which is the majority of the surface in our AOI), can reduce the runoff rate on average by 30% (Bombino et al., 2019). According to the U.S. Geological Survey (USGS) about 70% of the annual precipitation in the United States returns to the atmosphere through evaporation from land and water, and transpiration from vegetation (Water Science School (USGS), 2019). The other 30% ends up in streams, lakes, or an ocean through runoff and slower subsurface movement. In section 4.2.3 we will do a short evaluation of a simulation with reduced precipitation that reflects this discrepancy between the runoff and rainfall.

4.1.3. Sediment Flux

Due to our conclusions comparing the discharge, we will not take the map A from Figure 4.1 into account when comparing the sediment flux. In figure 4.2 three time steps are compared for each of the two higher resolution results. For selected time steps (t = 20, 500, and 1,000 years) a new scaling is applied to improve visibility. An expected difference between the two resolutions is the amount of sediment load that is present: a coarser resolution means larger grid cells, which means we have a larger area over which the sediment load is determined. What we see in both cases is a general decrease of total sediment transport with increasing time. Although the color bar shows a range of values that is the vast majority of the values that are present, both resolutions have some outliers (presented as white spots in the figure). For the resolution of map B from Figure 4.1 the maximum value which is present at t = 20yrs is ca. $6m^3/s$, with 378 cells (out of more than 300k) having a higher value than $1m^3/s$, and of which only 71 cells have a higher sediment load than $2m^3/s$. Most of these points are situated either in the Lower Rhine or in the Alps. For the resolution of map C from Figure 4.1, we see that the maximum value is $2.26m^3/s$, with only 17 cells with a value higher than $1m^3/s$. The difference in values can be accounted for by the cell size difference. This does not scale linearly, as the erosion rate scales to both the surface and slope with their respective powers. In addition to this, the slope can change based on different spatial interpolations.

An important observation is the lack of sediment load following the Rhine into the Upper Rhine Graben, which does show a discharge as shown in Figure 4.1. This area, similar to the lower altitude area west of the Alps, is being classified by Badlands as a lake: known lakes like Lake Constance and Lake Geneva have similar values and are indicated the same way on the maps. In these areas, sediment is actively deposited until the lake is filled up.

When we evaluate the sediment load that is present in the rivers that we do see (mainly the lower part of the Rhine in the time steps shown), and compare them to the known values given in Table 5.1 for this region, we see that the $1{,}824 \times 2{,}930$ simulation output for t = 1,000yrs is remarkably close to reality: within a factor 2, and often closer than that. t = 1,000yrs is likely a time when the sediment load is primarily defined by the erosion of residual topsoil. However, in the time before t = 1,000yrs within the same resolution result the sediment flux is much higher than our reference values. The relatively high values that are seen in the Alps are only of short duration: after about 70 years the majority of the lighter colors have turned black as we can see at t = 500yrs.

This brings us to a few aspects concerning Badlands processes and our inputs for these proof of concept runs. Firstly, the fast decline of high sediment flux in the total AOI and especially in the Alps, combined with the overestimated initial sediment flux in the Lower Rhine could be due to the rapid erosion and transportation of the topsoil, which has erodibility values that are many magnitudes higher than the bedrock underneath. This makes sense when we look at the stream power law, which is useful for understanding landscape evolution by explicitly representing the bedrock incision rate of rivers (Venditti et al., 2020). What is not taken into account in this law however, is the erosion of the loose topsoil. Because on the

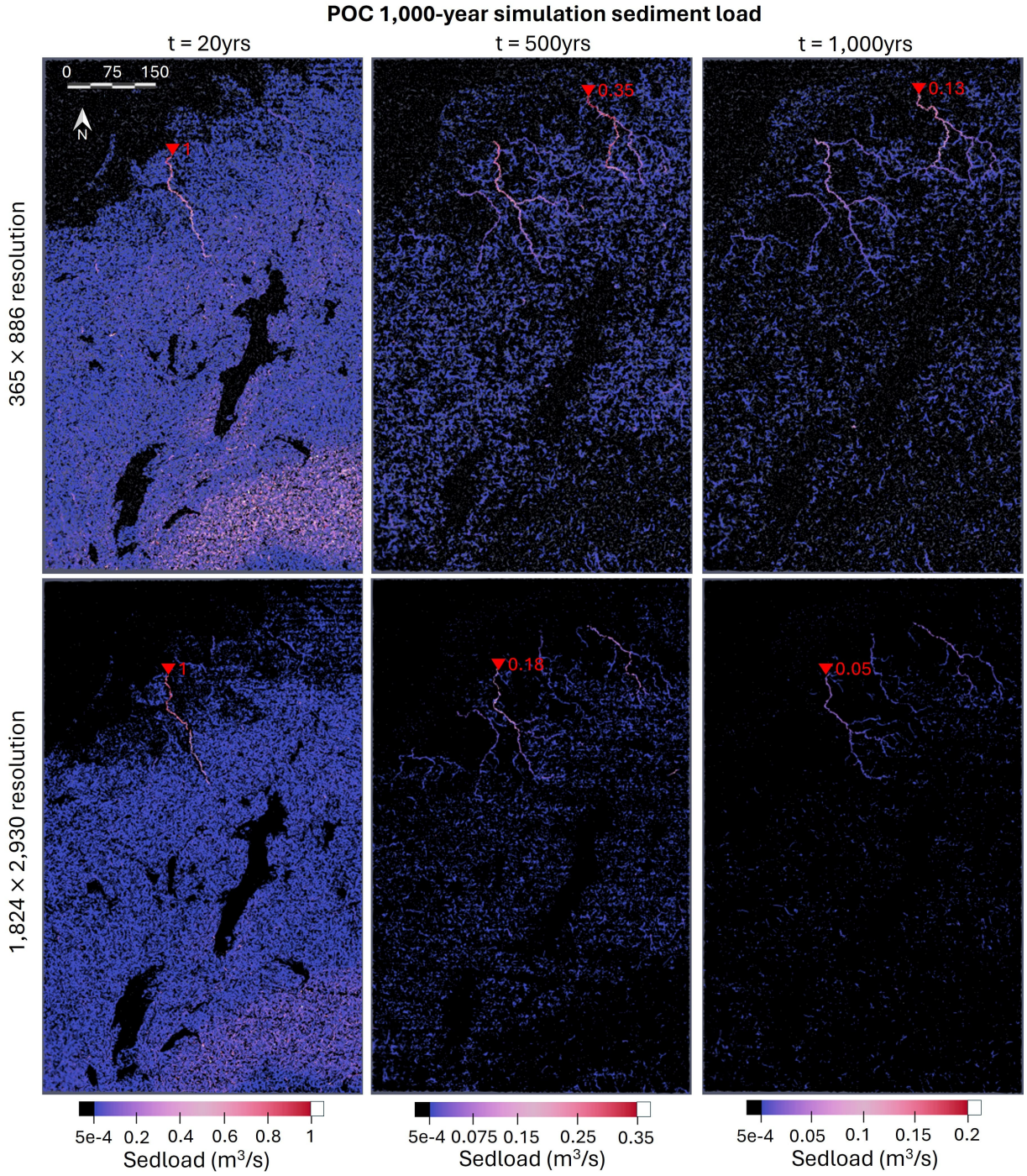

Figure 4.2: POC simulation: sediment load. For two resolutions indicated on the left. Three time steps are shown for each simulation. Each time step uses the color bar below, scaled to improve visibility. The red triangle indicates the maximum sediment load value in m^3/s. Note that this value is not always the maximum value of the color bar, this is for visualization purposes. Read 5e-4 as 0.0005. Maps made using ParaView V5.12.0.

investigated temporal scale, especially with the involvement of anthropogenic land use change, the topsoil plays an essential role and thus cannot be neglected/removed from our simulations.

Secondly, the sediment load throughout the rivers might be as high as it is (partially) due to the high discharge values. As stated before, this is likely due to 100% of the precipitation rate being converted as

runoff. This will be addressed in more detail in section 4.2.3. Thirdly, in the event that the sediment flux is mainly influenced by the topsoil, a situation where there is no infiltration of water, no vegetation, and related to both: soil production, the sediment load in the Lower Rhine is possibly defined by an *unreplenished* topsoil layer. All of these ideas will be evaluated in section 4.2.2. Lastly, the discharge and sediment load can be influenced by the Upper Rhine Graben acting like a lake. Because there is only one parameter related to lakes in our Badlands input, a sensitivity analysis is done for the discharge and sediment load values with respect to the maximum selected lake depth. This is given in section 4.1.5.

4.1.4. Sea Level and Coastline

Badlands uses a sea level reference point which is set to its default version of 0m. This corresponds to the global average and is in line with the sea level that is found on the Belgian, Dutch and German coastline. There is one problem that results from this reference level, however. Badlands bases its sea level and topography on the coordinate maps from an open source EPSG library (MapTiler Team et al., 2022). These do not carry information on anthropogenic coastal defences nor explicit knowledge of the state of the target positions. In our area of interest, significant parts of the Netherlands, Belgium, and to a lesser degree Northern Germany lie below sea level. This means that Badlands will interpret these areas as part of the sea, instead of identifying it as land. The extent to which this happens is shown in the rendering of the Badlands' interpretation of the topography/bathymetry of our AOI in Figure 4.3, and aligns with the termination of the fluvial channels in the northwestern part of Figure 4.1. The topography-imaging tool that was used to create this image only looks at the relative sea level to distinguish topography and bathymetry, but it does not produce any lakes. This is clear from both Lake Constance and Lake Geneva being portrait as dry Alpine valleys. The identification of lakes by Badlands will be discussed in the next section.

As artificially lowering the sea level to counter this effect would go against the climate scenarios and possibly alter the sediment flux due to a change in base level, and the artificial heightening of the low lying areas would disrupt the normal flow and thus decrease the accuracy of the simulated rivers, no action is taken to remove this effect. Although the area of the Netherlands that will be flooded is a densely populated and economically significant area in Europe, there are two reasons this will likely not impact the outcome of our research. Firstly, in order to meaningfully compare the simulated properties and present day values, comparable waterways are necessary. Badlands is not capable of reproducing the process of bifurcation, which is essential to this system that is consisting of multiple channels that have an active stream at the same time, and are heavily influenced by humans as well. As described in section 5.1.1, the Rhine-Meuse delta which is positioned in the 'flooded' area is so complex, that while Badlands could reproduce the main waterways in the delta, it would not be able to accurately reproduce the majority of the present waterways. Secondly, the time scale and corresponding sea level rises will cause the majority of the disputed area to be flooded after several hundreds of years. In addition to this, a meaningful comparison between the Rhine and its simulated counterpart can be done by looking at the point where the river crosses the Dutch-German border before it bifurcates.

4.1.5. Sensitivity Analysis Maximum Lake Depth

Now we will briefly discuss the influence of the lake mechanism in Badlands. We have seen that the output for sediment load and discharge for the maximum lake depth was set to 252m. In Figure 4.4 the lake classifications and depth, the discharge, and the sediment load for the maximum lake depth set to 200m (Badlands default value, Badlands Group (2019)) and 100m are given for our area of interest.

For all of the simulations the high resolution (1,824$\times$2,930) POC settings are used with only the maximum lake depth setting varying. A first order observation is the correct identification and average depths of both Lake Constance and Lake Geneva (when not limited by the maximum lake depth). These lakes have an average depth of 90m and 152m, respectively (ILEC, n.d.). Apart from these known lakes, the map shows several river valleys like that of the Moselle, Rhône, and the Upper Rhine Graben (URG) classified as lakes as well. It becomes clear that the depth of the URG 'lake' is the same as the depth of the valley. However, the relative low altitude of the valley with respect to the local topography causes a lake to be identified even if the maximum lake depth is set to 25m. Before we will talk about the impact this has on the discharge and sediment load, it is important to note that a large part of the surface of the valley is artificial land use in the form of major cities (e.g., Strasbourg, Karlsruhe, Mannheim, Mainz, and Frankfurt am Main) and accompanying infrastructure. Given that this area is heavily influenced by

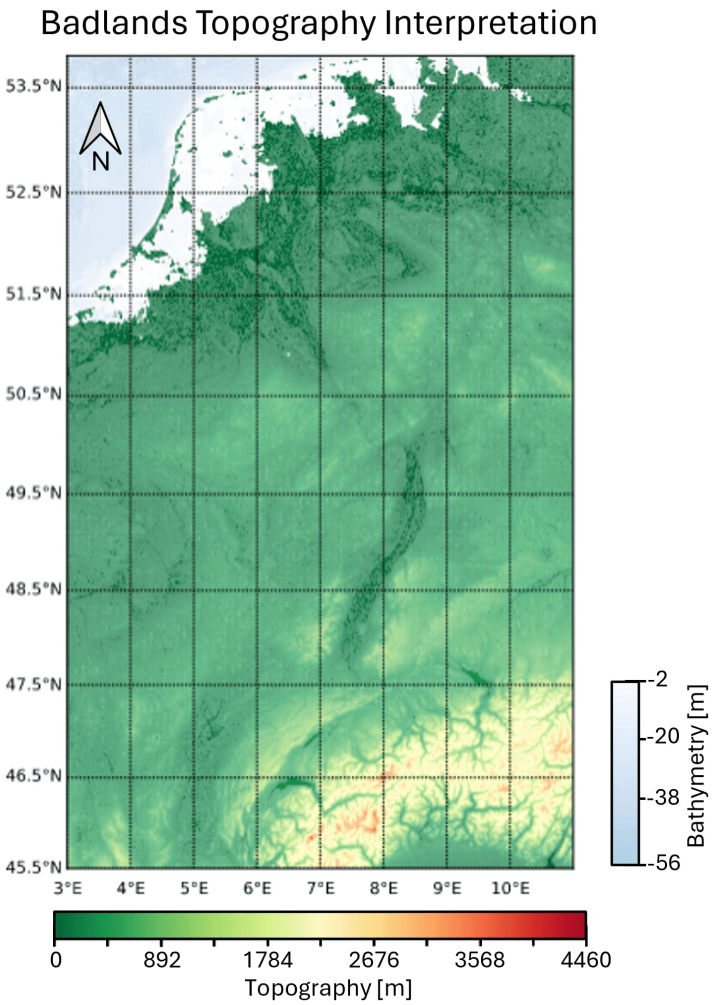

Figure 4.3: Badlands' interpretation of the topography and bathymetry of the area of interest. The Dutch dunes and Wadden islands are still defined as topography, while the areas behind them are interpreted as sea. Based on coordinates from MapTiler Team et al. (2022).

the Rhine, the implemented land use changes in this area that could significantly contribute to measured changes in sediment load will not contribute nearly as much, or at all when classified as a lake.

When we look at the discharge maps, there is an important difference between the two lake depth maxima in both the discharge and the channel paths of the 'Rhine'. For the maximal depth of a 100m, the upper Rhine and Lower Rhine never connect to eachother, while its tributary the Moselle is now part of the main Lower Rhine channel. The discharge of the Aare at its confluence with the Rhine on our map is already higher than 800m^3/s (compared to its real mean annual discharge of 559m^3/s (Uehlinger et al., 2009)), similar to the High Rhine (Rhine after Lake Constance). Among the reasons we have already discussed, this results in a very high discharge in the Rhine. The reason this discharge does not increase as much as the previous runs is likely because of the split of the Rhine: it never gets the opportunity to accumulate discharge along its full length. We can compare the discharge at the end of the two separated rivers of the Lower Rhine-Moselle and the upper half of the Rhine plus all tributaries and see that the majority of the discharge is from upstream.

When we compare the sediment load between the two runs, we see, as predicted, that the Meuse does not show any difference. Due to the 'splitting' of the Rhine in the 100m run, we do expect a difference in the Rhine however, which is only just visible in the figure: at the south part of the Lower Rhine we see the sediment load increase a little faster in the case of a full reach of the river Rhine.

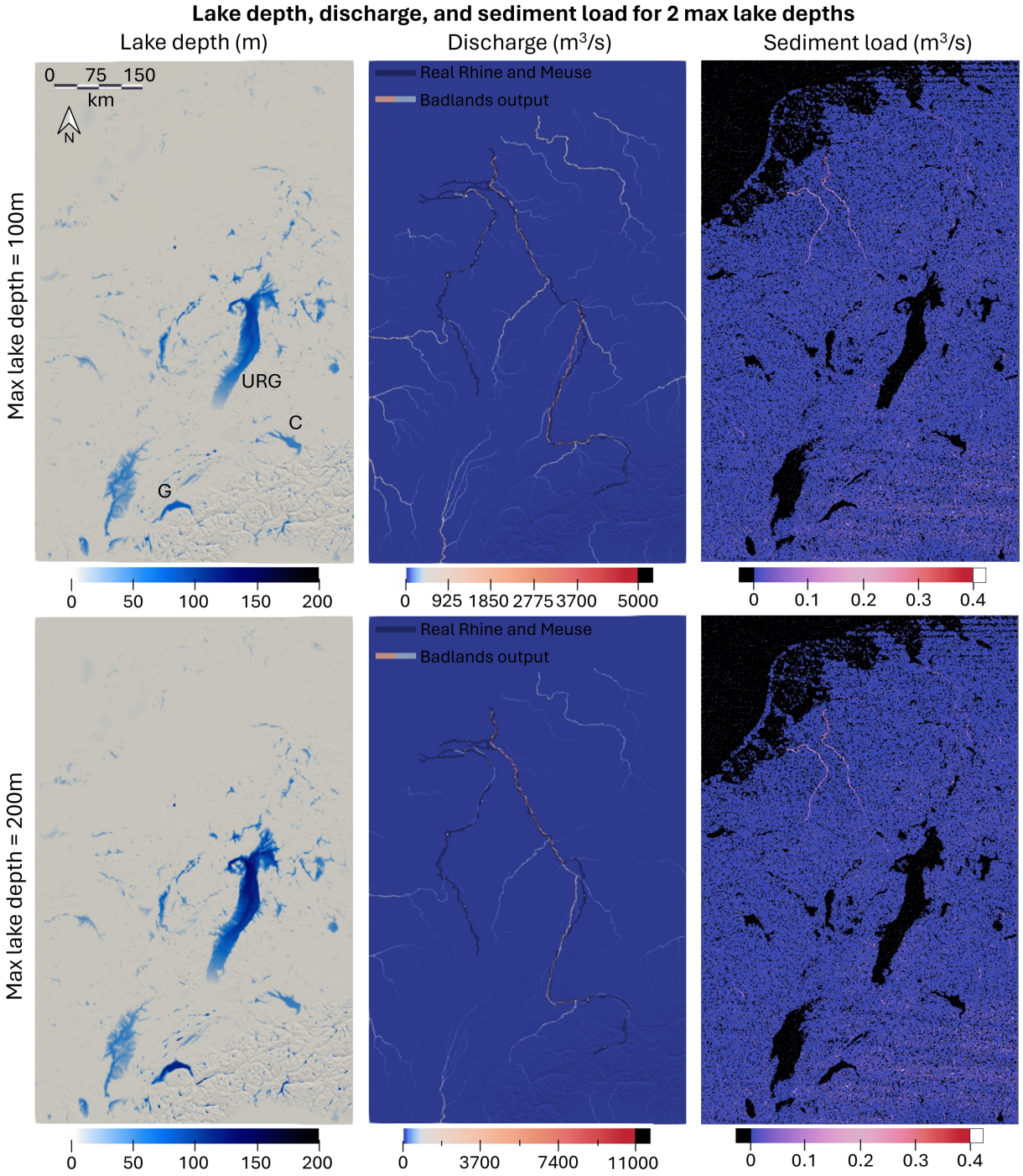

Figure 4.4: Lake depth, discharge, and sediment load outputs for the maximum lake depth set at 100m and 200m, time step t = 50yrs. C = Lake Constance, G = Lake Geneva, URG = Upper Rhine Graben. Maps made using ParaView V5.12.0.

In short, the differences in discharge and sediment load that we see between the maps are fully explained by the different configurations of the Rhine, where the Rhine is closest to its real-life length when the maximum lake depth is set to at least 200m. The classification of the Upper Rhine Graben as a lake is expected to change the outcome of our research concerning land use change significantly, however. Lowering the maximum lake depth to only 1m will only produce 'traces' of rivers, and apart from some small and random rivers, no realistic rivers are present, let alone one that resembles the Meuse or the

Rhine. As by lowering the maximum lake depth we do not get rid of this effect, and in addition divide the Rhine in two separate rivers when it is below 100m, this is not an option. A proposed solution to the miss-identification of lakes in Badlands is to artificially force the elevation of specific points in your TIN (T. Salles, personal communication, 2024). This, however, is a time-intensive process that requires one to identify every point of interest (which in our case is the Upper Rhine Graben, as well as parts of the Moselle river valley and possibly Rhône) and manually set its elevation. In our case, the elevation change of the valley compared to the lower elevations elsewhere, in particular to the southwest of the Vosges, could cause the Rhine to not turn right between the Vosges and Black Forest, but follow the now lower positioned route to the west towards Dijon in France. Unfortunately there is no alternative way to fix this problem for our specific use yet.

4.2. 10,000 Year POCs

Until now we have used simulations of a 1,000 years to evaluate several aspects of Badlands' output. The tectonic variation that we will test now only shows variation beyond the 1,000 years, so it is important to test this using simulations that last longer than this. As the case study in Part II will focus on a range of 10,000 years, we will do the following calibration steps and output analysis for simulations of 10,000 years into the future.

4.2.1. Tectonic Variations

Next, we will evaluate two realizations of 10,000 years, where we vary the temporal extent of the Fennoscandian and Alpine Glacial Isostatic Adjustments (GIAs). This the post-glacial rebound of the Fennoscandian and Alpine regions due to the melting of the major ice sheets that were there during the last glacial period (Barletta et al., 2006; Nocquet et al., 2016). We will distinguish between two tectonic cases. The first, which we will call T1, is where the GIAs last for the full 10,000 years of the simulation. The second variation, or T2, assigns a time limit for the Fennoscandian GIA and Alpine GIA. They will last for 3,600 years and 2,000 years, respectively. The origin and exact vertical displacement of these variations as well as the rest of the uplift and subsidence that is applied in all cases will be discussed in detail in section 7.2.3. These simulations are done using a maximum lake depth of 252m, and the two base maps for erodibility. From the evaluation of the fluvial channels, sediment load, and the discharge, the difference between the T1 and T2 is negligible and does not warrant a doubling of the amount of simulations that are run. In Figure 4.5 we see where the two versions differ in terms of discharge and fluvial channel position.

It is worth noting that in the 10,000 year runs, after 5,000 years the river channels do not change location often, and if they do it is only by the small steps as shown in the figure. The main divulsions happen in both the realizations and at the same time steps. It is likely that this lack of activity is at least partially due to the absence of a base level change, and the low level of sediment flux for the majority of the time. The sediment load for different time steps is shown in Figure 4.6.

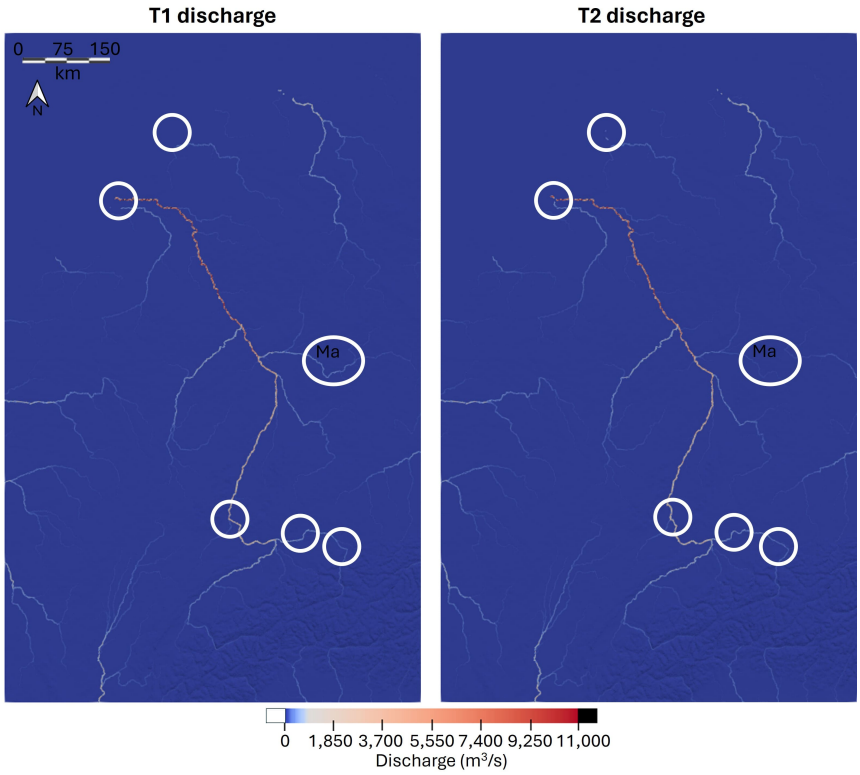

Figure 4.5: Differences in channel path and discharge between T1 and T2 displacements for t = 5,000yrs. The white circles indicate locations that show a difference in channel path between the two maps. The only significant difference in discharge is found in the river Main, indicated by 'Ma'. This difference in tributary discharge does not significantly change the main channels discharge as shown. Maps made using ParaView V5.12.0.

The first 1,000 years see a decrease of sediment load of three orders of magnitude. This is followed by a decrease of one order of magnitude until t = 2,500 years, after which there is no significant change anymore. The Lower Rhine and upper part of the Meuse are clearly visible in the first 600 years, after which the Meuse is less visible and not visible at all after t = 1,000yrs. After t = 1,000yrs, the sediment load decreases significantly, with a visible sediment load 'pulse' every other 200 or 300 years until t = 2,500 years. Between 2,500 and 10,000 years, the rivers are not visible anymore the majority of the time, with a somewhat clear pattern rarely emerging in the same magnitude of sediment flux ($\sim 10^{-4}$). We do see that within the Alps there are sediment loads of this magnitude throughout the remaining of the time. Although the sediment flux from the Alps via the Rhine is not directly visible on the maps, we do see an additional area that has sediment load appear in the south of the Upper Rhine Graben when comparing the last three maps: this indicates a supply of sediment and deposition in the southern part of the Upper Rhine Graben 'lake'.

Apart from the minor differences between the T1 and T2 simulation results, there is no significant change between these simulations. The sediment load that is given for T1 in Figure 4.6 is almost identical to the T2 output (thus it is not shown here). Because of these results, we will only apply the T1 setting in future simulations. This means we will implement no end of the Fennoscandian and Alpine GIAs within the 10,000 years of the simulations. This also corresponds with the inclusion of the GIA in the sea level curves derived by Clark et al. (2016) over the same period.

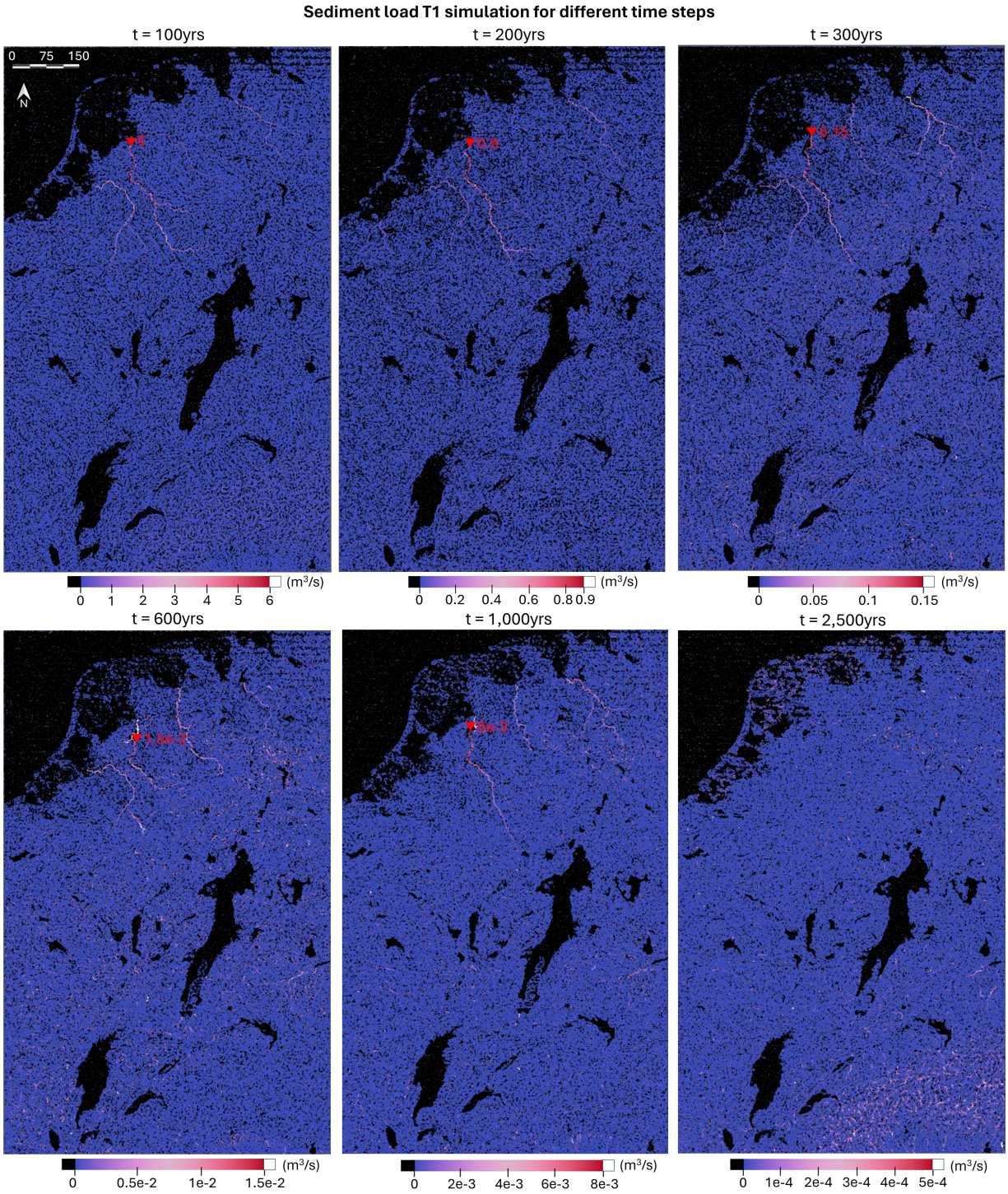

Figure 4.6: POC: sediment load outputs for different time steps from the T1 displacement simulation. The red triangle indicates the maximum sediment load value in m^3/s. Note that this value is not always the maximum value of the color bar, this is for visualization purposes. For the same reason the scale of each color bar is different. Read 5e-4 as 0.0005. Maps made using ParaView V5.12.0.

4.2.2. Erodibility Layer Evaluations

We will evaluate three variables regarding the erodibility maps. First, a simulation with no topsoil is performed to see if the topsoil erosion is responsible for the initial sediment flux, and what the 'background' bedrock-related sediment load in our fluvial systems is. Second, an increase of the topsoil layer thickness

is proposed. And thirdly, the topsoil erodibility values are scaled by a certain factor. A fourth simulation that combines the two last changes will be evaluated as well. As we have already done a full 10,000 year simulation with our 'default' inputs, we will compare our findings here with the sediment loads from Figure 4.6.

Single Bedrock Layer
In order to test the effect of the bedrock against the topsoil, a simulation over 10,000 years was done with only the bedrock layer defining the erodibility. In all other aspects, this realization had the same inputs and settings as the second POC T1 run as discussed above. The discharge in both cases is nearly identical, with the values being the same along the river paths. The path of the Meuse is identical in both simulations. The Rhine shows some differences in divulsing, which are mainly the same as shown in Figure 4.5. The sediment load for six time steps throughout the bedrock simulation is shown in Figure 4.7.

The first thing that is apparent is the lack of a high sediment load pulse as is the case with the simulation that has topsoil. We see an initial sediment load that is only visible on a scale that is two orders of magnitude smaller than our reference values of the present day Rhine. No clear river channel is visible even at this scale. As time passes the sediment load that is visible slowly increase in both magnitude and distribution over the modeled area, until at t = 900yrs the lower 'Rhine' suddenly starts to appear with a much higher sediment load than in the beginning, even though it's still on the low side compared with our reference values for the Lower Rhine. At the next step we see that the Lower Rhine has expanded towards the south. This reach and range of sediment load values are maintained for ca. 1,000 years until t = 2,000yrs, after which we see the river slowly fade away over a course of 500 years. At t = 2,500yrs we only see a trace of the Rhine that was there when we decrease our scale by two order of magnitudes. For the rest of the time, the sediment load slowly disappears. Small amounts of low value activity as seen on the last time step are present, as well as a somewhat higher sediment load for the river fragments that appear to be the Ems and Weser rivers in Northern Germany as we can see at t = 2,500yrs.

Amplified Topsoil Layer Thickness
An important factor to consider in LEMs is the soil production rate. G.K. Gilbert already proposed in 1877 that the conversion rate of bedrock into soil will reach a maximum when a certain optimal soil depth facilitates contact between bedrock and water "such that freeze–thaw and chemical weathering are maximized" (Gilbert, 1880; Humphreys and Wilkinson, 2007). As the topsoil is eroded away, there will be a replenishment of new soil that is created underneath, if the initial topsoil was thick enough (but not too thick to stop water from reaching the bedrock). This process is not modeled in Badlands. Because of this, it is possible that after our initial topsoil layer is eroded away, sediment load is solely determined by bedrock erosion. As bedrock has an erodibility factor of several orders of magnitude lower than that of topsoil, this would lead to a much lower sediment load as observed in the different simulations that were discussed with and without implementing a topsoil layer. A way to deal with this, is to determine what the average rate of soil production is and from this to calculate the total thickness of the produced soil layer over the simulation time. To simplify this already complex problem, we will only take into account the soil production that is derived from bedrock, and not from already weathered bedrock (saprolite, which is described by a different function). Wilkinson and Humphreys (2005) derived bedrock soil production rates averaging over timescales of 10^4 to 10^5 years, at scales ranging from sub-hillslope to catchment-size. They found that if the soil depth is relatively constant over time, the soil production rate equals the transport rate and thus is essential for sustainable erosion.

In order to define a Soil Production Function (SPF), it is important to take into account that soil production is a self-limiting process. In other words, when there is no topsoil layer and regolith, water that is essential to both thaw-freezing and chemical processes is unable to reach the bedrock due to runoff and thus soil production decreases. When soil is being produced and the topsoil layer becomes too thick, the thicker soil layer will progressively buffer the underlying bedrock for further weathering (N. J. Cox, 1980). Because many other factors influence the weathering of bedrock and resulting soil production, SPFs tend to be quite complex. Although the exact processes are difficult to quantify and vary per region, recent developments in the field have had some success (Ben-Asher et al., 2021; Benjaram et al., 2022; Heimsath et al., 2019; Humphreys and Wilkinson, 2007; Oeser and von Blanckenburg, 2020; Schaller and Ehlers, 2022).

The observed behavior between soil production and soil thickness is typically described using one of two functions. A 'humped' function, and a declining exponential function (Humphreys and Wilkinson, 2007), both of which are illustrated in Figure 4.8.

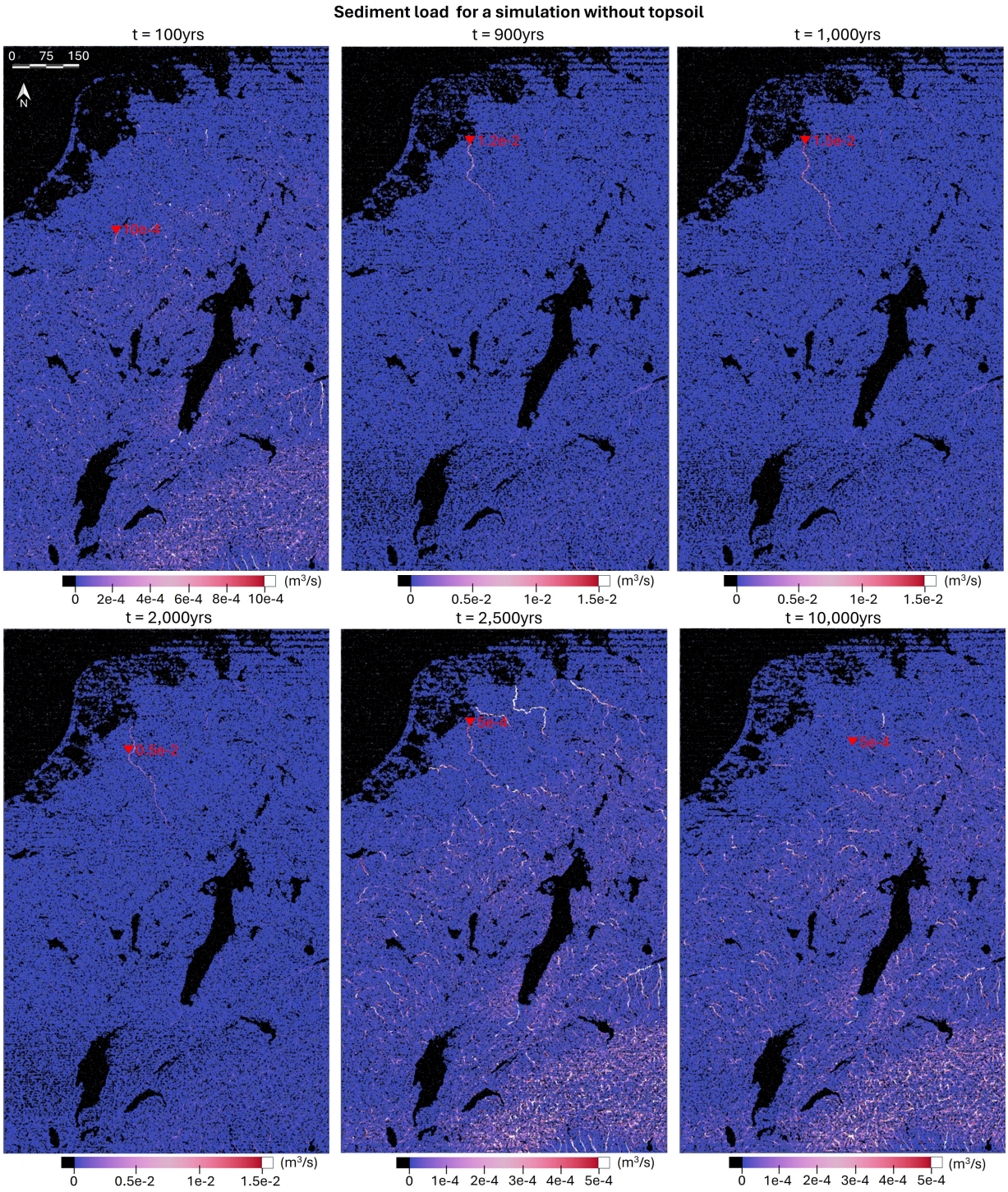

Figure 4.7: POC: sediment load results for bedrock erodibility, without a topsoil layer. The red triangle indicates the maximum sediment load value in m^3/s. Note that this value is not always the maximum value of the color bar, this is for visualization purposes. The color bars are scaled differently per map to increase visibility. Maps made using ParaView V5.12.0.

The humped, or bell-shaped polynomial function, may follow the intuition that maximum soil production occurs under a relatively thin soil layer (Heimsath et al., 1997), according to the observations of Dietrich et al. (1995) that the soil depths that are below the peak are unstable. They found that a declining exponential SPF agreed with observations in the field where there was no significant part of exposed rock. This function

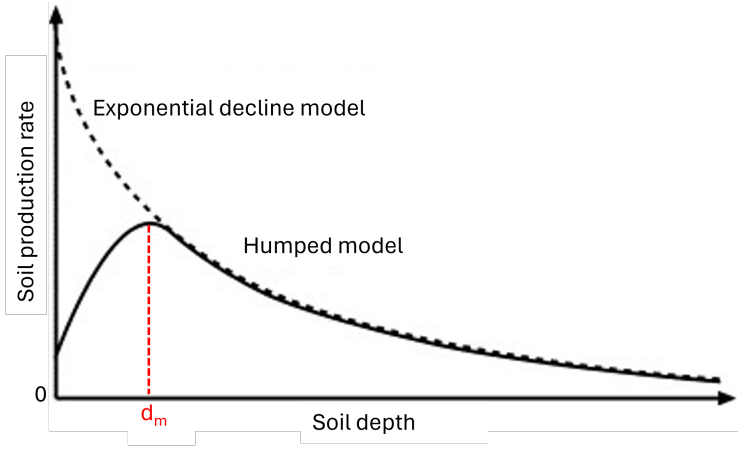

Figure 4.8: Example of a declining exponential function and a humped function relating soil thickness to soil production rate. d_m is the soil depth at which there is maximum production. Adapted from Humphreys and Wilkinson (2007).

is given by Equation 4.1.

$$SPR = (47 \pm 15)e^{-(0.020 \pm 0.007) \cdot H}, \tag{4.1}$$

where SPR is the Soil Production Rate in m/Myr, H is the soil thickness in cm, and the two fitted constants have the units m/Myr and cm^{-1}, respectively (Heimsath et al., 2009). When the measured values for exposed bedrock are taken into account, Heimsath et al. (2009) state that this function turns into a humped function, however the formula is not given. Equation 4.1 was developed for Arnhem land in northern Australia, but the authors state that this function is remarkably close to the SPF quantified for south-eastern Australia. According to the Köppen climate classification map, these regions have the same climate types as Western and Central Europe (Beck et al., 2018; Köppen, 2011). Even if this wasn't the case, Wilkinson and Humphreys (2005) state that all the soil generation rates that they found were remarkably close for regions with different lithologies, climates, and tectonic settings. This means we can apply this SPR to our region of interest. However, it is important to note that the units of the soil production rate are in m/Myr. When we plug in the mean value of our topsoil thickness of 31.5m, this returns a SPR of 25m/Myr, or a soil production of 0.25m per 10kyr. When we assume there is no outcropped rock (a reasonable assumption for most of northern Europe) and the declining exponential function works over the full range of soil depth, the maximum soil production over the 10,000 years of our simulations is 0.47m.

This is a negligible addition to the soil depth, which will likely not change the outcome and initial pulse of sediment load in our simulations. This is because although Wilkinson and Humphreys (2005) stated that soil production rate equals the transport rate in reality, we see that in our simulations the transport is mainly determined by the topsoil layer, which, due to their high erodibility values in combination with the stream power law that is used in Badlands, will overestimate the erosion and thus sediment flux. In other words, our system is not in equilibrium, which causes the soil depth to decrease faster than it could replenish through natural processes. An artificial increase of topsoil depth will therefore only lead to an increase in initial sediment load pulse, and this effect might be stretched out over more time steps due to the transport limit of rivers. Even if additional sediment from the Alpine region would be deposited in and thus fill up the URG 'lake', allowing fluvial processes to become active here, the artificial addition of sediments from this increase in topsoil thickness makes the evaluation of sediment loads compared to our reference values lose their real meaning and be less reliable. If the problem of the initial major sediment load pulse can be solved, a thicker topsoil layer to account for the faster than normal erosion rate might be possible.

Decreasing Topsoil Layer Erodibility

The alternative to increasing the topsoil layer thickness is to adjust the values of the topsoil erodibility. A first step to try and find the necessary adjustment factor is to compare the units of both the topsoil and bedrock erodibility. Because of the difficulty finding a factor that relates this to the contemporary topsoil K-factor units *t h MJ^{-1} mm^{-1}*, this will be done by looking at the difference in order of magnitudes. Because the main problem is likely caused by topsoil K-factors that are much higher than that of bedrock, we will

try to scale the topsoil erodibilities by a factor of 0.1. This brings the order of magnitude of these values closer to that of bedrock (see Figure 3.4). The sediment load for different time steps for decreased topsoil erodibility is shown in Figure 4.9.

The first thing that we observe is the lack of initial sediment load pulse. It is also noteworthy that the difference between the Rhine and Meuse are bigger than the previous runs, to the point where the sediment load scaled to the Rhine will make the Meuse nearly invisible. Given the large difference of the real rivers, this is closer to reality than previous simulations. The Rhine only appears at step t = 200yrs, which is why this is the first map that is shown.

From time step t = 5,800yrs we see that the Rhine has changed its course from the IJssel to be in line with the Nederrijn in the Dutch delta area, and the main sediment signal coming from upstream has changed to one of the Rhine tributaries, the Ruhr. The IJssel, Nederrijn, and the Ruhr are indicated in the figure.

When compared to Figure 4.6, the sediment load is more consistent over time. The first need for an order of magnitude decrease of the color bar to maintain visibility only happens around t = 3,000yrs, compared to t = 200yrs. The next order of magnitude decrease for the color bar is only necessary after ca. 2,800 years. At t = 3,400yrs the Rhine changes its northward path of the IJssel to the westward Nederrijn course. The river sediment load remains relatively stable until 4,200 years, when the upstream channel changes to a more eastern origin. This orientation remains with an exception of a larger sediment pulse which happens at t = 4,700yrs which follows the older channel again. The river position switches back the next time step but the sediment load is somewhat decreased. This sediment load is consistent up until t = 5,800yrs, which is shown in the figure. Here the role of the tributary Ruhr carrying the main upstream signal of sediment load into the Rhine is clear. After this time, the sediment load as well as the length of the visible fluvial channels upstream decreases incrementally until completely disappearing at t = 6,400yrs. The simulation ends similarly to Figure 4.6, where the sediment load is only visible as small and seemingly random patches, with some increased activity in the Alps, for the remainder of the time. The one difference is the occasional sediment load activity in the rivers in northern Germany.

The sediment load that is present in the first thousands of years is in the same range as our reference values for the Lower Rhine before it slowly decreases. This is likely due to the existing topsoil layer eroding away at a lower rate due to the decreased erodibility values. This does show promise as the initial order of magnitude of sediment load is representative of today's values and its change with respect to climate change or land use change would be indicative of actual changes. As this decrease of erodibility has stopped the initial pulse and too high sediment load values, but still shows a decrease, and later disappearing of realistically valued sediment load, a fourth test is proposed. In the next section we will evaluate a simulation with both a decrease of topsoil erodibility and an increase in topsoil layer thickness.

Decreased Topsoil Layer Erodibility and Increased Layer Thickness

The sediment load for the POC simulation with both a decrease of topsoil erodibility and an increase in topsoil layer thickness is shown in Figure 4.10. The layer thickness was calculated by multiplying the thickness map by a factor of 100. The erodibility of the topsoil and bedrock is the same as the previous POC run.

We see that the sediment load results are close to the previously elaborated results. The thicker topsoil layer results in an extension of the amount of time during which sediment load values are visible before they decrease. In other words: the sediment load is more consistent over the duration of the simulation. The same decrease of sediment load that happens between 200 and 1,000 years in the previous simulation now happens between 200 and 2,000 years, after which the order of magnitude in sediment load does not change for at least 3,000 years.

Similarly to the previous simulation, the Rhine changes its northward path of the IJssel to the westward Nederrijn course at t = 3,400yrs. The sediment load stays relatively stable until t = 4,200yrs, when an additional eastern river branch (which is the Rhine's tributary the Ruhr) meets with the existing channel. The dominant sediment load is supplied by either channel, switching between the two branches for ca. 800 years in each time step of 100 years. In the figure the 'fork' shape that results from the addition of the Ruhr is shown at t = 5,000yrs. From this time on, the dominant sediment supply is the Ruhr branch, and with the exception of some 'pulse' events the original channel is largely abandoned (in terms of sediment load). From t = 6,400yrs a gradual decrease of sediments across the rivers causes the channel to disappear

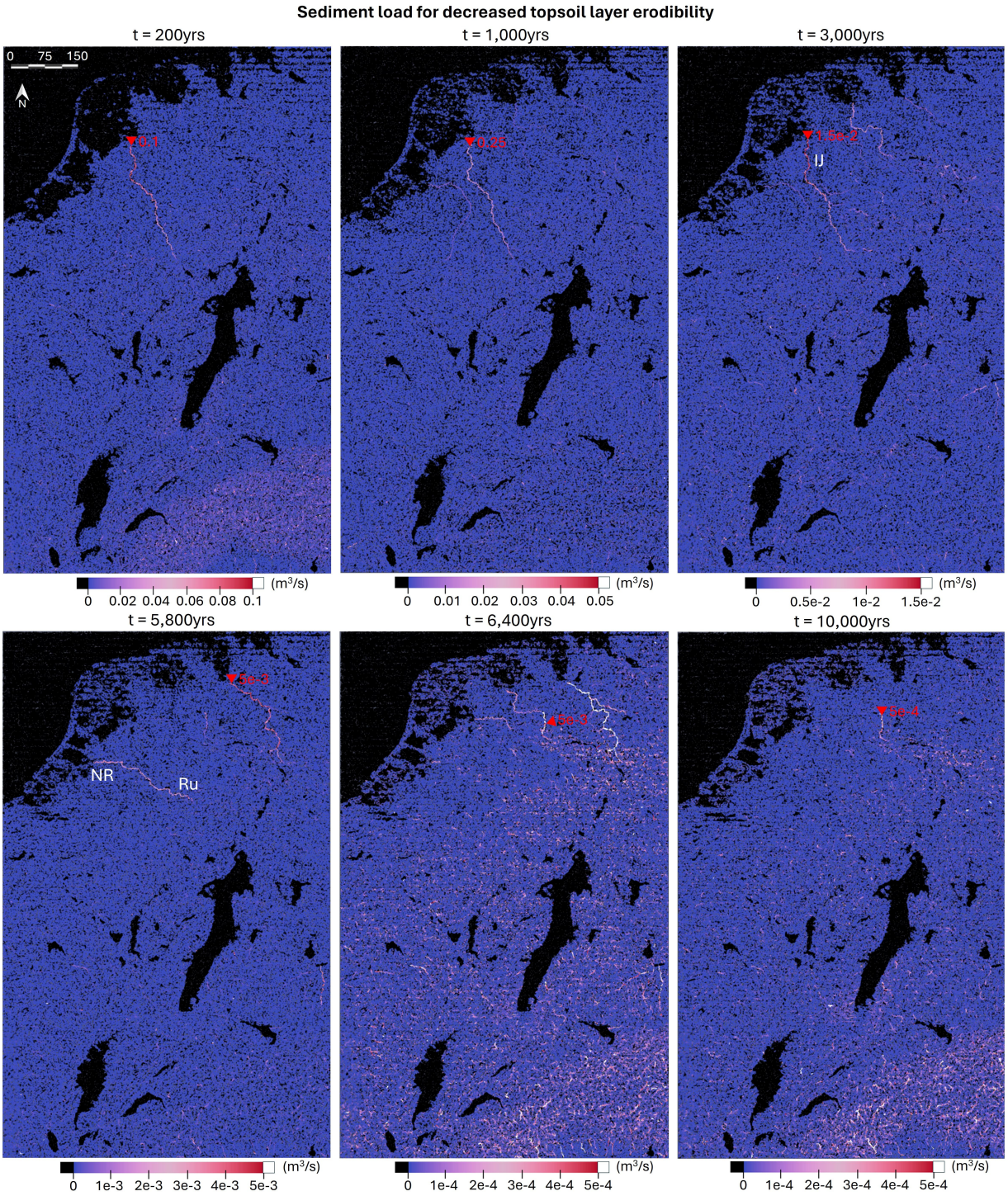

Figure 4.9: POC: sediment load results for decreased topsoil erodibility. IJ = IJssel, NR = Nederrijn, Ru = Ruhr. The red triangle indicates the maximum sediment load value in m^3/s. Note that this value is not always the maximum value of the color bar, this is for visualization purposes. The color bars are scaled differently per map to increase visibility. Read 5e-4 as 0.0005. Maps made using ParaView V5.12.0.

completely at t = 6,800yrs. The Rhine as well as the Meuse are not visible anymore until the end of the simulation, with the exception of four separate events in which a sediment pulse is produced of the order of $\sim 10^2 m^3/s$ that follows the Ruhr into the Lower Rhine. Although the resulting sediment load values are reasonably close to reality, these values are produced with an unrealistically high discharge. In the next

section we will evaluate the influence of the precipitation on the discharge, and consequently how this influences the sediment load.

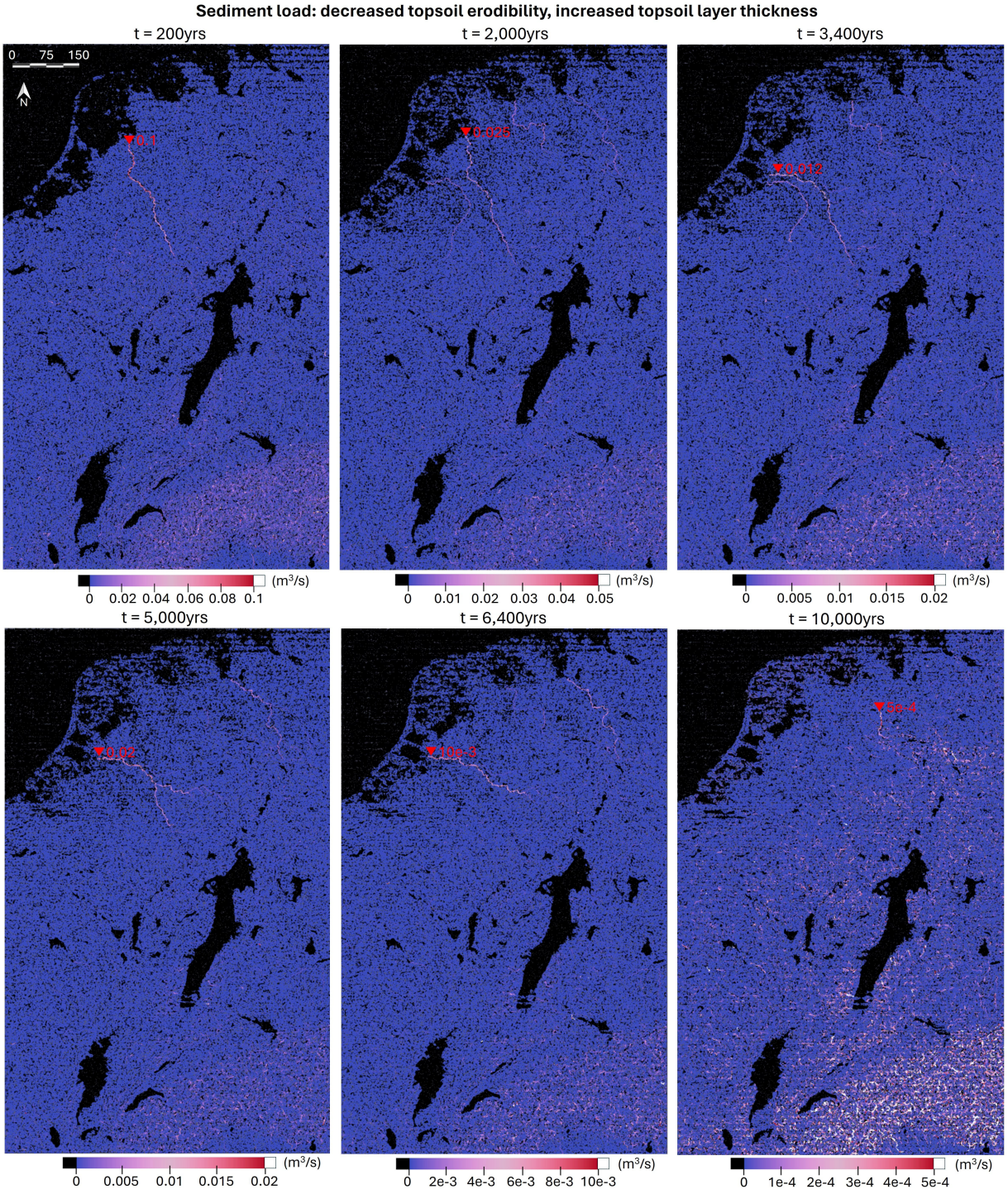

Figure 4.10: POC: sediment load for decreased topsoil erodibility (base map $\times 0.1$) and increased topsoil layer thickness. The white triangle indicates a value that is outside of the color bar range (o/r = out of range). The red triangle indicates the maximum sediment load value in m^3/s. Note that this value is not always the maximum value of the color bar, this is for visualization purposes. For the same reason the scale of each color bar is different. Read 5e-4 as 0.0005. Maps made using ParaView V5.12.0.

4.2.3. Decreased Precipitation Run

As discussed before, there is a discrepancy between the amount of precipitation and the resulting runoff in Badlands when compared to present day values. For these runs we have decreased the precipitation by 70%, which will result in a runoff that is ca. 30% of the precipitation as is stated by the Water Science School, USGS (2019). To evaluate to what degree this influences our erosion and discharge, a 10,000 year run was performed using the three different options concerning the erodibility values and topsoil layer thickness. These three realizations are the base values of erodibility and topsoil layer thickness, only decreased erodibility, and one run with both the erodibility values and topsoil layer thickness adjusted as the previous case that was discussed. Before we will evaluate the sediment load, the discharge resulting from this decrease in precipitation is shown in Figure 4.11.

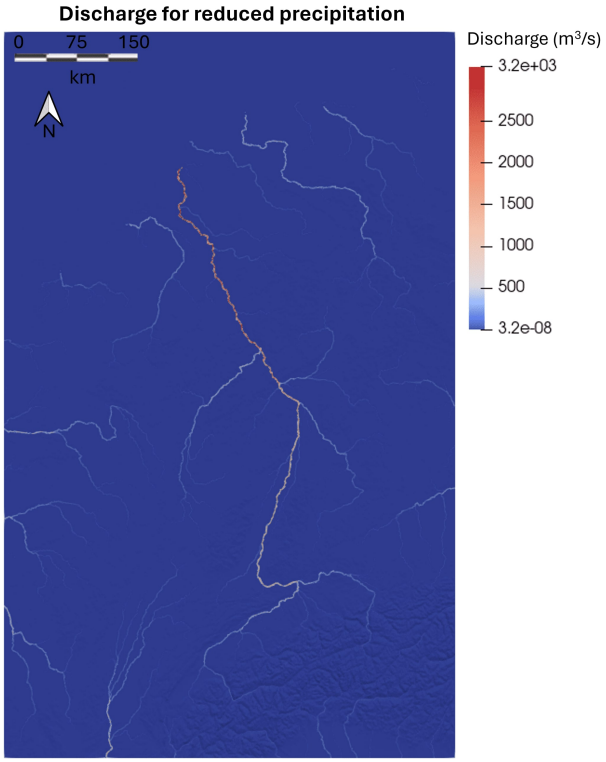

Figure 4.11: Discharge for decreased precipitation rate. Read 3.2e3 as 3,200. Map made using ParaView V5.12.0.

As expected, the decrease in precipitation caused a direct decrease in discharge. This discharge is much closer to the values that we find in the present-day for all reaches of the Rhine. There is no significant difference between the morphology of these rivers and the ones simulated with a much higher discharge.

The results for all three simulations showed the same behavior as with the base map precipitation runs discussed in the previous section. The run with unadjusted topsoil erodibility still shows the initial pulse of sediment within the first 1,000 years, a fast decrease in values and afterward no noticeable sediment load in the rivers left. The only difference is that the decrease in precipitation has also led to a decrease of erosion causing the sediment load in general to be lower than in Figure 4.6, although still higher than our reference values in the beginning. When we adjust the topsoil erodibility to be within the orders of magnitude as bedrock, we again see the initial pulse disappear. The initial values are on average $0.3 m^3/s$ and remain of this magnitude for the first 2,000 years. This is right within the range of the present-day reference values of sediment load in the Lower Rhine. After this the sediment load decreases to the order of $0.01 m^3/s$ for the next 1,800 years, until the sediment load of the Rhine completely disappears for the remainder of the simulation, with again some sporadic activity in the more northerly rivers. This brings us to the solution we have already applied in the last section, namely the increase of the topsoil layer thickness. This will again be done by scaling the topsoil thickness by an arbitrarily chosen factor 100. The results regarding sediment load for several time steps are given in Figure 4.12.

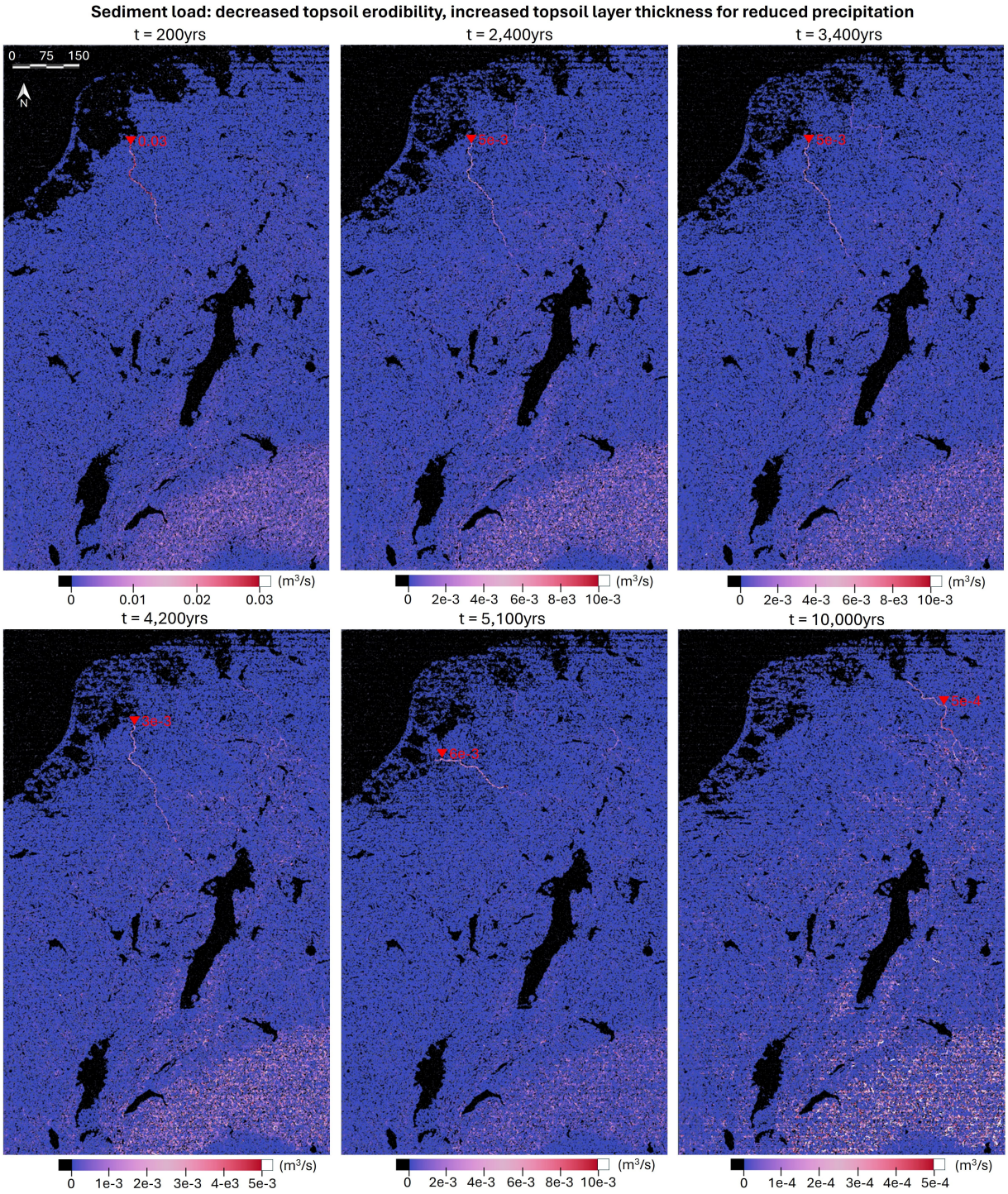

Figure 4.12: Sediment load for decreased topsoil erodibility (base map $\times 0.1$), increased topsoil layer thickness, and decreased precipitation. The red triangle indicates the maximum sediment load value in m^3/s. Note that this value is not always the maximum value of the color bar, this is for visualization purposes. The scale of each color bar is different to increase visibility. Read 5e-4 as 0.0005. Maps made using ParaView V5.12.0.

This run shows a sediment load that is lower than that with the regular precipitation, and again follows the same pattern as the other runs. Although the sediment load is in the reference range for the first few

thousand years, after t = 4,200yrs it decreases relatively fast until it disappears completely after a single large pulse at t = 5,100yrs (note that the scale had to be expanded to show the full range of values of this pulse), with some small 'pulses' that can be found in the remaining 4,900 years. This is likely due to the smaller precipitation rate causing a lower discharge, which is eroding the bedrock and topsoil at a much slower pace than the higher discharge of before. Because the initial decrease in erodibility was developed with the initial higher discharge in mind, it is possible that we can get a sediment load in the Rhine with a longer lifetime and realistic values when the topsoil erodibility is multiplied by a different factor, creating values that are larger than used in this simulation. This simulation was repeated three times using topsoil erodibilities that were multiplied by factors 0.15, 0.2, and 0.3 instead of the initial factor 0.1. As expected, with a higher erodibility the sediment load also increases. The sediment load does not increase significantly from the values that we see in Figure 4.12, however. The general pattern of evolution of sediment load throughout the simulations are all similar to Figure 4.12 as well, with the only difference of note being the duration of the visible signal in the Rhine. For the erodibility $K \times 0.15$ the signal disappears as early as t = 4,300yrs. For the erodibility $\times 0.2$ the signal disappears between t = 6,000 and 6,200yrs, these time steps, alongside others, are given in Figure 4.13. We see that for this simulation in particular the initial sediment load values correspond very well with the present-day values for the Lower Rhine, with a maximum deviation of 20%. Due to the limited reach of the Rhine for which we see sediment load, the figure consists of images that are only the top third of our initial area of interest map, with the top of the Upper Rhine Graben lake as the bottom of the new map.

For $K \times 0.3$ we see that the time that the sediment signal of the Rhine is visible decreases again, and disappears after t = 3,900yrs. This is likely due to the erodibility being so high that the erosion rate increased again, even with a lower discharge. For decreased precipitation, and consequently a realistic discharge, it seems that an erodibility multiplication factor of ca. 0.2 is optimal for the time of visible sediment load along the Rhine. Because of the sediment load that is close to the reference values in the beginning of the simulation, and because this is the case for a realistic range of discharges across the Rhine channel, we will use this simulation as the base output to which we compare all our realizations in our case study.

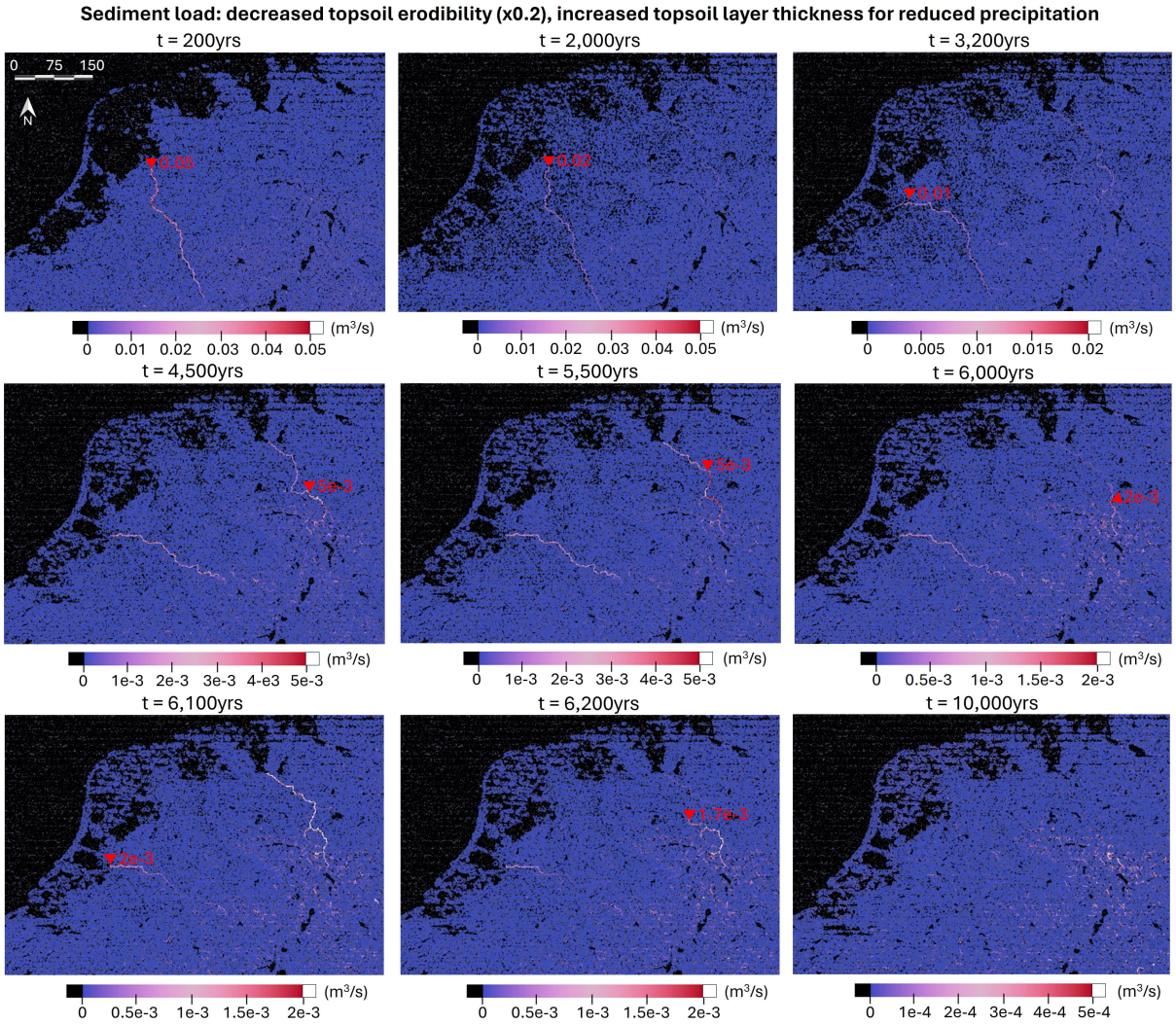

Figure 4.13: Sediment load for decreased topsoil erodibility (base map $\times 0.2$), increased topsoil layer thickness, and decreased precipitation. The red triangle indicates the maximum sediment load value in m^3/s. Note that this value is not always the maximum value of the color bar, this is for visualization purposes. For the same reason the scale of each color bar is different. The scale of each color bar is different to increase visibility. Read 5e-4 as 0.0005. Maps made using ParaView V5.12.0.

Part II

Case Study

Part II Description

In Part II of this thesis we show a case study on the impact of climatic and anthropogenic land use change on sediment load in the Lower Rhine. For this we will use the topsoil erodibility and precipitation that we have calibrated in Part I. First, we will introduce the setting of the case study, namely Western and Central Europe, where we will explore the general geography of this region including input parameters that are related to both the continent and the North Sea. The observed sediment load and discharge for the Rhine are given here as well. We will also explore the subsidence and uplift in this region (including the tectonic variation that was discussed in Part I).

This is followed by a discussion on the four emission-based scenarios that will be used in the case study. These scenarios are implemented through sea-level change and precipitation change. The latter will be evaluated in two ways: a uniformly averaged change over the full area of interest, and a non-uniform (i.e., regional) precipitation change. The next chapter gives an overview of all inputs that will be used, as well as how they are processed.

Next, a scenario tree that shows the structure of all simulations that are performed for this case study is given. Following this scenario tree, the results from all the simulations are presented. Using the sediment load and discharge output from Badlands, first a general analysis is done on the sea-level rise, after which the results for the land use scenarios and climate scenarios will be given.

We see that the duration of sediment load that is comparable to our reference simulation decreases as climate scenarios get more extreme. There is a significant difference between the outputs of uniform and non-uniform precipitation change, and in most cases the land use scenarios cause a decrease in sediment load with respect to the reference simulation. The results and their uncertainties are further analyzed in the discussion in Part III of this work, which is followed by a general conclusion about both the feasibility study and the case study.

5

Setting

5.1. Geography of Western and Central Europe

As we are interested in the sediment flux from the Rhine, our area of interest predominantly stretches across Western and Central Europe. This area entails parts of Belgium, France, Germany, the Netherlands, Lichtenstein, Switzerland, Italy, and Austria as shown in Figure 5.1a. The Rhine and Meuse and larger cities along these two rivers are also indicated on this map. Figure 5.1b shows the general topography of our area of interest, which will be an input for our simulations as initial topography. The total size of the area is approximately 560km by 920km, or 515,200km^2.

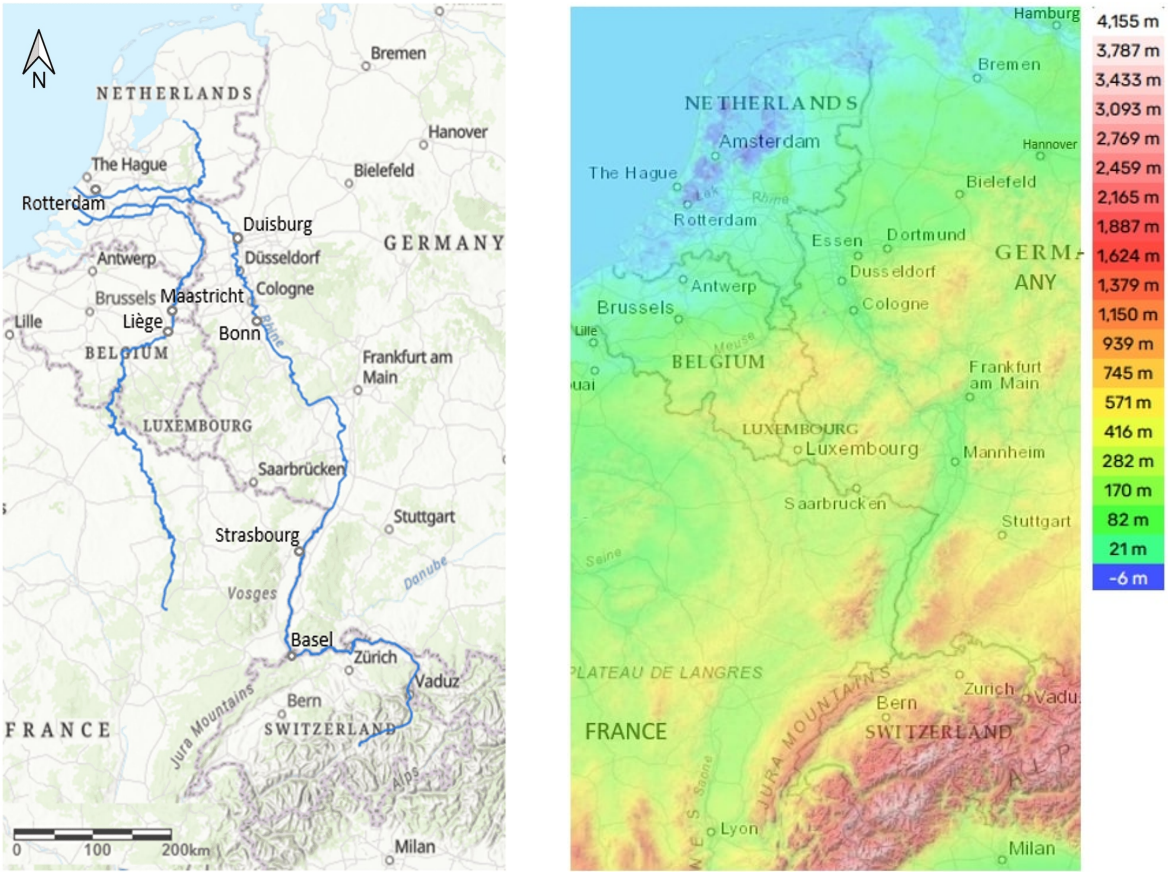

(a) Geographical map

(b) Topographical map

Figure 5.1: The area of interest including the rivers Rhine and Meuse (left) and its topography (right). Adapted from Lewis (2022) and ”Europe topographic map” (n.d.), respectively.

5.1.1. The Rhine and the Meuse

The main river we are interested in is the Rhine. Because the Rhine and the Meuse share a delta we will briefly discuss the Meuse too. The Rhine begins in the southeastern Swiss Alps, where it first defines a section of the Swiss-Lichtenstein border, after which it migrates north where the river again forms a natural border, between Germany and France. It flows further north through Germany, subsequently entering the Netherlands at the village of Spijk (due to a shift in borders, it used to be at the village of Lobith which is still known amongst the general Dutch public as the place where the Rhine crosses the border (Van Dalen, 1972)). The drainage basins of the Rhine and Meuse, as well as some tributaries of the Rhine are shown in Figure 5.2.

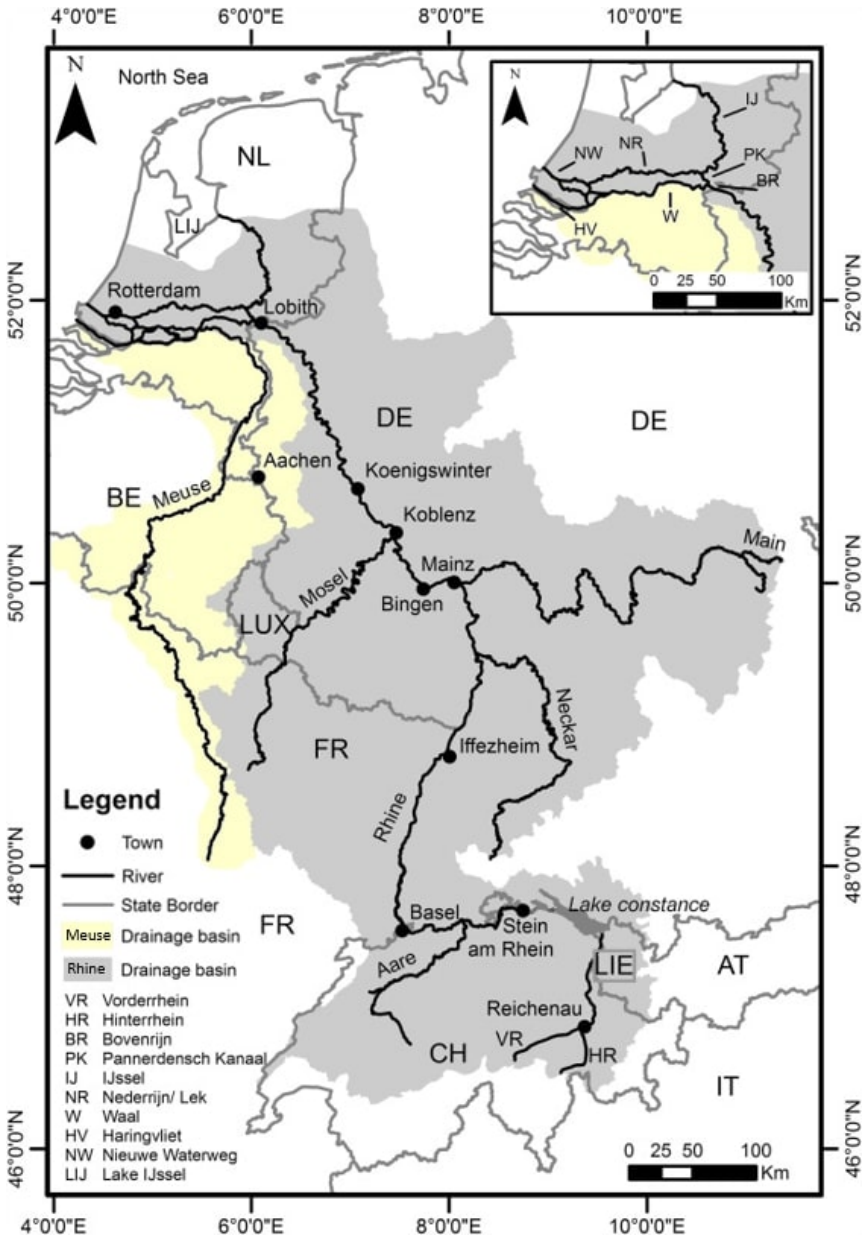

Figure 5.2: The Meuse, and the Rhine with its tributaries, and their drainage basins. A more detailed overview of the Rhine-Meuse Delta and the names of the rivers is given in Figure 5.7. Adapted from Frings et al. (2019).

The Meuse originates on the Plateau of Langres, France. From there it flows north entering Belgium and subsequently the Netherlands, where the river flows towards the Rhine. After which both the Rhine and Meuse flow approximately parallel westward towards the Dutch shore, where the two rivers and the

Scheldt river confluence into the Rhine-Meuse-Scheldt delta. This delta covers an area of approximately 25,347km^2, making it the largest delta in Europe (Tockner et al., 2009). A simplified overview of the Dutch waterways of which the Rhine and Meuse are a part of are also given, these will be discussed, together with the Rhine and the Meuse themselves, in greater detail below.

The Rhine

According to the International Commission for the Hydrology of the Rhine basin (CHR), the official total length of the Rhine is 1,232.7km (CHR, 2015). It is the second largest river in Europe, and Western and Central Europe's most important waterway (Uehlinger et al., 2009). It is used as a source of water for agriculture, industry, as well as households; it carries away waste waters; is one of the most important navigational trade routes connecting the port of Rotterdam, one of the worlds largest sea ports, to a large part of continental Europe, and accommodates multiple nature reserves (Frings, Gehres, et al., 2014). Apart from the port of Rotterdam, the Rhine is also home to the world's largest inland port located in Duisburg, Germany (Delta Alliance, n.d.). The Rhine has a drainage basin of ca. 185,000km^2 (272,203km^2 when the major tributaries Aare, Moselle, Main, and the Neckar are included) (Frings, Gehres, et al., 2014; Goergen et al., 2010; Tockner et al., 2009), inhabited by a population of more than 58 million people (European Sediment Network, n.d.-b). The Rhine is classified as a gravel bed river (European Sediment Network, n.d.-b), which will typically have a layer of coarse grains on the bed surface which decreases erosion of the finer grains 'sheltered' underneath (Sklar and Dietrich, 2006).

It is of note that the Rhine can be subdivided into six morphologically distinct river sections with two additional base levels apart from the sea (Lauterborn, 1916). These sections are, in order from upstream to downstream: The Alpine Rhine (Alpenrhein) which flows into Lake Constance as first baselevel, the High Rhine (Hochrhein), the Upper Rhine (Oberrhein), the Middle Rhine (Mittelrhein) which starts with the second baselevel consisting of a quartzite reef, the Lower Rhine (Niederrhein), and the Delta Rhine consisting of the Rhine-Meuse-Scheldt delta (Uehlinger et al., 2009). These sections and their gradient profile with baselevels are shown in Figure 5.3.

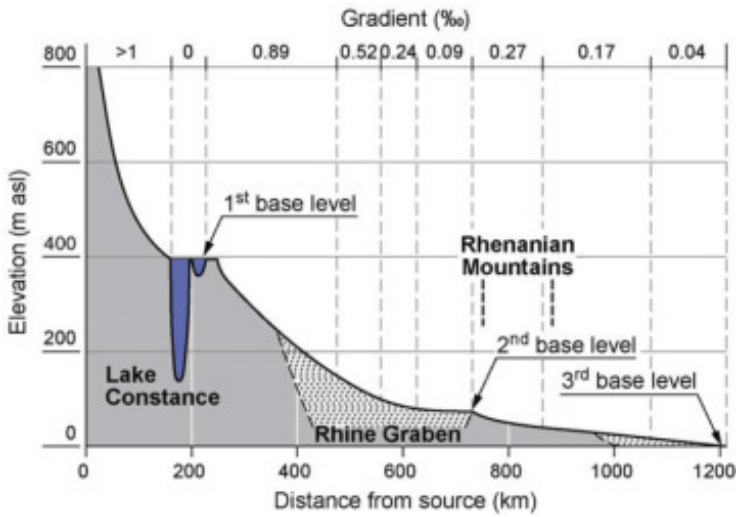

Figure 5.3: The longitudinal profile of the Rhine, with its gradient and baselevels. From Uehlinger et al. (2009), adapted from Mangelsdorf et al. (1990).

Upstream from each baselevel, the river attempts to reach a concave equilibrium curve. The resulting valley side-slopes have confined major parts of the Alpine headwaters, the High Rhine, and Middle Rhine. The Alpine Rhine together with the major tributary Aare provide ca. 34% of the total annual river discharge as measured at the Dutch-German border. In summer, this percentage is even above 50% (Uehlinger et al., 2009). In Figure 5.4 the average monthly discharge over 1931–2003 for four of the distinct sections of the Rhine are given. The average discharge at the measurement station near Rees (located ca. 20km upstream of the Dutch–German border) between 1980 and 2009 was 2,390m^3/s (Frings, Gehres, et al., 2014), while the largest discharge ever measured was 12,200m^3/s in 1926 (DGJ, 1926). As of 2025, the

flood protection works along the Lower Rhine have a capacity to safely deal with a discharge of 17,500m^3/s (Hegnauer et al., 2015).

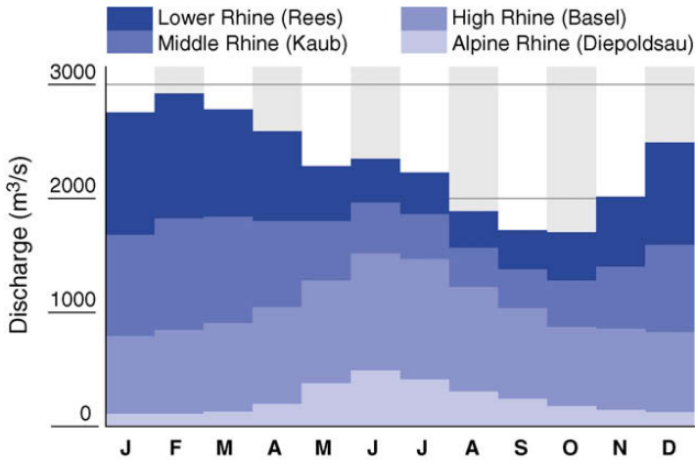

Figure 5.4: The discharge of the Rhine measured at four measuring stations located between Diepoldsau (Alpine Rhine) and Rees. The Kaub measurement station is located 45km upstream of the Rhine–Moselle River confluence. From Uehlinger et al. (2009).

Because the Rhine has been and still is an important economic vein and source of water throughout Europe, the river has experienced (and still is experiencing) a lot of anthopogenic changes. River engineers have narrowed and straightened the river at parts to improve navigation conditions, dams and dikes have been built in and around the main river as well as its tributaries (Frings, Gehres, et al., 2014). Likewise, the Lower Rhine and Delta have been heavily engineered (Delta Alliance, n.d.). This caused some major changes in the water discharge and sediment flux throughout the river and its tributaries. Presently, a major source of sediment is anthropogenic in nature. According to Frings, Gehres, at al. (2014) the artificial sediment supply as measured in a 285km section of the Upper and Middle Rhine accounted for ca. 44% of the total sediment budget. This sediment budget measured over km 336-621 (from the dam of Iffezheim until 20km upstream of Königswinter, DE) and km 640-865 (from Königswinter until Millingen a/d Rijn, NL) of the Rhine is shown in Figure 5.5. A reference of the Rhine kilometers is found in Figure 2.3.

The distribution of the different sediment flux contributions is not uniform. The majority of the artificial supply and dredging of sediments are found more upstream, while the contributions of tributaries (adding sediments) and floodplain deposits (removing sediments) are larger downstream (Frings, Gehres, et al., 2014). As reference for our simulations, the total average sediment transport by adding the individual suspended loads and bedloads together are given in Table 5.1.

Table 5.1: Sediment flux estimates for four locations along the Rhine.

Location (km of the Rhine)	Sediment flux (Mt/y)	Sediment flux (m^3/s)	Average porosity	Mineral density (tonnes/m^3)	Source
350	1.6	0.026	0.26	2.65	Frings, Gehres, et al., 2014
609	2.34	0.034	0.175		
640	2.15	0.031	0.16	2.6	Frings, Döring, et al., 2014
865	2.89	0.044	0.2		

For the conversion from a mass based sediment flux $q_{s,M}$ to a volumetric based sediment transport $q_{s,V}$ compatible with Badlands output, the mineral density ρ in tonnes/m^3 and average porosity ϕ for the total sediments that were used in the original papers are also given in the table. The conversion is done through $q_{s,V} = \frac{q_{s,M}}{\rho \cdot (1-\phi)} \cdot 3.1689 \cdot 10^{-2}$, where $3.1689 \cdot 10^{-2}$ is a conversion factor for millions of 1/y to 1/s. Although this does not cover the full extent of the Rhine, it will give us a good indication of values to compare the output of Badlands against.

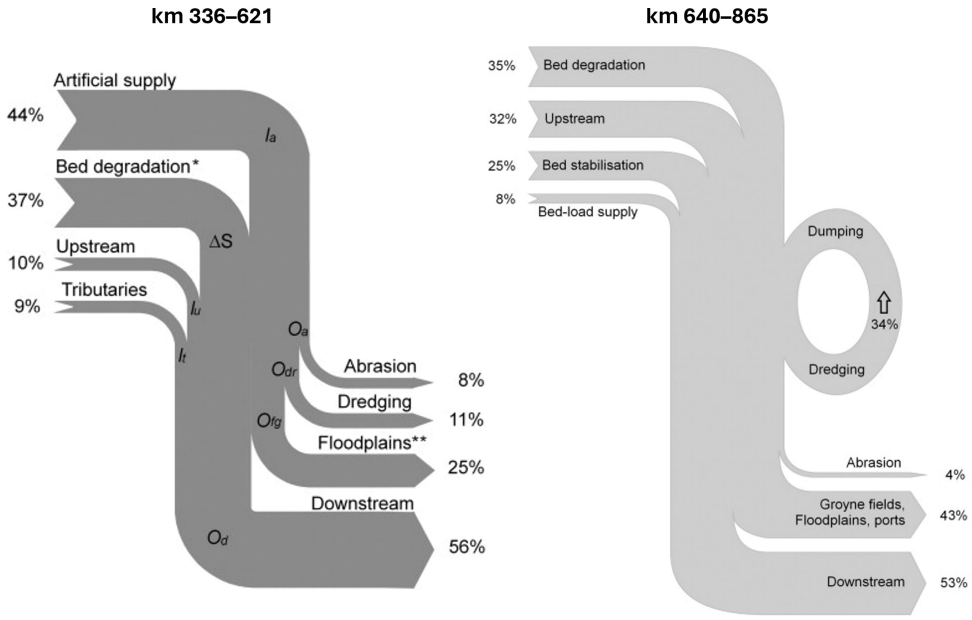

Figure 5.5: On the left the sediment budget between km 336 and 621 of the Upper and Middle Rhine for the period 1985-2006. On the right the sediment budget between km 640 and 865 in the Lower Rhine reach for the period 1991-2010. *Internal component of the channel. **estimated. From Frings, Gehres, at al. (2014) and Frings, Döring, et al. (2014), respectively.

The Meuse

Although the Meuse is not the primary subject of this thesis, it does contribute sediments to the Rhine-Meuse delta. For this reason we will shortly discuss the Meuse here as well. The Meuse is a typical lowland river with a length of approximately 905km, and a drainage basin of ca. 34,548km^2 (Descy, 2009; European Sediment Network, n.d.-a). The main driving forces determining the status of the river waters are urbanization, industrialization, agriculture, and navigation (European Sediment Network, n.d.-a). To this end, the river has been heavily regulated, mainly for navigation and flood management purposes. This has caused a decrease in biodiversity, and has severely decreased the natural functions of floodplains (Descy, 2009). The sediment flux in the river is highly influenced by human activity, mainly due to land use (this will be discussed in more detail in section 5.1.3) and the presence of sluices, weirs, and dams (European Sediment Network, n.d.-a).

The Meuse is a rain-fed river, and thus highly susceptible to changes in precipitation due to climate change. Over the last decades a slow increase of the annual discharge has been measured along the river, with an average annual flow of 316m^3/s (Descy, 2009). With increasing precipitation and the resulting water discharge, it is also expected that the sediment flux of the Meuse will increase (J. R. Cox, Dunn, et al., 2021). Unlike the Rhine, the Meuse has only one base level: the North Sea. The longitudinal profile of the Meuse with the four major tectonic basins which it passes is shown in Figure 5.6.

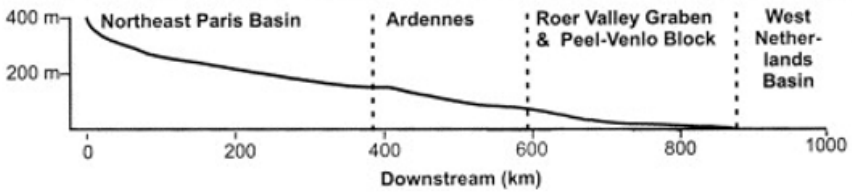

Figure 5.6: The longitudinal profile of the Meuse. Adapted from Tebbens et al. (2000).

The Rhine-Meuse Delta

The Rhine-Meuse catchment and delta area is mainly located in the Netherlands. The area is densely populated and intensively used for agriculture, industry, and transport (Olsthoorn and Tol, 2001). Approximately half of the total area is less than one meter above sea level, and about a quarter lies below it (ICPR, 2024). The Rhine-Meuse delta (RMD) is a complex distributary network of channels that has been heavily influenced by anthropogenic changes (J. R. Cox, Dunn, et al., 2021). The delta of the Rhine starts at the Dutch-German border. Here, the Rhine splits into two branches, the Waal and the Nederrijn. About 10km downstream, the river IJssel branches off in the northern direction and discharge55+s into the IJsselmeer. The Nederrijn changes its name a little further downstream into the Lek, and continues flowing westward where it is connected to the Rotterdam port canal. The Waal is the southern branch, and follows the same direction. When it reaches the Dutch town of Dordrecht it splits in several branches and these in turn feed the four interconnected branches of an estuary. The rivers Meuse as well as the Scheldt also debouch in this estuary (Delta Alliance, n.d.). To get a better overview of the complexity of the distributary network that makes up the RMD, as well as the anthropogenic influences in the form of canals and dams, the delta area is shown in Figure 5.7.

In order to protect the country from fluvial and marine floods, thousands of kilometers of dikes form a dense network covering more than half the country (Pleijster and Van der Veeken, 2015). The existing approach of reinforcing these dikes, maintaining and improving storm surge barriers, sand replenishment, and pumping is expected to protect the RMD area and the rest of the Netherlands from a sea level rise up to 5m (IenW (Dutch Ministry of Infrastructure and Water Management), 2024). The area in the estuarine delta that is protected by storm surge barriers has an area of ca. 250,000 ha. About half of this consists of water and wetlands (Delta Alliance, n.d.). The regions of the port of Rotterdam and surroundings (Between the Dordtse Kil and the Nieuwe Waterweg) as well as a large part of the area enclosed by this region and the Amsterdam-Rijn canal and the North Sea canal are a densely populated conurbation which includes the four largest cities in the Netherlands (Rotterdam, The Hague, Amsterdam, and Utrecht) with a combined population of ca. 8.4 million people (as of 2020, CBS (2023)) which is almost half of the total population of the Netherlands. This signifies the importance of the coastal and fluvial defences and water management in this area.

Due to the complexity of the waterways, the sediment flux in the system is equally complex (Vellinga et al., 2014). It is influenced by climate-induced changes, as well as anthropogenic processes like dam building (Syvitski and Kettner, 2011), dredging (Rovira et al., 2014), and river engineering measures such as canal construction and diversions (Ericson et al., 2006). In section 5.1.1 we have already seen that the sediment flux in the Upper and Middle Rhine is heavily altered by humans. This is likely also the case in the other parts of the Rhine, which makes it increasingly difficult if not impossible to find an accurate estimate of the total sediment flux that would occur due to natural processes alone. Some insight in the anthropogenic influence on sediment flux can be gained by comparing the values from the Badlands simulations of the RMD area to the derived values for sediment flux from J. Cox, Dunn, et al. (2021). In the J. Cox, Huismans, et al. (2021) study, the authors already conclude that human activities control the sediment budget in the highly urbanized RMD. In their evaluation of the present day sediment flux as well as a prediction for the sediment flux for the years 2050 and 2085, J. Cox, Dunn, et al. (2021) have taken into account as many as 6 upstream (fluvial) processes, 6 downstream (coastal) processes, and 7 anthropogenic processes. They predict an increase of (suspended) sediment flux of 1.8 and 2.15Mt/yr in 2050 and 2085 respectively, with respect to the average value taken over the period 2000-2018 of 1.5Mt/yr as measured at the Lobith station near the Dutch-German border.

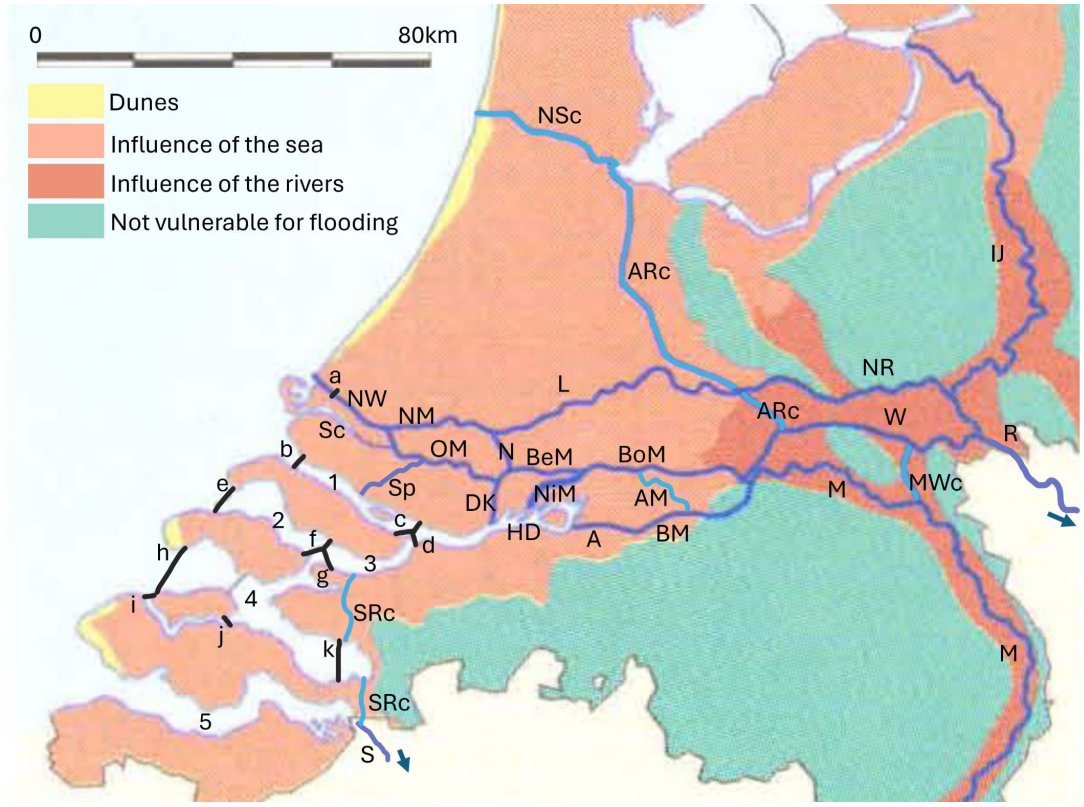

Rivers

R	Rijn (Rhine)
M	Maas (Meuse)
NR	Nederrijn
W	Waal
L	Lek
BoM	Boven Merwede
BeM	Beneden Merwede
NiM	Nieuwe Merwede
IJ	IJssel
S	Scheldt
DK	Dordtse Kil
NM	Nieuwe Maas
OM	Oude Maas
Sp	Spui
Sc	Scheur
NW	Nieuwe Waterweg
N	Noord
BM	Bergsche Maas
A	Amer
HD	Hollands Diep
AM	Afgedamde Maas (Dammed-up Meuse)

Canals

MWc	Maas-Waal canal
SRc	Schelde-Rijn canal
ARc	Amsterdam-Rijn canal
NSc	North Sea canal

Water bodies/estuaries

1	Haringvliet
2	Grevelingen
3	Volkerak
4	Oosterschelde
5	Westerschelde

Dams

a	Maeslantkering
b	Haringvlietdam
c	Hellegatsdam
d	Volkerakdam
e	Brouwersdam
f	Grevelingendam
g	Philipsdam
h	Oosterscheldekering
i	Veerse Gatdam
j	Zandkreekdam
k	Oesterdam

Figure 5.7: The Rhine-Meuse-Scheldt distributary network. Note this representation does not show all natural and anthropogenic waterways that are actually present, only the biggest ones. Adapted from Huisman et al. (1998).

5.1.2. The North Sea

The main base level in our area of interest is the relatively shallow North Sea. It is the northeastern arm of the Atlantic ocean, and has an average depth of 90m (European MSP Platform, n.d.). The part of the North Sea in our area of interest is relatively close to the Dutch, Belgian, and German shore and has a depth not exceeding 45m. In the southeastern part of the North Sea the low-lying Frisian island range (the Wadden) on the North coast of the Netherlands and Germany split the North Sea into the main body and the intertidal zone known as the Wadden Sea. In addition to this, the Dutch have built considerable dikes (Afsluitdijk - 'Closure dike', and the Markerwaarddijk) which have closed off the inland bay now consisting of the IJsselmeer (Lake IJssel) and Markermeer (originally planned to be reclaimed land, known as *poldering*, but this has been indefinitely postponed (Rijkswaterstaat (Department of Waterways and Public Works), n.d.)) that have influenced the depth and salinity in these areas. A bathymetry map of the

North Sea, as well as the location of these dikes and some North Sea measurement stations are shown in Figure 5.8.

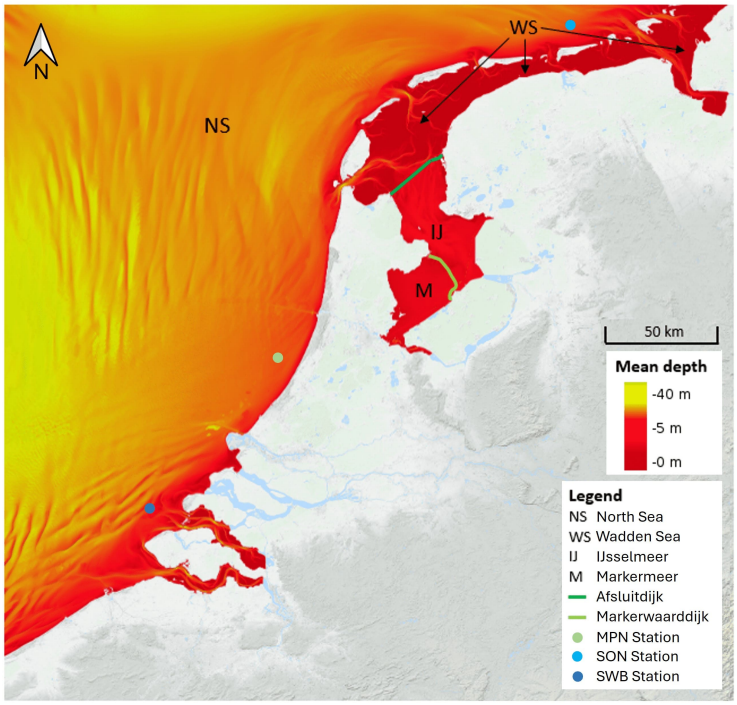

Figure 5.8: Bathymetry of the North Sea, Wadden Sea, IJsselmeer, and Markermeer as part of the area of interest. Measurement stations: MPN = Noordwijk, SWB = Schouwenbank, SON = Schiermonnikook Noord. Adapted from EMODnet (n.d.).

The default sea level reference in Badlands is set to 0m, and from there a predicted sea level change can be implemented through a file consisting of height increase relative to this point with corresponding time intervals (Badlands Group, 2019). The sea level changes implemented in this study are discussed in section 6.1.

Wave-related Transport Parameters

As discussed earlier, marine sediment transport will also play an important role in our simulations. This means several wave-related parameters concerning the North Sea are needed. Firstly, the maximum depth at which waves have an influence on net sediment transport is widely assumed to be at the -20m depth contour (Grasmeijer et al., 2019). For the other parameters, we will base our parameters mostly on data collected from the Dutch coast and Wadden intertidal area. This area represents the majority of the coast line in our area of interest, and has characteristic sections that are similar to the Belgian coast and German Wadden Sea area.

At lower shoreface, storm conditions will play an important role in net transport rates and thus have to be taken into account. Although the average wave direction as measured in the offshore Netherlands is approximately southwest, the wave directions during storms have more variability. Northwestern storms are more prominent, but southwestern storms occur as well (Grasmeijer, 2018). In Figure 5.9 the wave rose diagrams for the period 2013-2017 as measured along the Dutch shore are given, giving a value for the maximum significant wave height (H_s in meters, in blue), mean H_s (in meters, in red), and the 90% exceedance value (black) for each measurement station (Grasmeijer et al., 2022).

Typically, the wave heights measured are smaller at the Noordwijk station and the Schouwenbank station (MPN, and SWB, respectively in Fig. 5.8) than at Schiermonnikoog Noord (SON in Fig. 5.8) (Grasmeijer et al., 2019; Van der Spek et al., 2022). In Badlands it is possible to produce snapshots of wave-driven circulation distribution by implementing wave scenarios. These are based on the input of average wave direction, number of wave events, and the percentage of time each event is active during

the simulation runtime (Badlands Group, 2019). For the wave directions, we will use the three dominant approximate directions present in the rose diagrams, namely 245°, 285°, and 335°. Badlands defines the wave directions in degrees counting from the x-axis anti-clock wise: this means the directions given will correspond to an input of 205°, 165°, and 115°in Badlands, respectively. We also have to define the percentage of runtime each wave orientation is set to active in the simulations. This is done by adding the average occurrences (in percentage points) over all the rose diagrams in Figure 5.9 and normalizing them under the assumption that no other orientations are significant. The results are given in Table 5.2.

Table 5.2: Wave orientation parameters as Badlands input.

True wave orientation	Badlands input	Percentage active in wave climate
245°	205°	39%
285°	165°	25%
335°	115°	36%

For the initial significant wave height, the average of all the averages in Figure 5.9 will be used, as it is not possible to use local values for H_s in Badlands. This gives us $H_s = 1.15$m. According to Chaigneau et al. (2023), a general decrease of the mean and extreme (1-in-100-year scenario) significant wave height is predicted at the end of the 21st century using the SSP5-8.5 (Shared Socioeconomic Pathway 5-8.5, similar scenario to RCP8.5) for the northeastern Atlantic region, with almost no change for the Belgian and Dutch coast in particular. It is of note that there were significant changes in significant wave height when hourly sea level variations and wave conditions were applied. In particular, the extreme significant wave heights were larger by up to 40% (± 60cm) in areas where average tidal ranges were large (ca. 10m like in the Bay of Mont-Saint-Michel in France) (Chaigneau et al., 2023).

We will use the average value of $H_s = 1.15$m and assume no significant increase because of two reasons: the temporal range of hourly variations is several order of magnitudes smaller than our temporal resolution of years, and the tidal range for the coast along our area of interest (predominantly Belgian, Dutch, and the Wadden Sea intertidal area) is between 1.5 and 4m (Common Wadden Sea Secretariat, n.d.). Another important parameter concerning marine sediment transport is the mean grain diameter (d_{50}). This value depends on where the average of the grain sizes is taken. As we have established that the impact of waves on sediment transport is limited to the coastline until a depth of 20m, we will use grain size data from along the coast until this point. In general the average grain sizes along the Dutch and Belgian coasts are larger than at the Wadden Sea intertidal areas (Van der Spek et al., 2022). The Dutch Wadden Sea mainly consists of fine-grained sand of ca. 100-200μm, similar to other intertidal areas (De Glopper, 1967; Van der Spek et al., 2022; Wang et al., 2018). A study around the Wadden island Terschelling showed a grain size range of 197–237μm coarsening as we go further from the shore (Van der Spek et al., 2022). Along the Holland coast (approximately from Den Helder to Hoek van Holland in Fig. 5.9) the grain sizes are coarser, with a median grain size range of 217–323μm, and an average value of 273μm (Van der Spek et al., 2022). In order to take all of these values into account, we will follow the study *Sediment Transport on the Dutch Lower Shoreface* by Grasmeijer (2018), using a median grain size d_{50} of 250μm.

The last parameter that we will discuss is the maximum wave-induced erosion rate. In order to efficiently discuss this, we will divide the Dutch coast into three sections: the delta area (south of Hoek of Holland, Fig. 5.9), the coast of Holland (as mentioned above), and the Wadden area (north of Den Helder, Fig. 5.9).

The delta area is affected the most by erosion together with the Wadden area. In particular the western ends of the northern peninsulas are subject to severe erosion, ranging from 0.5 to 5m/yr (Dillingh and Stolk, 1989).

The Holland coast is relatively stable. Some erosion and accretion occurs (less than 1 m/yr) between Hoek van Holland and Wassenaar (located just below Scheveningen). From Wassenaar up to Egmond aan Zee the coastline is mostly stable. To the north of Egmond aan Zee up to Den Helder the coast is mostly eroding with a range of 0.5-1.5m/yr, where more erosion occurs further north. Between Noordwijk and Egmond aan Zee some local accretion of ca. 2-4.5m/yr is measured (Dillingh and Stolk, 1989).

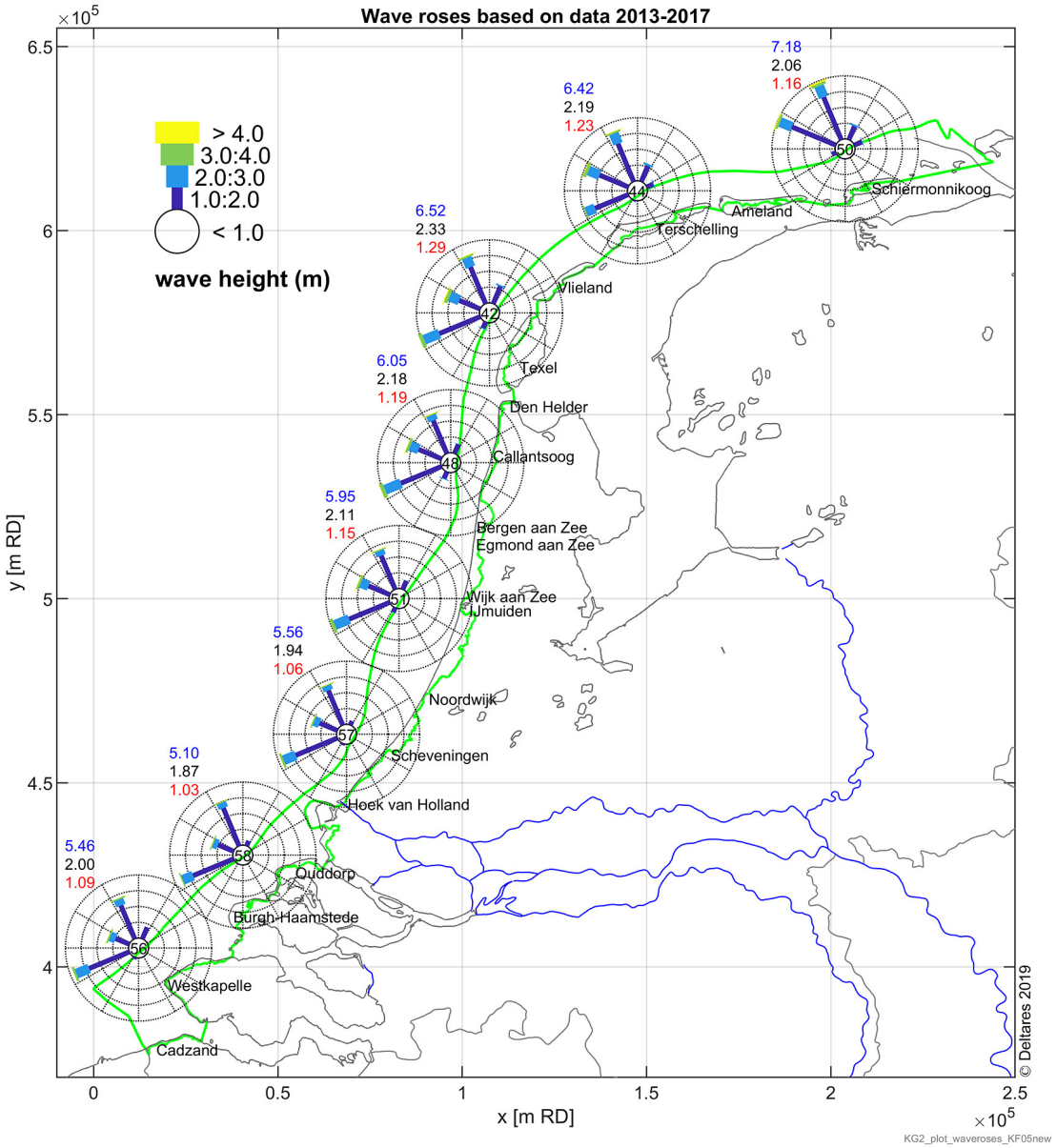

Figure 5.9: Wave rose diagrams for the Dutch coast over the period 2013-2017. From Grasmeijer et al. (2022).

The Wadden area consists of several small islands, of which Texel and Ameland in particular are suffering form erosion. The west coast of Texel is subject to erosion levels of up to 10m/yr, while in the north this is 5m/yr, and in the middle 'only' 1m/yr. In the central and western part of Ameland erosion levels of 3-5m/yr have been measured (Dillingh and Stolk, 1989). The erosion on most of the Wadden islands are affecting both nature reserves and water conservation areas.

It is important to note that humans have had and still have a considerable effect on Dutch coastal development. While the nature reserves are mostly left untouched, coastal management policy of the Netherlands can be described as: "the coastline will be kept in place, but not everywhere and not at any price" (Dillingh and Stolk, 1989). In practice, this means that if the erosion of the coast would endanger the hinterland, preventive measures will be taken. If there is no danger, the local interests that are threatened will be measured up to the cost. An example of this is the coastal nourishment. Dutch coastal nourishment volumes have been increased from 6.4 to 12 million m^3 per year since 2001 in order to keep the coastal zone in equilibrium with sea level rise, and this nourishment has been stable since (Brand et al., 2022; Grasmeijer et al., 2019). Coastal erosion is a complex process, and many values can be found in literature

for different areas and scales. Badlands only takes one value for a wave-induced erosion value, and thus we need to use a representative value. The question becomes, what natural as well as anthropological processes will determine the net coastal erosion in the far future? This question is impossible to answer with the large uncertainties in both climate change and human policy. In addition to this, we are mainly interested in influence of land use and climate change on sediment flux in the rivers, with expected sea level rise of at least 25m: coastal environments will be significantly different from the present-day, and so this value is of only minor importance to our research questions. With this in mind, we will use the lower average value of the erosion rates mentioned, which is equal to 1.66m/yr.

Parameters concerning the wave-induced erosion rate that have not been discussed will take their default Badlands value. A summary of the changed parameters is given in Table 5.3

Table 5.3: Wave-related sediment transport parameters.

Parameter(s)	Value(s)	Unit
Significant wave height H_s	1.15	m
Mean grain diameter	250	μm
Maximum wave influence depth	20	m
Wave directions (Badlands input)	205, 165, 115	°
Max. wave-induced erosion rate	1.66	m/yr

5.1.3. Land Usage

Humans have had a major impact on the environment by the way we use the land around us by as far back as the stone age. It has been widely accepted that a major contribution to anthropological landscape change was the introduction of agriculture (Nikulina et al., 2022). In modern times, ca. 80% of Europe's land surface has been changed by humans. These changes include urbanization and building of infrastructure (artificial surfaces), agriculture (cropland and pasture), as well as human management of forests, semi natural areas, and waterways/bodies (European Environment Agency, 2023). Many of these changes have had a big impact on environmental degradation as well as climate change. Modern land use in our area of interest is split up in five major categories: artificial surfaces, agricultural areas, forest and semi-natural areas, wetlands, and water bodies. The exact percentages of different land use surfaces per country are given in Table 5.4. For better visualization, the contribution of the land use categories in our area of interest as a percentage of the total surface is given in Figure 5.10.

Table 5.4: Land use for countries in our area of interest (% of total area in km^2). AT = Austria, BE = Belgium, FR = France, LI = Liechtenstein, LU = Luxembourg, and NL = the Netherlands. Data from European Environment Agency (2023).

Land use (% of total area in km^2)	AT	BE	FR	DE	LI	LU	NL
Artificial surfaces	5.94	20.91	6.00	9.37	13.25	10.57	13.75
Agricultural areas	31.88	56.93	58.65	56.50	20.05	52.55	59.7
Forest and semi-natural areas	61.09	21.12	33.76	31.3	64.41	36.51	10.76
Wetlands	0.25	0.36	0.70	1.25	0.98	0.02	7.15
Water bodies	0.86	0.68	0.89	1.59	1.31	0.35	8.65

A detailed table with the land usage in terms of percentage of corresponding river catchment for the Meuse, Rhine, and four major tributaries is given in Appendix B.

From both the figure and tables it is evident that agriculture is still the most significant land use in terms of surface area, covering as much as 57% and 74% of the Meuse and Rhine catchments, respectively. Forests and semi-natural areas are the second largest way of land usage, followed by artificial surfaces like cities and infrastructure (European Environment Agency, 2023). A detailed map showing the land use of our AOI is given in Appendix D.

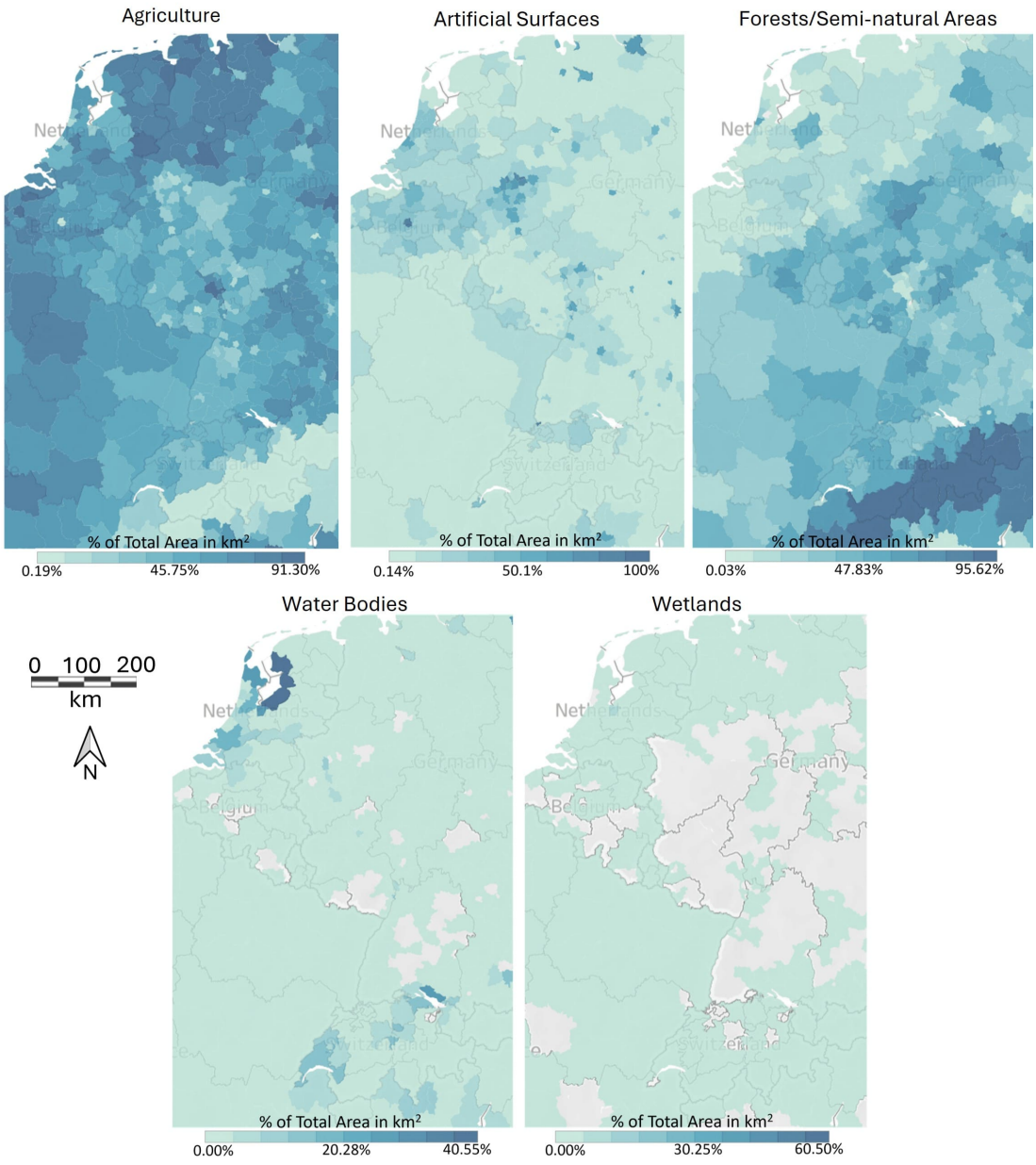

Figure 5.10: Five maps that show the distribution of different land use types in % of total surface area in km^2. Note that the colorbars have different scales per figure to optimize contrast. Adapted from European Environment Agency (2023), using CORINE^0 Land Cover (CLC) 2018 datasets.

Land use has a significant impact on the erodibility of the surface (Borrelli et al., 2017; Milazzo et al., 2022). For this reason, future land use change is one of the main factors that will be looked at in this study. Although much research is needed to understand erosional processes due to human impact (Poesen, 2018), we will discuss what the impact is of different land use changes on the environment and erosion as found in the present literature. The initial erodibility values for our area of interest will be discussed in section 3.

Agricultural Land Use

Agricultural land use is defined as the practice of cultivating soils, growing and producing crops, and maintaining pastures in order to raise livestock. This type of land use covers the most surface of our area of interest, and with the exceptions of Austria (of which only a small part lies on the eastern edge of our area of interest) and Lichtenstein (as the sixth smallest country in the world with a total surface of 161km^2 (Liechtenstein Office of Statistics, 2024) not the most impactful, surface-erosion-wise, in our simulations), it covers more than 50% of the surface area of each of the remaining countries.

Several studies have shown that soil losses due to precipitation will increase when vegetative cover (including straw) decreases or is removed (Alves et al., 2023; de Almeida et al., 2018; Rieger et al., 2016). This holds for both croplands as well as pastures (Alves et al., 2023). Consequently, agricultural land use has a positive effect on the erodibility of the soil as opposed to unprotected soils like barren landscapes (de Almeida et al., 2021). This is only the case when it is assumed that the agricultural land use is implemented sustainably, as bad agricultural practices can decrease the quality of the soil as well as being a direct source of erosion through bad water management or tilling practices and other factors, increasing its erodibility (Alves et al., 2023; de Almeida et al., 2018; Renard et al., 1997). Borrelli et al. (2021) have done a comprehensive statistical evaluation of soil erosion modeling results using 1697 articles. From this study, it was found that the mean erosion rate of bare soil was equal to $\hat{\epsilon} = 1.2$mm/yr, and that of agricultural areas was equal to one of three values depending on the defined agriculture type: $\hat{\epsilon} = 0.3$mm/yr (generic), $\hat{\epsilon} = 0.5$mm/yr (arable land), and $\hat{\epsilon} = 0.1$mm/yr (agroforestry). It is important to mention the vast majority of these studies focused on water related erosion, as opposed to wind, tilling, and/or harvest erosion. We can see that agricultural land use can cause a decrease in the erosion rate of a factor of 2.4 for arable land, up to a factor of 12 for agroforestry with respect to barren or unused land. Agroforestry is the integration of trees and shrubs into cropland and pastures (FAO, 2015).

Although the erosion rate is expected to decrease by applying agroforestry, does this form of agriculture allow for enough crop production and is it economically viable to be a feasible solution? Firstly, the fact that this question is asked is part of a larger problem, as classical agriculture practices have been mainly measured in terms of yield, but have had devastating effects on the natural environment and the climate (Pretty and Bharucha, 2014). In order to apply a more encompassing evaluation of agricultural land use which not only looks at yield, but also at environmental, socio-economical, and climatic impact (as a whole, as opposed to 'single media' focused research like carbon or nitrogen isolated), a 'fundamental departure' from conventional research is required (Rosenstock et al., 2014). It is important to mention an assumption that is often made with regards to agroforestry, which is the trade-off between cultivation and tree cover (Pretty and Bharucha, 2014). This is not only generally not the case, according to Zomet et al. (2009) "trees are an integral part of the agricultural landscape in *all* regions except North Africa/West Asia". Trees in agricultural fields have been shown to enhance soil nutrient status, reduce crop stress, reduce soil erosion through the binding of soil by roots as well as runoff effects, and the regulation of water supply by the hydraulic uplift of water due to deep roots, which all in turn increases the yield (Waldron et al., 2017). In addition to this, agroforestry was found to have a positive effect on biodiversity, social well-being (through recreational value), decreased firewood collection from natural forests, and can supply additional sources of income (and/or food) other than the increased crop yield (e.g., firewood, fruits, and other non-timber forest products (NTFPs) varying per region (Duffy et al., 2021; Herzog, 1998; Pretty and Bharucha, 2014; Rao et al., 2004; Waldron et al., 2017). All of this not only makes agroforestry a promising alternative to classic agricultural land use in terms of yield, in doing so it simultaneously enhances social and environmental goals such as the United Nations Sustainable Development Goals (SDGs) (Waldron et al., 2017). In Appendix C an overview is given of the three main ecosystem services and types of agroforestry.

[0]Coordination of Information on the Environment

Forestation and Semi-Natural Areas

According to the Food and Agriculture Organization of the United States (FAO), forests are defined as ”lands of more than 0.5 hectares, with a tree canopy cover of more than 10 percent, which are not primarily under agricultural or urban land use” (FAO, 2020). According to the Intergovernmental Science-Policy Platform on Biodiversity and Ecosystem Services (IPBES), semi-natural areas or ecosystems are defined as natural areas with most of its processes and biodiversity intact, but have been altered or ’assisted’ by humans ”in strength or abundance relative to the natural state” (IPBES, n.d.).

As seen in Table 5.4, Liechtenstein and Austria have the most surface area covered with forests and semi-natural area: both more than 60%. For all countries in the AOI with the exception of the Netherlands, forests and semi-natural areas cover more surface area than artificial surfaces. The core bio-climate in terms of forest cover found in Western and Central Europe is temperate oceanic forest (named after mild climate conditions due to oceanic influence), with deciduous broad-leaved trees as main vegetation type. The exception is Switzerland, which mainly has a temperate mountain system. This system is characterized by pine forests (de Rigo et al., 2016). No differentiation in tree-type was made in the Borrelli et al. (2021) study on erosion rates, thus only one value for forests was supplied. The mean erosion rate for forests and semi-natural areas was found to be the same, and with a value of $\hat{\epsilon} = 0.2$mm/yr. An interesting observation is the higher erosion rate in forests compared to agroforestry. In general, the involvement of forests or grassland in agriculture can have a major positive impact on soil erosion and sustainability (Milazzo et al., 2022), as discussed earlier in the agricultural land use section.

A different way forests can impact erosion is by influencing runoff. Although no differentiation was made in tree species when modeling erosion rates, the tree species can make a difference in the runoff during precipitation events. An evaluation of 92 published studies by Rahman et al. (2023) showed that conifers (e.g., pine trees) provided a better protection against runoff through higher interception and transpiration values than broad-leaved trees, but broad-leaved species provided better soil infiltration, decreasing drying out of soil. Both in forested areas as well as urban ’forests’ the mixing of both species will result in maximized reduction of runoff, in particular during storms. Although Badlands does not take into account vegetation directly, the effects will be included through the erodibility. Although not possible in Badlands, the effect of tree diversification needs to be taken into account in an overall analysis of land use effects.

Artificial Land Use

In Europe, all land use per surface area stayed relatively constant in the last few decades, with the exception of artificial surfaces. During the period 2000-2018, artificial surfaces in Europe have increased by 6%, or by 14,049km^2 (European Environment Agency, 2023). Effectively, the Netherlands has more surface area used for human made structures and infrastructure than it has forests and semi-natural areas. This artificial land use reduces the soil erosion by covering significant portions of the soil with human-made, virtually impermeable materials like asphalt, pavement, and cement. This process is also called *soil sealing*. Soil sealing effectively stops the natural erosion processes at the surface with respect to the soil, and thus the soil erosion in this land use category is assumed to be negligible. Notable negative effects of this type of land use include loss of biodiversity and loss of potential carbon sequestration (European Environment Agency, 2023).

A possible change in future artificial land use is the implementation of ’the symbiotic city’. This is the adjustment and/or building of cities to have ”social-ecological, circular, institutional and technical networks that reconnect soil, water, wind and organisms in urban practices” (Stuiver, 2023). The increase of ’green’ in urban areas specifically is not only vital for cooling down cities in warming conditions, but has been found to play an important role in increasing air quality, improving population-level mental health, and promoting a more sustainable lifestyle (Aram et al., 2019; Barton and Rogerson, 2017; E. A. Richardson et al., 2012; Szulczewska et al., 2014). According to De Roo (2011), ca. 25% of the total urban area within the symbiotic, or ’green’, city should be allocated to green areas like parks, distributed over the city. For this scenario we will assume that this increase in natural areas increases the erodibility within artificial land use. This will be discussed in section 7.2.6.

An important factor related to artificial land use is population growth. Although no dominant trend between urban land expansion (ULE) and population growth has been observed in different continents, generally cities with a higher ULE than population growth are found in Europe (Mahtta et al., 2022). Simulations based on future fertility, mortality, and migration rates show a general population increase

until 2026, followed by a gradual decline until 2050, and then a faster decline up to 2100. Only one projected population trajectory shows an increase in population up to 2100, and this increase is insignificant compared to the total population today (Eurostat, 2023). Although the average European population is expected to go down in most scenarios, the predictions between individual countries vary considerably. Belgium, France, Luxembourg, the Netherlands, Austria and Switzerland are among the countries that have a predicted increase in population up to 2100, mainly due to immigration. Most of these countries are projected to have a population increase of up to 8%, with the exception being Switzerland (+16%) and Luxembourg (+54%) (Eurostat, 2023). Given the small population of Luxembourg, this large increase will result in a population that is still less than a million people (993,916, growth with respect to the numbers of 2022) (STATEC, 2022).

5.2. Subsidence and Uplift

The total subsidence signal can be divided into two main contributors: anthropogenic subsidence and natural (or 'background') subsidence (Candela et al., 2020; Fokker et al., 2018; NWA-LOSS, 2022). These main contributors can be divided again, into the following sub-contributors:

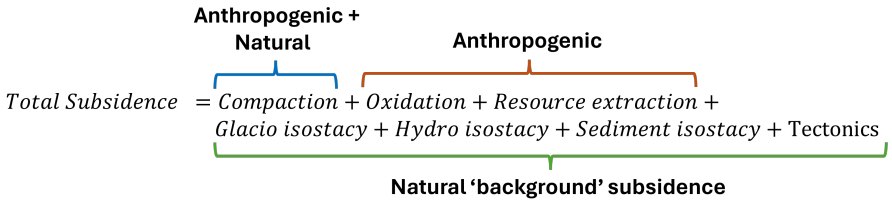

Figure 5.11: Main and sub-contributors of total subsidence. Adapted from NWA-LOSS (2022).

In Figure 5.12 a high resolution map of the total vertical displacement in Europe is given. Due to the absence of data on Switzerland, this gap was filled in using areas of average displacement as defined by Brockmann et al. (2012).

The vertical displacement as shown in Figure 5.12 is the accumulated uplift rate of all different mechanisms present on regional or even local scales. This means part of this displacement is due to human involvement, the duration of which might not span the full 10,000 year runtime of the simulation. We will now explore some of the sub-contributors and their expected temporal effect in some detail using regions in our AOI where they are relevant.

5.2.1. The Alps/Switzerland

The average values given to the Swiss areas were determined using a leveling-derived model, and take the values of: -0.1±0.1 (area N), -0.1±0.2 (W), 0.2±0.1 (C), and 0.9±0.3 (Alps), all in mm/year. It is of note that although the average uplift value for the Alpine arc area in Switzerland (indicated by 'Alps' in the figure) is around 1mm/yr, locally the uplift rate can be as high as 2mm/yr (Vanoise-Zermatt area, southwestern point of Switzerland) and 2.5mm/yr (found at the Central Alps area near Davos, at the Swiss-Austrian border; Sternai et al., 2019). There is still uncertainty about the different mechanisms that cause uplift in the European Alps (Mey et al., 2016), and the individual contribution (magnitudes) of these uplift mechanisms in the Alps are under debate (Sternai et al., 2019). The main mechanisms described in literature are the uplift as a response to glacier shrinkage (glacial isostatic adjustment (GIA)) (Barletta et al., 2006; Nocquet et al., 2016), isostatic response to erosion (Nocquet et al., 2016; Schlatter et al., 2005), isostatic adjustment to lithospheric structural changes (e.g., slab detachment, delamination of the continental lithosphere, Champagnac et al., 2009; Sternai et al., 2019), dynamic traction due to sub-lithospheric mantle convection (Braun, 2010; Gvirtzman et al., 2016; Sternai et al., 2019), and lastly the uplift due to an orogenetic, tectonic process (e.g., the penetration of the Adriatic block into the European lithosphere due to its counterclockwise rotation) (Mey et al., 2016; Nocquet and Calais, 2004; Schlatter et al., 2005). Our area of interest mainly includes a part of the Western European Alps. This part of the mountain range presently has virtually zero horizontal velocity boundary conditions (Nocquet et al., 2016). This means we will only take the vertical displacement of this area into account. However, what are the temporal scales at which different factors contribute to the vertical displacement of the Alps in the next

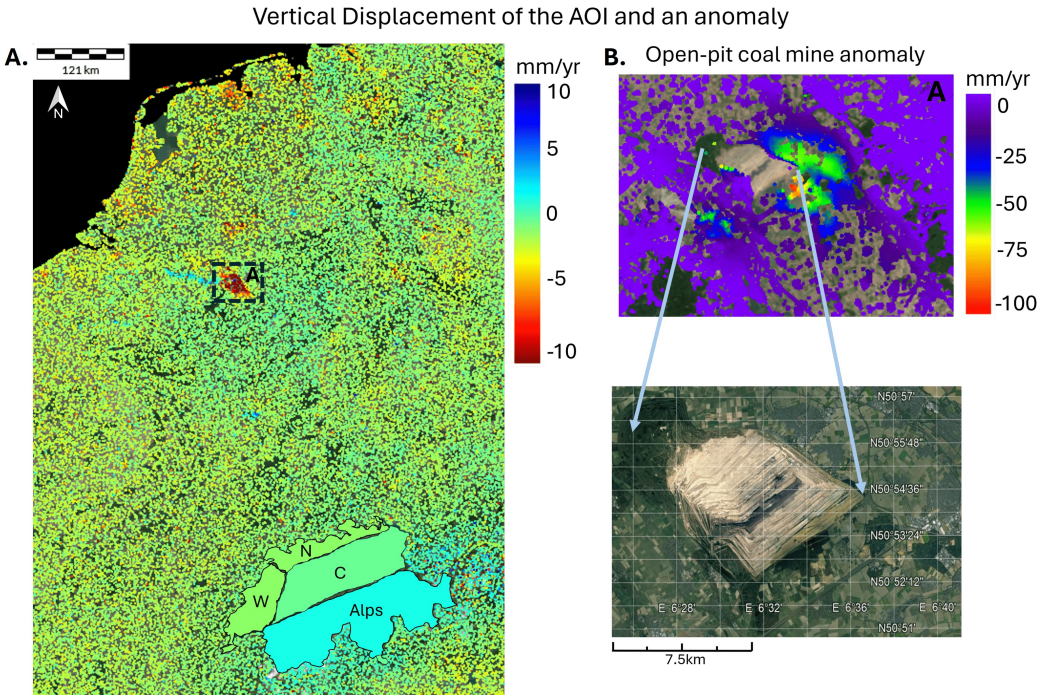

Figure 5.12: A: a high resolution vertical displacement map of Europe with the average vertical displacement of Switzerland from Brockmann et al. (2012). B: a zoomed in map with Google Earth image of a significant displacement anomaly on the right. From Copernicus Sentinel data (Copernicus Land Monitoring Service (CLMS), 2021), Brockmann et al. (2012), and Google Earth Pro.

10,000 years?

According to several studies, a significant portion of the present-day uplift of the Western and Central Alps region is due to the GIA, where estimates range between 30% up to 90% (Grosset et al., 2023; Mey et al., 2016; Nocquet et al., 2016; Sternai et al., 2019). Estimates concerning the extent of the GIA are usually done by looking at the last glacial maximum (LGM). This is defined as the period where ice sheets were at their greatest extent, from approximately 26.5 kyr to 20kyr ago (Clark et al., 2009). Typically, Earth's viscous response (isostatic adjustment) happens on the scale of thousands of years (Lloyd et al., 2023). As an example, the GIA in Fennoscandia has been going on since the first substantial ice-melting after the LGM 19,000 years ago (completely melted away around 9.7 cal kyr BP = 9.7 kyr before 1950 (calibrated 'Before Present' date) Stroeven et al. (2016)), and is expected to continue for the next thousands of years at least. A very rough estimation of the remaining time of continuing uplift in this region can be calculated from the Amantov and Fjeldskaar (2016) estimation of the remaining isostatic uplift of 40m in the Gulf of Bothnia and the present average uplift rate there of 10.12mm/yr (Lidberg et al., 2010). When we assume this rate will remain approximately the same in the future, this results in a roughly estimated remaining time of active GIA of ca. 3,600 years. The ice sheet thickness in this region was over 2.5km (Siegert et al., 2001). The ice sheet covering the Alps during this LGM is estimated to have been 1,400m (with a surface elevation of 3,010m, Kelly et al. (2004)), in addition to covering a substantially smaller surface area. This means we can expect the effects of the glacial isostatic adjustment in the Alps to last for some thousands of years, but likely not the full duration of our simulation. Due to the present uncertainty on the contribution of GIA on the uplift in the Alps, in addition to the change in the total uplift and possible change in contribution dynamics as a consequence of the GIA reaching equilibrium, it is virtually impossible to find accurate, complete estimations for uplift in the Western Alps for the duration of our simulations. Fluvial systems could react to a change in GIA, however. In order to check this we will define two vertical displacement predictions based on the GIA scenario in our simulations. The predictions differ in the remaining temporal extent of the GIA in Fennoscandia as well as the Alps.

The isostatic adjustments to surface mass redistribution due to erosion, and to lithospheric structural changes are contributions that will be relevant at scales of 10 kyrs (Sternai et al., 2019). The maximal uplift

due to erosion and sediment redistribution in the Central Alps was estimated by Mey et al. (2016) to be ca. 0.5mm/yr, while a time-averaged uplift rate calculated using a late-Quaternary erosion and sediment deposition reaches 0.25mm/yr. Although a possible uplift contribution by asthenospheric upwelling (Zhao et al., 2016), as well as a slab detachment event during the Pliocene-Pleistocene below the Western Alps (Lippitsch et al., 2003) were proposed, still much uncertainty exists about these possible contributions (Sternai et al., 2019; Zhao et al., 2016). It is true however that the models that account for deglaciation effects, sediment redistribution, as well as lithospheric heterogeneities, show significant differences with the modern uplift measurements. To account for these differences, uplift due to contributions of the solid Earth should be considered. Sternai et al. (2019) considers these contributions to possibly be in the order of 30% of the total uplift across the whole orogen. In the Western Alps, results have shown that the dynamic adjustment due to sub-lithospheric mantle flow has caused either slightly negative to no uplift at all (Sternai et al., 2019).

5.2.2. Short-term Anthropogenic Influences

An interesting anomaly in Figure 5.12, indicated by *A*, is the Hambach opencast lignite mine located between the towns Jülich and Kerpen in North Rhine-Westphalia, Germany. The mine is still active, outputting 23 million tonnes of coal per year (as of end of 2021), and at its deepest point lies 411m below global mean sea level (GMSL) (RWE, 2021), which explains the high rate of subsidence measured. Due to the European Union's commitment to reduce CO_2 emissions by at least 55% by 2030, Germany has adopted the Act to Reduce and End Coal-Fired Power Generation (SMARD, 2021). As part of the resulting coal phase-out, the coal extraction in the Hambach mine will end in 2029 (RWE, 2021). In order to avoid the creation of unrealistic lakes and activating different corresponding sedimentary processes in Badlands due to this anomaly in the map, the elevation of the mine will be artificially corrected by interpolation of surrounding values.

Another anomaly is the relatively fast subsiding area in the north of the Netherlands, which is caused by the consequences of natural gas production of the Groningen gas field. As per October 2023 the production of this field, which is the largest natural gas field in Europe, has ceased indefinitely (Rijksoverheid [Government of the Netherlands], 2023). In the worst case scenario as modeled by Van Thienen-Visser and Fokker (2017), the local subsidence will continue until flattening out around 2080. This will then have resulted in a total subsidence of ca. 46cm at the center of the affected area, with decreasing total subsidence going down to 0cm in the afflicted area of a radius of ca. 20km.

5.2.3. The North Sea Area

For the vertical displacement of the sea floor, we will use the rough predictions of Holocene (the last ca. 11,700 years of Earth's history) tectonic subsidence as determined from mean sea level (MSL) residuals by Vink et al. (2007). Specifically, we will only apply the values that were found to significantly reflect subsidence, and interpolate the rest of the North Sea area from these points. These data points are from the Dutch North Sea west, the oyster grounds located NW of the Dutch coast, and the E-W shipping route as measured just to the north of the German island 'Juist'.

5.2.4. General Vertical Displacements

For the remainder of our area of interest, it is also important to differentiate between vertical displacements from anthropogenic, tectonic sources, and glacial isostatic adjustment (Van Camp et al., 2011).

Van Camp et al., 2011 has investigated repeated absolute gravity measurements at nine stations over a period of 8 to 15 years (depending on the location). These stations are mainly located in the Belgian Ardennes and Eifel area (Membach, Sprimont, Manhay, Werpin, Sohier, Monschau) and Roer Valley Graben (Jülich, Bensberg), and one is located on the Belgian coastline at Oosteinde. When accounting for GIA, all stations showed a negligible tectonic vertical displacement with exception of the station at Jülich (influenced by the nearby Hambach mine) and Sohier (possibly biased due to the relatively short timespan of time series data) (Van Camp et al., 2011). Over the research area, the GIA induced subsidence was found to be a practically constant vertical movement of -0.5 ± 0.9mm/yr.

Furthermore, we will use data from Henrion et al. (2020) for vertical displacements of the Upper Rhine Graben area, and subsidence in the Netherlands from Kooi et al. (1998) and Vink et al. (2007). The vertical displacement map from Le et al. (2024) will mainly be used for the data points in the north and northeast of our AOI (e.g., middle and north of Germany). We will assume that the extent of the Fennoscandian GIA

in Europe is negligible south of the 50°latitude line, approximately following Lidberg et al. (2010). The implementation of the interplay between the GIA and the local and regional displacements caused by other tectonic and anthropogenic causes are beyond the scope of this project and will likely not influence our results significantly.

Some synthetic points will be calculated or read from given displacement maps in order to both get enough points along the edges to properly define our area of interest during interpolation, and to account for the gap between resolution and actual processes. An example of this is the insertion of a denser collection of points in the Upper Rhine Graben and the Vosges to account for the difference in the movement of the Graben with respect to its 'shoulders': this could otherwise lead to the Rhine being forced to divert to the west through France or take another route that does not conform with the present-day situation.

As we have seen, there is a lot of uncertainty in the vertical displacement rates for the area of interest, and in particular areas that are influenced by glacial isostatic adjustment and the temporal range of this contribution. For this reason, as stated before, two vertical displacement scenarios will be used. One in which the present uplift and subsidence rates will be assumed to remain constant (a 'business as usual' scenario) for the next 10,000 years, and a scenario where the GIA contribution is limited to its (coarsely) predicted temporal range of 3,600 years for Fennoscandia and (an arbitrarily chosen) 2,000 years for the Alps, and thus less overall uplift/subsidence will occur in these specific areas. The data points and the resulting interpolated displacement maps for each of these scenarios are given in section 7.2.3.

6

Climate Scenarios

6.1. Sea Level Predictions

Sea level is one of the extrinsic forcings available in Badlands, and is an essential part of the source-to-sink system. In Badlands, the sediment supply to a basin margin (e.g., the sea/coastline) is dynamically determined through interactions between (amongst others) climatic and eustatic variations (Ding et al., 2019). Sea level change is a major consequence of anthropogenic climate change (Dangendorf et al., 2015; IPCC, 2014; Slangen et al., 2016). In order to more accurately predict the landscapes of the future, feasible predictions for sea level change are essential.

The global mean sea level (GMSL) changes mostly through a combination of a decrease in land-water storage, oceanic thermal expansion caused by increased heat uptake (IPCC, 2014), and ”an increase in mass loss from land ice (glaciers and ice sheets)” (Clark et al., 2016). Since 1970, the predominant cause of sea level rise, both globally and in European regional seas, has been anthropogenic forcing. Thermal expansion of ocean water has been surpassed as the main contributor of sea level rise by melting of glaciers and of the Antarctic and Greenland ice sheets since the year 2000 (Fox-Kemper et al., 2021; Oppenheimer et al., 2022). The response time of the GMSL to perturbations in the different components varies: for land water there is a short response (10^0yr), for shallow-to-intermediate ocean temperatures and glaciers this response time is intermediate (10^1-10^2yr), and a long response time (10^3-10^4yr) corresponds to both ice sheets (Wigley, 1995) and deep ocean temperatures (due to slow mixing of the energy deviation into the large ocean thermal reservoir (Bryan et al., 1982; Hansen et al., 1985; Siegenthaler and Oeschger, 1984; Stouffer, 2004)).

We introduce four 10kyr sea level simulations by Clark et al. (2016) that will be used as input in our LEM. These four future sea level changes, including the sea level change of the past 20kyr as reference, are shown in Figure 6.1.

These simulations are based on the different factors contributing to sea level change described above, in relation to four future emission scenarios: 1,280, 2,560, 3,840, and 5,120 PgC as indicated in the figure (Clark et al., 2016), where 1 PgC is equal to 1 Gigatonne of carbon emissions. It was assumed these levels of emission are accumulated between 2000 and 2300, after which a net zero emission state is assumed to be reached. The local effects of Glacial Isostatic Adjustment is also taken into consideration in the sea level rise. According to Eby et al. (2009) and National Research Council (2011) nearly 100% of any emission scenario related sea level rise will remain after 10,000 years. The current cumulative anthropogenic carbon footprint is already rapidly approaching the 1,280 PgC emissions scenario. According to Jones et al. (2023) global accumulative CO_2 emissions in the period 1851–2021 were approximately 674 PgC (converted from $PgCO_2$ to PgC using a conversion factor of 3.664, Størens (n.d.)). This is based on the accumulative emissions of CO_2 only: the accumulative CO_2 equivalent emissions of methane (CH_4) and nitrous oxide (N_2O) are not taken into account as these gasses have a different atmospheric residence time and thus would not influence the temperature and/or sea level change at the same time scale, overestimating the resulting sea level on the longer term. If policy measures to reduce emissions and remove atmospheric CO_2 are not enacted soon, the 1,280 PgC emission scenario is ”all but guaranteed”, resulting in a significant millennia-scale sea level change (Clark et al., 2016). The highest emission scenario of 5,120 PgC is substantially lower than the potential emissions of the ”known and currently attainable carbon reserves and resources, which are estimated to be between $\sim$9,500 and 15,700 PgC” (Clark et al., 2016; Rogner

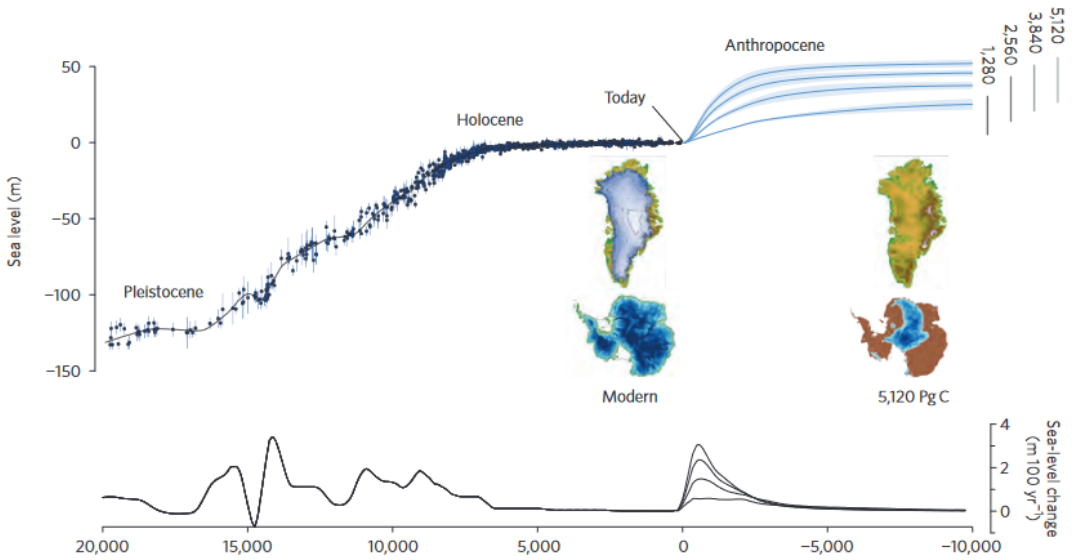

Figure 6.1: Past and future changes in sea level. From Clark et al. (2016).

et al., 2012). This means that although it is our worst case scenario, it is not *the* worst case scenario with regards to climate change and its consequences. An illustration of the state of the Greenland and Antarctic ice sheets corresponding to the 5,120 PgC scenario is given in Figure 6.1.

As mentioned before, the GMSL does not necessarily correspond to European regional seas. However, the Dutch North Sea (being our oceanic basin of interest) is part of the European coastline where the relative sea level is projected to be reasonably similar to the global mean sea level (European Environment Agency, 2024). This means the sea levels predicted by Clark et al. (2016) can be used reliably (in as much as uncertainties in future predictions allow for reliability) for our simulations.

6.2. Precipitation Predictions

Rainfall is also one of the extrinsic forcings available in Badlands. As discussed in section 2.2.5, a precipitation map covering the area of interest will be used for our simulations. For this we need to look into different factors concerning precipitation in our area of interest.

An important factor related to precipitation is temperature change (Collins et al., 2013). In Clark et al. (2016), ice sheet and glacier simulations were based on a mapping between the cumulative emissions and increasing temperature. In order for our simulations to stay consistent in the use of the CO_2 emissions and sea level rise from Clark et al. (2016), we will apply the same temperature increase for our simulations. The emission levels (1,280, 2,560, 3,840, and 5,120 PgC) correspond to a mean global temperature increase of 2.5, 4.5, 6, and 7°C, respectively. According to Collins et al. (2013), it is virtually certain that long term global precipitation will increase with increasing global mean surface temperature. It is estimated that the global mean precipitation will increase by 1 to 3% per degree Celsius of warming (Collins et al., 2013). Global climate models used by the IPCC generally provide consistent and reliable simulations of climate variability, but do this only at the continental to global scales. This is largely due to the use of typical spatial resolutions larger than 100km, which is larger than mountains and land cover features that influence local climate (IPCC, 2014). As our area of interest is sub-continental scale, we also need to look into regional precipitation changes.

Higher temperatures in continental (i.e., areas with a predominant continental climate) warm seasons are expected to be accompanied by lower precipitation amounts. This means that over land, strong negative correlations between temperature and precipitation dominate (IPCC, 2007). It is also expected, that at latitudes poleward of 40°(most of Europe, with exceptions of southern Spain/Portugal and southern Italy) positive correlations dominate in cold seasons as the lower temperature limits the water-holding capacity of the atmosphere (IPCC, 2007). These large-scale correlations between the monthly mean temperature and precipitation in Europe have stood up to the test of time since they were formulated by

Madden and Williams (1978). From this seasonal precipitation data, the average annual precipitation in a region can be determined. On Continental European scale, the average annual precipitation has shown no significant changes since 1960 (Haylock et al., 2008). However, on a regional scale significant changes are predicted. Specifically in Northern Europe the precipitation is predicted to increase significantly, and in Southern Europe the precipitation is predicted to decrease (European Environment Agency, 2021). Our area of interest is located in Western and Central Europe, where the smallest to no changes in average precipitation are predicted, in line with average annual European predictions overall. This trend is the same for any emission scenario simulated by the IPCC, as shown in Figure 6.2. The Representative Concentration Pathways (RCPs, i.e., emission scenarios) RCP2.6, RCP4.5, and RCP8.5 in the figure correspond to a CO_2 equivalent atmospheric concentration of 880, 1,276, and 2,597 PgC, respectively, by 2100.

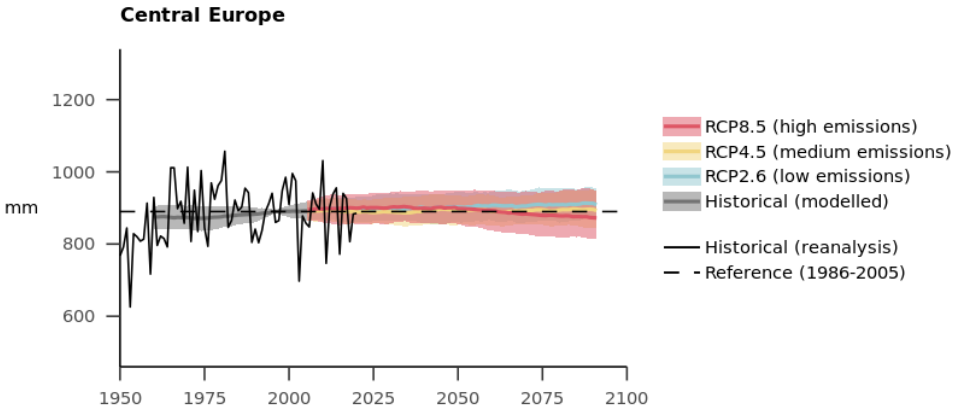

Figure 6.2: Annual precipitation data from 1950-2020 and projections until ±2085. From European Environment Agency (2021).

While the average precipitation over Western and Central Europe stays approximately the same, the different scenarios can show us the differences in the distribution of precipitation, with higher emission levels corresponding to larger regional differences. The predicted precipitation change between the periods 2011-2040 and 2071-2099 for both the RCP2.6 and RCP8.5 are given in Figure 6.3.

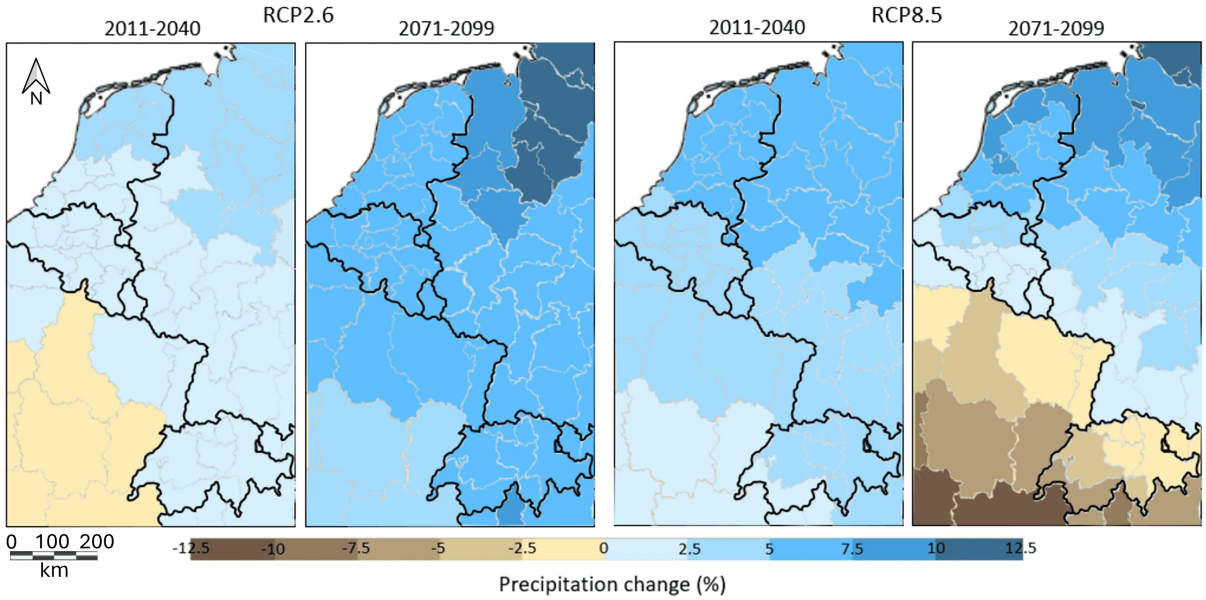

Figure 6.3: Predicted change in accumulated precipitation for periods 2011-2040 and 2071-2099, for RCP2.6 and RCP8.5. Adapted from European Environment Agency (2021).

It is not reliable to linearly extrapolate the presented precipitation changes as given in Figure 6.3 to the temporal scale that is relevant to this study, namely 10kyr in the future (Collins et al., 2013). While the applied temporal resolution for our simulation is far greater than the latest predictions of the IPCC up to the year 2100, it is expected that the general patterns of precipitation change as seen in Figure 6.3 stay similar (European Environment Agency, 2021). Due to the geographical location of our area of interest, the average annual precipitation is expected to increase in the upper coastal regions and the northeast (The Netherlands, N-NW Germany, and Belgium), and will either increase or decrease in the south and southwest, depending on the scenario. For the CO_2 emission scenarios used in this thesis (1,280, 2,560, 3,840, and 5,120 PgC) it is expected that the precipitation change distribution will follow the trend of RCP8.5 (approximately equal to our 2,560 PgC scenario) in Figure 6.3. This distribution is also influenced by geopolitics however, hence the boundaries of change are equal to the regional borders. This is of course not the case in reality, and thus we will apply a change that follows the trend, but is independent on the regional borders as shown in the figure. The percentile change in precipitation is dependent on the total temperature increase caused by the emission level. This means the change will reach its maximum when the emission levels and subsequently the temperature has reached their maximum too.

The capacity of air to hold water increases by ca. 7% per 1°C warming (Trenberth, 2011). This means that the intensity of precipitation events will increase. In addition to this, storm tracks are projected to shift poleward, likely increasing the amount of rainfall in heavy precipitation events in the whole of our area of interest as well (IPCC, 2014; O'Gorman, 2015). Thermodynamic effects due to the increased moisture holding capacity of air will likely cause an increase in precipitation variability over scales from daily to multiyear (Zhang et al., 2021). This change in variability can potentially be modeled by forcing that a given precipitation must occur during a shorter amount of time in the simulation. Due to the time step size of 100yrs however, changes on a daily-to-multiyear will not be able to be applied and could be subject to future research. We will mainly focus on the average change in precipitation over longer scales, where some variability in precipitation change (in terms of precipitation amounts, not events) on the regional scale is applied following the structure as shown in the RCP8.5 scenario in Figure 6.3.

While we have discussed the changes in precipitation, we have not introduced a baseline precipitation map which we will use as initial input. We will use a high resolution (0.1°, or 11.1km) data set comprising of the mean annual precipitation over the period 2011-2023 (Cornes et al., 2018). This will then be interpolated to correspond to the resolution of the topographical grid (which determines the resolution/size of all datasets in Badlands). The initial map (or base map) for annual precipitation is given in Figure 6.4. Note that there are no precipitation measurement stations on the North Sea, thus the lack of precipitation there. This will not impact the simulations, as the sea level rise is determined by a separate input independent from rainfall.

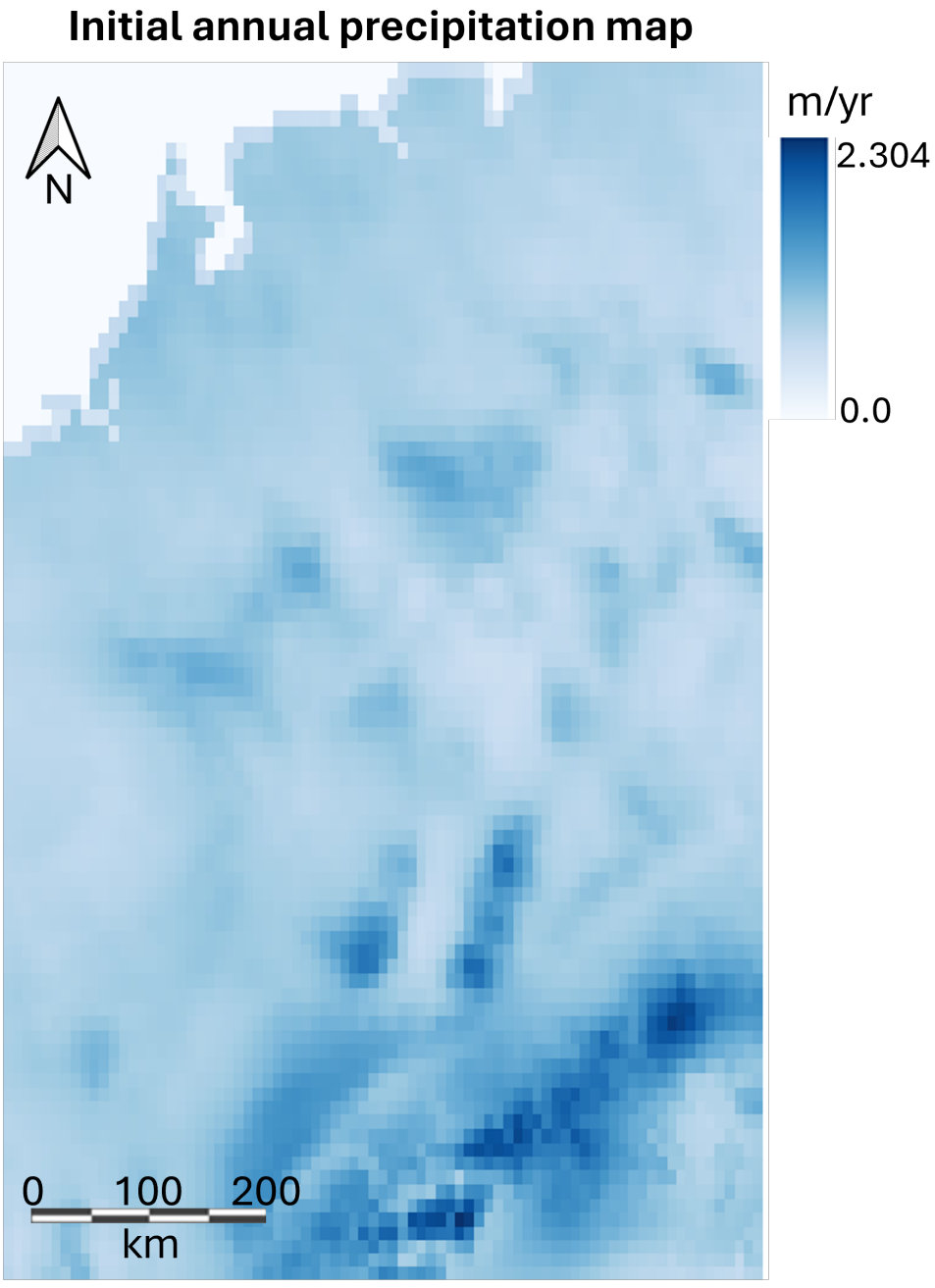

Figure 6.4: Map showing initial annual precipitation in meters per year in the area of interest. The precipitation was calculated by averaging over the annual precipitations of the years 2011-2023. Data from Cornes et al. (2018).

7

Defining and Processing Inputs

Many of the required parameters and datasets that will be used as input for our simulations were discussed in earlier sections, and the calibration of the precipitation and erodibility values were discussed in Part I of this thesis. Here, a structured overview of all the data and non-default parameters will be given. Additionally, the processing methods of the 2D data maps (e.g., precipitation map, topographic grid map, etc.) will be explained in some detail.

7.1. Overview of Input Data

As touched upon earlier in this report, the user input files and parameters can be given to Badlands through an XML parser. In Appendix G a full example of such an XML input file is given, with the parameters and settings representative of the simulations that were performed.

7.2. Processing Methods

In order to combine different datasets with variable spatial and temporal resolutions, as well as fill in gaps in the data, some processing is necessary. The different inputs and how they were processed are discussed next.

7.2.1. Data Ordering

The 2D input datasets are required to be structured in a 1D column, ordered from the lower left corner to the upper right corner through row-wise indexing (Badlands Group, 2019). This structure is shown in Figure 7.1. From this regular grid, Badlands will create a triangulated grid to perform its calculations, as explained in section 2.3.

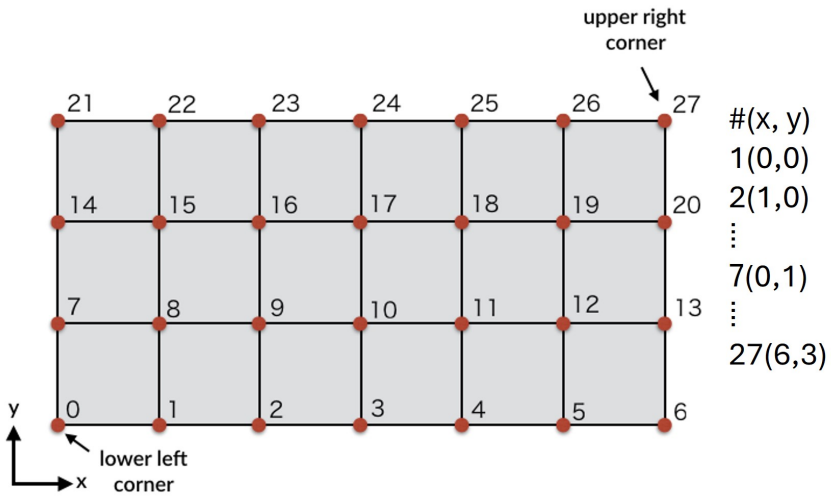

Figure 7.1: The required ordering scheme for 2D datasets. From Badlands Group (2019).

7.2.2. Topographic Maps

As discussed in section 2.3, the topographic map used for simulations will be imported as a CRS: WGS84/Pseudo-Mercator coordinate dataset from the EPSG registry (MapTiler Team et al., 2022). This will then be converted to a TIN in Badlands (Badlands Group, 2019). The 'cubic' interpolation method (also known as Finite Element Method) is used to create a smooth surface which brings out local trends in the dataset accurately (Mitas and Mitasova, 1999). The coordinates of the four corners of the map are given in Table 7.1.

Table 7.1: Coordinates for the four outer corners of the AOI. Given in decimal degrees (latitude, longitude), EPSG:3857.

	Lower left corner	Lower right corner	Upper left corner	Upper right corner
Coordinates	45.5°, 3.00°	45.5°, 11.0°	53.8°, 3.00°	53.8°, 11.0°

The resolution that is suited for our purposes, and thus will be used for all maps, is 1,824$\times$2,930 grid cells, where each cell is 307m$\times$314m. The reason for using this resolution is given in section 4.

7.2.3. Vertical Displacements

Because the spread of vertical displacement in Western and Central Europe is not that big (generally on the order of $\pm$1mm/yr with exception of the Alps and specific human made anomalies), the vertical displacement map is made through a cubic TIN interpolation (in order to represent local trends accurately) of 75 data points. These points are determined by regional ground station (gravimetry) data as well as satellite data and data collected from models based on this primary data. The input file is then structured as discussed in the section on data ordering above, with the values in the column representing the cumulative displacements during the given period in meters. We introduce our two scenarios: scenario T1 represents a continuous vertical displacement as present day for the next thousand years. The second scenario consists of three vertical displacement maps. The first which will use the same displacement rates as the T1 map for the first 2,000 years. After this point, the GIA part for the Alps is removed, which constitutes the second map until 1,600 years later. This is when, after a total of 3,600 years, the Fennoscandian GIA is assumed to have reached equilibrium and this influence will be removed. The third map then consists of the total vertical displacement of the area of interest for 3,600 until 10,000 years in the future, without any GIA related displacement. The interpolated vertical displacement maps for each of these scenarios together with the location of the original data points are given in Figure 7.2.

7.2.4. Precipitation Maps

As stated in section 6.2 the precipitation change will be applied in two ways to the AOI. The first is a change in precipitation based on the distribution shown in Figure 6.3. This distribution is influenced by geopolitics, and therefore should only be used as a general indication of change, and not as an accurate map corresponding to reality. In order to remove the geo-political bias in the data, as well as simplify the implementation of the precipitation change to the base map, the change distribution in the figure was discretized into a polygon layer in QGIS that corresponds to the general gradient that is present in the predicted precipitation change map. For every scenario, this gradient consists of a range of 10 values that were scaled based on the range given in the RCP8.5 scenario in Figure 6.3. This range was normalized and scaled to the maximum percentile precipitation increase per degree Celsius (= 3%/°C, Collins et al. (2013)), in combination with the respective predicted temperature ranges from Clark et al. (2016) for each scenario. The uniform precipitation change for each scenario was determined by calculating the area-weighted-average of the non-uniform precipitation change. A general example of the polygons used for both the non-uniform and the uniform precipitation change are shown in Figure 7.3.

An overview of the temperature increases and corresponding non-uniform and uniform precipitation change per scenario is given in Table 7.2. The average uniform precipitation change for Western and Central Europe calculated from the non-uniform data is in line with the general predicted global precipitation change (and that of continental Europe).

The increased precipitation rate will be implemented after the first 300 years in the simulations. The first 300 years the base map will be used. This assumes the atmospheric CO_2 and corresponding temperature will be at their maximum after this time, after which a net zero emission state is reached. This follows

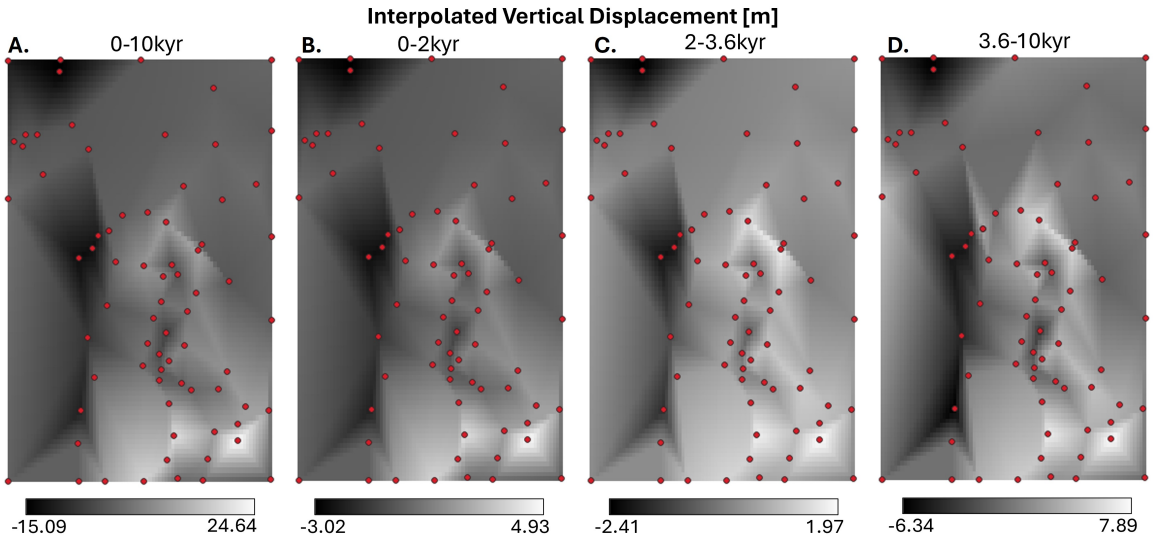

Figure 7.2: The interpolated cumulative vertical displacement maps showing original data points in red. Image A on the left is the cumulative vertical displacement corresponding to T1. Images B, C, and D are the cumulative displacement for the situation in where the GIAs do not last the full 10,000 years. Every image (B-D) corresponds to the cumulative vertical displacement for a period in which a change in vertical displacement has occurred. Made using QGIS (QGIS.org, 2024).

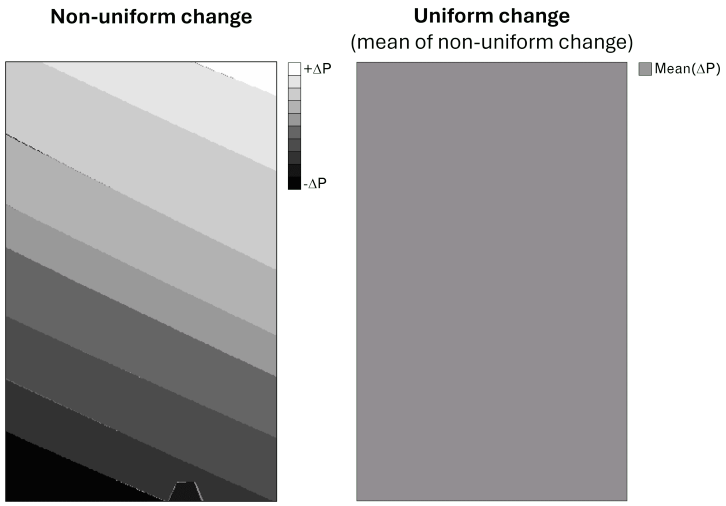

Figure 7.3: The polygons used to implement precipitation change (ΔP) to the base map. A positive sign means increase, negative sign a decrease.

Table 7.2: The temperature increases and corresponding non-uniform and uniform precipitation change (in percentage) per emission scenario. ΔP is the change in precipitation.

Emission scenario (PgC)	1,280	2,560	3,840	5,120
Temperature increase (°C)	2.5	4.5	6	7
ΔP Range (%)	-7.5 to 7.5	-13.5 to 13.5	-18 to 18	-21 to 21
ΔP Area-weighted-average (%)	1.61	1.62	1.63	1.63

the assumption made by Clark et al. (2016) used for the sea level predictions. Although the increase of precipitation will already occur in these initial 300 years, there is no data supporting how this increase will go. In order to not impose or create data ourselves without supporting evidence, a simple step function is

used from the base level up to the maximally changed precipitation after 300 years. As we are simulating over a period of 10,000 years, this is likely not of significant impact, it however has to be taken into account if sudden changes are observed in the initial time period.

All of the precipitation maps will also be multiplied by a factor of 0.3 (in case of the non-base map this is done after applying the climatic changes) to account for evapotranspiration and infiltration-related reduction of the amount of water that will determine the discharge. This is further explained in section 4.

7.2.5. Generating Sea Level Curves

The sea level curves are directly based on the results of Clark et al. (2016), and have been extracted from the plots shown in Figure 6.1. This was done using the web-based plot digitizing tool WebPlotDigitizer (Rohatgi, 2024). The validity and reliability of WebPlotDigitizer was analyzed by Drevon et al. (2017), and they show that there was a near-perfect relationship between the values calculated from extracted data using WebPlotDigitizer and the original reported values (with a Pearson correlation coefficient of r = 0.989, $p < 0.001$), concluding it is a reliable and valid tool for data extraction.

The files containing the sea levels consist of two columns. The first is the time in years, the second is the corresponding sea level in meters. The data does not have to be equally spaced, as Badlands will use linear interpolation to find the values in between data points (Badlands Group, 2019).

7.2.6. Land Use Changes

The land use will be changed using the artificial land use and agricultural land use (excluding vineyards and olive groves) areas as defined by the CLMS (2020) map. These areas (or polygons) are shown in Figure 7.4. Using these areas, the necessary changes are projected on the erodibility map (e.g., changing all artificial land use erodibility factors to 0). Given the projected population increase over our AOI, and

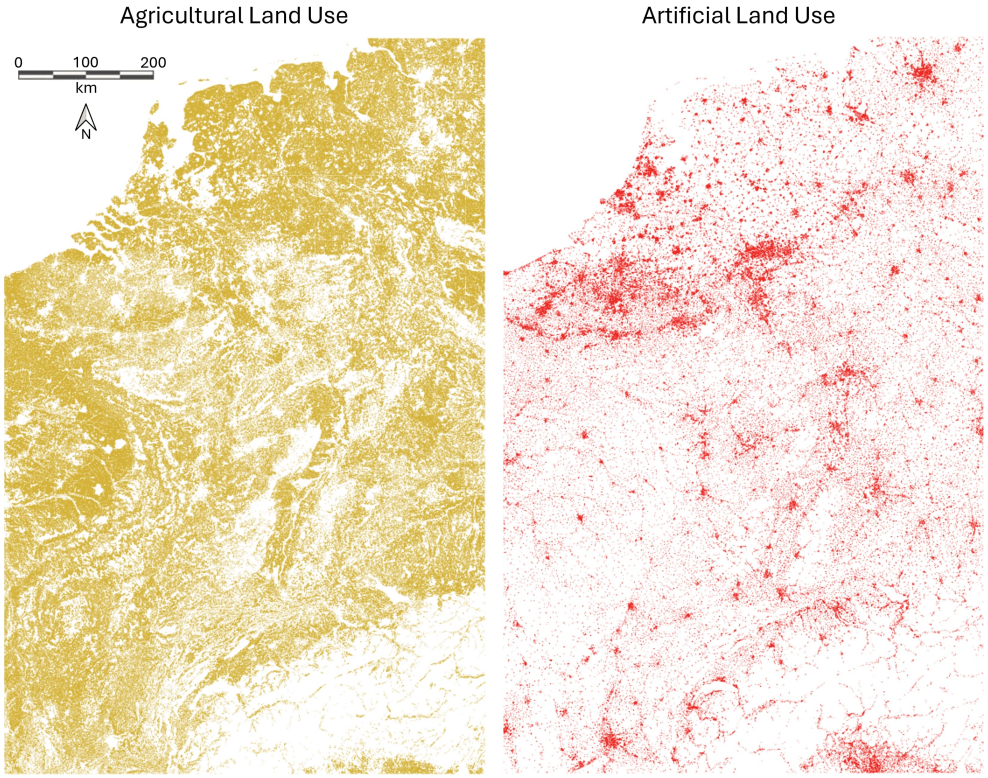

Figure 7.4: The isolated images showing agricultural land use on the right and artificial land use on the left. The polygons used for defining and changing land use are based on these maps. Data from Copernicus Land Monitoring Service (2020).

given the spatial resolution of our simulations, the potential urban land expansion would still be smaller than a radial expansion of the largest urban areas. For this reason, together with the high uncertainty of

predicted urbanization rates in the far future (after the year 2100) and the complexity in applying such a change, we will keep the total area of artificial land use stable throughout our simulation runtime. For the third land use scenario where the inclusion of more nature in artificial land use areas causes an increase in erodibility, we will base this change on De Roo (2011). It is not realistic nor possible within the software used to accurately and stochastically define 25% of the artificial land use as patches of natural surface area, either manually or through algorithm. An alternative to this is to increase the erodibility for all of the artificial land use area, but do this by only 25% of the base topsoil value.

7.2.7. Erodibility Maps and Layer Thicknesses

As discussed before, the topsoil erodibility value is used to represent land use change. This means that for each land use method, a different topsoil erodibility map is used. For each of these maps we will use the same soil thickness map. All of these data sets have been interpolated linearly in order to prevent values that were outside the minimum and maximum values, as can be the case with a cubic interpolation. As we only use a single other layer for the bedrock erodibility, we will assume this layer is practically infinite in depth. In Badlands, the relative short duration of the simulations with respect to geological time, and the low orders of magnitude for the bedrock erodibility means that an arbitrary depth of 500m acts as an infinite thickness.

Because of the high uncertainty within the erodibility values that were initially found for the topsoil and bedrock, and to get a feeling for the processes in Badlands regarding topsoil/bedrock erosion, the configuration of two separate layers with their respective K-factors will initially be used in the proof-of-concept simulations, and compared to a similar simulation using only a bedrock layer.

Based on these initial results all simulations will use the topsoil erodibility maps that are scaled by a factor 0.2, and the topsoil layer thickness map that is scaled by a factor 100. The average erodibility calculated for the erodibility maps corresponding to the three land use scenarios are given in Figure 3.4.

8

Modeled Realizations

The simulated realizations (i.e., combination of different scenarios) have several variables. In particular, the sea level (S), precipitation (P), and land use (L) combination will vary between model realizations. This is done following the structure illustrated in Figure 8.1.

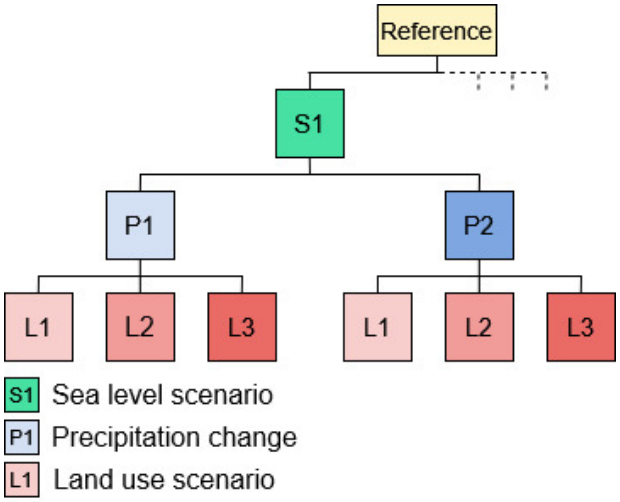

Figure 8.1: Realization tree for a single sea level scenario. The dashed line indicates the repetition of this scheme for the other three sea level scenarios. S = sea level scenario, P = precipitation change scenario/map, and L = land use change scenario.

The background of the main contributing variables of sea level, precipitation, tectonics, and land use have been discussed in previous sections. In order to efficiently communicate the use of each variable in the modeled realization and outside of it we will introduce the following notation, given in Table 8.1. The reference simulation has the artificial land use erodibility set to zero just like the L1 scenario in order to more meaningfully compare them.

Table 8.1: Simulation scenarios and symbols.

Sea level scenarios	
Symbol	**Scenario description**
S1	1,280 PgC scenario: sea level rise to ca. 25m
S2	2,560 PgC scenario: sea level rise to ca. 37m
S3	3,840 PgC scenario: sea level rise to ca. 45m
S4	5,120 PgC scenario: sea level rise to ca. 52m
Tectonic (GIA) variability	
Symbol	**Scenario description**
T1	Vertical displacement unchanged for 10,000 years
Precipitation scenario	
Symbol	**Scenario description**
P1	Uniform precipitation change
P2	Non-uniform precipitation change
Land use scenario	
Symbol	**Scenario description**
L1	No land use change in the next 10,000 years
L2	Agricultural lands to agroforestry
L3	Symbiotic cities: erodibility of cities is non-zero

As an example: a simulation that uses the first scenario of each parameter given in the table will be indicated by 'S1P1L1'. As the tectonic variability only has one setting, this letter is omitted from the labels. The 'Reference' in Figure 8.1 is the simulation of the present, and has been done in Part I (cf. Figure 4.13 in section 4.2.3). This realization uses no change in precipitation (only using the base precipitation map given in Figure 6.4, adjusted by the factor 0.3 as discussed.), the same uplift and subsidence as all other realizations, no sea level rise (i.e., the sea level rise remains at the current level for the full 10,000 years), and lastly we will use the L1 land use scenario which counts as our reference model. This means in total there will be $4 \times 2 \times 3 + 1 = 25$ simulations, including the reference simulation. In the next part we will show the results from all of the simulations.

9

Comparing Realizations

Due to the classification of the Upper Rhine Graben as a lake as we have seen in Part I of this study, and thus changing our attention to the Lower Rhine instead of the full river, there is no reason to visualize the full area of interest anymore. From here on, the images will consist of the upper third of the area of interest, with the boundary being the northmost point of the main body of the URG lake (e.g., Figure 4.13).

9.1. Sea Level

The precipitation change and sea level change are coupled through the emission levels. This means that there are no realizations where sea level is the only changing variable. In order to get an idea of the effect of sea level change only, four additional simulations are run. These have identical inputs as the reference POC simulation, with the only difference being the four different sea level changes.

Across all sea level scenarios we see the Rhine losing ground to the sea. For the first 1,000 years we see no difference in sediment load range and distribution of values across the Lower Rhine or its tributaries. At t = 1,000yrs we see the Utrecht Hill Ridge still being a part of the mainland in S1, but has turned into an island in the other scenarios. This is shown in Figure 9.1. The original coastline is shown in the maps for reference.

When the base level differences are larger, we see more variability occur in both the range of sediment load values and the addition of a sediment signal from tributaries. This is not always the case, however. An example of this is shown at t = 3,300yrs in the figure. At this time step, the length of the Lower Rhine is significantly shorter for higher sea levels. Yet, the sediment load that is present in the main channel as well as the Ruhr tributary is identical in each scenario. In contrast to this, when we look at t = 3,900yrs we do see major differences between the sediment load. For the lowest lea level the sediment load at this time step is highest of all scenarios, with the scenarios in order of low to high sediment load: S3 - S4 - S2 - S1. This order seems random as it changes each time step. The prominence of sediment signals of different tributaries of the Rhine for different scenarios also varies. In particular the S4 run shows a strong sediment signal in both the remainder of the Ruhr, which flows into the sea directly instead of flowing into the Rhine at this sea level, and the tributary Sieg. Both of these are indicated in the figure at t = 3,900yrs for the S4 scenario. The signal of the Rhine for the S1 scenario disappears after t = 4,600yrs, for S2 at 4,800yrs, and for S3 and S4 around t = 5,200yrs and 5,400yrs, respectively.

When we compare this to our base simulation without a base level change, we see that the sediment load disappears earlier in all sea level rise cases. It is important to mention that in all cases the discharge in the river does not seem to react to the base level rise, as it is only determined by the precipitation. When we compare the sediment load between the sea level rise runs and our reference simulation we see that there is little to no difference in the values when studying the different time steps. It is important to note that due to the sea level rise we cannot actually compare a large part of the Lower Rhine and delta area against itself, as different parts are flooded for different sea level rise. The sediment load signal also tends to go further upstream as the base level rises, meaning there are areas of the Rhine that have sediment load in some simulations but not (meaning only background sediment load, but not a distinguishable river pattern) in others. The channel between the Ruhr and the Sieg is largely visible in all of the simulations, and thus this part of the Rhine was used for a direct comparison.

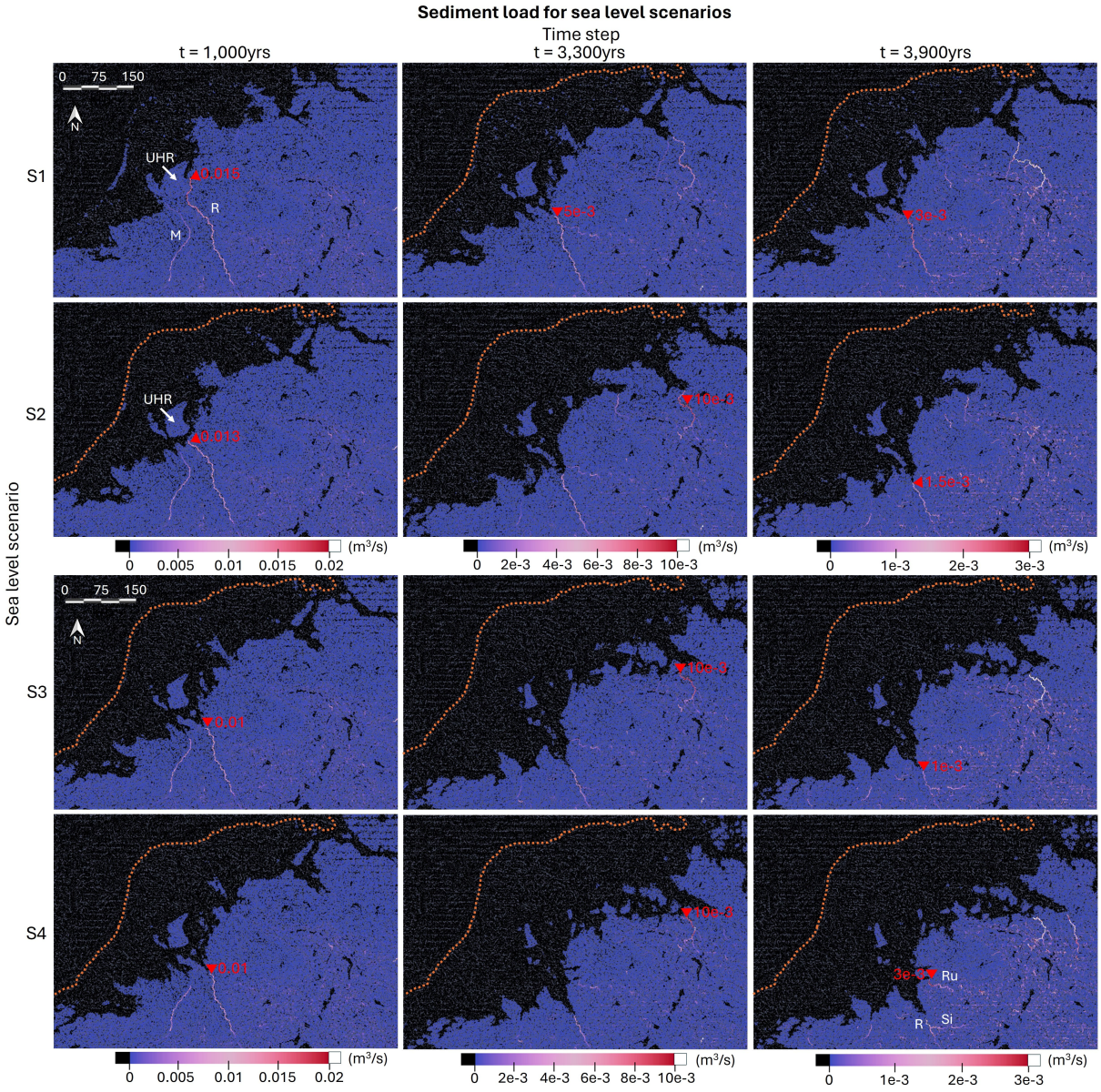

Figure 9.1: Sediment load for the base simulation with sea level change (i.e. S1, S2, S3, and S4) added. Each time step has consistent scaling across the scenarios. The orange dashed line shows the original coast line before sea level rise. R = Rhine, M = Meuse, Ru = Ruhr, Si = Sieg, UHR = Utrecht Hill Ridge. The red triangle indicates the maximum sediment load value in m^3/s. Note that this value is not always the maximum value of the color bar, this is for visualization purposes. Read 2e-3 as 0.002. Maps made using ParaView V5.12.0.

9.2. Precipitation and Land Use Effects

9.2.1. Sediment Load and Discharge of the Lower Rhine

In order to evaluate the sediment load in constantly moving fluvial channels, it is not feasible to individually select the grid cells with coordinates that correspond to these rivers. In order to still select the sediment load from the fluvial channels specifically, a simple high-pass filter can be applied. As we are interested in the sediment load in the Rhine, we apply a high-pass filter on the discharge, using a cut-off value of $2{,}400 m^3/s$. This value is based on Figure 4.11, where it is clear that the Rhine is the only river in our area of interest with such a high discharge, and specifically a discharge higher than $2{,}400 m^3/s$ only in the section we are interested in: the Lower Rhine. Specifically this cut-off filters the river just after the

major tributary Moselle joins the Rhine, and as such it integrates all of the major upstream discharge and sediment load changes. There is another filter that we need to apply however. In the flow output, Badlands adds discharge values irrespective of the base level in the simulation. Although the depositional environment and thus processes change, there are still discharge values in the area where physically there is no river anymore. In order to get rid of these discharges a low-pass filter is also applied using a cut-off value of 3,000m^3/s. When we combine these two it means one band-pass filter is applied to the discharge to identify the Lower Rhine section in the data. An exception for the cut-off values are made for six outputs that show different values than the rest. A minimum cut-off value of 750m^3/s is applied to the S2P2 realizations, and a minimum cut-off value of 1,500m^3/s is applied to the S3P2 realizations.

In Figure 9.2 the average sediment load and discharge of the lower Rhine (here defined as the Niederrhein and lower half of the Mittelrhein reaches combined, or from the city of Koblenz (where the Moselle enters the Rhine) until the Dutch-German border) for the S1 realizations are given. When we compare the two plots showing the sediment load we see a clear pattern. The reference sediment load starts of by an initialization from t = 0yrs, where the first sediments are starting to be produced. When it reaches the first peak it forms an unstable platform that remains within the same range of sediment load for about 2,500 years. After this, the sediment load decreases relatively fast over the following 2,500 years until it reaches (near) zero and it remains there for remainder of the simulation. This decrease is likely due to the combination of initial fast erosion followed by reaching an equilibrium incision depth with respect to the base-level increase. When we look at the P1 sediment load plot we see that the land use scenarios follow the reference trend well, but show a higher volatility in their values. Especially the peak of L1 at about t = 1,000yrs, and the two troughs of L2 and L3 around t = 1,800yrs are good examples of this. Apart from the peak of L1, this plot follows the reference plot closer than the other land use scenarios. The course nature of the graph is due to the sediment load being averaged over the full reach of the Lower Rhine as well as averaged over 200 years for each time step. +

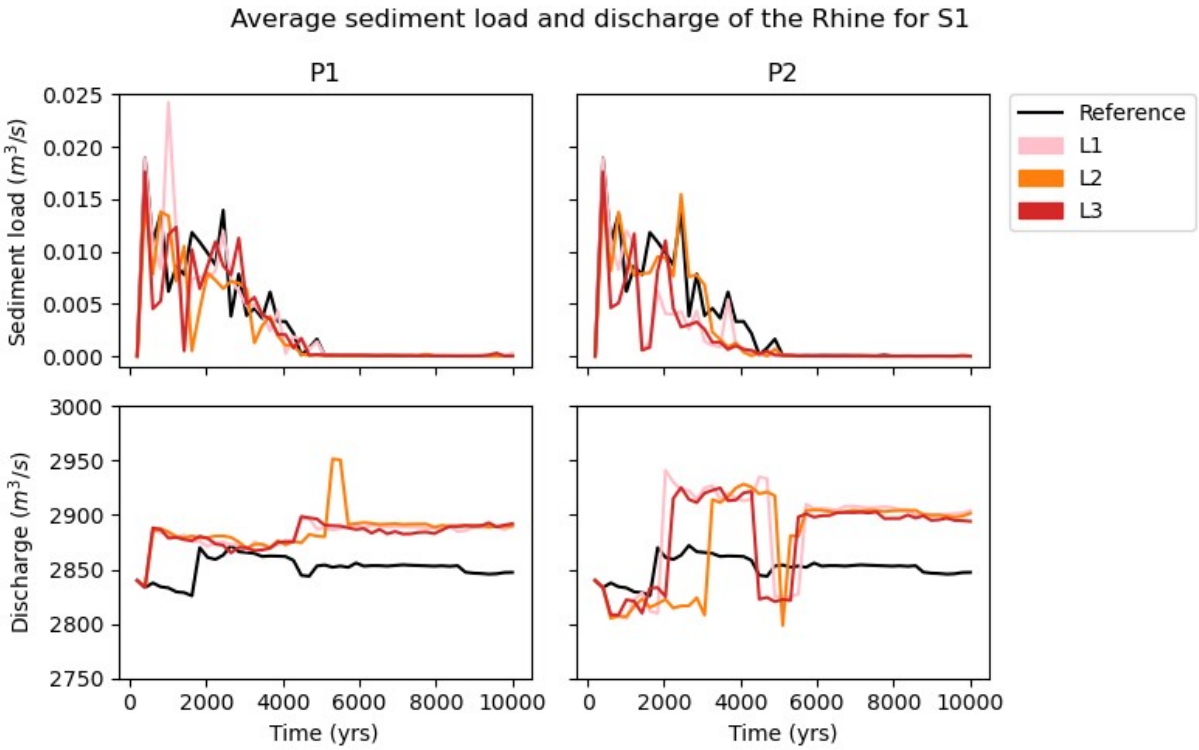

Figure 9.2: Sediment load and the discharge against simulation time for the S1 realization. The outputs for uniform precipitation (P1) on the left and non-uniform precipitation (P2) on the right.

When we look at the P2 sediment load plot in Figure 9.2 we see a similar pattern, with two important differences. Firstly, there is no L1 peak anymore, nor is there a trough in the L2 plot. The trough that is present for the L3 scenario lasts longer than its P1 plot counterpart. The second important difference is that

all the land use scenario plots do not follow the reference plot as well anymore, although it is not a drastic difference. The L1 and L3 plots tend to have lower values than the reference, and these decrease earlier as well as faster than the reference values. The L2 plot differs here as it still follows the initial platform that the reference plot shows, but after this platform the sediment load decreases much faster and it converges with the L3 plot. In order to test if the sediment load from different land use scenarios as well as from the P1 and P2 plots share a distribution (i.e. are not inherently significantly different from each other) among themselves or with the reference values, a Kolmogorov-Smirnov test is applied to the data. The specifics about this test and its results can be found in Appendix F. It is important to keep in mind that the shown sediment load is the average over the whole reach of the Lower Rhine at a certain time step. This means the values in the plots are not a precise reflection of the sediment load in the Rhine.

The discharge that is shown is the average discharge taken over the reach of the Rhine that was discussed above for each time step. The discharges for both plots are quite similar. When the precipitation change is initiated at t = 300yrs we see the immediate response in both plots. As stated before, this abrupt effect was anticipated. Interestingly, it leads to a general increase for P1 immediately, while for P2 it leads to a small decrease in discharge. Next the discharge for P2 increases to a level that is slightly higher than for P1, and this remains the case for the majority of the time except for one moment when the discharge decreases shortly around t = 5,000yrs. Although we can see one small tributary move from the Rhine to the Meuse and back throughout the simulation on the discharge maps, this does not explain this sudden increase in discharge in the P2 case. There is also no visible change in catchment-identification which would lead to discharge being channeled to or from a different river than the Rhine.

When we compare the sediment load plots to the discharge there seems to be a disconnect. There is no change in the discharge that would naturally correspond to a systematic and rapid decrease in sediment load for the P1 plots. For the P2 plots the sudden increase in discharge around t = 2,000yrs for L3 seems to correspond to the sediment load decrease. We also see that the increase in discharge for L2 happens later, which also corresponds to a later decline of the sediment load. For L1 the connection is less clear however. There also seems to be no response in sediment load to the sudden decrease in discharge between t = 4,200 and 5,800yrs. For the reference sediment load and discharge there is also no clear response visible between the two.

Next we will look at the average sediment load and discharge of the Lower Rhine for the S2 realizations, which are given in Figure 9.3.

The sediment load of P1 shows a similar pattern to the P1 plot in Figure 9.2. We see the initial rise and an unstable platform, followed by a decrease of sediment load until it reaches (near) zero. A key difference is that the duration of the platform is much shorter, as the time until it starts decreasing roughly halved compared to the ca. 2,500 years in Figure 9.2. The peak we saw for L1 in the previous figure has been replaced by a peak in the L3 plot with a somewhat lower maximum. Another difference is that the decrease of sediment load after the platform happens more rapidly for each land use scenario than the reference. We see that at the time step in Figure 9.2 where we saw a trough in the L2 and L3 plots, the sediment load doesn't return to the higher platform level but continues having a lower range of values until it reaches zero in Figure 9.3. For the sediment load of P2 however, there is a major change. The sediment load only has a small initial spike in the first few time steps, after which it decreases rapidly and has values close to zero the majority of the time. There is no significant difference between any of the land use scenarios.

When we look at the discharge, we see a bigger difference between the P1 plots of Figures 9.2 and 9.3. Instead of having only the initial increase caused by the precipitation change, the discharge in Figure 9.3 shows two instances where the discharge increases by approximately the same amount (by about $50 m^3/s$). The second increase happens at the same time step as when the reference discharge shows such an increase. Again, this is likely caused by the creation of a minor tributary that in this case is formed in all realizations of S2P1. In the case of the land use scenarios, this second increase of discharge corresponds to the rapid decrease of sediment load. This is counterintuitive, as we would expect an increase of sediment load when the discharge increases. Just before t = 5,000yrs we see another relatively small increase in discharge for our land use scenario simulations. It seems there is no corresponding sediment load response to this pulse. The discharge of P2 however shows a large contrast to all the other plots we have discussed thus far. The initial discharge is already much lower than the reference discharge and the discharges that we have seen for the same land use scenarios. We then see a steep decrease after the precipitation change is initiated (at t = 300yrs), which corresponds exactly to the onset of the rapid

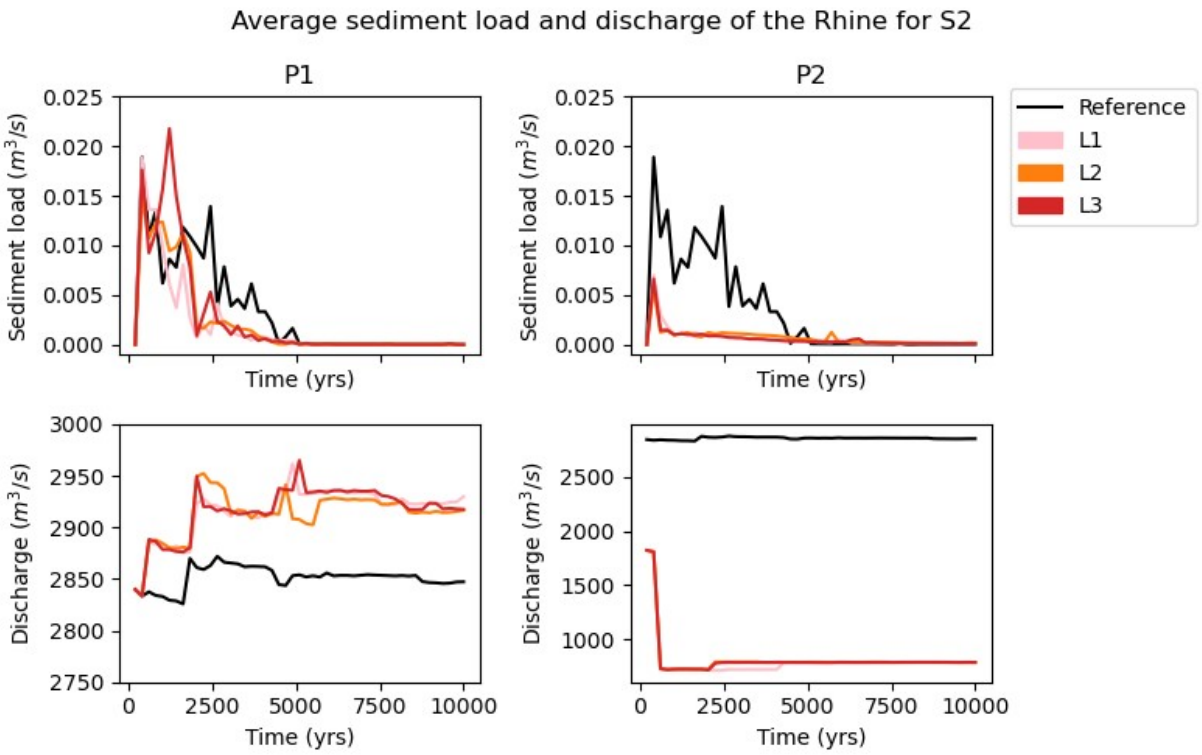

Figure 9.3: Sediment load and the discharge against simulation time for the S2 realization. The outputs for uniform precipitation (P1) on the left and non-uniform precipitation (P2) on the right.

decrease in sediment load. After this decrease, the discharge maintains this level for the full remaining duration and for all land use scenarios. The low discharges are not only a strange range of values in general, as we would expect something more similar to the P2 discharge in Figure 9.2, but the decrease is of significant size as well. The discharge drops from ca. 1,750m^3/s to ca. 750m^3/s. When we look at the visualization of the discharges between t = 200 and 400yrs given by Figure E.1 in Appendix E, we see the majority of the Rhine completely disappear from our map at t = 400yrs. Because we apply a band-pass filter based on discharge, and as the Rhine is missing completely from our map, the data that we see here is actually not of the Lower Rhine but of the largest remaining river(s). This explains the much lower values for discharge and corresponding lower sediment load. Why the Rhine disappears from the outputs like this is unknown. The disappearance of the Rhine on the discharge map does not coincide with an increase in discharge for other channels, which means water mass is likely not a conserved quantity in Badlands.

Next we will evaluate the average sediment load and discharge of the Lower Rhine for the S3 realizations, which are given in Figure 9.4. We see a continuing trend for the P1 sediment load, as the general shape of each of the plots again follow the same phases. First an initial increase, followed by an unstable platform ending in a rapid decrease, after which the values quickly converge to zero until the end of the simulation. The time step at which the rapid decrease takes place is again earlier than in the previous figures. Now we see this decrease happen around t = 1,300yrs. We observe that the peak in the L1 plot as we saw in Figure 9.2 has returned around the same time, with the same maximum. The rapid decrease after the platform also seems to happen faster, with less 'ripples' (small changes in the sediment load) present in the plots directly after. The P2 sediment load shows similar behavior to its namesake in Figure 9.3. We see the initial peak and immediate drop to near zero, after which the values don't noticeably change anymore until the end of the simulation. In this case, the maximum of the peak is almost double the maximum of the peak in Figure 9.3. This is the only realization where the Kolmogorov–Smirnov test results given in Appendix F show that not one of the P2 simulation sediment load outputs share a distribution between any of the other simulations, including the other P2 simulations. This signifies its difference between all other realizations.

When we look at the discharge we see both similarities and differences with respect to the previous

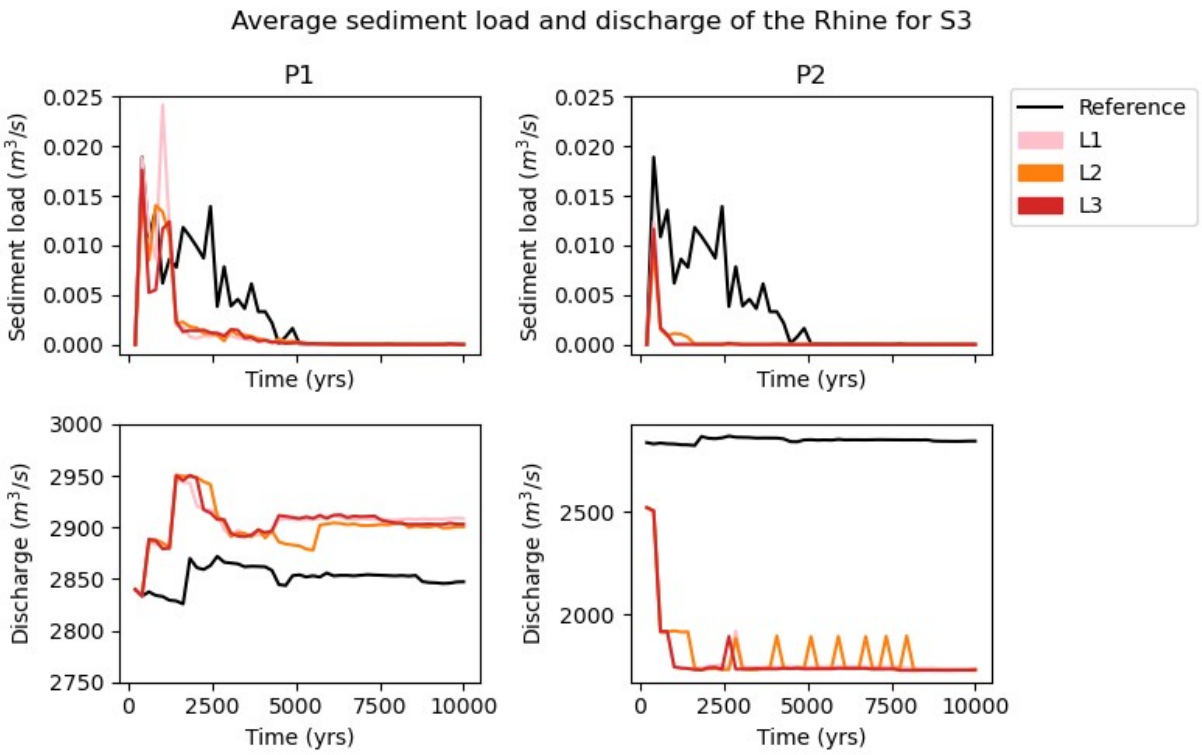

Figure 9.4: Sediment load and the discharge against simulation time for the S3 realization. The outputs for uniform precipitation (P1) on the left and non-uniform precipitation (P2) on the right.

discharges that we have discussed. For the P1 discharge, we see a similar ladder structure as in Figure 9.3 representing an initial rise in discharge due to the initialization of the precipitation change and a second increase of similar size a little later. It is of note that the second increase in discharge happens earlier in the simulation (ca. t = 1,300yrs versus ca. t = 2,500yrs), and again corresponds to the sediment load decrease we have discussed. Around t = 2,000yrs the discharge decreases by approximately 30m^3/s, during which we see no clear response from the sediment load. After a short while the discharge decreases by another 20m^3/s. Here we do see an apparent response in the sediment load, as we see a marginal increase during this period. Further changes in the discharge do not show a response anymore. The P2 discharge shows similar behavior as its counterpart in Figure 9.3. After the initialization of the precipitation change the discharge drops significantly, followed by a smaller decrease after a few hundred years. The initial discharge is higher than in Figure 9.3, and the decrease of 750m^3/s is also lower. This is because we see the same behaviour of the discharge output as the S2P2 plots, however here only half of the Rhine disappears instead of the whole Rhine. This disappearance of the downstream-located half of the Rhine is shown in Figure E.2 in Appendix E. The second smaller decrease in discharge as well as the repeating peaks of discharge, especially for the L2 plot, are caused by an additional repeating dis- and re-appearance of a part of the Rhine. This is illustrated in Figure E.3 in Appendix E. Although the discharge of the Rhine in the remaining half is big enough to select it using our adjusted band-pass filter, this reach is mainly located in the Upper Rhine Graben. Because of the identification of a lake here, and resulting basin-related sediment deposition, the sediment load is zero. This illustrates again that Badlands treats discharge separately from it's identification of lakes (a discharge output through a lake will remain its discharge values regardless if there is a lake there or not). Sediment load is affected though, due to the change of depositional processes.

Lastly, we look at the average sediment load and discharge of the Lower Rhine for the S4 realizations, which are given in Figure 9.5. We again see the same trend for the P1 sediment load. Similarly the rapid decrease of the sediment load happens earlier and faster than in the previous realizations. The time between the decrease here and in the previous figure is not as large as the times observed between the previous figures, with the decrease happening around t = 1,250yrs in Figure 9.5. We do not see a second

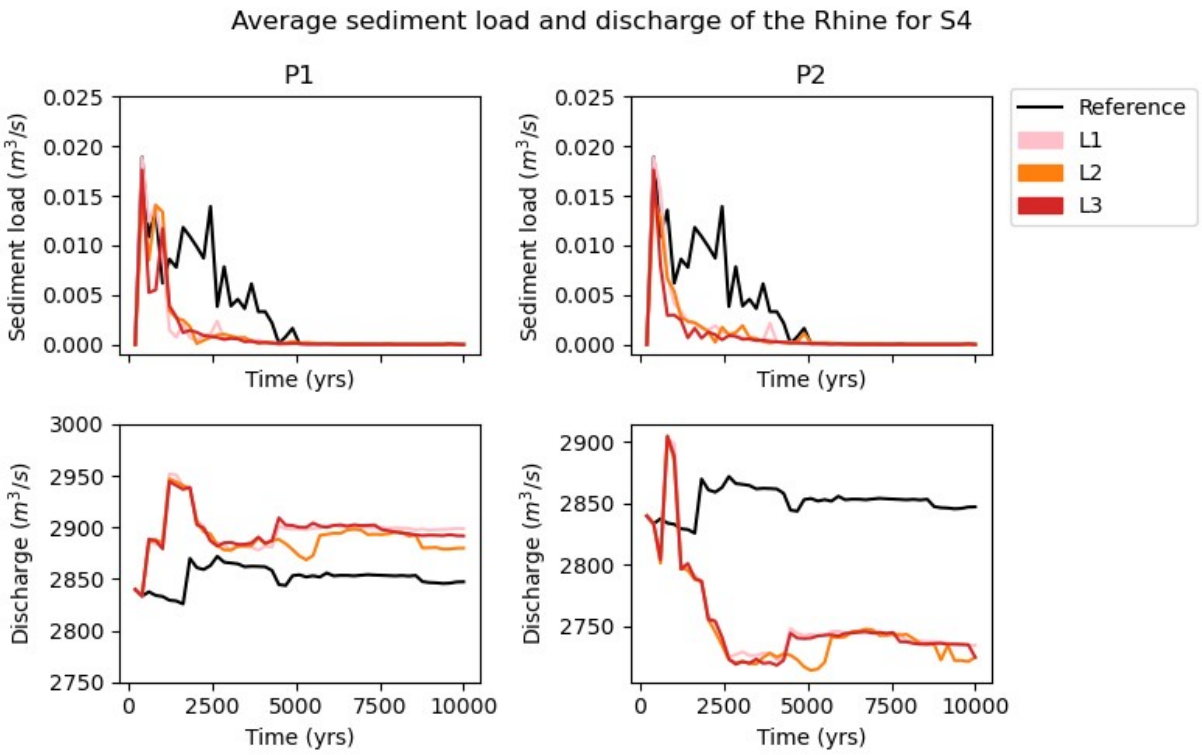

Figure 9.5: Sediment load and the discharge against simulation time for the S4 realization. The outputs for uniform precipitation (P1) on the left and non-uniform precipitation (P2) on the right.

peak in the sediment load for L1 nor L3 scenarios, which were present in the previous results. In contrast to Figures 9.3 and 9.4, the sediment load results in the P2 plot are similar to those shown in Figure 9.2. The sediment load peak in the beginning is the same for both P1 and P2, but we see that the rapid decrease of sediment load directly follows this peak. The L3 sediment load seems to decrease the fastest, while the L1 and L2 plots follow a slower decline and have a lot of overlap. The small changes in the sediment load after this vast decline , or 'ripples', do last longer compared to those in the P1 plot.

The discharge for P1 looks almost identical to the discharge we see in Figure 9.4. The two phases of sediment load increase in the beginning of the simulation are shorter than for the S3 realization. Although the maximum value that the sediment load reaches is the same for the P1 plot for both the S3 and S4 realizations, the corresponding land use scenario and time for which this maximum is reached differs. We see that only the L1 scenario in Figure 9.5 reaches this maximum for just 185 years, compared to all three the scenarios reaching this maximum of which the L2 and L3 scenarios for more than double this time in Figure 9.4. This is followed by a steeper and shorter decrease, after which the discharge increases a little after about 2,500 years for the L1 and L3 scenarios. In both Figure 9.4 and 9.5 the L2 discharge first decreases before meeting the L1 and L3 discharge levels again. This effect which is visible as a little trough in both plots is larger for the S3 case. For the remainder of the time the discharge in both the S3P1 and S4P1 plots stay relatively constant, with the exception of the L2 scenario in Figure 9.5 which decreases slightly around t = 8,750yrs. Even with all these changes, we can say that the discharge of all P1 plots follow a general evolution that is similar to the reference discharge, with most if not all of the differences explained by the variability in tributaries in each realization. When we look at the P2 discharge there is a large difference when compared to the reference however. After a small initial decrease, the discharge increases by about 100m^3/s, after which it follows a steep decrease like we saw in Figure 9.4. This decrease can be split into two main phases. The initial rapid decrease which happens in a short time span, and the second phase of decrease which is more gradual and takes more than a thousand years to reach the minimum. After reaching this minimum the discharge of all scenarios have a slight (approximately 25m^3/s) increase after several thousands of years, where the L2 scenario again shows a delay with respect to the L1 and L3 scenarios before it increases to the same level. The discharge remains relatively stable

for the remainder of the simulation. There are two things that are important to note about this discharge. Firstly, although the land use scenario plots look to vary quite a bit when compared to the reference, the total difference between the minimum and maximum discharge we see here is only about 175m^3/s. The decrease corresponds to the rate at which the sea level rises and in doing so limits the full range of the discharge when averaging over the available reach (the parts of the Rhine with the highest discharge are flooded, resulting in the average discharge to decrease). The more rapid decreases correspond to the sea level rise dividing a tributary like the Ruhr from the main river. Secondly, the changes in the discharge do not seem to correspond to changes of the sediment load. In other words, we don't see a clear response of the sediment load to a clear change in the discharge. If anything, the sediment load has already started to decrease substantially before the decrease in discharge is initiated. The main decrease in sediment load has happened before the second phase of discharge decrease has started, and this second phase does not seem to have a large impact, if any, on the remaining sediment load.

9.2.2. Comparing Sediment Load

Next, we will plot the sediment load from our realizations against the reference sediment load that was shown in the previous section. Because we want to look at the behavior of sediment load in a region where the values are not clearly affected by the discrepancy between the topsoil erodibility and bedrock incision model, a cut-off is determined for the time-range of each of the realizations that isolates the sediment load from the fast decline due to this effect. The cut-off values are given in Table 9.1.

Table 9.1: Temporal cut-off values for sediment load analysis. The same cut-off was used for any land use scenario within the given combinations of S and P.

Realization	S1P1	S1P2	S2P1	S2P2
Cut-off time (yrs)	2,500	2,500	1,200	1,200
Realization	S3P1	S3P2	S4P1	S4P2
Cut-off time (yrs)	1,000	800	1,000	800

These values will allow us to observe if the trends of these sediment loads in this temporal range are different or not. Due to the results shown in the previous section the S1 and S4 realizations, and the S2 and S3 realizations are grouped together in the next figures.

The sediment load resulting from the S1 and S4 realizations plotted against the reference output are given in Figure 9.6. On the left we see the plots for a uniform precipitation change and on the right for the non-uniform precipitation change. Using the trends plotted in the figure we can more meaningfully compare the different sediment loads with respect to the reference values. Starting with the S1P1 plot, we observe that the land use scenario that is essentially the same as the reference with the addition of the climatic forcing (L1) has an overall higher sediment load. This is what we would expect, as in this case the precipitation has increased resulting in an increased discharge with respect to the reference as we have seen in the previous section. It is important that the L1 trend is skewed towards the lower range of values due to the presence of the sediment load peak as seen in Figure 9.2. When the erodibility of the topsoil is decreased for the L2 scenario, we see it results in a trend that is lower than our reference case even with this increased precipitation. An unexpected result is that the L3 scenario has the lowest sediment load trend among all of the simulations. As the L3 erodibility map was made by only increasing the K-factor for artificial land use with respect to the L1 map, we would expect a sediment load that is higher than L1. Instead we see that except for the values on the lower end it is even lower than the L2 scenario. This is an unexpected result, and this is strengthened by the fact that the average erodibility of the L3 map is much higher than that of L2, closer to the value of L1. When we compare the result to the S1P2 plot we see similar behavior. The gradient of the L1 trend has decreased a little, causing the trend to be further removed from the reference at the higher value range but bringing the average sediment load closer to the reference value. It is clear that the majority of this trend is still above the reference trend line. We also see that the L2 and L3 trend lines do not cross each other anymore, causing the L3 trend to be lowest when compared to any of the other trends in the plot in any range of sediment load. There is little to no change visible in the L2 trend.

When we look at the S4P1 plot we see that the L1 trend line is completely located above the reference

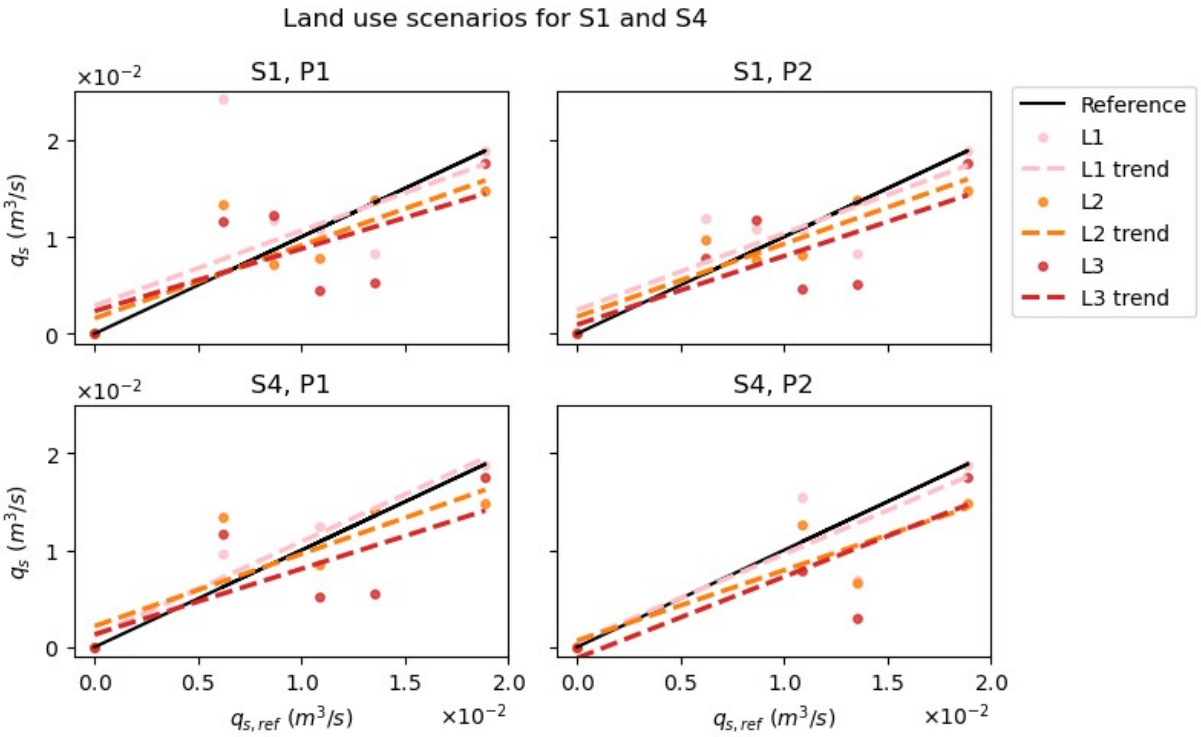

Figure 9.6: Sediment load (q_s) plotted against the reference sediment load ($q_{s,ref}$) for uniform precipitation (P1) and non-uniform precipitation (P2) precipitation change of the S1 and S4 realizations. The trends were produced through a weighted linear regression.

trend line. This is not surprising, as we are looking at the result of the most extreme increase of precipitation of all our realizations. The L2 and L3 trend lines are similar to those for S1P2. When compared to S1P1, the L3 trend shows a downward vertical shift, indicating that the result of more rainfall counterintuitively leads to less sediment load in the rivers in the L3 case. In contrast to this, the L2 trend is seen to shift upward. This shift is not large however, showing that although there is an increase in erosion of agricultural land, the decrease of its erodibility due to the implementation of agroforestry has caused this surface area to be relatively resistant to erosion as a result from increased precipitation. In addition to this, the (small) majority of the sediment load is still below our reference trend line, indicating a decrease of sediment in the Rhine (and potentially other rivers). When we look at the S4P2 plot on the lower right corner in Figure 9.6 we see some clear differences. First, although the L3 trend line at the higher value range has remained in position, the line has move down significantly in the lower range of sediment load. This means that the L3 sediment load has significantly decreased with respect to our reference simulation. Secondly, the L2 trend line shows a general downward shift, resulting in the trend line to lie below the reference for most of its range. The L2 sediment load shows a general decrease with respect to both the S4P1 plot and S1P2 plot as well. Although we would expect an increase in sediment load with an increase of precipitation, the non-uniform nature of the precipitation change results in a net decrease of precipitation for a large part of our area of interest. This in turn results in a decrease in erosion further upstream of the Rhine, as well as a general decrease of discharge as is clearly visible in Figure 9.5. Because we have a large lake in the place of the Upper Rhine Graben, the decrease in sediment load here is likely the directly result in the decrease of discharge, as the sediment signals from further upstream are deposited in the lake instead of following the river downstream to the Lower Rhine reach. Although the sediment load of the lower range is still above the L3 trend, at the higher end of values the two trend lines meet and overlap for the last quarter of the range.

Next we will evaluate the sediment load resulting from the S2 and S3 realizations plotted against the reference output, which are given in Figure 9.7. The first thing we notice in the S2P1 plot is the position of the L3 trend line. This is the only simulation where the L3 scenario shows this behavior. The position of

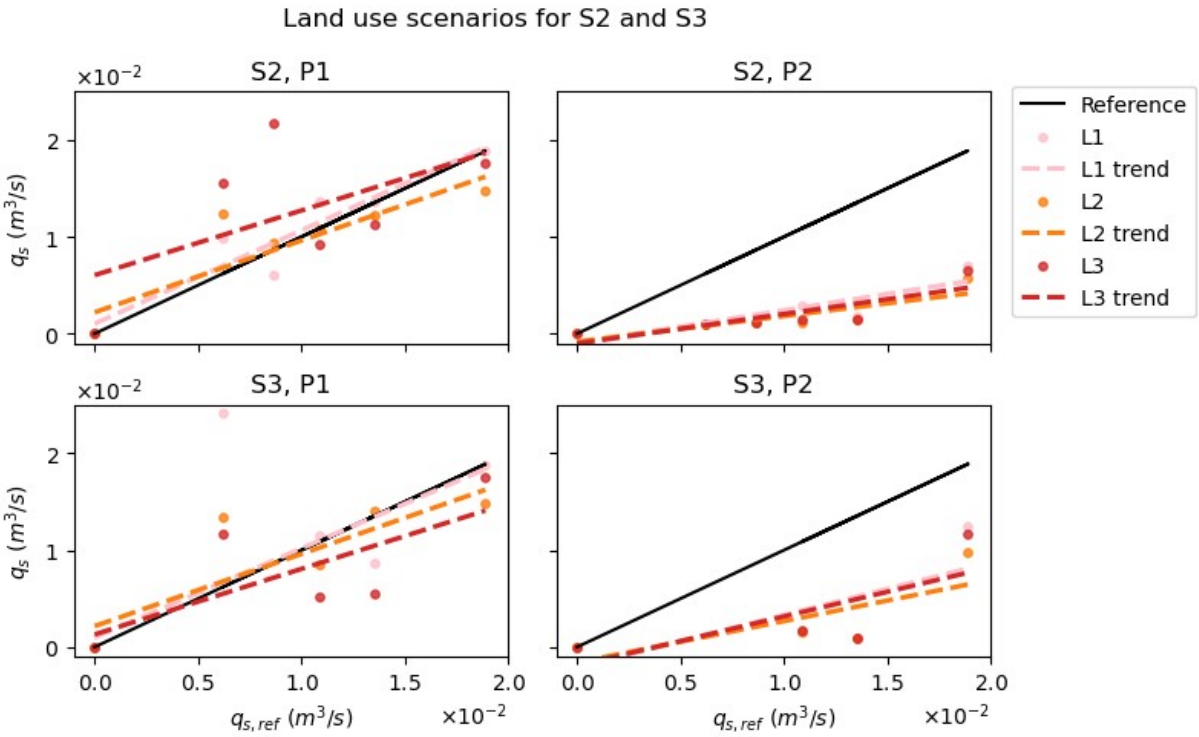

Figure 9.7: Sediment load (q_s) plotted against the reference sediment load ($q_{s,ref}$) for uniform precipitation (P1) and non-uniform precipitation (P2) precipitation change of the S2 and S3 realizations. The trends were produced through a weighted linear regression.

this line is caused by the influence of the sediment load peak that is visible in the P1 plot in Figure 9.3. This skews all values towards the higher end of sediment load, while this is not the case for the L1 and L3 scenarios. The L1 trend line is positioned just above the reference trend, which is the expected behavior that we would expect. As we don't have a large sediment peak there is no skew in the trend that we see in Figure 9.6. When we compare the L1 trend to the S4P1 L1 trend we see that it is slightly lower, which is also expected since the precipitation change for the S2 realizations is smaller. The L2 trend is very similar to its counterpart in both P1 plots in Figure 9.6.

The trend lines in the S2P2 plot are the result of the lower discharge and resulting lower sediment load that we have seen in Figure 9.3. All of the land use scenario trends are very close to each other and show a very low sediment load with respect to the reference. Although this behavior is likely not accurate, the vertical ordering of these trend lines do follow the general averages of the erodibility maps that are associated to each scenario. We see the same behavior for the P2 plot of the S3 realization. The only difference are the higher values for sediment load due to the higher discharge.

The S3P1 plot is closer to the P1 plots of the S1 and S4 realizations. The L1 trend is pretty much the same as the reference trend, with a difference too subtle to evaluate from the plot. In this case, this trend is lower than the ones we have seen for either the S1 and S4 plots, which is not something we expect when we look at the difference in precipitations between all these realizations. The L2 trend shows a small vertical shift upwards with respect to the L2 trend in the S2P1 plot. We have seen this behavior before, from the L2 trends between the S1 and S4 P1 plots and is the behavior that we expect when we take into account the change in precipitation and erodibility of the topsoil. The small change in the L2 trend between each of the realizations shows that a large scale decrease of erodibility of agricultural land results in relatively stable erosion when uniform precipitation changes are applied. This does not hold up when the range of changes in precipitation are more accurately applied in the form of the non-uniform precipitation change. Just like the S1 and S4 P1 plots the L3 trend line lies mostly below the reference trend, which is consistent with previous results. This behavior of the L3 trend is discussed more in section 10.

Part III

Closure

10 Discussion

10.1. Lake Identification

In Part I of this thesis we have seen a lake being identified in the Upper Rhine Graben (amongst others, cf. Figure 4.4). This creates a problem because we are not able to faithfully recreate sediment load and discharge, as well as erosional processes and the general environment of the present-day. In the case of this thesis it meant a significant decrease of the reach of the Rhine that could be investigated for sediment load change. As areas like the URG are not unique to Europe, any study dealing with predicting future landscapes could encounter the same problem. During the Quaternary period the Upper Rhine Graben saw the presence of numerous interconnected lakes spread throughout the fluvial plain during stagnant times of the cold glacial season (Przyrowski and Schäfer, 2015). This means that the existence of a lake or more lakes in the URG is not unrealistic from a geomorphological perspective. When focused on these processes in the context of paleolandscapes, the identification of certain regions as lakes that have since changed conditions are not a problem, and could potentially create a paleolandscape that is more accurate with respect to modern findings like the lakes in the Upper Rhine Graben. Before Badlands can be reliably used for future landscape prediction in areas with similar rifting zones or river valleys, the process of identifying lakes needs to be adapted. Although there does exist a 'hack' to force elevation in these misidentified areas causing the region to be identified correctly, this solution could not be applied to our specific situation due to time constraints in combination with the possibility that it would impact the morphology of the Rhine and remove the river from a densely populated area that would likely influence the sediment flux of the Rhine due to land use practices.

There is no consistent sediment signal for the Alpine and the High Rhine. We do see the deposition of sediments happen in the south of the URG over longer time spans. This is visible through the appearance and northward expansion of the area in which we see background runoff, located in the south of the Upper Rhine Graben Lake (cf. Figure 4.6, the area turns from black to blue). This means that there is little sediment load present. The reason for the small quantity is likely the lack of topsoil in the Alps, combined with local deposition in the valleys as well as Lake Constance.

10.2. Sea level

Badlands operates with a single scalar value that determines the relative position of the sea (the default relative sea level is defined at 0m, Badlands Group (2019)). Because a significant part of the Netherlands lies below this relative sea level, Badlands interprets this area as sea, unable to recognize dikes and dams. Because of the sea level rise in our simulations, and the limitation on the river reach that is evaluated, this does not pose a problem regarding this research. For studies specifically interested in low-lying coastal areas that are heavily engineered like the Rhine-Meuse delta, models that explicitly include anthopologenic management of water, sediment, and water-related engineering like dikes and dams are advised. When the influence of humans is not of interest, and scenarios in which nature runs its course are valid, Badlands is a good alternative because of its ability to include many different factors that influence landscape evolution.

10.3. Precipitation

In section 4.2.3 we mention that about 70% of the liquid precipitation is returned to the atmosphere and will not act as runoff/end up in fluvial channels. When we reduce the precipitation to account for this fact the

erosion rate as a result of a decreased discharge also decreases. The results for base precipitation (e.g., Figure 4.1) versus reduced precipitation (Figure 4.11) simulations show that the decreased precipitation might produce a discharge that is closer to present-day values, but that this discharge is not enough to reproduce the reference sediment load from a bedrock layer. It was able to produce a realistic sediment load for a topsoil layer with high (compared to the average bedrock) erodibility. This indicates a discrepancy between using realistic discharge values and erosion. Most studies using LEMs do not decrease their precipitation to account for the loss of water through evapotranspiration, and may even use an increased precipitation rate due to paleoclimate circumstances. This means that the postdicted erosion that is measured in landscape evolution models using a stream power law based fluvial bedrock incision is only realistic due to an overestimation of precipitation related discharge. This overestimation is partly countered through the fact that these models do not use a topsoil layer or soil generation through bedrock weathering, which would decrease the total erosion due to bedrock being much more difficult to erode than when including soil that would also have been present (with exception of regions with steep slopes or outcropped rock). This result agrees with Murphy et al. (2016), who state that ”incorporating the quantified relationships between local rainfall and erodibility into a commonly used river incision model is necessary to predict the rates and patterns of downcutting of these rivers. In contrast to using only precipitation-dependent river discharge to explain the climatic control of bedrock river incision, the mechanism of chemical weathering can explain strong coupling between local climate and river incision”. Another reason why a ’high’ precipitation level can still produce realistic values is that the coupling between the amount of precipitation and the amount of water that would not immediately impact the discharge and resulting erosion is implicitly included in the bedrock incision models. In other words, the fluvial incision models were designed to produce realistic outputs using precipitation levels that do not take into account losses due to evapotranspiration and infiltration.

When we use the initial precipitation map (not multiplied by 0.3) in combination with a bedrock erodibility map exclusively, we see there is almost a negligible (compared to our reference values) sediment load for the majority of the time (cf. Figure 4.7). This is likely partially due to the effect of the Upper Rhine Graben lake acting as a depositional basin for sediment from upstream and partially because in the region of the map where the sediment load will end up in the Lower Rhine, there is a low average precipitation of 0.65m/yr (compared with an average of 1m/yr of the lower half of the map, including precipitation in the Alps as high as 2.3m/yr). Without these factors, a higher sediment load is expected following the results of Salles, Ding, Webster, et al. (2018) who produced realistic sediment loads using their paleoclimatic up to modern-day precipitation rates in combination with a similar bedrock erodibility. An important difference between Salles, Ding, Webster, et al. (2018) and this work is the choice of fluvial incision model. Salles, Ding, Webster, et al. (2018) used the detachment-limited model and we used the transport-limited model. This could potentially explain some of the differences in sediment load as well. The sensitivity of these different models with respect to precipitation rates and corresponding sediment load is an area for future research.

10.4. Topsoil

In this study we have implemented land use scenarios through change of the (adjusted) topsoil erodibility (see section 4.2.2). Not only is soil in general often absent from landscape evolution models, the erosional processes are all based around bedrock. This means that the inclusion of a topsoil layer in a LEM that is not equipped for soil will result in inaccurate erosion and thus inaccurate deposition and sediment flux outputs. This is also what we have seen happen in the simulations using Badlands. Although we have calibrated the topsoil erodibility in order to produce representative sediment load values for a limited time in each simulation, the topsoil layer had to be adapted in a way that does not make physical sense. If one gets realistic results only when tweaking the inputs in a way that is not consistent with nature, one can ask what the validity is of the acquired results. Then again, every model is but an approximation of what it is trying to represent, with varying degrees of accuracy in varying spatial and temporal ranges. This also means that sometimes changing the inputs is the only way to deal with the limitations within a LEM itself. Our implementation of topsoil is one example of that, the decrease of precipitation to take into account the absence of evapotranspiration and infiltration of soil is another. As the results have shown, the sediment load values tend to be relatively stable and (the changes at least) are representative of reality for short initial time ranges. Depending on the way of implementing the precipitation change, this temporal range can vary from hundreds to some thousands of years.

This work has made it clear that evolution of landscapes is a complex problem. The addition of soil makes this even more complex. Soils and landscapes can show a complex non-linear evolution, especially when under a changing climate or land use change (Van der Meij, 2021). The understanding of the complex dynamics of the co-evolution of soils, landscapes, as well as hydrological systems is fundamental for finding ways to adapt land management in light of climate change (Van der Meij et al., 2018). As Badlands does not have built-in soil dynamics and related processes, and relies on bedrock-based fluvial incision models, it is not suited for detailed studies concerning the topsoil. For this, specialized Soil-Landscape Evolution Models (SLEMs) are necessary. A major challenge of these models, aside from the general difficulties in LEMs, is the linking of pedogenic (soil-related) and hydrological processes.

Even though Badlands does not include soil dynamics and related hydrological processes, the ability of Badlands to include vertical and horizontal tectonics, geomorphology, climatic influences, as well as the unique addition of carbonate production lends it for a more holistic approach for studying reef systems and paleoclimate-related landscape evolution. Even with the known limitations, it is important to mention that although we were not able to evaluate the sediment load with respect to land use changes over the full 10,000 years, Badlands did produce a realistic output of Western and Central European rivers and a corresponding sediment load representative of present-day values, especially early in the simulation time. The main driver for the inaccuracy in topsoil erosion are the bedrock-based incision models that are typical for any LEM. The adjustments that were made to the topsoil layer did lead to the possibility of evaluating relative changes of sediment load between realizations for a limited time range. Because of the necessity of fine-tuning of the erodibility factor with the use of observed sediment load values as a reference for the output, the uncertainty for produced sediment load increases rapidly after a certain simulation time. This time can be found through calibration of the parameters. This means results generated with Badlands could be used as a baseline for investigating general influences of climate and to a certain extent land use changes on landscape dynamics like sediment load. When applying this to land use changes on shorter time spans than thousands of years it is crucial to first adjust the topsoil erodibility and thickness to produce a realistic and verifiable sediment load for the rivers of interest. It is also advised to use smaller time steps for these simulations. This is because smaller time steps will allow Badlands to solve its governing equations at steps that are closer to eachother in time, reducing the error in averaging them when upscaling. This can decrease the frequency of the extremes (peaks and troughs) that we have seen in the results.

10.5. Results

10.5.1. The S2P2 and S3P2 Realization

In section 9.2 we have seen that the S2P2 and S3P2 realizations show strange behavior (e.g., Figures 9.3 & 9.4). The discharge in these realizations is very low compared to all other realizations, including the two realizations that are based on the same general climate (S2P1 and S3P1). The very low sediment load in these realizations is likely the direct consequence of this discharge. There was no indication of inconsistencies, major differences, or anomalies in the inputs and parameters that were used for these realizations. The values of the data sets representing the precipitation that underwent non-uniform change lie between the values for the similar data sets created for the S1 and S4 realizations. The simulations were run several times to check if it was caused by any model noise and always resulted in the same outcome. It is not clear what has caused this behavior.

10.5.2. Topsoil Erodibility and Sediment Load

We have amply discussed the weaknesses and problems concerning the implementation of topsoil erodibility together with the fluvial bedrock-incision models. There are still some behaviors regarding the sediment load outputs that are unexpected. First, the averages for the three land use erodibility maps were calculated and added to the erodibility scale (see Figure 3.4). The average K-factor for the agroforestry scenario was the lowest value, as expected. The average value for the L3 (urban greenification) was lower than that of the base land use scenario L1. The L3 erodibility map was directly based on the L1 map, where the only applied change is that the erodibility of the artificial land use is increased. This means that we should expect an average K-factor for this map that is higher than the one we get for L1. This problem was discovered too late in the process of this thesis to adapt the land use maps. When the data sets of the different maps were directly compared we did see that some values in the L3 map data had increased with respect to the L1 map, although some values were lower. This indicates the values were likely changed as the result of upscaling and interpolation of the data to make it agree with the resolution of the topography

map. The new distribution of numbers resulted in an average that is 6.8% lower than that of the L1 average. For comparison, the differences between the L1 and L3, and L2 and L3 averages, are 21.4% and 14.6%, respectively.

This does not explain the results of our simulations however. When we exclude the S2P2 and S3P2 results, all but one of the realizations give a sediment load trend for the L3 scenario that is lower than all others. This can possibly be explained by the combination of our focus on the Lower Rhine and the heavy presence of artificial land use in especially Belgium and the Ruhr industrial area. The increase of erodibility for artificial land use in this area would have had a larger impact on the amount of sediment load here than on areas with a lower artificial land use, resulting in lower sediment load values. Areas where the artificial land use is much less prominent, namely the south of our area of interest, would have potentially offset this regional difference. Because we only focused on the Lower Rhine reach, and the sediment signal that could have come from upstream was likely deposited in the Upper Rhine Graben lake, this led to a much lower sediment load than would have otherwise been the case.

The S2P2 and S3P2 realizations are likely much less affected by this effect as the low discharge was not able to erode enough to notice these differences. This explains why the sediment load trends for each land use scenario is very low compared to all other realizations, why there is a much smaller difference between each land use trend, and finally, why the vertical order of these trends does follow the logical order based on our calculated erodibility averages.

10.5.3. Discharge and Sediment Load

The last thing we will discuss in this section is the relation between discharge and the sediment load. Again, when the S2P2 and S2P3 runs are excluded, we see a clear pattern emerge. After the initial sediment load and discharge increase, we see that for all of the simulations (except the reference) a second increase in discharge coincides with the rapid decrease of the sediment load. The discharge increase in the reference simulation does not correspond to a significant change in sediment load. The S2P2 and S2P3 realizations show strange behavior compared to the other realizations that we are unable to explain. These realizations show a strong decrease in discharge coinciding with a strong decrease in sediment load. The S4P3 realization does show a decreasing discharge and decreasing sediment load, but there is a delay between the response of the discharge and the sediment load (discharge lagging behind the sediment load). The underlying cause for all these different results regarding the discharge and its relation to sediment load is unknown.

10.6. General LEM Limitations

In general there are four main causes of uncertainty regarding the use of landscape evolution models. The first uncertainty is our inability to fully describe the initial conditions of the model (Valters, 2016). An important initial condition is the topography of the area of interest. For postdictive landscape evolution modeling, the paleotopography is usually unknown and hard to reconstruct (Barnhart et al., 2020). In our case our initial topography is the present-day topography of Europe which has been mapped in 3D with modern Earth observation techniques. Even th ough this data is reliable, there are still limitations and uncertainties connected with it. One example is the possible errors that occur when different coordinate systems are translated to one general system which is needed to span large areas like our area of interest. Typical transformation errors between coordinate systems can be on the order of meters for transformations dealing with resolutions of multiple hundreds of meters (like our resolution of ca. $300\text{m} \times 300\text{m}$, Ganić et al. (2017)). When the area of interest is much larger than this, cumulative errors may result in topographical differences that influence fluvial channels. In addition to this, the creation of a TIN based on the coordinate points of this resolution can create artifacts that could act as barriers to fluvial streams as well. Although the effect of different initial conditions are acknowledged in the literature, not many studies have been done to explore and quantify the extent of this influence (Perron and Fagherazzi, 2012).

The second point is our inability to represent all of the processes that possibly govern landscape evolution (Valters, 2016). This is reflected in three ways. Firstly, many LEMs are limited to just one part of the sediment routing system, like fluvial geomorphology or coastal erosion. Secondly, LEMs that do incorporate multiple processes do so by building upon simple laws that are commonly derived from diffusion-based equations that require large resolutions (multi-kilometer scale). We have already discussed shortly in the beginning of this thesis how the Badlands framework is intended to address

these shortcomings (Badlands Group, 2019). Even though there are many processes incorporated into Badlands as it explicitly links land, marine, and reef environments together, there will always be processes that are missing or approximations made through the implementation of the governing equations or for computational efficiency (Valters, 2016). Not only is the coupling of different processes a challenge in the spatial domain, there can be significant differences in the interactions between processes and varying degrees of influence of certain processes on the landscape at different time scales (Temme et al., 2022). The third reason is the presence of processes that scale non-linearly or are dependent on (not always realistic) thresholds (e.g., shear stress threshold for erosion). In particular, Tucker (2004) and Temme et al. (2022) state that non-linearity that results from threshold effects can have an impact on topography and the dynamic response of landscapes to tectonic and climatic forcing. The coupling of non-linear scaling processes is an ongoing challenge in landscape evolution modeling (Valters, 2016).

Thirdly, uncertainty may stem from the inaccuracies in the input data, choice of the model parameters, and the initial model boundary conditions and if these boundary conditions change through time (Valters, 2016). Although the incorporation of many linked processes will (hopefully) improve the accuracy of a LEM, it also brings with it the need for more model inputs. This in turn will inevitably introduce uncertainties based on the quality and necessary pre-processing of these inputs. For this thesis, not taking into account the 'constant' model parameters, we have had to prepare a topographical map, erodibility maps, precipitation maps, vertical displacement maps, and sea level curves. All of these inputs have their own uncertainties through the way they were measured, a lack of understanding (or available data) of responsible processes and their potential evolution through time (e.g., tectonics and precipitation change), as well as the data rescaling that was necessary for their input in Badlands. Through the calibration of different inputs to ensure an accurate output (or at least maximized agreement with observed data from real landscapes), the uncertainty can be decreased (Oreskes et al., 1994; Trucano et al., 2006).

The last main source of uncertainty is our inability to know with certainty what the accuracy of the predicted outcome is (Beven, 1996; Pelletier et al., 2015). When we are interested in recreating landscapes this uncertainty is mainly the case when the resulting topography is based on a non-realistic initial state (e.g., abstract shape) or the result is a paleotopography which is hard to verify. A way to deal with this is to choose a known topography such as the present one as the expected end of the simulation. A different way to validate your LEM is to check if the resolution is fine enough to accurately portray the geologic processes that are expected to occur (Valters, 2016). It is important to realize however, that model validation does not necessarily establish the accuracy or truth of your model predictions but says something about the internal consistency of your software (Oreskes et al., 1994). Salles, Ding, Webster, et al. (2018) have evaluated the accuracy of Badlands by using it to evaluate the formation of the Great Barrier Reef, and successfully cross-referencing lithographic and carbonate production output to existing data. This is a validation for Badlands' accuracy of erosional and depositional processes, and carbonate production. Because we have used Badlands to predict future changes of sediment flux, we lack the validation data for both the future topography, future climate, and sediment load data. For this reason the closest we could get to validation of our results is to run the simulation for the present-day and compare the discharge and sediment load outputs to observed data. Badlands was able to reproduce the majority of both major and minor rivers in the area of interest, with both a representative discharge and sediment load within a reasonable margin after calibration of the inputs. Because of the inherently high level of uncertainty that comes with prediction of the future, a scenario-based approach was taken similar to the approach described in the IPCC reports (Arias et al., 2021; Seneviratne et al., 2021; Ylla Arbos et al., 2021). In addition to this, the resolution that is used is fine enough for all geologic or geomorphic processes that were expected to play a role.

11

Conclusion

In order to maintain an overview we will repeat each research question that was introduced in the beginning of this thesis followed by an answer.

RQ1: What is the impact of long-term climate change and anthropogenic land use on the sediment flux of the Rhine?

Based on the results from this study, any implementation of more sustainable land use like agroforestry and the greenification of cities is predicted to decrease the sediment load of the Rhine. This agrees with the findings of Asselman et al. (2003) and Middelkoop and Asselman (2008). The more extreme the climate conditions, the larger the effect is likely to become. When there is no change to the land use, the increase in precipitation in the northern area of Europe will likely lead to more sediment load in natural river systems. The predicted decrease in precipitation in southern Europe will likely decrease the sediment load that is coming from the Alps and Upper Rhine. The direct and likely significant long-term impact of humans on both the hydrological and sedimentological aspects of fluvial systems are subjects for further research.

RQ2: Can the current path and metrics of the Rhine be predicted by the process based landscape evolution model Badlands?

The proof of concept simulations show that Badlands is able to reproduce all the major rivers in Western and Central Europe, with some small differences that are explained by natural variation and non-linear behavior of fluvial processes, as well as the topography not being an exact copy of reality. When the erodibility factor of topsoil is calibrated correctly, it is possible to approximately reproduce the sediment flux of the Lower Rhine to the correct order of magnitude. The difference between the base simulation sediment load and the sediment flux measurement at the Dutch-German border at the first time step is 12% ($0.05m^3/s$ vs $0.044m^3/s$). It is important to remember the Badlands output value does not include anthropogenic sediment management and removal from the rivers.

RQ3: Is Badlands suitable to be used for research regarding (future) anthropogenic land use change?

Anthropogenic land use change has to be implemented in Badlands through the erodibility factor. Specifically the erodibility factor of the topsoil. As we have discussed in this work, Badlands does not incorporate topsoil dynamics and other topsoil related factors like vegetation and infiltration, and uses fluvial incision models that are designed for bedrock incision. We have worked around this by decreasing the erodibility factor of the topsoil to something more alike to bedrock and decreased the precipitation to account for the lack of evapotranspiration and infiltration, but this is not an optimal solution. For these reasons, when research necessitates specific modeling of soils and human influence on soil erodibility, a specialized Soil-Landscape Evolution Model is preferred (see Van der Meij et al. (2023) for example). In particular, SLEMs do not rely only on bedrock incision/erosion models, but use other methods to more accurately describe the soil-based erosion due to surface runoff (e.g., shear stress based). That said, we were able to produce a realistic sediment load for the Lower Rhine for different land use scenarios. Under the right

conditions described in section 10 there is potential for Badlands to be used to evaluate the effect of (anthropogenic) land use on sediment load for short-term high-resolution predictions.

RQ4: Will either climate change scenarios or (anthropogenic) land use change have a dominant effect on the sediment flux in the Rhine source-to-sink system on a 10kyr scale?

There is no straightforward answer to this question as the dominance of an effect depends on many factors, and a detailed sensitivity analysis on the effect of land use change as well as the effect of different representations of climate change in our models is needed to fully answer this question. The differences in sediment load between land use scenarios are greater when we compare them between the different types of precipitation change averaging (P1 vs P2), than when we compare them between climate scenarios with the same type of precipitation change (e.g., S1P1 vs S4P1). This indicates that the way we implement the climatic forcings is of greater importance than the differences in land use scenario, or even the climate forcing itself (at least in our model). Furthermore, we argue that the non-uniform precipitation change is a more accurate representation of possible climate change as it takes into account regional effects. When we look at the differences in sediment load between different land use scenarios we see that the severity of the effect depends on the land use scenario in particular. For the agroforestry scenario the non-uniform precipitation causes relatively large differences between different climate circumstances. The differences are smaller for the changes applied to artificial land use.

RQ5: Is there a significant difference in the predicted sediment flux in the simulated rivers between using either a uniform precipitation, or non-uniform precipitation change over the simulated period?

The average difference between the sediment load produced using uniform precipitation and non-uniform precipitation when compared to the reference simulation is 9.75%pt. This is the average calculated using the outputs from the S1 and S4 realizations only. The S2 and S3 realization were excluded here on the basis of their unexpected and extreme behavior in the non-uniform precipitation simulations. When we also take into account the S2 and S3 realizations this average difference increases to 38%pt. It is safe to conclude that there is a significant difference in the predicted sediment flux in the simulated river between using either a uniform precipitation, or non-uniform precipitation change over the simulated period with respect to the reference output. For most cases (S1, S2, and S3) the distribution of the sediment load produced using the different precipitation changes are also significantly different. This is corroborated by the Kolmogorov–Smirnov test results given in Appendix F. In case of the S4 outputs, the statistical test results show that the distribution of the resulting outputs when comparing the precipitation changes are not significantly different. This does not mean there is no difference between them. For these, the mean difference in sediment load between the uniform and non-uniform precipitation are 3%, 11%, 1.8% for the L1, L2, and L3 cases respectively. From these results we conclude that a regional precipitation change is preferred over a uniformly averaged change, if the predicted regional changes over a certain area do not follow the same trend (i.e., a part of the map is predicted to see an increase in precipitation and another part will see a decrease). In this case the averaged uniform change will see a decrease in reliability due to an increasing loss in accuracy as the regional differences grow.

RQ6: How would the greenification of urban areas or reallocation of agricultural lands in Western and Central Europe influence the sediment flux in the different climate scenarios? And in addition, how does this influence the sediment flux in the downstream area of the Rhine-Meuse delta located in the Netherlands?

Even with an average erodibility factor that is closer to the average K-factor of the L1 scenario than to the L2 scenario, the greenification of urban areas scenario (L3) shows a strong decrease of sediment load with respect to the reference simulation. The only exception (the result for the S2P1L3 realization) showed

a strong increase of sediment load with respect to the reference. Given the circumstances that have led to these L3 results as discussed in section 10, this result is to be taken with a grain of salt.

The results of all simulations agree that the substantial transition of agricultural lands to agroforestry would result in a net decrease of sediment load, even in the most extreme climatic scenarios that are tested. When we take into account that Badlands does not include vegetation (neither roots binding the soil nor leaves providing cover) the results are likely conservative indications, as these factors would decrease soil erosion and thus lowering the sediment load even more.

The sediment flux in the Rhine-Meuse delta area could not directly be evaluated due to the sea level rise in each scenario. When we look at the sediment load in the Lower Rhine at the location where the delta begins near the Dutch-German border, it is above the average values found throughout the simulations, and in the beginning very close to the observed values of today. The fact that at this location in the river the sediment load is almost always highest is not surprising given that Badlands does not take into account anthropogenic sediment removal from upstream of the Rhine. This means that the majority of sediments that are transported will end up in the downstream delta area given no sea level rise, and assuming 70% of the water does not reach fluvial channels.

Concluding Remarks

Although Badlands is not perfectly suited for research regarding anthropogenic influences, specifically those that require the implementation of a topsoil, we have nevertheless succeeded in answering our research questions to different degrees of satisfaction. Where this answer was not complete or demands further research, we have been able to identify the reasons why this is the case and have recommended alternative ways to improve upon this work (see section 12). Through this study we have identified the strengths and weaknesses of Badlands. It has shown its impressive versatility and adaptability, and shows potential to be used for the growing demand of studies that focus on predicting future influences of different processes in light of climate change using a holistic process-based approach.

12

Recommendations

Here we provide a brief overview of the primary recommendations for future research that follow up or are a continuation on this thesis.

For landscape evolution modeling of future landscapes on a smaller than geological time scale (i.e., smaller than 10,000s of years) with an interest in looking at sediment flux, the topsoil layer will play an increasingly important role as the time of interest closes in to present day, when the assumption of working only with bedrock is not accurate anymore. This is especially the case when land use is the research subject. As most LEMs use a version of the stream power law to simulate fluvial incision, this limits their applicability and potential accuracy for this area of research. For simple process-based modeling with the intention to solidify our understanding of general concepts and test certain parameter dependencies, general LEMs such as Badlands are a possibility, given that the parameters and inputs are calibrated and simulation time is restricted to sub-geologic scales (i.e., hundreds of years). For detailed studies on the climatic and anthropogenic effects on future sediment load in fluvial systems a more specialized Soil-Landscape Evolution Model or other similar soil-inclusive models are necessary.

When interpreting present day or future landscapes in regions that contain areas that are low compared to their surroundings, or contain coastlines that are below the value that is used as a reference point for initial sea level, Badlands will interpret these areas as a lake or sea (e.g. Upper Rhine Graben and the Dutch/Belgian shore in this work, respectively). The main reasons this could interfere with a potential research subject is when the topography/hydrology of these areas in particular is of interest (so that an artificial elevation of land or decrease in sea level is not possible/desired), or the subject of research is the impact of humans on these areas. For this reason, for future work with Badlands the reasoning behind the interpretation of certain areas as lakes needs to be investigated and documented. This way this issue can either be avoided by carefully selecting the areas of research, or the future improvement of the software itself can be a topic for future work.

As already mentioned in the conclusion, a detailed sensitivity analysis on the effect of different representations of climate change, and in particular precipitation, in our models is needed to improve our understanding of the impact of our modeling choices and in what situation different implementations of climate parameters are warranted. In addition to this the direct and likely significant long-term impact of humans on both the hydrological and sedimentological aspects of fluvial systems, as well as how our land use impacts both of these aspects are subjects for further research.

References

Abratis, M., Viereck, L., Büchner, J., & Tietz, O. (2015). Route to the volcanoes in germany – conceptual model for a geotourism project interconnecting geosites of cenozoic volcanism. *Zeitschrift der Deutschen Gesellschaft für Geowissenschaften*, *166*. https://doi.org/10.1127/zdgg/2015/0035

Alves, M. A. B., de Souza, A. P., de Almeida, F. T., Hoshide, A. K., Araújo, H. B., da Silva, A. F., & de Carvalho, D. F. (2023). Effects of land use and cropping on soil erosion in agricultural frontier areas in the cerrado-amazon ecotone, brazil, using a rainfall simulator experiment. *Sustainability*, *15*(6). https://doi.org/10.3390/su15064954

Amantov, A., & Fjeldskaar, W. (2016). Ice age and coastal adaptations. https://doi.org/10.21610/conferencearticle_58b43153b7e56

Andrade, C. (2019). The p value and statistical significance: Misunderstandings, explanations, challenges, and alternatives. *Indian Journal of Psychological Medicine*, *41*, 210. https://doi.org/10.4103/IJPSYM.IJPSYM_193_19

Andrews, D. J., & Bucknam, R. B. (1987). Fitting degradation of shoreline scarps by a nonlinear diffusion model. *Journal of Geophysical Research: Solid Earth*, *92*(B12), 12857–12867. https://doi.org/10.1029/JB092iB12p12857

Appel, B. (2005). *Outcropping beds of White Jurassic limestone at the edge of the landslide at Hirschkopf near Mössingen*. Retrieved May 25, 2024, from https://en.wikipedia.org/wiki/Geology_of_Germany#/media/File:Moessingen-Rutschung-Detail.jpg

Aram, F., Higueras Garcia, E., Solgi, E., & Mansournia, S. (2019). Urban green space cooling effect in cities. *Heliyon*, *5*, 1339. https://doi.org/10.1016/j.heliyon.2019.e01339

Archer, D. F., & Brovkin, V. (2008). The millennial atmospheric lifetime of anthropogenic co2. *Climatic Change*, *90*, 283–297. https://doi.org/10.1007/s10584-008-9413-1

Archer, D. F., Eby, M., Brovkin, V., Ridgwell, A., Cao, L., Mikolajewicz, U., Caldeira, K., Matsumoto, K., Munhoven, G., Montenegro, A., & Tokos, K. (2009). Atmospheric lifetime of fossil fuel carbon dioxide. *Annual Review of Earth and Planetary Sciences*, *37*(1), 117–134. https://doi.org/10.1146/annurev.earth.031208.100206

Arias, P. A., Bellouin, N., Coppola, E., Jones, R. G., Krinner, G., Marotzke, J., Naik, V., Palmer, M. D., Plattner, G.-K., Rogelj, J., Rojas, M., Sillmann, J., Storelvmo, T., Thorne, P. W., Trewin, B., Achuta Rao, K., Adhikary, B., Allan, R. P., Armour, K., … Zickfeld, K. (2021). Technical summary. In V. Masson-Delmotte, P. Zhai, A. Pirani, S. L. Connors, C. Péan, S. Berger, N. Caud, Y. Chen, L. Goldfarb, M. I. Gomis, M. Huang, K. Leitzell, E. Lonnoy, J. B. R. Matthews, T. K. Maycock, T. Waterfield, O. Yelekçi, R. Yu, & B. Zhou (Eds.), *Climate change 2021: The physical science basis. contribution of working group i to the sixth assessment report of the intergovernmental panel on climate change* (33−144). Cambridge University Press. https://doi.org/10.1017/9781009157896.002

Arnold, J. G., Srinivasan, R., Muttiah, R. S., & Williams, J. R. (1998). Large area hydrologic modeling and assessment part i: Model development. *JAWRA Journal of the American Water Resources Association*, *34*(1), 73–89. https://doi.org/10.1111/j.1752-1688.1998.tb05961.x

ArtMechanic. (2002). *Sandstone layers of Triassic age in Thuringia*. Retrieved May 25, 2024, from https://en.wikipedia.org/wiki/Geology_of_Germany#/media/File:Stadtroda_Sandstein.jpg

Arunrat, N., Sereenonchai, S., Kongsurakan, P., & Hatano, R. (2022). Soil organic carbon and soil erodibility response to various land-use changes in northern thailand. *CATENA*, *219*, 106595. https://doi.org/10.1016/j.catena.2022.106595

Asselman, N. E. M., Middelkoop, H., & Van Dijk, P. M. (2003). The impact of changes in climate and land use on soil erosion, transport and deposition of suspended sediment in the river rhine. *Hydrological Processes*, *17*(16), 3225–3244. https://doi.org/10.1002/hyp.1384

Badlands Group. (2019). *Getting started with badlands* (Revision bdd519ce.). University of Sydney. https://badlands.readthedocs.io/en/latest/index.html

Baker, V. R. (n.d.). Valley - hillslopes. In T. E. of Encyclopædia Britannica (Ed.), *Encyclopaedia britannica*. https://www.britannica.com/science/valley/Valley-cross-profiles

Barletta, V., Ferrari, C., Diolaiuti, G., Carnielli, T., Sabadini, R., & Smiraglia, C. (2006). Glacier shrinkage and modeled uplift of the alps. *Geophysical Research Letters*, *33*(14). https://doi.org/10.1029/2006GL026490

Barnhart, K. R., Tucker, G. E., Doty, S. G., Shobe, C. M., Glade, R. C., Rossi, M. W., & Hill, M. C. (2020). Inverting topography for landscape evolution model process representation: 3. determining parameter ranges for select mature geomorphic transport laws and connecting changes in fluvial erodibility to changes in climate. *Journal of Geophysical Research: Earth Surface*, *125*(7), e2019JF005287. https://doi.org/10.1029/2019JF005287

Barrett, S., & Webster, J. M. (2017). Reef sedimentary accretion model (reefsam): Understanding coral reef evolution on holocene time scales using 3d stratigraphic forward modelling. *Marine Geology*, *391*, 108–126. https://doi.org/10.1016/j.margeo.2017.07.007

Barton, J., & Rogerson, M. (2017). The importance of greenspace for mental health. *BJPsych. International*, *14*(4), 79–81. https://doi.org/10.1192/S2056474000002051

Beck, H., Zimmermann, N. E., McVicar, T., Vergopolan, N., Berg, A., & Wood, E. (2018). Present and future köppen-geiger climate classification maps at 1-km resolution. *Scientific Data*, *5*, 180214. https://doi.org/10.1038/sdata.2018.214

Ben-Asher, M., Haviv, I., Crouvi, O., Roering, J. J., & Matmon, A. (2021). The convexity of carbonate hilltops: 36Cl constraints on denudation and chemical weathering rates and implications for hillslope curvature. *GSA Bulletin*, *133*(9-10), 1930–1946. https://doi.org/10.1130/B35658.1

Benjaram, S. S., Dixon, J. L., & Wilcox, A. C. (2022). Capturing the complexity of soil evolution: Heterogeneities in rock cover and chemical weathering in montana's rocky mountains. *Geomorphology*, *404*, 108186. https://doi.org/10.1016/j.geomorph.2022.108186

Beven, K. (1996). Equifinality and uncertainty in geomorphological modelling. *The scientific nature of geomorphology.*, *Proceeding of the 27th Binghamton Symposium in Geomorphology held 27-29 September 1996*, 289–314.

BGR. (2005). The 1:5 million international geological map of europe and adjacent areas (IDME5000) (WMS) [Identifier: 7A4A2412-0B32-4FF1-86B0-A565EDDD5EF2, IGME5000, ©BGR Hannover, 2007]. https://data.geus.dk/egdi/?mapname=egdi_new_structure#baslay=baseMapGEUS&extent=2655029.9107148796,1560592.0693338318,4804126.841282579,3575090.0272146193&layers=igme5000

Blauwwind's offshore wind farm successful breeding ground for flat oysters. (2024). Retrieved February 16, 2024, from https://www.derijkenoordzee.nl/en/news/blauwwinds-offshore-wind-farm-successful-breeding-ground-for-flat-oysters

Bombino, G., Denisi, P., Gómez, J. A., & Zema, D. A. (2019). Water infiltration and surface runoff in steep clayey soils of olive groves under different management practices. *Water*, *11*(2). https://doi.org/10.3390/w11020240

Borrelli, P., Robinson, D., Fleischer, L., Lugato, E., Ballabio, C., Alewell, C., Meusburger, K., Modugno, S., Schütt, B., Ferro, V., Bagarello, V., Oost, K., Montanarella, L., & Panagos, P. (2017). An assessment of the global impact of 21st century land use change on soil erosion. *Nature Communications*, *8*. https://doi.org/10.1038/s41467-017-02142-7

Borrelli, P., Alewell, C., Alvarez, P., Anache, J. A. A., Baartman, J., Ballabio, C., Bezak, N., Biddoccu, M., Cerdà, A., Chalise, D., Chen, S., Chen, W., De Girolamo, A. M., Gessesse, G. D., Deumlich, D.,

Diodato, N., Efthimiou, N., Erpul, G., Fiener, P., … Panagos, P. (2021). Soil erosion modelling: A global review and statistical analysis. *Science of The Total Environment*, *780*, 146494. https://doi.org/10.1016/j.scitotenv.2021.146494

Bosboom, J., & Stive, M. J. F. (2021). *Coastal dynamics* (3rd ed.). Delft University of Technology.

Brand, E., Ramaekers, G., & Lodder, Q. (2022). Dutch experience with sand nourishments for dynamic coastline conservation – an operational overview. *Ocean & Coastal Management*, *217*, 106008. https://doi.org/10.1016/j.ocecoaman.2021.106008

Braun, J., & Sambridge, M. (1997). Modelling landscape evolution on geological time scales: A new method based on irregular spatial discretization. *Basin Research*, *9*(1), 27–52. https://doi.org/10.1046/j.1365-2117.1997.00030.x

Braun, J., & Willett, S. D. (2013). A very efficient o(n), implicit and parallel method to solve the stream power equation governing fluvial incision and landscape evolution. *Geomorphology*, *180-181*, 170–179. https://doi.org/10.1016/j.geomorph.2012.10.008

Braun, J. (2010). The many surface expressions of mantle dynamics. *Nature Geoscience*, *3*(12), 825–833.

Brockmann, E., Ineichen, D., Marti, U., Schaer, S., Schlatter, A., & Villiger, A. (2012). Determination of tectonic movements in the swiss alps using gnss and levelling. *International Association of Geodesy Symposia*, *136*, 689–695. https://doi.org/10.1007/978-3-642-20338-1_85

Bryan, K., Komro, F. G., Manabe, S., & Spelman, M. J. (1982). Transient climate response to increasing atmospheric carbon dioxide. *Science*, *215*(4528), 56–58. https://doi.org/10.1126/science.215.4528.56

Bucheli, V. P., & Bokelmann, W. (2017). Agroforestry systems for biodiversity and ecosystem services: The case of the sibundoy valley in the colombian province of putumayo. *International Journal of Biodiversity Science, Ecosystem Services & Management*, *13*(1), 380–397. https://doi.org/10.1080/21513732.2017.1391879

Buitink, J., Melsen, L. A., & Teuling, A. J. (2021). Seasonal discharge response to temperature-driven changes in evaporation and snow processes in the rhine basin. *Earth System Dynamics*, *12*(2), 387–400. https://doi.org/10.5194/esd-12-387-2021

Candela, T., Koster, K., Stafleu, J., Visser, W., & Fokker, P. (2020). Towards regionally forecasting shallow subsidence in the netherlands. *Proceedings of the International Association of Hydrological Sciences*, *382*, 427–431. https://doi.org/10.5194/piahs-382-427-2020

CBS. (2023). *Bevolking op 1 januari en gemiddeld; geslacht, leeftijd en regio*. Retrieved March 15, 2024, from https://opendata.cbs.nl/statline/#/CBS/nl/dataset/03759ned/table?dl=DA8F

Chaigneau, A., Law-Chune, S., Melet, A., Voldoire, A., Reffray, G., & Aouf, L. (2023). Impact of sea level changes on future wave conditions along the coasts of western Europe. *Ocean Science*, *19*(4), 1123–1143. https://doi.org/10.5194/os-19-1123-2023

Champagnac, J.-D., Schlunegger, F., Norton, K., von Blanckenburg, F., Abbühl, L., & Schwab, M. (2009). Erosion-driven uplift of the modern central alps [TOPO-EUROPE: The Geoscience of coupled Deep Earth-surface processes]. *Tectonophysics*, *474*(1), 236–249. https://doi.org/10.1016/j.tecto.2009.02.024

CHR. (2015). *Length of the rhine (update 2015)*. Retrieved February 21, 2024, from https://www.chr-khr.org/en/news/length-rhine-update-2015

CHR. (n.d.). *The Runoff Regime of the River Rhine and its Tributaries in the 20th Century Analysis, Changes, Trends*. Retrieved April 12, 2024, from https://www.chr-khr.org/sites/default/files/extended_abstract_i_22_e.pdf

Clark, P. U., Shakun, J. D., Marcott, S. A., Mix, A. C., Eby, M., Kulp, S., Levermann, A., Milne, G. A., Pfister, P. L., Santer, B. D., et al. (2016). Consequences of twenty-first-century policy for multi-millennial climate and sea-level change. *Nature Climate Change*, *6*(4), 360–369. https://doi.org/10.1038/nclimate2923

Clark, P. U., Dyke, A. S., Shakun, J. D., Carlson, A. E., Clark, J., Wohlfarth, B., Mitrovica, J. X., Hostetler, S. W., & McCabe, A. M. (2009). The last glacial maximum. *Science*, *325*(5941), 710–714. https://doi.org/10.1126/science.1172873

Collins, M., Knutti, R., Arblaster, J., Dufresne, J.-L., Fichefet, T., Friedlingstein, P., Gao, X., Gutowski, W. J., Johns, T., Krinner, G., Shongwe, M., Tebaldi, C., Weaver, A. J., Wehner, M. F., Allen, M. R., Andrews, T., Beyerle, U., Bitz, C. M., Bony, S., & Booth, B. B. B. (2013). Long-term climate change: Projections, commitments and irreversibility. In T. F. Stocker, D. Qin, G. Plattner, M. M. B. Tignor, S. K. Allen, J. Boschung, A. Nauels, Y. Xia, V. Bex, & P. M. Midgley (Eds.), *Climate change 2013 - the physical science basis* (pp. 1029–1136). Cambridge University Press.

Common Wadden Sea Secretariat. (n.d.). *Taking shape*. Retrieved February 24, 2024, from https://www.waddensea-worldheritage.org/taking-shape

Copernicus Land Monitoring Service (CLMS). (2020). *Corine land cover 2018 (raster 100 m), europe, 6-yearly - version 2020_20u1*. https://doi.org/10.2909/960998c1-1870-4e82-8051-6485205ebbac

Copernicus Land Monitoring Service (CLMS). (2021). *European ground motion service: Copernicus sentinel data [2021], europe*. Retrieved March 3, 2024, from https://egms.land.copernicus.eu/

Cornes, R. C., Van der Schrier, G., Van den Besselaar, E. J. M., & Jones, P. D. (2018). An ensemble version of the e-obs temperature and precipitation data sets. *Journal of Geophysical Research: Atmospheres*, *123*(17), 9391–9409. https://doi.org/10.1029/2017JD028200

Coulthard, T. J., Neal, J. C., Bates, P. D., Ramirez, J., de Almeida, G. A. M., & Hancock, G. R. (2013). Integrating the lisflood-fp 2d hydrodynamic model with the caesar model: Implications for modelling landscape evolution. *Earth Surface Processes and Landforms*, *38*(15), 1897–1906. https://doi.org/10.1002/esp.3478

Courant, R., Friedrichs, K., & Lewy, H. (1967). On the partial difference equations of mathematical physics. *IBM journal of Research and Development*, *11*(2), 215–234.

Cox, J. R., Dunn, F., Nienhuis, J., Van der Perk, M., & Kleinhans, M. (2021). Climate change and human influences on sediment fluxes and the sediment budget of an urban delta: The example of the lower rhine—meuse delta distributary network. *Anthropocene Coasts*, *4*, 251–280. https://api.semanticscholar.org/CorpusID:244925793

Cox, J. R., Huismans, Y., Knaake, S. M., Leuven, J. R. F. W., Vellinga, N. E., Van der Vegt, M., Hoitink, A. J. F., & Kleinhans, M. G. (2021). Anthropogenic effects on the contemporary sediment budget of the lower rhine-meuse delta channel network [e2020EF001869 2020EF001869]. *Earth's Future*, *9*(7), e2020EF001869. https://doi.org/10.1029/2020EF001869

Cox, N. J. (1980). On the relationship between bedrock lowering and regolith thickness. *Earth Surface Processes*, *5*(3), 271–274.

Crosby, B. T., Whipple, K. X., Gasparini, N. M., & Wobus, C. W. (2007). Formation of fluvial hanging valleys: Theory and simulation. *Journal of Geophysical Research: Earth Surface*, *112*(F3). https://doi.org/10.1029/2006JF000566

Crutzen, P. (2002). Geology of mankind. *Nature*, *415*, 23. https://doi.org/10.1038/415023a

Dangendorf, S., Marcos, M., Müller, A., Zorita, E., Riva, R., Berk, K., & Jensen, J. (2015). Detecting anthropogenic footprints in sea level rise. *Nature communications*, *6*(1), 7849.

de Almeida, W. S., Seitz, S., de Oliveira, L. C., & de Carvalho, D. (2021). Duration and intensity of rainfall events with the same erosivity change sediment yield and runoff rates. *International Soil and Water Conservation Research*, *9*(1), 69–75.

de Almeida, W. S., Panachuki, E., de Oliveira, P. T. S., da Silva Menezes, R., Sobrinho, T. A., & de Carvalho, D. F. (2018). Effect of soil tillage and vegetal cover on soil water infiltration. *Soil and Tillage Research*, *175*, 130–138.

De Glopper, R. J. (1967). *Over de bodemgesteldheid van het waddengebied*. Tjeenk Willink.

de Jalón, S. G., Graves, A., Palma, J., Crous-Duran, J., Giannitsopoulos, M., & Burgess, P. (2017). *Modelling the economics of agroforestry at field- and farm-scale* (tech. rep. No. AGFORWARD 613520) (Deliverable 6: Field- and farm-scale evaluation of innovations). European Commission.

De Roo, M. (2011). *The symbiotic city: Nature-positive urban futures* (M. Long, Ed.) [ISBN: 978-94-91127-00-7 NUR 100.]. Zwaan Printmedia.

Delaunay, B., Vide, S., Lamémoire, A., & De Georges, V. (1934). Bulletin de l'academie des sciences de l'urss. *Classe des sciences mathématiques et naturelles*, *6*, 793–800.

Delta Alliance. (n.d.). *Rhine-meuse delta*. Retrieved February 24, 2024, from http://www.delta-alliance.org/deltas/rhine-meuse-delta

de Rigo, D., Houston Durrant, T., Caudullo, G., & Barredo, J. (2016). European forests: An ecological overview. In J. San-Miguel-Ayanz, D. de Rigo, G. Caudullo, T. Houston Durrant, & A. Mauri (Eds.), *European atlas of forest tree species* (e01e873+). Off. EU, Luxembourg.

Descy, J.-P. (2009). Chapter 5 - continental atlantic rivers. In K. Tockner, U. Uehlinger, & C. T. Robinson (Eds.), *Rivers of europe* (pp. 151–198). Academic Press. https://doi.org/10.1016/B978-0-12-369449-2.00005-9

DGJ. (1926). *Deutsches gewässerkundliches jahrbuch 1926: Rheingebiet teil i–iii*. Bundesanstalt für Gewässerkunde.

DiBiase, R. A., Whipple, K. X., Heimsath, A. M., & Ouimet, W. B. (2010). Landscape form and millennial erosion rates in the san gabriel mountains, ca. *Earth and Planetary Science Letters*, *289*(1), 134–144. https://doi.org/10.1016/j.epsl.2009.10.036

Dietrich, W. E., Reiss, R., Hsu, M.-L., & Montgomery, D. R. (1995). A process-based model for colluvial soil depth and shallow landsliding using digital elevation data. *Hydrological Processes*, *9*(3-4), 383–400. https://doi.org/10.1002/hyp.3360090311

Dillingh, D., & Stolk, A. (1989). *A short review of the dutch coast: Dutch contribution to the report of the project corine 'coastal erosion' of the commission of the european communities*. Rijkswaterstaat, Dienst Getijdewateren. https://books.google.nl/books?id=2oSB0AEACAAJ

Ding, X., Salles, T., Flament, N., & Rey, P. (2019). Quantitative stratigraphic analysis in a source-to-sink numerical framework. *Geoscientific Model Development*, *12*(6), 2571–2585. https://doi.org/10.5194/gmd-12-2571-2019

Drevon, D., Fursa, S. R., & Malcolm, A. L. (2017). Intercoder reliability and validity of webplotdigitizer in extracting graphed data [PMID: 27760807]. *Behavior Modification*, *41*(2), 323–339. https://doi.org/10.1177/0145445516673998

Duffy, C., Toth, G., Hagan, R., McKeown, P., Rahman, S., Widyaningsih, Y., Sunderland, T., & Spillane, C. (2021). Agroforestry contributions to smallholder farmer food security in indonesia. *Agroforestry Systems*, *95*. https://doi.org/10.1007/s10457-021-00632-8

Dunn, A. (2010). Grid-induced biases in connectivity metric implementations that use regular grids. *Ecography*, *33*(3), 627–631. Retrieved February 19, 2024, from http://www.jstor.org/stable/20751611

Eby, M., Zickfeld, K., Montenegro, A., Archer, D., Meissner, K. J., & Weaver, A. J. (2009). Lifetime of anthropogenic climate change: Millennial time scales of potential co2 and surface temperature perturbations. *Journal of Climate*, *22*(10), 2501–2511. https://doi.org/10.1175/2008JCLI2554.1

Ericson, J. P., Vörösmarty, C. J., Dingman, S. L., Ward, L., & Meybeck, M. (2006). Effective sea-level rise and deltas: Causes of change and human dimension implications. *Global and Planetary Change*, *50*(1), 63–82. https://doi.org/10.1016/j.gloplacha.2005.07.004

Europe topographic map [Data source: https://tessadem.com/.]. (n.d.). Retrieved February 9, 2024, from https://en-gb.topographic-map.com/map-cvtgt/Europe/?center=45.52174%2C9.05273&base=4&lock=6%2C-6%2C4155&zoom=5

European Environment Agency. (2024). *Global and european sea level rise*. Retrieved February 7, 2024, from https://www.eea.europa.eu/en/analysis/indicators/global-and-european-sea-level-rise

European Environment Agency. (2023). *Land use*. Retrieved February 26, 2024, from https://www.eea.europa.eu/en/topics/in-depth/land-use?size=n_10_n&filters%5B0%5D%5Bfield%5D=readingTime&filters%5B0%5D%5Btype%5D=any&filters%5B0%5D%5Bvalues%5D%5B0%5D%5Bname%5D=All&filters%5B0%5D%5Bvalues%5D%5B0%5D%5BrangeType%5D=fixed&filters%5B1%5D%5Bfield%5D=issued.date&filters%5B1%5D%5Btype%5D=any&filters%5B1%5D%5Bvalues%5D%5B0%5D=Last%205%20years&filters%5B2%5D%5Bfield%5D=language&filters%5B2%5D%5Btype%5D=any&filters%5B2%5D%5Bvalues%5D%5B0%5D=en

European Environment Agency. (2021). *Wet and dry — mean precipitation*. Retrieved February 13, 2024, from https://www.eea.europa.eu/publications/europes-changing-climate-hazards-1/wet-and-dry-1/wet-and-dry-mean-precipitation

European Marine Observation and Data Network (EMODnet). (n.d.). *Emodnet map viewer*. Retrieved February 19, 2024, from https://emodnet.ec.europa.eu/geoviewer/

European MSP Platform. (n.d.). *North sea*. Retrieved February 23, 2024, from https://maritime-spatial-planning.ec.europa.eu/sea-basins/north-sea

European Sediment Network. (n.d.-a). *Moving sediment management forward: River basin case studies - the meuse* [Prepared for “Moving Sediment Management Forward – The Four SedNet Messages”, see www.sednet.org]. Retrieved February 8, 2024, from https://sednet.org/

European Sediment Network. (n.d.-b). *Moving sediment management forward: River basin case studies - the rhine* [Prepared for “Moving Sediment Management Forward – The Four SedNet Messages”, see www.sednet.org]. Retrieved February 8, 2024, from https://sednet.org/

Eurostat. (2023). *Population projections in the eu*. Retrieved February 29, 2024, from https://ec.europa.eu/eurostat/statistics-explained/index.php?oldid=497115#Population_projections

Fan, Y., Li, H., & Miguez-Macho, G. (2013). Global patterns of groundwater table depth. *Science*, *339*(6122), 940–943. https://doi.org/10.1126/science.1229881

FAO. (2015). *Agroforestry - definition* [Last updated on Oct 23, 2015]. Retrieved February 27, 2024, from https://www.fao.org/forestry-fao/agroforestry/en/

FAO. (2020). *Global forest resources assessment 2020 - terms and definitions* (tech. rep.). Food and Agriculture Organization of the United States (FAO). FAO Forestry Department, Rome, IT. www.fao.org/forestry/fra

Ferré, T. A., & Warrick, A. (2005). Infiltration. In D. Hillel (Ed.), *Encyclopedia of soils in the environment* (pp. 254–260). Elsevier. https://doi.org/10.1016/B0-12-348530-4/00382-9

Fokker, P. A., Van Leijen, F. J., Orlic, B., Van der Marel, H., & Hanssen, R. (2018). Subsidence in the dutch wadden sea. *Netherlands Journal of Geosciences*, *97*(3), 129–181. https://doi.org/10.1017/njg.2018.9

Foster, G. R., Mccool, D. K., Renard, K. G., & Moldenhauer, W. C. (1981). Conversion of the universal soil loss equation to si metric units. *Journal of Soil and Water Conservation*, *36*(6), 355–359. https://api.semanticscholar.org/CorpusID:129296083

Foufoula-Georgiou, E., Ganti, V., & Dietrich, W. E. (2010). A nonlocal theory of sediment transport on hillslopes. *Journal of Geophysical Research: Earth Surface*, *115*(F2). https://doi.org/10.1029/2009JF001280

Fox-Kemper, B., Hewitt, H. T., Xiao, C., Aðalgeirsdóttir, G., Drijfhout, S. S., Edwards, T. L., Golledge, N. R., Hemer, M., Kopp, R. E., Krinner, G., Mix, A., Notz, D., Nowicki, S., Nurhati, I. S., Ruiz, L., Sallée, J.-B., Slangen, A. B. A., & Yu, Y. (2021). Ocean, cryosphere and sea level change. In V. Masson-Delmotte, P. Zhai, A. Pirani, S. L. Connors, C. Péan, S. Berger, N. Caud, Y. Chen, L. Goldfarb, M. I. Gomis, M. Huang, K. Leitzell, E. Lonnoy, J. B. R. Matthews, T. K. Maycock, T. Waterfield, O. Yelekçi, R. Yu, & B. Zhou (Eds.), *Climate change 2021: The physical science basis. contribution of working group i to the sixth assessment report of the intergovernmental panel on climate change* (pp. 1211–1362). Cambridge University Press. https://doi.org/10.1017/9781009157896.011

Frings, R., Döring, R., Beckhausen, C., Schüttrumpf, H., & Vollmer, S. (2014). Fluvial sediment budget of a modern, restrained river: The lower reach of the rhine in germany. *CATENA*, *122*, 91–102. https://doi.org/10.1016/j.catena.2014.06.007

Frings, R., Gehres, N., Promny, M., Middelkoop, H., Schüttrumpf, H., & Vollmer, S. (2014). Today's sediment budget of the rhine river channel, focusing on the upper rhine graben and rhenish massif. *Geomorphology*, *204*, 573–587. https://doi.org/10.1016/j.geomorph.2013.08.035

Frings, R., Hillebrand, G., Gehres, N., Banhold, K., Schriever, S., & Hoffmann, T. (2019). From source to mouth: Basin-scale morphodynamics of the rhine river. *Earth-Science Reviews*, *196*, 102830. https://doi.org/10.1016/j.earscirev.2019.04.002

Ganić, A., Milutinović, A., & Gojković, Z. (2017). Standard deviations of coordinates due transformation between ellipsoids. *Podzemni radovi*, *2017*, 77–83. https://doi.org/10.5937/podrad1731077G

Geyer, G., Buschmann, B., & Elicki, O. (2014). A new lowermost middle cambrian (series 3, stage 5) faunule from saxony (germany) and its bearing on the tectonostratigraphic history of the saxothuringian domain. *Paläontologische Zeitschrift*, *88*, 239–262. https://doi.org/10.1007/s12542-013-0195-z

Gilbert, G. (1880). *Report on the geology of the henry mountains* (2nd ed.). U.S. Government Printing Office. https://doi.org/10.3133/70039916

Goergen, K., Beersma, J., Brahmer, G., Buiteveld, H., Carambia, M., de Keizer, O., Krahe, P., Nilson, E., Lammersen, R., Perrin, C., & Volken, D. (2010). Assessment of climate change impacts on discharge in the rhine river basin: Results of the rheinblick2050 project.

Grasmeijer, B. (2018). *Method for calculating sediment transport on the dutch lower shoreface* (tech. rep.) (Report number: 1220339-000-ZKS-0041). Rijkswaterstaat.

Grasmeijer, B., Schrijvershof, R., & Van der Werf, J. (2019). *Modelling dutch lower shoreface sand transport* (tech. rep.) (Report number: 1220339-005-ZKS-0008). Rijkswaterstaat Water, Verkeer en Leefomgeving.

Grasmeijer, B., Huisman, B., Luijendijk, A., Schrijvershof, R., Van der Werf, J., Zijl, F., de Looff, H., & de Vries, W. (2022). Modelling of annual sand transports at the dutch lower shoreface. *Ocean & Coastal Management*, *217*, 105984. https://doi.org/10.1016/j.ocecoaman.2021.105984

Green, D. S. (2016). Effects of microplastics on european flat oysters, ostrea edulis and their associated benthic communities. *Environmental Pollution*, *216*, 95–103. https://doi.org/10.1016/j.envpol.2016.05.043

Gropp, W., Lusk, E., & Skjellum, A. (1999). *Using mpi: Portable parallel programming with the message-passing interface* (Vol. 1). MIT press.

Grosset, J., Mazzotti, S., & Vernant, P. (2023). Glacial-isostatic-adjustment strain rate–stress paradox in the western alps and impact on active faults and seismicity. *Solid Earth*, *14*, 1067–1081. https://doi.org/10.5194/se-14-1067-2023

Gvirtzman, Z., Faccenna, C., & Becker, T. W. (2016). Isostasy, flexure, and dynamic topography. *Tectonophysics*, *683*, 255–271.

Hansen, J., Russell, G., Lacis, A., Fung, I., Rind, D., & Stone, P. (1985). Climate response times: Dependence on climate sensitivity and ocean mixing. *Science*, *229*(4716), 857–859. Retrieved February 6, 2024, from http://www.jstor.org/stable/1695287

Hasalová, P., Schulmann, K., Tabaud, A. S., & Oliot, E. (2015). Microstructural evidences for mineralogical inheritance in partially molten rocks: Example from the vosges mts. *Bulletin de la Societe Geologique de France*, *186*, 145–169. https://doi.org/10.2113/gssgfbull.186.2-3.131

Haylock, M. R., Hofstra, N., Klein Tank, A. M. G., Klok, E. J., Jones, P. D., & New, M. (2008). A european daily high-resolution gridded data set of surface temperature and precipitation for 1950–2006. *Journal of Geophysical Research: Atmospheres*, *113*(D20). https://doi.org/10.1029/2008JD010201

HDF Group et al. (1997). Hierarchical data format version 5.

Hegnauer, M., Kwadijk, J., & Klijn, F. (2015). *The plausibility of extreme high discharges in the river rhine* (tech. rep.) (Report number: 1220042-004-ZWS-0008). Rijkswaterstaat.

Heimsath, A. M., Chadwick, O., Roering, J., & Levick, S. R. (2019). Quantifying erosional equilibrium across a slowly eroding, soil mantled landscape. *Earth Surface Processes and Landforms*, *45*. https://doi.org/10.1002/esp.4725

Heimsath, A. M., Dietrich, W. E., Nishiizumi, K., & Finkel, R. (1997). The soil production function and landscape equilibrium. *Nature*, *388*(6640). https://doi.org/10.1038/41056

Heimsath, A. M., Fink, D., & Hancock, G. R. (2009). The 'humped' soil production function: eroding Arnhem Land, Australia. *Earth Surface Processes and Landforms*, *34*(12), 1674–1684. https://doi.org/10.1002/esp.1859

Henrion, E., Masson, F., Doubre, C., Ulrich, P., & Meghraoui, M. (2020). Present-day deformation in the upper rhine graben from gnss data. *Geophysical Journal International*, *223*. https://doi.org/10.1093/gji/ggaa320

Herzog, F. (1998). Streuobst: A traditional agroforestry system as a model for agroforestry development in temperate europe. *Agroforestry Systems*, *42*, 61–80. https://doi.org/10.1023/A:1006152127824

Hobbs, P. R. N., Hallam, J. R., Forster, A., Entwisle, D., Jones, L., Cripps, A. C., Northmore, K. J., Self, S., & Meakin, J. L. (2002). Engineering geology of British rocks and soils: mudstones of the Mercia Mudstone Group [British Geological Survey Research Report, RR/01/02.], 116 pp.

Horton, B. P., Khan, N. S., Cahill, N., Lee, J. S. H., Shaw, T. A., Garner, A. J., Kemp, A. C., Engelhart, S. E., & Rahmstorf, S. (2020). Estimating global mean sea-level rise and its uncertainties by 2100 and 2300 from an expert survey. *npj Climate and Atmospheric Science*, *3*, 18. https://doi.org/10.1038/s41612-020-0121-5

Howard, A., Dietrich, W., & Seidl, M. (1994). Modeling fluvial erosion on regional to continental scales. *Journal of Geophysical Research-Solid Earth*, *99*, 13971–13986. https://doi.org/10.1029/94JB00744

Huisman, P., Van den Akker, C., Colenbrander, H. J., Cramer, W., Van Ee, G., Feddes, R. A., Hooghart, J. C., Kusse, P., Meinardi, C. R., Schultz, E., Schuurmans, C. J. E., Steenvoorden, J. H. A. M., Volker, A., Wessel, J., Zuidema, F. C., & Salz, H. (1998). *Water in the Netherlands* (tech. rep. No. NHV-special 3) (ISBN 90-803565-2-2. NUGI 672.). Netherlands Institute of Applied Geoscience TNO.

Humphreys, G. S., & Wilkinson, M. T. (2007). The soil production function: A brief history and its rediscovery. *Geoderma*, *139*(1), 73–78. https://doi.org/10.1016/j.geoderma.2007.01.004

ICPR. (2024). *Delta rhine*. Retrieved March 18, 2024, from https://www.iksr.org/en/topics/rhine/sub-basins/delta-rhine

IenW (Dutch Ministry of Infrastructure and Water Management). (2024). *Ruimte voor zeespiegelstijging: Een verkenning van denkrichtingen om Nederland ook op lange termijn veilig en leefbaar te houden bij zeespiegelstijging* (tech. rep. No. IenW/BSK-2024/55021) (Attachment 2 of Parliamentary paper "Kamerbrief over 1e resultaten alternatieve denkrichtingen voor zeespiegelstijging op de lange termijn"). https://www.rijksoverheid.nl/documenten/rapporten/2024/03/04/bijlage-2-samenvattend-rapport-bijlage-kamerbrief

ILEC. (n.d.). *World Lake Database* [ILEC = International Lake Environment Committee Foundation. For Lake Constance: URL + 'Display/html/3495', Lake Geneva: URL + 'Display/html/3469'.]. Retrieved April 19, 2024, from https://wldb.ilec.or.jp/

IPBES. (n.d.). *Semi-natural ecosystems - glossary*. Retrieved February 27, 2024, from https://www.ipbes.net/glossary/semi-natural-habitats

IPCC. (2007). 3.3.5 consistency and relationships between temperature and precipitation. In S. Solomon, D. Qin, M. Manning, Z. Chen, M. Marquis, K. Averyt, M.Tignor, & H. Miller (Eds.), *Climate change 2007: The physical science basis. contribution of working group i to the fourth assessment report of the intergovernmental panel on climate change*. Cambridge University Press.

IPCC. (2022). *Climate change 2022: Impacts, adaptation and vulnerability*. Cambridge University Press.

IPCC. (2014). Sea level change. In *Climate change 2013 – the physical science basis: Working group i contribution to the fifth assessment report of the intergovernmental panel on climate change* (pp. 1137–1216). Cambridge University Press.

Jones, M., Peters, G., Gasser, T., Andrew, R., Schwingshackl, C., Gütschow, J., Houghton, R., Friedlingstein, P., Pongratz, J., & Quéré, C. (2023). National contributions to climate change due to historical emissions of carbon dioxide, methane, and nitrous oxide since 1850. *Scientific Data*, *10*. https://doi.org/10.1038/s41597-023-02041-1

Jonsson, I. (1966). Wave boundary layers and friction factors. *Coastal Engineering Proceedings*, *1*(10), 9. https://doi.org/10.9753/icce.v10.9

Karypis, G., & Kumar, V. (1998). A fast and high quality multilevel scheme for partitioning irregular graphs. *SIAM Journal on Scientific Computing*, *20*(1), 359–392. https://doi.org/10.1137/S1064827595287997

Kelly, M., Buoncristiani, J.-F., & Schlüchter, C. (2004). A reconstruction of the last glacial maximum (lgm) ice-surface geometry in the western swiss alps and contiguous alpine regions in italy and france. *Eclogae Geologicae Helvetiae*, *97*, 57–75. https://doi.org/10.1007/s00015-004-1109-6

Kent, E., Whittaker, A., Boulton, S., & Alçiçek, M. (2020). Quantifying the competing influences of lithology and throw rate on bedrock river incision. *GSA Bulletin*, *133*. https://doi.org/10.1130/B35783.1

Kim, J.-H., & Choi, I. (2019). Choosing the level of significance: A decision□theoretic approach. *Abacus*, *57*. https://doi.org/10.1111/abac.12172

Kirby, E., & Whipple, K. X. (2001). Quantifying differential rock-uplift rates via stream profile analysis. *Geology*, *29*(5), 415–418. https://doi.org/10.1130/0091-7613(2001)029<0415:QDRURV>2.0.CO;2

Klösch, M., ten Brinke, W., Krapesch, M., & Habersack, H. (2021). *Sediment management in the Rhine catchment: Inventory of knowledge, research and monitoring, and an advice on future sediment research* (tech. rep. No. I-27 of the CHR) (ISBN 789070980429). International Commission for the Hydrology of the Rhine Basin (KHR/CHR).

Knuth, D. E. (1997). Chapter 3.3.1.B - General Test Procedures for Studying Random Data: The Kolmogorov-Smirnov test. In *The art of computer programming: Seminumerical algorithms* (3rd ed., pp. 48–55, Vol. 2). Addison-Wesley.

Kooi, H., Johnston, P., Lambeck, K., Smither, C., & Molendijk, R. (1998). Geological causes of recent ($\sim$100 yr) vertical land movement in the netherlands. *Tectonophysics*, *299*(4), 297–316. https://doi.org/10.1016/S0040-1951(98)00209-1

Kopecký, M., Macek, M., & Wild, J. (2021). Topographic wetness index calculation guidelines based on measured soil moisture and plant species composition. *Science of The Total Environment*, *757*, 143785. https://doi.org/10.1016/j.scitotenv.2020.143785

Köppen, W. (2011). The thermal zones of the earth according to the duration of hot, moderate and cold periods and to the impact of heat on the organic world [Translated and edited version of the paper "Die Wärmezonen der Erde, nach der Dauer der heissen, gemässigten und kalten Zeit und nach der Wirkung der Wärme auf die organische Welt betrachtet", W. Köppen (1884)]. *Meteorologische Zeitschrift*, *20*(3), 351–360. https://doi.org/10.1127/0941?2948/2011/105

Korup, O. (2002). Recent research on landslide dams - a literature review with special attention to new zealand. *Progress in Physical Geography*, *26*, 206–235. https://doi.org/10.1191/0309133302pp333ra

Langston, A., & Tucker, G. E. (2018). Developing and exploring a theory for the lateral erosion of bedrock channels for use in landscape evolution models. *Earth Surface Dynamics*, *6*(1), 1–27. https://doi.org/10.5194/esurf-6-1-2018

Larsen, I., & Montgomery, D. (2012). Landslide erosion coupled to tectonics and river incision. *Nature Geoscience*, *5*, 468–473. https://doi.org/10.1038/ngeo1479

Lauterborn, R. (1916). *Die geographische und biologische gliederung des rheinstrom*. C. Winter. https://books.google.nl/books?id=GwAizgEACAAJ

Le, N., Männel, B., Bui, L., & Schuh, H. (2024). Identifying Neotectonic Motions in Germany Using Discontinuity-corrected GNSS Data. *Pure and Applied Geophysics*, *181*, 87–108. https://doi.org/10.1007/s00024-023-03390-z

Lewis, B. (2022). *World rivers* [Data source: http://www.naturalearthdata.com/. Last Modified: 08-04-2021]. Retrieved February 9, 2024, from https://worldmap.maps.arcgis.com/home/webmap/viewer.html?useExisting=1

Lidberg, M., Johansson, J., Scherneck, H.-G., & Milne, G. (2010). Recent results based on continuous gps observations of the gia process in fennoscandia from bifrost. *Journal of Geodynamics*, *50*, 8–18. https://doi.org/10.1016/j.jog.2009.11.010

Liechtenstein Office of Statistics. (2024). *Liechtenstein in figures 2024* (tech. rep.). Office of Statistics, PRINCIPALITY OF LIECHTENSTEIN. www.statistikportal.li

Lipp, A. G., Shorttle, O., Sperling, E. A., Brocks, J. J., Cole, D. B., Crockford, P. W., Del Mouro, L., Dewing, K., Dornbos, S. Q., Emmings, J. F., Farrell, U. C., Jarrett, A., Johnson, B. W., Kabanov, P., Keller, C. B., Kunzmann, M., Miller, A. J., Mills, N. T., O'Connell, B., … Yang, J. (2021). The composition and weathering of the continents over geologic time. *Geochemical perspectives letters / European Association of Geochemistry.*, *17*, 6. https://doi.org/10.7185/geochemlet.2109

Lippitsch, R., Kissling, E., & Ansorge, J. (2003). Upper mantle structure beneath the alpine orogen from high-resolution teleseismic tomography. *Journal of Geophysical Research*, *108*. https://doi.org/10.1029/2002JB002016

Lloyd, A. J., Crawford, O., Al-Attar, D., Austermann, J., Hoggard, M. J., Richards, F. D., & Syvret, F. (2023). GIA imaging of 3-D mantle viscosity based on palaeo sea level observations – Part I: Sensitivity kernels for an Earth with laterally varying viscosity. *Geophysical Journal International*, *236*(2), 1139–1171. https://doi.org/10.1093/gji/ggad455

Loch, R. J., Silburn, D., et al. (1997). Soil erosion. *Sustainable crop production in the sub-tropics: an Australian perspective.*, 27–41.

Longuet-Higgins, M. S. (1970). Longshore currents generated by obliquely incident sea waves: 2. *Journal of Geophysical Research (1896-1977)*, *75*(33), 6790–6801. https://doi.org/10.1029/JC075i033p06790

Macedo, P. M. S., Oliveira, P. T. S., Antunes, M. A. H., Durigon, V. L., Fidalgo, E. C. C., & de Carvalho, D. F. (2021). New approach for obtaining the c-factor of rusle considering the seasonal effect of rainfalls on vegetation cover. *International Soil and Water Conservation Research*, *9*(2), 207–216. https://doi.org/10.1016/j.iswcr.2020.12.001

Madden, R. A., & Williams, J. (1978). The correlation between temperature and precipitation in the united states and europe. *Monthly Weather Review*, *106*(1), 142–147. https://doi.org/10.1175/1520-0493(1978)106<0142:TCBTAP>2.0.CO;2

Mahtta, R., Fragkias, M., Güneralp, B., Mahendra, A., Reba, M., Wentz, E., & Seto, K. (2022). Urban land expansion: The role of population and economic growth for 300+ cities. *npj Urban Sustainability*, *2*, 5. https://doi.org/10.1038/s42949-022-00048-y

Mangelsdorf, J., Scheurmann, K., & Weiß, F.-H. (1990). Investigations in river morphology. In *River morphology: A guide for geoscientists and engineers* (pp. 193–210). Springer Berlin Heidelberg. https://doi.org/10.1007/978-3-642-83777-7_8

MapTiler Team, Pridal, P., Pohanka, T., Ashraf, A., & Kacer, R. (2022). *Epsg.io: Find coordinate systems worldwide*. Retrieved February 9, 2024, from https://epsg.io/

Meehl, G. A., Washington, W. M., Collins, W. D., Arblaster, J. M., Hu, A., Buja, L. E., Strand, W. G., & Teng, H. (2005). How much more global warming and sea level rise? *Science*, *307*(5716), 1769–1772. https://doi.org/10.1126/science.1106663

Merritt, W., Letcher, R. A., & Jakeman, A. J. (2003). A review of erosion and sediment transport models [The Modelling of Hydrologic Systems]. *Environmental Modelling & Software*, *18*(8), 761–799. https://doi.org/10.1016/S1364-8152(03)00078-1

Mey, J., Scherler, D., Wickert, A. D., Egholm, D., Tesauro, M., Schildgen, T., & Strecker, M. (2016). Glacial isostatic uplift of the european alps. *Nature Communications*, *7*(1), 1–10. https://EconPapers.repec.org/RePEc:nat:natcom:v:7:y:2016:i:1:d:10.1038_ncomms13382

Middelkoop, H., & Asselman, N. (2008). Impact of climate and land use change on river discharge and the production, transport and deposition of fine sediment in the rhine basin - a summary of recent results. https://doi.org/10.1007/3-540-36606-7_9

Milazzo, F., Fernández, P., Peña, A., & Vanwalleghem, T. (2022). The resilience of soil erosion rates under historical land use change in agroecosystems of southern spain. *Science of The Total Environment*, *822*, 153672. https://doi.org/10.1016/j.scitotenv.2022.153672

Mil-Homens, J. (2016, March). *Longshore sediment transport - bulk formulas and process based models* [PhD thesis]. Delft University of Technology [Available at http://repository.tudelft.nl/].

Mitas, L., & Mitasova, H. (1999). Spatial interpolation. In P. Longley, M. F. Goodchild, D. J. Maguire, & D. W. Rhind (Eds.), *Geographical information systems: Principles, techniques, management and applications* (481−492). Wiley.

Mitchell, N., & Yanites, B. (2021). Bedrock river erosion through dipping layered rocks: Quantifying erodibility through kinematic wave speed. *Earth Surface Dynamics*, *9*(4), 723–753. https://doi.org/10.5194/esurf-9-723-2021

Murphy, B., Johnson, J., Gasparini, N., & Sklar, L. S. (2016). Chemical weathering as a mechanism for the climatic control of bedrock river incision. *Nature*, *532*, 223–227. https://doi.org/10.1038/nature17449

National Research Council. (2011). *Climate stabilization targets: Emissions, concentrations, and impacts over decades to millennia*. The National Academies Press. https://doi.org/10.17226/12877

Neubauer, F. (2014). Gondwana-land goes europe. *Austrian Journal of Earth Sciences*, *107*.

Nikulina, A., MacDonald, K., Scherjon, F., Pearce, E., Davoli, M., Svenning, J.-C., Vella, E., Gaillard, M.-J., Zapolska, A., Arthur, F., Martinez, A., Hatlestad, K., Mazier, F., Serge, M., Lindholm, K.-J., Fyfe, R., Renssen, H., Roche, D., Kluiving, S., & Roebroeks, W. (2022). Tracking hunter-gatherer impact on vegetation in last interglacial and holocene europe: Proxies and challenges. *Journal of Archaeological Method and Theory*, *29*, 1–45. https://doi.org/10.1007/s10816-021-09546-2

Nocquet, J.-M., & Calais, E. (2004). Geodetic measurements of crustal deformation in the western mediterranean & europe. *Pure and Applied Geophysics*, *161*, 661–681. https://doi.org/10.1007/s00024-003-2468-z

Nocquet, J.-M., Sue, C., Walpersdorf, A., Tran, D., Lenôtre, N., Vernant, P., Cushing, E., Jouanne, F., Masson, F., Baize, S., Chery, J., & Beek, P. (2016). Present-day uplift of the western alps. *Nature Science Reports*, *6*. https://doi.org/10.1038/srep28404

NWA-LOSS. (2022). Wp1.3 – subsidence, relative sea-level rise, gia [A NWA-LOSS Work Package description. Last accessed: 19-01-2024]. https://nwa-loss.nl/en/work-packages/wp1-measuring-and-monitoring/wp1-3-subsidence-relative-sea-level-rise-gia/

O'Callaghan, J. F., & Mark, D. M. (1984). The extraction of drainage networks from digital elevation data. *Computer Vision, Graphics, and Image Processing*, *28*(3), 323–344. https://doi.org/10.1016/S0734-189X(84)80011-0

Oeser, R. A., & von Blanckenburg, F. (2020). Do degree and rate of silicate weathering depend on plant productivity? *Biogeosciences*, *17*(19), 4883–4917. https://doi.org/10.5194/bg-17-4883-2020

O'Gorman, P. (2015). Precipitation extremes under climate change. *Current Climate Change Reports*, *1*. https://doi.org/10.1007/s40641-015-0009-3

Olsthoorn, A. A., & Tol, R. S. J. (2001). *Floods, flood management and climate change in the netherlands*. Dept. of Economics; Technology.

Oppenheimer, M., Glavovic, B. C., Hinkel, J., Van de Wal, R., Magnan, A. K., Abd-Elgawad, A., Cai, R., Cifuentes-Jara, M., DeConto, R. M., Ghosh, T., Hay, J., Isla, F., Marzeion, B., Meyssignac, B., & Sebesvari, Z. (2022). Sea level rise and implications for low-lying islands, coasts and communities. In H.-O. Pörtner, D. C. Roberts, V. Masson-Delmotte, P. Zhai, M. Tignor, E. Poloczanska, K. Mintenbeck, A. Alegría, M. Nicolai, A. Okem, J. Petzold, B. Rama, & N. M. Weyer (Eds.), *The ocean and cryosphere in a changing climate: Special report of the intergovernmental panel on climate change* (pp. 321–446). Cambridge University Press.

Oreskes, N., Shrader-Frechette, K., & Belitz, K. (1994). Verification, validation, and confirmation of numerical models in the earth sciences. *Science*, *263*(5147), 641–646. https://doi.org/10.1126/science.263.5147.641

OSPAR Commission. (2020). *Status assessment 2020 - european flat oyster and ostrea edulis beds*. Retrieved February 16, 2024, from https://oap.ospar.org/en/ospar-assessments/committee-assessments/biodiversity-committee/status-assesments/european-flat-oyster/

Oysters and artificial reefs in the water for new nature in wind farm on the north sea. (2018). Retrieved February 16, 2024, from https://www.derijkenoordzee.nl/en/news/oysters-and-artificial-reefs-in-the-water-for-new-nature-in-wind-farm-on-the-north-sea

Panagos, P., Meusburger, K., Ballabio, C., Borrelli, P., & Alewell, C. (2014). Soil erodibility in europe: A high-resolution dataset based on lucas. *Science of The Total Environment*, *479-480*, 189–200. https://doi.org/10.1016/j.scitotenv.2014.02.010

Pechlivanidou, S., Cowie, P. A., Hannisdal, B., Whittaker, A. C., Gawthorpe, R. L., Pennos, C., & Riiser, O. S. (2018). Source-to-sink analysis in an active extensional setting: Holocene erosion and deposition in the sperchios rift, central greece. *Basin Research*, *30*(3), 522–543.

Pelletier, J. D., Brad Murray, A., Pierce, J. L., Bierman, P. R., Breshears, D. D., Crosby, B. T., Ellis, M., Foufoula-Georgiou, E., Heimsath, A. M., Houser, C., Lancaster, N., Marani, M., Merritts, D. J., Moore, L. J., Pederson, J. L., Poulos, M. J., Rittenour, T. M., Rowland, J. C., Ruggiero, P., … Yager, E. M. (2015). Forecasting the response of earth's surface to future climatic and land use changes: A review of methods and research needs. *Earth's Future*, *3*(7), 220–251. https://doi.org/10.1002/2014EF000290

Pelletier, J. D., Broxton, P. D., Hazenberg, P., Zeng, X., Troch, P. A., Niu, G., Williams, Z., Brunke, M., & Gochis, D. (2016). Global 1-km gridded thickness of soil, regolith, and sedimentary deposit layers. https://doi.org/10.3334/ORNLDAAC/1304

Perron, J., & Fagherazzi, S. (2012). The legacy of initial conditions in landscape evolution. *Earth Surface Processes and Landforms*, *37*, 52–63. https://doi.org/10.1002/esp.2205

Pleijster, E.-J., & Van der Veeken, C. (2015). *Dijken van nederland [dutch dikes]*. nai010.

Poesen, J. (2018). Soil erosion in the anthropocene: Research needs. *Earth Surface Processes and Landforms*, *43*(1), 64–84. https://doi.org/10.1002/esp.4250

Pretty, J., & Bharucha, Z. (2014). Sustainable intensification in agricultural systems. *Annals of Botany*, *114*(8), 1571–1596. https://doi.org/10.1093/aob/mcu205

Przyrowski, R., & Schäfer, A. (2015). Quaternary fluvial basin of northern upper rhine graben. *Zeitschrift der Deutschen Gesellschaft für Geowissenschaften*, *166*, 71–98. https://doi.org/10.1127/1860-1804/2014/0080

QGIS.org. (2024). QGIS Geographic Information System. *Open Source Geospatial Foundation Project*. http://qgis.org

Rahman, M., Pawijit, Y., Xu, C., Moser-Reischl, A., Pretzsch, H., Rötzer, T., & Pauleit, S. (2023). A comparative analysis of urban forests for storm□water management. *Scientific Reports*, *13*. https://doi.org/10.1038/s41598-023-28629-6

Rao, M., Palada, M. C., & Becker, B. (2004). Medicinal and aromatic plants in agroforestry systems. In P. R. Nair, M. Rao, & L. Buck (Eds.), *New vistas in agroforestry: A compendium for 1st world*

congress of agroforestry, 2004 (pp. 107–122). Springer Netherlands. https://doi.org/10.1007/978-94-017-2424-1_8

Refice, A., Giachetta, E., & Capolongo, D. (2012). Signum: A matlab, tin-based landscape evolution model. *Computers & Geosciences*, *45*, 293–303. https://doi.org/10.1016/j.cageo.2011.11.013

Rempe, D., & Dietrich, W. E. (2014). A bottom-up control on fresh-bedrock topography under landscapes. *Proceedings of the National Academy of Sciences of the United States of America*, *111*. https://doi.org/10.1073/pnas.1404763111

Renard, K. G., Foster, G. R., Weessies, G. A., & McCool, D. K. (1997). *Predicting soil erosion by water: A guide to conservation planning with the revised universal soil loss equation (rusle)* (D. C.Yoder, Ed.) [Agricultural Handbook No. 703]. US Department of Agriculture, Agricultural Research Service.

Richardson, E. A., Mitchell, R., Hartig, T., De Vries, S., Astell-Burt, T., & Frumkin, H. (2012). Green cities and health: A question of scale? *Journal of Epidemiology and Community Health*, *66*, 160–165. https://doi.org/10.1136/jech.2011.137240

Richardson, K., Steffen, W., Lucht, W., Bendtsen, J., Cornell, S. E., Donges, J. F., Drüke, M., Fetzer, I., Bala, G., von Bloh, W., Feulner, G., Fiedler, S., Gerten, D., Gleeson, T., Hofmann, M., Huiskamp, W., Kummu, M., Mohan, C., Nogués-Bravo, D., … Rockström, J. (2023). Earth beyond six of nine planetary boundaries. *Science Advances*, *9*(37), eadh2458. https://doi.org/10.1126/sciadv.adh2458

Rieger, F. A., Zolin, C. A., Paulino, J., de Souza, A. P., Matos, E. d. S., Magalhães, C. A. d. S., & Farias Neto, A. L. d. (2016). Water erosion on an oxisol under integrated crop-forest systems in a transitional area between the amazon and cerrado biomes. *Revista Brasileira de Ciência do Solo*, *40*.

Rijksoverheid [Government of the Netherlands]. (2023). *Gaswinning groningen stopt per 1 oktober 2023 [gas extraction in groningen will stop on october 1, 2023]*. Retrieved March 7, 2024, from https://www.rijksoverheid.nl/actueel/nieuws/2023/06/23/gaswinning-groningen-stopt-per-1-oktober-2023

Rijkswaterstaat (Department of Waterways and Public Works). (n.d.). *Markermeer*. Retrieved February 23, 2024, from https://www.rijkswaterstaat.nl/water/vaarwegenoverzicht/markermeer

Rockström, J., Steffen, W., Noone, K., Persson, Å., Chapin III, F. S., Lambin, E. F., Lenton, T., Scheffer, M., Folke, C., Schellnhuber, H., Nykvist, B., De Wit, C., Hughes, T., Van der Leeuw, S., Rodhe, H., Sörlin, S., Snyder, P., Costanza, R., Svedin, U., & Foley, J. (2009). A safe operating space for humanity. *Nature, v.461, 472-475*, *46*.

Roering, J., Kirchner, J., & Dietrich, W. (2001). Erratum: “hillslope evolution by nonlinear, slope-dependent transport: Steady state morphology and equilibrium adjustment time scales”. *Journal of Geophysical Research*, *106*, 26787–26789. https://doi.org/10.1029/2001JB000323

Roering, J., Kirchner, J., Sklar, L. S., & Dietrich, W. (2001). Hillslope evolution by nonlinear creep and landsliding: An experimental study. *Geology*, *29*. https://doi.org/10.1130/0091-7613(2001)029<0143:HEBNCA>2.0.CO;2

Rogner, H.-H., Aguilera, R. F., Bertani, R., Bhattacharya, C., Dusseault, M. B., Gagnon, L., Haberl, H., Hoogwijk, M., Johnson, A., Rogner, M. L., Wagner, H., & Yakushev, V. (2012, October). Chapter 7: Energy resources and potentials. In G. W. Team (Ed.), *Global energy assessment: Toward a sustainable future*. Cambridge University Press; IIASA. http://www.globalenergyassessment.org

Rohatgi, A. (2024). Webplotdigitizer: Version 4.7. https://automeris.io/WebPlotDigitizer

Rosenstock, T., Tully, K., Arias-Navarro, C., Neufeldt, H., Butterbach-Bahl, K., & Verchot, L. (2014). Agroforestry with n2-fixing trees: Sustainable development’s friend or foe? *Current Opinion in Environmental Sustainability*, *6*, 15–21. https://doi.org/10.1016/j.cosust.2013.09.001

Rovira, A., Ballinger, R., Ibáñez, C., Parker, P., Dominguez, M. D., Simon, X., Lewandowski, A., Hochfeld, B., Tudor, M., & Vernaeve, L. (2014). Sediment imbalances and flooding risk in european deltas and estuaries. *Journal of Soils and Sediments*, *14*, 1493–1512. https://doi.org/10.1007/s11368-014-0914-4

Roy, S. G., Koons, P. O., Upton, P., & Tucker, G. E. (2015). The influence of crustal strength fields on the patterns and rates of fluvial incision. *Journal of Geophysical Research: Earth Surface*, *120*(2), 275–299. https://doi.org/10.1002/2014JF003281

RWE. (2021). *Hambach mine site*. Retrieved March 3, 2024, from https://www.rwe.com/en/the-group/countries-and-locations/hambach-mine-site/

Salles, T. (2016). Badlands: A parallel basin and landscape dynamics model. *SoftwareX*, *5*, 195–202. https://doi.org/10.1016/j.softx.2016.08.005

Salles, T. (2022). Coastline evolution notes - longshore drift [lecture notes]. coastal processes, environments & systems. https://tristansalles.github.io/Coast/welcome.html

Salles, T. (2019). Escape: Regional to global scale landscape evolution model v2.0. *Geoscientific Model Development*, *12*(9), 4165–4184. https://doi.org/10.5194/gmd-12-4165-2019

Salles, T., Ding, X., & Brocard, G. (2018). Pybadlands: A framework to simulate sediment transport, landscape dynamics and basin stratigraphic evolution through space and time. *PLOS ONE*, *13*(4), e0195557. https://doi.org/10.1371/journal.pone.0195557

Salles, T., Ding, X., Webster, J. M., Vila-Concejo, A., Brocard, G., & Pall, J. (2018). A unified framework for modelling sediment fate from source to sink and its interactions with reef systems over geological times. *Sci Rep*, *8*, 5252. https://doi.org/10.1038/s41598-018-23519-8

Salles, T., & Duclaux, G. (2015). Combined hillslope diffusion and sediment transport simulation applied to landscape dynamics modelling. *Earth Surface Processes and Landforms*, *40*(6), 823–839. https://doi.org/10.1002/esp.3674

Salles, T., & Hardiman, L. (2016). Badlands: An open-source, flexible and parallel framework to study landscape dynamics. *Computers & Geosciences*, *91*, 77–89. https://doi.org/10.1016/j.cageo.2016.03.011

Salles, T., Husson, L., Rey, P., Mallard, C., Zahirovic, S., Boggiani, B. H., Coltice, N., & Arnould, M. (2023). Hundred million years of landscape dynamics from catchment to global scale. *Science*, *6635*(379), 918–923. https://doi.org/10.1126/science.add2541

Salles, T., Mallard, C., & Zahirovic, S. (2020). Gospl: Global scalable paleo landscape evolution. *Journal of Open Source Software*, *5*(56), 2804. https://doi.org/10.21105/joss.02804

Satterfield, D. A., Rollinson, H., & Suthren, R. J. (2019). The eastern french pyrenees: From mountain belt to foreland basin. *Geology Today*, *35*, 228–240. https://doi.org/10.1111/gto.12291

Schaller, M., & Ehlers, T. A. (2022). Comparison of soil production, chemical weathering, and physical erosion rates along a climate and ecological gradient (chile) to global observations. *Earth Surface Dynamics*, *10*(1), 131–150. https://doi.org/10.5194/esurf-10-131-2022

Schlatter, A., Schneider, D., Geiger, A., & Kahle, H.-G. (2005). Recent vertical movements from precise levelling in the vicinity of the city of basel, switzerland. *International Journal of Earth Sciences*, *94*, 507–514. https://doi.org/10.1007/s00531-004-0449-9

Seneviratne, S. I., Zhang, X., Adnan, M., Badi, W., Dereczynski, C., Luca, A. D., Ghosh, S., Iskandar, I., Kossin, J., Lewis, S., Otto, F., Pinto, I., Satoh, M., Vicente-Serrano, S. M., Wehner, M., & Zhou, B. (2021). Weather and climate extreme events in a changing climate. In V. Masson-Delmotte, P. Zhai, A. Pirani, S. L. Connors, C. Péan, S. Berger, N. Caud, Y. Chen, L. Goldfarb, M. I. Gomis, M. Huang, K. Leitzell, E. Lonnoy, J. B. R. Matthews, T. K. Maycock, T. Waterfield, O. Yelekçi, R. Yu, & B. Zhou (Eds.), *Climate Change 2021: The Physical Science Basis. Contribution of Working Group I to the Sixth Assessment Report of the Intergovernmental Panel on Climate Change* (pp. 1513–1766). Cambridge University Press. https://doi.org/10.1017/9781009157896.013

Shewchuk, J. R. (2002). Delaunay refinement algorithms for triangular mesh generation [16th ACM Symposium on Computational Geometry]. *Computational Geometry*, *22*(1), 21–74. https://doi.org/10.1016/S0925-7721(01)00047-5

Shiferaw, H. (2021). Study on the influence of slope height and angle on the factor of safety and shape of failure of slopes based on strength reduction method of analysis. *Beni-Suef University Journal of Basic and Applied Sciences*, *10*. https://doi.org/10.1186/s43088-021-00115-w

Siegenthaler, U., & Oeschger, H. (1984). Transient temperature changes due to increasing co2 using simple models. *Annals of Glaciology*, *5*, 153–159. https://doi.org/10.3189/1984AoG5-1-153-159

Siegert, M., Dowdeswell, J., Hald, M., & Svendsen, J.-I. (2001). Modeling the eurasian ice sheet through a full (weichselian) glacial cycle. *Global and Planetary Change*, *31*, 367–385. https://doi.org/10.1016/S0921-8181(01)00130-8

Skinner, B., Porter, S., & Park, J. (2003). *The dynamic earth: An introduction to physical geology* (5th ed.). Wiley.

Sklar, L. S., & Dietrich, W. E. (2006). The role of sediment in controlling steady-state bedrock channel slope: Implications of the saltation–abrasion incision model. *Geomorphology*, *82*(1-2), 58–83.

Skrzypek, E., Schulmann, K., Tabaud, A.-S., & Edel, J.-B. (2014). Palaeozoic evolution of the variscan vosges mountains. *Geological Society, London, Special Publications*, *405*(1), 45–75.

Slangen, A. B. A., Church, J. A., Agosta, C., Fettweis, X., Marzeion, B., & Richter, K. (2016). Anthropogenic forcing dominates global mean sea-level rise since 1970. *Nature Climate Change*, *6*(7), 701–705.

SMARD. (2021). *End of coal power as part of the energy transition: Coal phase-out under KVBG Act* [SMARD is the Bundesnetzagentur's electricity market information platform]. Retrieved March 3, 2024, from https://www.smard.de/page/en/topic-article/5892/206022

Smith, R. B., & Barstad, I. (2004). A linear theory of orographic precipitation. *Journal of the Atmospheric Sciences*, *61*(12), 1377–1391. https://doi.org/10.1175/1520-0469(2004)061<1377:ALTOOP>2.0.CO;2

Solomon, S., Plattner, G.-K., Knutti, R., & Friedlingstein, P. (2009). Irreversible climate change due to carbon dioxide emissions. *Proceedings of the National Academy of Sciences*, *106*(6), 1704–1709. https://doi.org/10.1073/pnas.0812721106

Sonneveld, M. P. W., Temme, A. J. A. M., Schoorl, J. M., Claessens, L. F. G., Viveen, W., Baartman, J. E. M., Lesschen, J. P., & van Gorp, W. (2010). Landscape - Soilscape Evolution Modelling: LAPSUS [Division Symposium 1.2.; Soil Solutions for a Changing World ; Conference date: 01-08-2010 Through 06-08-2010]. In R. J. Gilkes & N. Prakongkep (Eds.), *Proceedings of the 19th world congress of soil science; soil solutions for a changing world, brisbane, australia, 1-6 august 2010* (pp. 12–15). IUSS.

Soulsby, R. L. (1997). *Dynamics of marine sands: A manual for practical applications*. Thomas Telford.

Soulsby, R. L., Hamm, L., Klopman, G., Myrhaug, D., Simons, R. R., & Thomas, G. P. (1993). Wave-current interaction within and outside the bottom boundary layer [Special Issue Coastal Morphodynamics: Processes and Modelling]. *Coastal Engineering*, *21*(1), 41–69. https://doi.org/10.1016/0378-3839(93)90045-A

STATEC. (2022). *Le luxembourg en chiffres [luxembourg in numbers]* (STATEC, Ed.; tech. rep.) (ISSN: 1019-6471). https://statistiques.public.lu/fr/publications/series/luxembourg-en-chiffres/2022/luxembourg-en-chiffres-2022.html

Steffen, W., Richardson, K., Rockström, J., Schellnhuber, H., Dube, O. P., Dutreuil, S., Lenton, T., & Lubchenco, J. (2020). The emergence and evolution of earth system science. *Nature Reviews Earth & Environment*, *1*, 54–63. https://doi.org/10.1038/s43017-019-0005-6

Sternai, P., Sue, C., Husson, L., Serpelloni, E., Becker, T. W., Willett, S. D., Faccenna, C., Di Giulio, A., Spada, G., Jolivet, L., Valla, P., Petit, C., Nocquet, J.-M., Walpersdorf, A., & Castelltort, S. (2019). Present-day uplift of the european alps: Evaluating mechanisms and models of their relative contributions. *Earth-Science Reviews*, *190*, 589–604. https://doi.org/10.1016/j.earscirev.2019.01.005

Stock, J. D., & Montgomery, D. R. (1999). Geologic constraints on bedrock river incision using the stream power law. *Journal of Geophysical Research: Solid Earth*, *104*(B3), 4983–4993.

Stokes, G. G. (1847). On the theory of oscillatory waves. *Reports of the British Association*, *6*, 441–455. http://resolver.tudelft.nl/uuid:eb3cd025-0b1c-4af5-ad3f-5e485aad6086

Størens, E. (n.d.). *The carbon cycle* [Last updated on 10-07-2021.]. Retrieved February 7, 2024, from https://egilstoren.no/en_carbon_cycle.html

Stouffer, R. J. (2004). Time scales of climate response. *Journal of Climate*, *17*(1), 209–217. https://doi.org/10.1175/1520-0442(2004)017<0209:TSOCR>2.0.CO;2

Strahler, A. (1952). HYPSOMETRIC (AREA-ALTITUDE) ANALYSIS OF EROSIONAL TOPOGRAPHY. *GSA Bulletin*, *63*(11), 1117–1142. https://doi.org/10.1130/0016-7606(1952)63[1117:HAAOET]2.0.CO;2

Stroeven, A. P., Hättestrand, C., Kleman, J., Heyman, J., Fabel, D., Fredin, O., Goodfellow, B. W., Harbor, J. M., Jansen, J. D., Olsen, L., Caffee, M. W., Fink, D., Lundqvist, J., Rosqvist, G. C., Strömberg, B., & Jansson, K. N. (2016). Deglaciation of fennoscandia [Special Issue: PAST Gateways (Palaeo-Arctic Spatial and Temporal Gateways)]. *Quaternary Science Reviews*, *147*, 91–121. https://doi.org/10.1016/j.quascirev.2015.09.016

Stuiver, M. (2023). *The symbiotic city: Nature-positive urban futures* [Brochure]. Wageningen University & Research. https://www.wur.nl/en/research-results/research-institutes/environmental-research/programmes/green-cities.htm

Sudomo, A., Leksono, B., Tata, H. L., Rahayu, A. A. D., Umroni, A., Rianawati, H., Asmaliyah, Krisnawati, Setyayudi, A., Utomo, M. M. B., Pieter, L. A. G., Wresta, A., Indrajaya, Y., Rahman, S. A., & Baral, H. (2023). Can agroforestry contribute to food and livelihood security for indonesia's smallholders in the climate change era? *Agriculture*, *13*(10). https://doi.org/10.3390/agriculture13101896

Suthren, R. J. (2022). *Geology of the Eastern French Pyrenees* [Web page with further information concerning]. Retrieved May 25, 2024, from https://www.virtual-geology.info/regional-geol/pyrenees.htm#loc13

Syvitski, J., & Kettner, A. (2011). Sediment flux and the anthropocene. *Philosophical transactions. Series A, Mathematical, physical, and engineering sciences*, *369*, 957–75. https://doi.org/10.1098/rsta.2010.0329

Szulczewska, B., Giedych, R., Borowski, J., Kuchcik, M., Sikorski, P., Mazurkiewicz, A., & Stańczyk, T. (2014). The Green City Guidelines: Techniques for a healthy liveable city, 99 pp. https://doi.org/10.1016/j.landusepol.2013.11.006

Tebbens, L. A., Veldkamp, A., Van Dijke, J. J., & Schoorl, J. M. (2000). Modeling longitudinal-profile development in response to late quaternary tectonics, climate and sea-level changes: The river meuse [Environmental Tectonics and Climate: The Netherlands Environmental Earth System Dynamics Initiative]. *Global and Planetary Change*, *27*(1), 165–186. https://doi.org/10.1016/S0921-8181(01)00065-0

Temme, A. J. A. M., & Vanwalleghem, T. (2016). LORICA - A new model for linking landscape and soil profile evolution: Development and sensitivity analysis. *Computers and Geosciences*, *90*(Part b), 131–143. https://doi.org/10.1016/j.cageo.2015.08.004

Temme, A. J. A. M., Schoorl, J. M., Claessens, L., & Veldkamp, A. (2022). 10.11 - quantitative modeling of landscape evolution. In J. F. Shroder (Ed.), *Treatise on geomorphology (second edition)* (Second Edition, pp. 162–183). Academic Press. https://doi.org/10.1016/B978-0-12-818234-5.00140-1

Tetzlaff, D. (2005). Modelling coastal sedimentation through geologic time. *8th Annual Conference*, 443–448. https://doi.org/10.2112/04-704A.1

Thieulot, C., Steer, P., & Huismans, R. S. (2014). Three-dimensional numerical simulations of crustal systems undergoing orogeny and subjected to surface processes. *Geochemistry, Geophysics, Geosystems*, *15*(12), 4936–4957. https://doi.org/10.1002/2014GC005490

Thomas, D. S. G. (2008). *The dictionary of physical geography* (D. S. G. Thomas & A. Goudie, Eds.; 3rd ed.). Blackwell Publishing Ltd.

Tockner, K., Uehlinger, U., Robinson, C., Tonolla, D., Siber, R., & Peter, F. (2009). Introduction to european rivers. https://doi.org/10.1016/B978-0-12-369449-2.00001-1

Trenberth, K. (2011). Changes in precipitation with climate change. climate change research. *Climate Research*, *47*, 123–138. https://doi.org/10.3354/cr00953

Trucano, T., Swiler, L. P., Igusa, T., Oberkampf, W., & Pilch, M. (2006). Calibration, validation, and sensitivity analysis: What's what. *Reliability Engineering and System Safety*, *91*(10), 1331–1357. https://doi.org/10.1016/j.ress.2005.11.03

Tucker, G. E. (2004). Drainage basin sensitivity to tectonic and climatic forcing: Implications of a stochastic model for the role of entrainment and erosion thresholds. *Earth Surface Processes and Landforms*, *29*(2), 185–205. https://doi.org/10.1002/esp.1020

Tucker, G. E. (2009). Natural experiments in landscape evolution. *Earth Surface Processes and Landforms*, *34*(10), 1450–1460.

Tucker, G. E., & Bradley, D. N. (2010). Trouble with diffusion: Reassessing hillslope erosion laws with a particle-based model. *Journal of Geophysical Research: Earth Surface*, *115*(F1). https://doi.org/10.1029/2009JF001264

Tucker, G. E., & Hancock, G. R. (2010). Modelling landscape evolution. *Earth Surface Processes and Landforms*, *35*(1), 28–50. https://doi.org/10.1002/esp.1952

Tucker, G. E., Lancaster, S., Gasparini, N., & Bras, R. (2001). The channel-hillslope integrated landscape development model (CHILD). In R. S. Harmon & W. W. Doe (Eds.), *Landscape erosion and evolution modeling* (pp. 349–388). Springer US. https://doi.org/10.1007/978-1-4615-0575-4_12

Turowski, J. M., Lague, D., & Hovius, N. (2007). Cover effect in bedrock abrasion: A new derivation and its implications for the modeling of bedrock channel morphology. *Journal of Geophysical Research: Earth Surface*, *112*(F4). https://doi.org/10.1029/2006JF000697

Turowski, J. M., Pruß, G., Voigtländer, A., Ludwig, A., Landgraf, A., Kober, F., & Bonnelye, A. (2023). Geotechnical controls on erodibility in fluvial impact erosion. *EGUsphere*, *2023*, 1–31. https://doi.org/10.5194/egusphere-2023-76

Uehlinger, U., Arndt, H., Wantzen, K., & Leuven, R. S. E. (2009). Chapter 6 - the rhine river basin. In K. Tockner, U. Uehlinger, & C. T. Robinson (Eds.), *Rivers of europe* (pp. 199–245). Academic Press. https://doi.org/10.1016/B978-0-12-369449-2.00006-0

Unterfrauner, H. (2020). *Germany, Field/acre*. Retrieved May 25, 2024, from https://www.soilbook.info/soil_samples/96

US National Park Service. (2022). *River systems and fluvial landforms* [Image from T. L. Thornberry-Ehrlich.]. Retrieved February 5, 2024, from https://www.nps.gov/subjects/geology/fluvial-landforms.htm

Valters, D. (2016). Modelling Geomorphic Systems: Landscape Evolution. In *Geomorphological techniques*. British Society for Geomorphology.

Van Camp, M., de Viron, O., Scherneck, H.-G., Hinzen, K.-G., Williams, S. D. P., Lecocq, T., Quinif, Y., & Camelbeeck, T. (2011). Repeated absolute gravity measurements for monitoring slow intraplate vertical deformation in western europe. *Journal of Geophysical Research: Solid Earth*, *116*(B8). https://doi.org/10.1029/2010JB008174

Van Dalen, A. G. (1972). *Rondom het Tolhuys aan Rijn en Waal: uit de geschiedenis van Lobith, Tolkamer, Spijk, Herwen en Aredt*. De Walburg Pers.

Van de Wiel, M. J., Coulthard, T. J., Macklin, M. G., & Lewin, J. (2007). Embedding reach-scale fluvial dynamics within the caesar cellular automaton landscape evolution model [Reduced-Complexity Geomorphological Modelling for River and Catchment Management]. *Geomorphology*, *90*(3), 283–301. https://doi.org/10.1016/j.geomorph.2006.10.024

Van der Beek, P. (2013). Modelling landscape evolution. In *Environmental modelling* (pp. 309–331). John Wiley & Sons, Ltd. https://doi.org/10.1002/9781118351475.ch19

Van der Meij, W. M. (2021). Evolutionary pathways in soil-landscape evolution models. *SOIL Discussions*. https://doi.org/10.5194/soil-2021-133

Van der Meij, W. M., Temme, A. J. A. M., Binnie, S. A., & Reimann, T. (2023). ChronoLorica: Introduction of a soil–landscape evolution model combined with geochronometers. *Geochronology*, *5*(1), 241–261. https://doi.org/10.5194/gchron-5-241-2023

Van der Meij, W. M., Temme, A. J. A. M., Lin, H. S., Gerke, H. H., & Sommer, M. (2018). On the role of hydrologic processes in soil and landscape evolution modeling: Concepts, complications and partial solutions. *Earth-Science Reviews*, *185*, 1088–1106. https://doi.org/10.1016/j.earscirev.2018.09.001

Van der Spek, A. J. F., Van der Werf, J., Oost, A., Vermaas, T., Grasmeijer, B., & Schrijvershof, R. (2022). The lower shoreface of the dutch coast – an overview. *Ocean & Coastal Management*, *230*, 106367. https://doi.org/10.1016/j.ocecoaman.2022.106367

Van Thienen-Visser, K., & Fokker, P. (2017). The future of subsidence modelling: Compaction and subsidence due to gas depletion of the groningen gas field in the netherlands. *Netherlands Journal of Geosciences*, *96*, 1–12. https://doi.org/10.1017/njg.2017.10

Vaughan-Hammon, J. D., Luisier, C., Baumgartner, L. P., & Schmalholz, S. M. (2021). Alpine peak pressure and tectono-metamorphic history of the monte rosa nappe: Evidence from the cirque du véraz, upper ayas valley, italy. *Swiss journal of geosciences*, *114*(1), 20. https://doi.org/10.1186/s00015-021-00397-3

Vellinga, N. E., Hoitink, A. J. F., Van der Vegt, M., Zhang, W., & Hoekstra, P. (2014). Human impacts on tides overwhelm the effect of sea level rise on extreme water levels in the rhine–meuse delta. *Coastal Engineering*, *90*, 40–50. https://doi.org/10.1016/j.coastaleng.2014.04.005

Venditti, J. G., Li, T., Deal, E., Dingle, E., & Church, M. (2020). Struggles with stream power: Connecting theory across scales [The Binghamton Geomorphology Symposium: 50 years of Enhancing Geomorphology]. *Geomorphology*, *366*, 106817. https://doi.org/10.1016/j.geomorph.2019.07.004

Vink, A., Steffen, H., Reinhardt, L., & Kaufmann, G. (2007). Holocene relative sea-level change, isostatic subsidence and the radial viscosity structure of the mantle of northwest europe (belgium, the netherlands, germany, southern north sea). *Quaternary Science Reviews*, *26*, 3249–3275. https://doi.org/10.1016/j.quascirev.2007.07.014

Voigt, T. (n.d.). *Rhyolith: Location of the rock rhyolite near the village allzunah* [From the Friedrich Schiller University Jena]. Retrieved May 25, 2024, from https://www.igw.uni-jena.de/en/events/rock-garden-exhibition/rhyolith

Voronoi, G. (1908). Nouvelles applications des paramètres continus à la théorie des formes quadratiques. deuxième mémoire. recherches sur les parallélloèdres primitifs. *Journal für die reine und angewandte Mathematik (Crelles Journal)*, *1908*(134), 198–287. https://doi.org/doi:10.1515/crll.1908.134.198

Waldron, A., Garrity, D., Malhi, Y., Girardin, C., Miller, D. C., & Seddon, N. (2017). Agroforestry can enhance food security while meeting other sustainable development goals. *Tropical Conservation Science*, *10*, 1940082917720667. https://doi.org/10.1177/1940082917720667

Walker, J. C. G., & Kasting, J. F. (1992). Effects of fuel and forest conservation on future levels of atmospheric carbon dioxide. *Global and Planetary Change*, *5*(3), 151–189. https://doi.org/10.1016/0921-8181(92)90009-Y

Wang, Z. B., Elias, E. P. L., Van der Spek, A. J. F., & Lodder, Q. J. (2018). Sediment budget and morphological development of the dutch wadden sea: Impact of accelerated sea-level rise and subsidence until 2100. *Netherlands Journal of Geosciences*, *97*(3), 183–214. https://doi.org/10.1017/njg.2018.8

Warrlich, G., Waltham, D., & Bosence, D. (2002). Quantifying the sequence stratigraphy and drowning mechanisms of atolls using a new forward modeling program (carbonate 3-d). *Basin Research - BASIN RES*, *14*, 379–400. https://doi.org/10.1046/j.1365-2117.2002.00181.x

Water Science School (USGS). (2019). *Rain and Precipitation*. Retrieved April 30, 2024, from https://www.usgs.gov/special-topics/water-science-school/science/rain-and-precipitation#overview

Whipple, K. X., & Tucker, G. E. (2002). Implications of sediment□flux□dependent river incision models for landscape evolution. *Journal of Geophysical Research: Solid Earth*, *107*(B2). https://doi.org/10.1029/2000jb000044

Whipple, K. X., Snyder, N. P., & Dollenmayer, K. (2000). Rates and processes of bedrock incision by the Upper Ukak River since the 1912 Novarupta ash flow in the Valley of Ten Thousand Smokes, Alaska. *Geology*, *28*(9), 835–838. https://doi.org/10.1002/2016JB013310

Wigley, T. M. L. (2005). The climate change commitment. *Science*, *307*(5716), 1766–1769. https://doi.org/10.1126/science.1103934

Wigley, T. M. L. (1995). Global-mean temperature and sea level consequences of greenhouse gas concentration stabilization. *Geophysical Research Letters*, *22*(1), 45–48. https://doi.org/10.1029/94GL01011

Wilkinson, M. T., & Humphreys, G. S. (2005). Exploring pedogenesis via nuclide-based soil production rates and osl-based bioturbation rates. *Australian Journal of Soil Research*, *43*, 767–779. https://doi.org/10.1071/SR04158

Wilson, J. P., & Gallant, J. C. (2000). Primary topographic attributes.

Wischmeier, W., & Smith, D. D. (1978). *Predicting rainfall erosion losses: A guide to conservation planning* [Agricultural Handbook No. 537]. Department of Agriculture, Science; Education Administration.

Wischmeier, W., Johnson, C. B., & Cross, B. (1971). Soil erodibility nomograph for farmland and construction sites. *Journal of Soil and Water Conservation*, *26*, 5189. https://api.semanticscholar.org/CorpusID:127568318

Yanites, B. J., Becker, J. K., Madritsch, H., Schnellmann, M., & Ehlers, T. A. (2017). Lithologic effects on landscape response to base level changes: A modeling study in the context of the eastern jura mountains, switzerland. *Journal of Geophysical Research: Earth Surface*, *122*, 2196–2222. https://api.semanticscholar.org/CorpusID:134137481

Yi, Y., Liu, Q., Zhang, J., & Zhang, S. (2021). How do the variations of water and sediment fluxes into the estuary influence the ecosystem? *Journal of Hydrology*, *600*, 126523. https://doi.org/10.1016/j.jhydrol.2021.126523

Ylla Arbos, C., Blom, A., & Schielen, R. (2021). Channel Response of the Lower Rhine River to Climate Change and Human Intervention over the 21st Century [Provided by the SAO/NASA Astrophysics Data System]. *AGU Fall Meeting Abstracts*, *2021*, Article EP53A-06.

Zhang, W., Furtado, K., Wu, P., Zhou, T., Chadwick, R., Marzin, C., Rostron, J., & Sexton, D. (2021). Increasing precipitation variability on daily-to-multiyear time scales in a warmer world. *Science Advances*, *7*(31), eabf8021. https://doi.org/10.1126/sciadv.abf8021

Zhao, L., Paul, A., Malusà, M. G., Xu, X., Zheng, T., Solarino, S., Guillot, S., Schwartz, S., Dumont, T., & Salimbeni, S. (2016). Continuity of the alpine slab unraveled by high-resolution p wave tomography. *Journal of Geophysical Research: Solid Earth*, *121*(12), 8720–8737. https://doi.org/10.1002/2016JB013310

Zomer, R. J., Trabucco, A., Coe, R., & Place, F. (2009). Trees on farm: Analysis of global extent and geographical patterns of agroforestry. *ICRAF Working Paper-World Agroforestry Centre*, (89), 63 pp.

Zondervan, J. R., Whittaker, A. C., Bell, R. E., Watkins, S. E., Brooke, S. A., & Hann, M. G. (2020). New constraints on bedrock erodibility and landscape response times upstream of an active fault. *Geomorphology*, *351*, 106937. https://doi.org/10.1016/j.geomorph.2019.106937

A

Landscape Evolution Models

In Table A.1 a concise overview of some landscape evolution models are given. A short description for each LEM highlights the main purpose and practical information about these models. For a more detailed overview of different landscape evolution models see Temme et al. (2022) and for a more detailed overview and explanation of soil-landscape evolution models in particular see Van der Meij et al. (2018). Because of the suitable combination of the many available parameters and processes as well as the temporal and spatial resolution that fits our purpose, and the elimination of the other mentioned LEMs because of a lack of one of the necessary outputs (like sediment load), missing processes (like sea level), or not having the right spatial and temporal resolutions available, the LEM Badlands was chosen for this thesis.

Table A.1: An overview of different Landscape Evolution Models.

LEM	Description	Source
Badlands	Used for describing Earth surface evolution and sedimentary basins formation. Includes feedback mechanisms between tectonics, climate, erosion and sedimentation. Has sea, coastal, and fluvial processes. Spatial scales: regional to continental. Temporal scale: hundreds to millions of years. See section 2.2 for a detailed description of simulated processes and governing equations.	Salles, Ding, and Brocard, 2018
CAESAR	Cellular LEM that emphasizes on fluvial processes. Models the morphological change in river catchments. Is able to model floodplains and levee breaches. See CAESAR Lisflood model.	Van de Wiel et al., 2007
CAESAR Lisflood	Combination of the CAESAR model with the Lisflood-FP 2D hydrodynamic flow model. Simulates erosion and deposition in river catchments and reaches. Spatial scales: $1km^2$-$1000km^2$. Temporal scales: hours to thousands of years.	Coulthard et al., 2013
CHILD	Computes the time evolution of topographical surfaces by fluvial and hillslope erosion and sediment transport. Includes (not an exhaustive list) climate forcings via discrete storm events with variable duration, intensity, and interval time; generation of runoff though either infiltration-excess or saturation-excess mechanisms; erosion through channelized surface runoff; meandering and floodplain deposition. No restrictions on temporal scale except the time of an individual storm event. Best suited for relatively small scales (less than $100km^2$)	Tucker et al., 2001
eSCAPE	Modelling Earth surface dynamics, primarily for global scales over geological time.	Salles, 2019
GOSPL	Global scale reconstruction of basins and landscape simulation.	Salles et al., 2020
LAPSUS	A dynamic landscape evolution model which includes overland erosion, landsliding, tillage erosion (soil), and tectonics. It is able to deal with several human landscape interventions and suited to quantify catchment-scale erosion processes. Temporal scales from years to millennial. Spatial scales from 1 to $1000m^2$.	Sonneveld et al., 2010
LORICA	A Soil-Landscape model used to study interaction between soil and landscape development. It is based on LAPSUS. It includes soil formation processes, soil profile heterogeneity, negative feedback from vegetation and armouring of soil as well as the selectivity of particle size on the erosion-deposition process. It also includes processes as evaporation and infiltration. It does not however, include sea level, nor does it include sediment flux as an output. Must run at either smaller temporal resolution or larger spatial resolution.	Temme and Van-walleghem, 2016

B

Land Use in Percentage of River Catchment

The land use as a percentage of river catchment for the six distinguishable sections of the Rhine, four major tributaries, the total of the Rhine + tributaries, and the Meuse are given in Table B.1. The data was taken from Tockner et al., 2009.

Table B.1: Land usage as percentage of river catchment. Agriculture includes both croplands and pastures. Adapted from Tockner et al., 2009.

	Alpine Rhine	**High Rhine**	**Upper Rhin**	**Middle Rhine**	**Lower Rhine**	**Delta Rhine**	**Aare (High Rhine)**	**Neckar (Upper Rhine)**	**Main (Upper Rhine)**	**Moselle (Middle Rhine)**	**Total Rhine (with tributaries)**	**Meuse**
Catchment Area (km^2)	6155	30148	62967	41810	18836	25347	17606	13950	27251	28133	272203	34548
Land use of Catchment (%)												
Urban	0.4	0.9	2.1	1.1	9.0	3.9	0.7	2.1	1.8	1.0	2.4	11.4
Agriculture	19.8	55.0	74.1	83.5	79.4	89.7	50.5	74.6	80.2	84.6	74.2	56.8
Forest	52.4	32.4	23.7	15.1	10.9	1.9	32.3	23.3	18.0	14.1	20.1	28.7
Natural grassland	6.8	1.6	0.0	0.0	0.2	0.1	2.7	0.0	0.0	0.0	0.5	1.7
Wetland	1.4	0.2	0.0	0.0	0.0	0.0	0.4	0.0	0.0	0.0	0.08	0.4
Shrub	17.9	3.1	0.0	0.0	0.0	0.0	5.2	0.0	0.0	0.0	1.1	0.0
Open water	0.0	5.2	0.2	0.3	0.6	4.4	5.4	0.0	0.0	0.3	1.5	0.9
Barren/sparce vegetation	1.3	1.7	0.0	0.0	0.0	0.0	2.8	0.0	0.0	0.0	0.4	0.1
Protected area	0.0	0.4	0.2	0.3	1.0	0.9	0.4	0.0	0.0	0.5	0.4	0.2

C

Ecosystem Services and Effects of Agroforestry

In Figure C.1 the different ecosystem services and effects of agroforestry are shown. Agroforestry can be divided in three main categories: agrisilviculture, silvopastoral, and agrosilvopastoral. Agrisilvicultural systems consist of the combination of crops and trees. Silvopastoral systems combine the grazing of domesticated animals on pastures or rangelands with forestry. Lastly, agrosilvopastoral systems combine the previous two, and consist of a system of crops, trees, and animals (FAO, 2015).

Figure C.1: Ecosystem services and effects of agroforestry. From Sudomo et al., 2023, adapted from Bucheli and Bokelmann, 2017

D

Detailed Land Use Map of Western and Central Europe

In Figure D.1 the legend for the land use map given in Figure D.2 is shown. An interactive version of this map can be found at Copernicus Land Monitoring Service (CLMS), 2020.

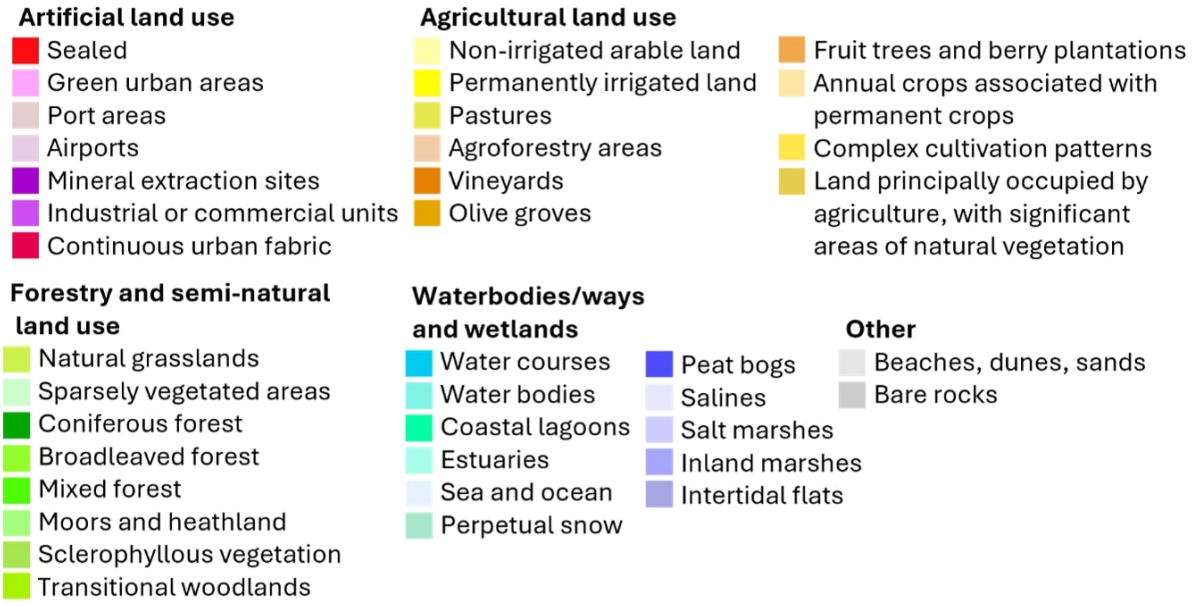

Figure D.1: Legend of Figure D.2. Prepared using data from Copernicus Land Monitoring Service (CLMS), 2020.

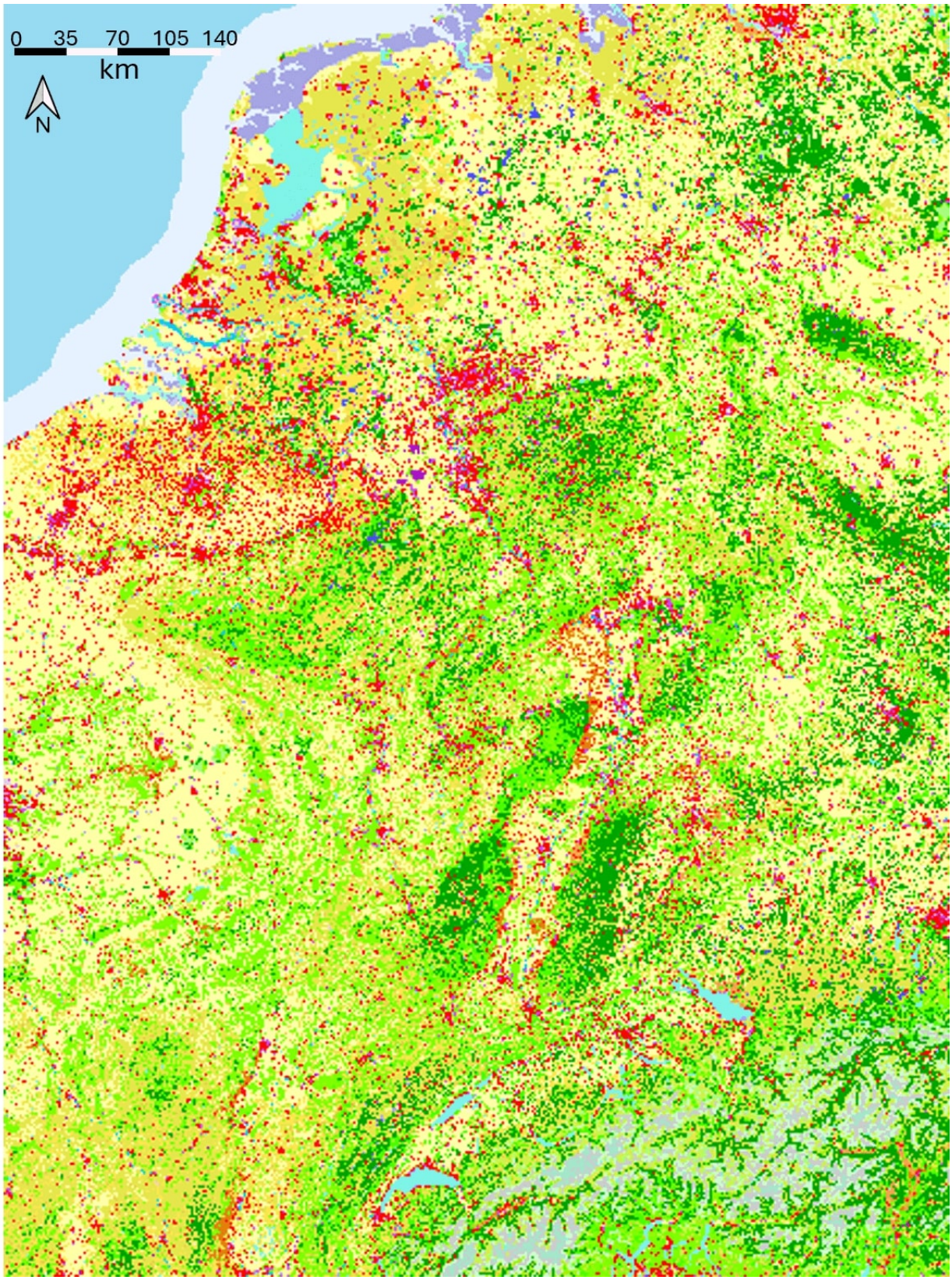

Figure D.2: Detailed land use map for the greater area of interest. See Figure D.1 for the corresponding legend. Prepared using data from Copernicus Land Monitoring Service (CLMS), 2020. The reader is referred to the given reference for an interactive map of the one given here.

E

The disappearing of the Rhine

In Figure E the discharge maps for two time steps of the S2P2L1 simulation are shown. In the left image for t = 200yrs the Rhine is still clearly visible with a higher discharge than any other rivers present. One time step later at t = 400yrs as shown in the right picture of the figure we see the clear discharge signal of the Rhine disappear across the whole reach from Lake Constance until the Delta Rhine. The tributaries along the whole length of the Rhine, as well as the Alpine Rhine until Lake Constance do not disappear nor do they show a change in discharge. These tributaries should at least supply the channel of the Rhine with some water, producing a small discharge along the channel. This is not the case however. The reason for this disappearing of the Rhine is unknown.

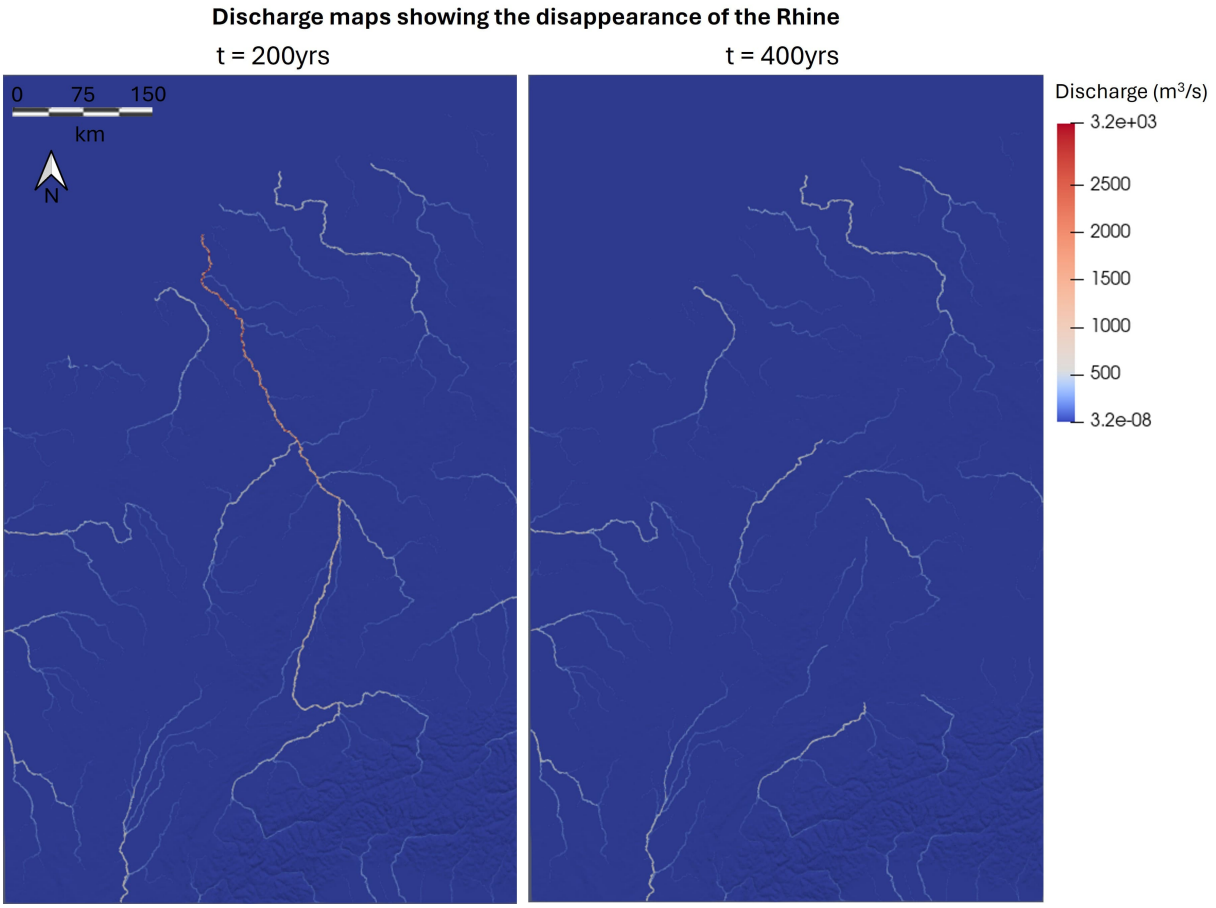

Figure E.1: The discharge maps for t = 200yrs and t = 400yrs for the S2P2L1 simulation. On the right map we see the Rhine suddenly disappear. Maps made using ParaView V5.12.0.

In Figure **??** the discharge maps for two time steps of the S3P2L2 simulation are shown. In the left

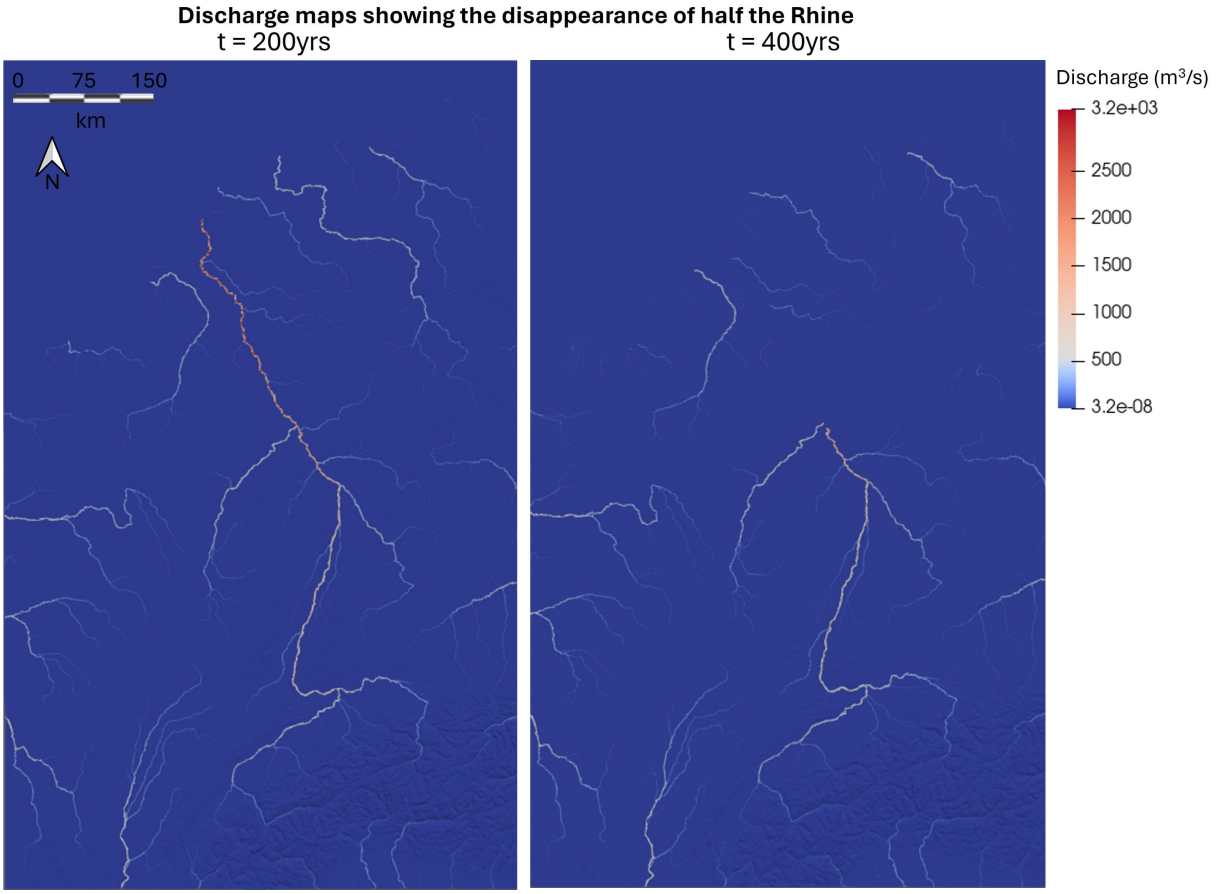

Figure E.2: The discharge maps for t = 200yrs and t = 400yrs for the S3P2L2 simulation. On the right map we see the Middle, Lower, and Delta Rhine suddenly disappear. Maps made using ParaView V5.12.0.

image for t = 200yrs the Rhine is still clearly visible with a higher discharge than any other rivers present. One time step later at t = 400yrs as shown in the right picture of the figure we see the clear discharge signal of the Rhine disappear across the reach from the Middle Rhine until the Delta Rhine. This is before the second smaller decrease in discharge. The tributaries along the whole length of the disappeared part of the Rhine do not disappear nor do they show a change in discharge similar to Figure E.1. In contrast to Figure E.1, the larger river in the northeast of the map also disappears while the smaller rivers very close to it are virtually unchanged. This river disappears from the upstream however, while the downstream half of the Rhine disappeared. The second smaller decrease of the discharge in the P2L2 plot in Figure 9.4 after the initial decrease in discharge is caused by an additional small section of the Rhine that disappears. The additional variability visible as the small peaks in Figure 9.4 are caused by the same section that re- and disappears again throughout the simulation. One such change is shown in Figure E.3.

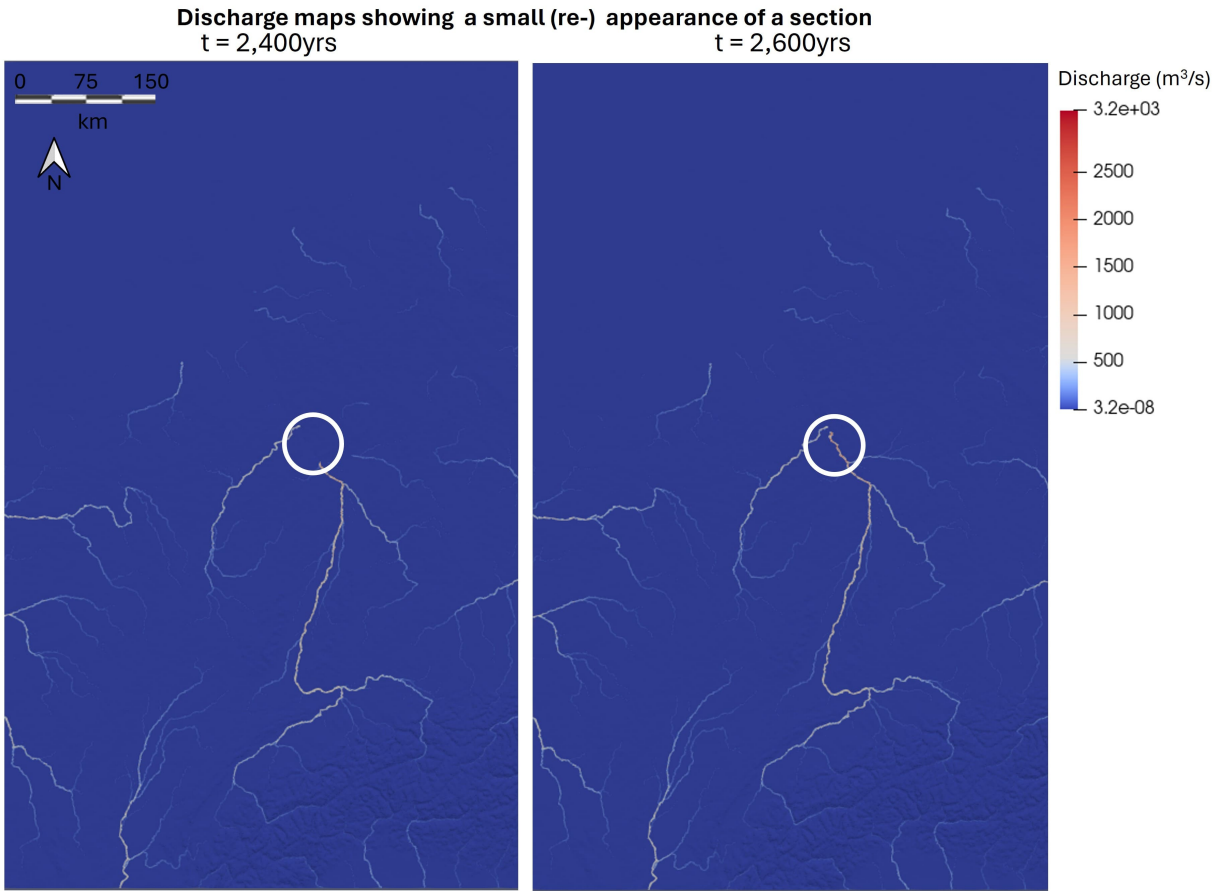

Figure E.3: The discharge maps for t = 2,400yrs and t = 2,600yrs for the S3P2L2 simulation. On the right map we see the additional small section (indicated by the circle) of the Rhine suddenly appear, before it disappears again one time step after this. Maps made using ParaView V5.12.0.

F

Kolmogorov–Smirnov test

A two-sample Kolmogorov–Smirnov (KS) test is a statistical test that gives us a measure for the difference in the distribution of two data sets. It is a nonparametric test, meaning it makes minimal assumptions about the distribution of the studied data (Knuth, 1997). We introduce the null hypothesis as 'the two data sets (or samples) are drawn from the same distribution'. The alternative hypothesis is that the two data sets do not share a distribution, i.e. one of the data sets is different. When the p-value resulting from this test is lower than the significance level α, we reject the null hypothesis. This translates to 'the two data sets are different from eachother'. It is important to note that this test does not tell us in what way or how much the values and/or the distributions of these data sets differ.

The significance level is usually taken to be $\alpha = 0.05$ (Andrade, 2019). Although this is an arbitrary choice usually based on convention (Kim and Choi, 2019), in our case it is a good significance level based on the sample size, uncertainty, and power of the statistical test. For our KS test, we reject the null hypothesis (i.e. the two data sets are different) when the following condition holds:

$$D_{n,m} > \sqrt{-\ln\left(\frac{\alpha}{2}\right) \cdot \frac{1 + \frac{m}{n}}{2m}}, \tag{F.1}$$

where $D_{n,m}$ is the KS test statistic, m and n are the sample sizes, and α is the significance level. For $alpha = 0.05$ and our sample size of $n = m = 50$ we find $D_{50,50} > 0.271$.

The D-statistics and p-values resulting from the KS test on our realizations are given below. Table F.1 has the values for the S1 realizations, Table F.2 for S2, Table F.3 for S3, and Table F.4 for the S4 realizations.

Table F.1: D-statistic and p-values from the Kolmogorov–Smirnov test for all S1 realizations. The values are given as ($D_{50,50}$,p).

S1 KS test results							
	R	**P1L1**	**P1L2**	**P1L3**	**P2L1**	**P2L2**	**P2L3**
R	(0, 1)	(0.12, 0.87)	(0.1, 0.97)	(0.2, 0.27)	(0.34, 0.006)	(0.28, 0.04)	(0.34, 0.006)
P1L1		(0, 1)	(0.1, 0.97)	(0.2, 0.27)	(0.38, 0.001)	(0.34, 0.006)	(0.34, 0.006)
P1L2			(0, 1)	(0.12, 0.87)	(0.38, 0.001)	(0.34, 0.006)	(0.38, 0.001)
P1L3				(0, 1)	(0.42, 2e-4)	(0.46, 4e-5)	(0.46, 4e-5)
P2L1					(0, 1)	(0.18, 0.4)	(0.12, 0.87)
P2L2						(0, 1)	(0.18, 0.4)
P2L3							(0, 1)

Table F.2: D-statistic and p-values from the Kolmogorov–Smirnov test for all S2 realizations. The values are given as ($D_{50,50}$,p).

S2 KS test results							
	R	**P1L1**	**P1L2**	**P1L3**	**P2L1**	**P2L2**	**P2L3**
R	(0, 1)	(0.38, 0.001)	(0.26, 0.07)	(0.24, 0.11)	(0.42, 2e-4)	(0.52, 2e-6)	(0.5, 5e-6)
P1L1		(0, 1)	(0.22, 0.18)	(0.16, 0.55)	(0.5, 5e-6)	(0.52, 2e-6)	(0.52, 2e-6)
P1L2			(0, 1)	(0.1, 0.97)	(0.56, 1e-7)	(0.56, 1e-7)	(0.56, 1e-7)
P1L3				(0, 1)	(0.48, 1e-5)	(0.5, 5e-6)	(0.5, 5e-6)
P2L1					(0, 1)	(0.22, 0.18)	(0.2, 0.27)
P2L2						(0, 1)	(0.22, 0.18)
P2L3							(0, 1)

Table F.3: D-statistic and p-values from the Kolmogorov–Smirnov test for all S3 realizations. The values are given as ($D_{50,50}$,p).

S3 KS test results							
	R	**P1L1**	**P1L2**	**P1L3**	**P2L1**	**P2L2**	**P2L3**
R	(0, 1)	(0.38, 0.001)	(0.28, 0.04)	(0.36, 0.003)	(0.74, 1e-13)	(0.62, 3e-9)	(0.74, 1e-13)
P1L1		(0, 1)	(0.26, 0.07)	(0.22, 0.18)	(0.74, 1e-13)	(0.62, 3e-9)	(0.52, 2e-6)
P1L2			(0, 1)	(0.22, 0.18)	(0.74, 1e-13)	(0.62, 3e-9)	(0.56, 1e-7)
P1L3				(0, 1)	(0.74, 1e-13)	(0.62, 3e-9)	(0.52, 2e-6)
P2L1					(0, 1)	(0.64, 6e-10)	(0.42, 2e-4)
P2L2						(0, 1)	(0.42, 2e-4)
P2L3							(0, 1)

Table F.4: D-statistic and p-values from the Kolmogorov–Smirnov test for all S4 realizations. The values are given as ($D_{50,50}$,p).

S4 KS test results							
	R	**P1L1**	**P1L2**	**P1L3**	**P2L1**	**P2L2**	**P2L3**
R	(0, 1)	(0.38, 0.001)	(0.28, 0.04)	(0.36, 0.003)	(0.32, 0.01)	(0.3, 0.02)	(0.34, 0.006)
P1L1		(0, 1)	(0.2, 0.27)	(0.08, 0.998)	(0.14, 0.72)	(0.18, 0.40)	(0.1, 0.97)
P1L2			(0, 1)	(0.18, 0.40)	(0.18, 0.40)	(0.12, 0.87)	(0.14, 0.72)
P1L3				(0, 1)	(0.16, 0.55)	(0.16, 0.55)	(0.12, 0.87)
P2L1					(0, 1)	(0.18, 0.40)	(0.12, 0.87)
P2L2						(0, 1)	(0.2, 0.27)
P2L3							(0, 1)

G

XML File Example with Input Values for the S1P1L1 Realization

Here an overview of the input file used by Badlands is given. We will use the example of realization S1P1L1. We will start with the input of the topography through a regular grid structure in Figure G.1, followed by the simulation time structure in Figure G.2, and the sea level structure in Figure G.3. Figure G.4 shows the tectonic structure, and Figure G.5 shows the precipitation structure. Figures G.6 and G.7 together show the stream power law structure. Figure G.8 shows the flux-dependent function structure (where the fluvial incision model is defined), followed by the erodibility structure in Figure G.9. The hillslope diffusion parameters are given in Figure G.10. In Figures G.11 and G.12 the wave global parameters are given, including the definition of the wave orientation and significant wave heights in the 'wave climate' in G.12. Lastly, the command to define a name for an output folder is given in G.13.

```
−<badlands>
   <!-- Regular grid structure -->
  −<grid>
     <!-- Digital elevation model file path -->
     <demfile>Data/Topography Maps/TopoMap_1500.csv</demfile>
    −<!--
        Optional parameter (integer) used to decrease TIN resolution.
                    The default value is set to 1. Increasing the factor
                    value will multiply the digital elevation model resolution
                    accordingly.
     -->
     <resfactor>1</resfactor>
     <!-- Boundary type: flat, slope, fixed or wall -->
     <boundary>slope</boundary>
    −<!--
        Optional parameter (integer) used to force depression-less
                    surface at the start of the simulation. The default value is 0
                    to turn the option off, put it to 1 to enable it.
     -->
     <nopit>0</nopit>
   </grid>
```

Figure G.1: The first part of the XML input file, where a regular grid structure is defined. Find a different example at Badlands Group, 2019.

```
<!-- Simulation time structure -->
-<time>
   <!-- Simulation start time [a] -->
   <start>0.</start>
   <!-- Simulation end time [a] -->
   <end>10000.</end>
   <!-- Minimum time step [a]. Default is 1. -->
   <mindt>100.</mindt>
   <!-- Display interval [a] -->
   <display>200.</display>
  -<!--
      Mesh output frequency based on the display interval. (integer)
                  Considering a display interval of T yrs and a mesh output of K
                  the mesh will be stored every T*K yrs - (optional default is 1)
   -->
   <meshout>1</meshout>
</time>
```

Figure G.2: Part of the XML input file where the simulation time structure is defined. Find a different example at Badlands Group, 2019.

```
<!-- Sea-level structure -->
-<sea>
   <!-- Relative sea-level position [m] -->
   <position>0.</position>
   <!-- Sea-level curve - (optional) -->
   <curve>Data/Sea levels/Sealv1_1280PgC.csv</curve>
</sea>
```

Figure G.3: Part of the XML input file where the sea level curve is defined. Find a different example at Badlands Group, 2019.

```
<!-- Tectonic structure -->
<tectonic>
  <!--
      Is 3D displacements on ? (1:on - 0:off). Default is 0.
  -->
  <disp3d>0</disp3d>
  <!--
      Only relevant when 3D displacements is on.
                  Closest distance [m] between nodes before
                  merging happens. This is optional if not given
                  the merging distance is set to half the resolution
                  of the digital elevation input file.
  -->
  <merge3d>200.</merge3d>
  <!--
      Only relevant when 3D displacements is required.
                  This is useful if the horizontal displacements provided
                  in each maps are larger than the TIN resolution. In this
                  case, it is recommended to split each displacement periods
                  in evenly spaced intervals of given time duration [a].
  -->
  <time3d>5000.</time3d>
  <!-- Number of tectonic events -->
  <events>1</events>
  <!-- Displacement definition -->
  <disp>
    <!-- Displacement start time [a] -->
    <dstart>0.</dstart>
    <!-- Displacement end time [a] -->
    <dend>10000.</dend>
    <!-- Displacement map [m] -->
    <dfile>Data/Subsidence Maps/Subs_10k_fltrd_res1500.csv</dfile>
  </disp>
</tectonic>
```

Figure G.4: Part of the XML input file where the tectonic structure is defined. For T2 the amount of events was set to 3, and the section between <disp> and </disp> was repeated three times, adjusting the subsidence/uplift map, and the time it should be active. Find a different example at Badlands Group, 2019.

```
<!--
    Precipitation structure
            The following methods can be used:
               - an uniform precipitation value for the entire region [m/a]
               - a map containing precipitation values for each nodes of the regular grid
               - a linear elevation dependent precipitation function
               - an orographic precipitation computed using Smith & Barstad theory (2004)

 -->
<precipitation>
   <!-- Number of precipitation events -->
   <climates>2</climates>
   <!-- Precipitation map definition -->
   <rain>
      <!-- Rain start time [a] -->
      <rstart>0.</rstart>
      <!-- Rain end time [a] -->
      <rend>300.</rend>
      <!-- Precipitation map [m/a] -->
      <map>
         Data/Precipitation Maps/PrecipMap_ini_01deg_res1500.csv
      </map>
   </rain>
   <!-- Precipitation map definition -->
   <rain>
      <!-- Rain start time [a] -->
      <rstart>300.</rstart>
      <!-- Rain end time [a] -->
      <rend>10000.</rend>
      <!-- Precipitation map [m/a] -->
      <map>
         Data/Precipitation Maps/Precip_Uni_1280_max_res1500.csv
      </map>
   </rain>
</precipitation>
```

Figure G.5: Part of the XML input file where the precipitation structure is defined. Here we use a non-uniform precipitation map. It is also possible to give badlands one values which will then be used for the whole map. Find an example of this at Badlands Group, 2019.

```
-<!--
    Stream power law parameters:
            The stream power law is a simplified form of the usual expression of
            sediment transport by water flow, in which the transport rate is assumed
            to be equal to the local carrying capacity, which is itself a function of
            boundary shear stress.
 -->
-<sp_law>
  -<!--
      Make the distinction between purely erosive models (0) and erosion /
                deposition ones (1). Default value is 1.
   -->
   <dep>1</dep>
  -<!--
      Critical slope used to force aerial deposition for alluvial plain,
                in [m/m] (optional).
   -->
   <slp_cr>0.001</slp_cr>
  -<!--
      Maximum percentage of deposition at any given time interval from rivers
                sedimentary load in alluvial plain. Value ranges between [0,1] (optional).
   -->
   <perc_dep>0.5</perc_dep>
  -<!--
      Maximum lake water filling thickness. This parameter is used
                to defined maximum water level in depression area.
                Default value is set to 200 m. Based on Lake Constance depth
   -->
   <fillmax>252.</fillmax>
  -<!--
      Values of m and n indicate how the incision rate scales
                with bed shear stress for constant value of sediment flux
                and sediment transport capacity.
                Generally, m and n are both positive, and their ratio
                (m/n) is considered to be close to 0.5
   -->
   <m>0.5</m>
   <n>1.0</n>
  -<!--
      The erodibility coefficient is scale-dependent and its value depends
                on lithology and mean precipitation rate, channel width, flood
                frequency, channel hydraulics. In case where the erodibility
                structure is turned on, this coefficient is applied to the reworked
                sediments.
   -->
   <erodibility>1.e-6</erodibility>
  -<!--
      Number of steps used to distribute marine deposit.
                Default value is 5 (integer). (optional)
   -->
   <diffnb>5</diffnb>
```

Figure G.6: First part of the XML input file where the stream power law parameters are defined. This part continues in Figure G.7. Find a different example at Badlands Group, 2019.

```
<!--
    Proportion of marine sediment deposited on downstream nodes. It needs
                to be set between ]0,1[. Default value is 0.9 (optional).
 -->
 <diffprop>0.9</diffprop>
<!--
    Scaling parameter for diffprop value that is dependent on local
                topographic slope. Recommended value is 2000.0. Comment out or remove
                to revert to fixed diffprop value for entire domain. See Thran et
                al. 2020, G-cubed
 -->
 <propa>2000.</propa>
<!--
    Additional necessary scaling parameter for slope-dependent diffprop.
                Recommended value is 0.005. Comment out or remove to revert to fixed
                diffprop value for entire domain.
 -->
 <propb>0.005</propb>
<!--
    Critical density of water+sediment flux to trigger hyperpycnal current
                off shore - (optional)
 -->
 <dens_cr>1060.</dens_cr>
<!--
    Deep basin depth under which hyperpycnal flow are forced to
                deposit [m] - (optional)
 -->
 <deepbasin>-2500.</deepbasin>
</sp_law>
```

Figure G.7: Second part of the XML input file where the rest of the stream power law parameters are defined. Find a different example at Badlands Group, 2019.

```
-<!--
    Flux-dependent function structure  (optional)
            It is possible to modify the general detachment limited law to simulate channel
            evolution governed by sediment flux-dependent bedrock incision rules.
            Visit tinyurl.com/badlands-incision for more information.

 -->
-<sedfluxfunction>
  -<!--
      Incision model type is defined with an integer between 0 and 4:
                  + 0 - detachment limited (default) does not require to set additional parameters.
                  + 1 - generalised undercapacity model (linear sedflux dependency) [cover effect]
                  + 2 - parabolic sedflux dependency [tool & cover effect]
                  + 3 - Turowski sedflux dependency [tool & cover effect]
                  + 4 - saltation abrasion incision model
                 See Hobley et al. (2011), JGR, 116 for more information.

   -->
   <modeltype>3</modeltype>
  -<!--
      Volumetric sediment transport capacity formulation is built with a stream power law
                 and requires the definition of 2 exponents for water discharge (mt) and slope (nt).
   -->
   <mt>1.5</mt>
   <nt>1.</nt>
  -<!--
      Transportability of channel sediment (erodibility coefficient)
   -->
   <kt>2.e-6</kt>
   <!--2.e-6 is default value-->
  -<!--
      Power law relation between channel width and discharge
   -->
   <kw>1</kw>
   <b>0.5</b>
  -<!--
      Erodibility dependence to the precipitation is defined with an exponent.
                Default value is set to 0. See Murphy et al. (2016), Nature, 532.
   -->
   <mp>0.</mp>
  -<!--
      Bedload versus slope dependency. This option changes the amount of incision based on
                 the proportion of bedload material (i.e. gravels) present in stream. For any point in
                 the landscape the amount of bedload material is assumed slope-dependent. The user can
                 choose between the following options:
                  + 0 - no dependency (default)
                  + 1 - linear dependency
                  + 2 - exponential growth
                  + 3 - logarithmic growth

   -->
   <bedslp>0</bedslp>
 </sedfluxfunction>
```

Figure G.8: Part of the XML input file used for defining the flux-dependent function structure. Note that not all parameters shown here are used in the simulations due to the choice of fluvial incision model. Find a different example at Badlands Group, 2019.

```
<!--
    Erodibility structure simple
            This option allows you to specify different erodibility values either on the surface
           or within a number of initial stratigraphic layers.
 -->
<erocoeff>
   <erolayers>2</erolayers>
  <!--
      The layering is defined from top to bottom, with:
   -->
  <!--
      Variable erodibilities and constant layer thickness
   -->
  <erolay>
     <!-- Variable erodibilities for the considered layer. -->
    <eromap>
       Data/K-Factor Maps/K_factor_UrbanKto0_res1500_kx02.csv
     </eromap>
    <!--
       Variable thicknesses for the considered layer [m].
     -->
     <thmap>Data/Layer Thickness/ThicknessMap_Soil_res1500.csv</thmap>
   </erolay>
  <erolay>
     <!-- Variable erodibilities for the considered layer. -->
     <eromap>Data/K-Factor Maps/Bedrock_Kfactor_res1500.csv</eromap>
    <!--
       Uniform thickness value for the considered layer [m].
     -->
     <thcst>500</thcst>
   </erolay>
 </erocoeff>
```

Figure G.9: Part of the XML input file where the erodibility structure is defined. Both the erodibility, as well as the thickness of the corresponding layers are defined here. Find a different example at Badlands Group, 2019.

```
<!--
    Hillslope diffusion parameters:
            Parameterisation of the sediment transport includes the simple creep transport
            law which states that transport rate depends linearly on topographic gradient.
 -->
<creep>
   <!-- Surface diffusion coefficient [m2/a] -->
   <caerial>0.001</caerial>
   <!-- Marine diffusion coefficient [m2/a] -->
   <cmarine>0.005</cmarine>
  <!--
      Critical slope for non-linear diffusion [m/m] - optional.
                  Default value is set to 0 meaning non-linear diffusion is not considered.
   -->
   <cslp>0.8</cslp>
  <!--
      River transported sediment diffusion
                  coefficient in marine realm [m2/a]
   -->
   <criver>10.</criver>
  <!--
      Critical slope above which slope failure are triggered [m/m] - optional.
                  Default value is set to 0 meaning non-linear diffusion is not considered.
   -->
   <sfail>0.274</sfail>
  <!--
      Triggered failure sediment diffusion coefficient [m2/a]
   -->
   <cfail>3.</cfail>
 </creep>
```

Figure G.10: Part of the XML input file where the hillslope diffusion parameters are defined. Find a different example at Badlands Group, 2019.

```
<!-- Wave global parameters structure -->
<waveglobal>
  <!--
     Wave model to consider either SWAN or WaveSed.
                 Default is WaveSed (wmodel = 0).
  -->
  <wmodel>0</wmodel>
  <!-- Wave interval [a] -->
  <twave>250.</twave>
  <!-- Wave grid resolution [m] -->
  <wres>1000.</wres>
  <!-- Maximum depth for wave influence [m] -->
  <wbase>20</wbase>
  <!-- Number of wave climate temporal events. -->
  <events>1</events>
  <!-- Mean grain size diameter [m] -->
  <d50>0.00025</d50>
  <!--
     Wave sediment diffusion coefficient. Default is 50.
  -->
  <wCd>50.</wCd>
  <!--
     Wave sediment entrainment coefficient. Value needs to be
                 set between ]0,1]. Default is 0.5
  -->
  <wCe>0.5</wCe>
  <!-- Maximum wave-induced erosion [m] -->
  <wEro>1.66</wEro>
  <!-- Maximum depth for wave influence [m] -->
  <wbase>20</wbase>
  <!--
      Steps used to perform sediment transport.
                Default is 1000.
  -->
  <tsteps>1000</tsteps>
  <!--
      Steps used to perform sediment diffusion.
                Default is 1000.
  -->
  <dsteps>1000</dsteps>
</waveglobal>
```

Figure G.11: First part of the XML input file where the wave parameters are defined. This part continues in Figure G.12. Find a different example at Badlands Group, 2019.

```
<!-- Climatic wave definition for WaveSed model. -->
<climate>
<!--
Percentage of time this event is active during the time interval.
-->
<perc>0.39</perc>
<!-- Significant wave height (in m) -->
<hs>1.15</hs>
<!--
Wave direction in degrees (between 0 and 360) from the
X-axis (horizontal) anti-clock wise. It specifies where the waves are
actually coming from. The wave directions are reduced to 8 possible ones:
East (dir = 0) - North (dir = 90) - West (dir = 180) - South (dir = 270) -
NE (0<dir<90) - NW (90<dir<180) - SW (180<dir<270) - SE (dir>270).
-->
<dir>205</dir>
</climate>
<!-- Climatic wave definition for WaveSed model. -->
<climate>
<!--
Percentage of time this event is active during the time interval.
-->
<perc>0.36</perc>
<!-- Significant wave height (in m) -->
<hs>1.15</hs>
<!--
Wave direction in degrees (between 0 and 360) from the
X-axis (horizontal) anti-clock wise. It specifies where the waves are
actually coming from. The wave directions are reduced to 8 possible ones:
East (dir = 0) - North (dir = 90) - West (dir = 180) - South (dir = 270) -
NE (0<dir<90) - NW (90<dir<180) - SW (180<dir<270) - SE (dir>270).
-->
<dir>115</dir>
</climate>
<!-- Climatic wave definition for WaveSed model. -->
<climate>
<!--
Percentage of time this event is active during the time interval.
-->
<perc>0.25</perc>
<!-- Significant wave height (in m) -->
<hs>1.15</hs>
<!--
Wave direction in degrees (between 0 and 360) from the
X-axis (horizontal) anti-clock wise. It specifies where the waves are
actually coming from. The wave directions are reduced to 8 possible ones:
East (dir = 0) - North (dir = 90) - West (dir = 180) - South (dir = 270) -
NE (0<dir<90) - NW (90<dir<180) - SW (180<dir<270) - SE (dir>270).
-->
<dir>165</dir>
</climate>
</wave>
```

Figure G.12: Second part of the XML file for defining the wave parameters. Here the significant wave height, wave orientation, and percentage of time this orientation of waves are present in the simulation are defined. Find a different example at Badlands Group, 2019.

```
<!-- Output folder path -->
<outfolder>Output/output_S1_T1_P1_L1_res1500</outfolder>
</badlands>
```

Figure G.13: Final part of the XML input file where the output folder and path is defined.